Bringing exoplanets into sharper view

Storm chasing on distant worlds

Sutlieff, B.J.

Publication date
2023

Document Version
Final published version

BRINGING EXOPLANETS INTO SHARPER VIEW

BEN J. SUTLIEFF

BRINGING EXOPLANETS

INTO SHARPER VIEW

STORM CHASING ON DISTANT WORLDS

BEN JAMES SUTLIEFF

Bringing Exoplanets Into Sharper View

STORM CHASING ON DISTANT WORLDS

Ben James Sutlieff

contact: b.j.sutlieff@uva.nl, bensutlieff@gmail.com
ORCID iD: 0000-0002-9962-132X

Bringing Exoplanets Into Sharper View: Storm Chasing on Distant Worlds
PhD Thesis, Anton Pannekoek Institute for Astronomy, Universiteit van Amsterdam

Cover by Sophie Marshall (sophcavell@gmail.com, Instagram: @sophiecavelldesign)
Printed by Gildeprint

ISBN: 978-94-6419-800-3

UNIVERSITY OF AMSTERDAM

The research included in this thesis was carried out at the Anton Pannekoek Institute for Astronomy (API) of the University of Amsterdam (UvA). It was supported by the Netherlands Research School for Astronomy (NOVA). Support was occasionally provided by the Leids Kerkhoven-Bosscha Fonds (LKBF). This thesis was written in LaTeX. The API Equity, Diversity and Inclusion logo was designed by aristhought art (https://aristhought.com/).

Bringing Exoplanets Into Sharper View
Storm Chasing on Distant Worlds

ACADEMISCH PROEFSCHRIFT

ter verkrijging van de graad van doctor
aan de Universiteit van Amsterdam
op gezag van de Rector Magnificus
prof. dr. ir. P.P.C.C. Verbeek
ten overstaan van een door het College voor Promoties ingestelde commissie,
in het openbaar te verdedigen in de Agnietenkapel
op donderdag 8 juni 2023, te 10:00 uur

door

Ben James Sutlieff

geboren te Frimley

Promotiecommissie

Promotor:	prof. dr. S.B. Markoff	Universiteit van Amsterdam
Copromotores:	prof. dr. J.L. Birkby	University of Oxford
	dr. M.A. Kenworthy	Universiteit Leiden
Overige leden:	dr. J.M.L.B. Desert	Universiteit van Amsterdam
	prof. dr. L. Kaper	Universiteit van Amsterdam
	dr. A. Oklopčić	Universiteit van Amsterdam
	prof. dr. B.R. Brandl	Universiteit Leiden
	dr. J. Vos	American Museum of Natural History
	prof. dr. R.A.D. Wijnands	Universiteit van Amsterdam

Faculteit der Natuurwetenschappen, Wiskunde en Informatica

Dedicated to my family, for their unconditional support, love, & patience

We shall not cease from exploration
And the end of all our exploring
Will be to arrive where we started
And know the place for the first time.
T.S. Eliot

Contents

Chapter 1

Introduction

1.1 Worlds beyond our own

One of the most exciting aspects of exoplanetary science is that it strives to answer some of the most fundamental questions posed by humanity. Are there worlds beyond our own? If so, what are they like? Are they too inhabited by life? While these questions have long been contemplated, today we are in the best position yet to formalise detailed answers to them and perhaps even, through a newfound understanding of other worlds, shed light on the nature of our own origin.

We have known of the existence of the five planets in our own Solar System that appear brightest in the night sky (Mercury, Venus, Mars, Jupiter, and Saturn) since antiquity, but our understanding of their nature was largely confined to philosophical thought until the first studies with optical telescopes in the 17th century. Early observations demonstrated that these objects were not mere points of light; spots and bands could be seen on Jupiter, there were giant rings around Saturn, and the planets possessed moons of their own (e.g. Galilei 1610; Huygens 1659; Cassini 1673, 1686). The mountains and craters of our own Moon were also seen clearly for the first time, painting a vivid picture of a world not entirely unlike Earth. In the centuries that followed, countless new Solar System objects were discovered through telescopic observations, including the icy planets Uranus and Neptune (Herschel & Watson 1781; Adams 1846; Le Verrier 1846a,b; Galle 1846).[1] The worlds of our Solar System would become ever more familiar to us as time went on, especially as they were visited by the first space probes in the latter half of the 20th century, which returned detailed photographs of the planets and their moons from up close.

While the planets of the Solar System have now been studied for hundreds of years, it was only relatively recently that the first *exoplanets* – planets beyond our solar system – were discovered. Unexpectedly, the first two exoplanets were discovered in orbit not around

[1] Both Uranus and Neptune were actually observed on multiple occasions prior to their discovery as planets, but were mistaken for stars. William Herschel identified Uranus as a Solar System object in 1781 and was credited with its discovery, but he originally believed it to be a comet; follow-up observations by others in the astronomy community later confirmed its status as a planet.

a typical star, but around a pulsar: a rapidly rotating remnant left behind when after a supergiant star undergoes a supernova explosion (Wolszczan & Frail 1992). A third exoplanet was discovered in this system soon after (Wolszczan 1994).[1] The first exoplanet orbiting a typical sun-like star on its main sequence, 51 Pegasi b, was discovered just a few years after the first pulsar exoplanets (Mayor & Queloz 1995). However, this system too was very different from our own. 51 Pegasi b lies far closer to its host star than any of the planets in our Solar System do to the Sun, completing an orbit every ∼4.2 Earth days (compared to Mercury's ∼87.97 days). Its surface temperature is superheated to ∼1300 K due to its close proximity to its star, almost double that of Venus.[2] As of 1st January 2023, there are 5235 confirmed exoplanets (see Figure 1.1), with a further ∼7000 candidate exoplanets awaiting confirmation.[3] We now know that not only are there countless worlds beyond our own, but that these worlds possess a remarkable diversity of properties and exist in a wide range of environments.

In this introduction, I aim to provide a short overview of the field of exoplanets, with a particular focus on the areas most relevant to the work presented in this thesis. In Section 1.2, I discuss how we define an 'exoplanet' and describe some of the other objects that sometimes fall under the umbrella of this term. I then summarise the techniques used to detect exoplanets in Section 1.3, including the methodology and instrumentation used for high-contrast imaging, the approach underlying this thesis work. In Section 1.4, I discuss what we can learn about exoplanets through direct high-contrast imaging of exoplanets. Lastly, in Section 1.5 I describe the focus of the work presented here and outline each of the remaining chapters in this thesis.

1.2 A spectrum of substellar objects

How do we define an 'exoplanet'? In our own solar system, the question of how we define a planet is still a contentious topic, and famously led to the reclassification of Pluto from 'planet' to 'dwarf planet' in 2006 (Basri & Brown 2006). It is therefore perhaps unsurprising that it is also difficult to assign a clear definition for exoplanets, especially given the diversity of substellar objects now known to exist.

One widely used metric for differentiating between exoplanets and other substellar objects is mass. This issue of what would constitute a lower limit for exoplanet mass has been largely avoided thus far, mainly due to the challenge of detecting smaller and lower mass exoplanets (see Section 1.3). The least massive exoplanet discovered to date by far is the innermost of the aforementioned pulsar planets, PSR B1257+12 b, which has a mass of 0.020 $M_\oplus$, ten times that of Pluto (Konacki & Wolszczan 2003). However, a number of indirect detections have been made of small non-planetary objects, such as exocomets or planetesimal fragments

[1] This pulsar and its exoplanets are commonly referred to by their numerical designations PSR B1257+12 A, b, c, and d. However, they also have the official names Lich, Draugr, Poltergeist, and Phobetor, after supernatural or undead creatures from mythology, reflecting the system's 'undead' post-supernova nature.

[2] Mercury is closer to the Sun, but Venus is significantly hotter because its dense, cloudy atmosphere causes a runaway greenhouse effect.

[3] These values were obtained from the NASA Exoplanet Archive, at https://exoplanetarchive.ipac.caltech.edu/.

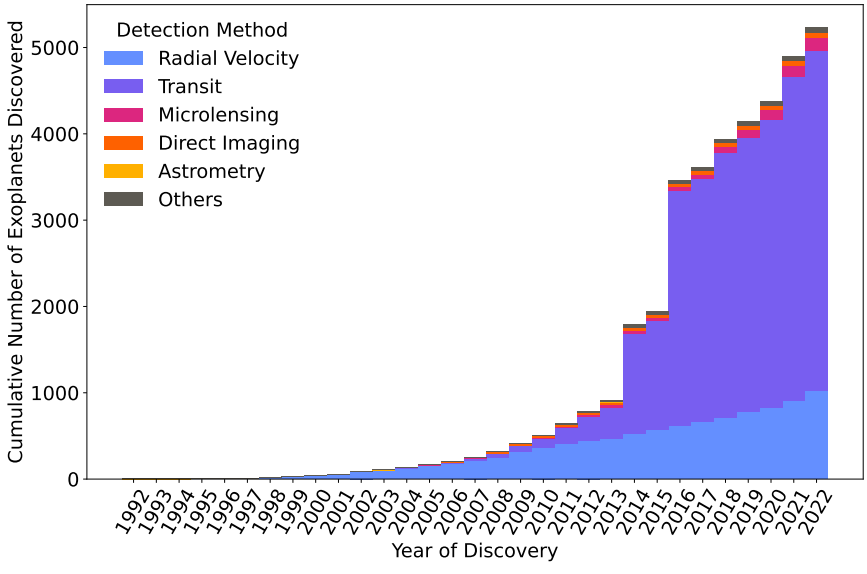

Figure 1.1: Cumulative histogram showing the number of exoplanets discovered over the thirty years from the first discovery in 1992 up to 1st January 2023, based on data from the NASA Exoplanet Archive. The colours reflect the method by which the exoplanets were discovered. While most exoplanets were discovered using indirect approaches such as the radial velocity and transit methods, the work in this thesis is focused on the technique of direct imaging.

(e.g. Ferlet et al. 1987; Boyajian et al. 2016; Rappaport et al. 2018; Ansdell et al. 2019; Zieba et al. 2019). Natural satellites are also expected to exist in orbit around exoplanets themselves. Such objects may exist in a range of sizes and masses, from smaller 'exomoons' to larger objects that form a binary with the host exoplanet (e.g. Limbach & Turner 2013; Heller et al. 2014; Lazzoni et al. 2022). While exomoon and binary planet candidates have been observed, there have not yet been any definite detections (e.g. Teachey & Kipping 2018; Rodenbeck et al. 2018; Lazzoni et al. 2020).

On the upper end of the mass scale, the picture is made more complicated by brown dwarfs. Main-sequence stars produce energy by converting hydrogen into helium in their cores through nuclear fusion (e.g. Eddington 1920; Bethe 1939). Brown dwarfs – first predicted to exist in the 1960s and sometimes referred to as 'failed stars' – are substellar objects that are not massive enough to sustain this process (Kumar 1962; Hayashi & Nakano 1963). The first brown dwarfs were later discovered in 1995 by Nakajima et al. (1995) and Rebolo et al. (1995), the same year that the first exoplanet orbiting a main-sequence star was discovered; but they are distinct from giant exoplanets as they are still massive enough to fuse deuterium (and in some cases lithium). Based on the criterion that define the transitions from exoplanet to brown dwarf and from brown dwarf to star (i.e. the deuterium burning and hydrogen burning limits, respectively), it is generally accepted that brown dwarf masses span a mass range of roughly $\sim$13-80M_{Jup} (e.g. Spiegel et al. 2011; Dieterich et al. 2014; Chabrier et al. 2022). This would suggest an approximate exoplanet upper mass limit of $\sim$13M_{Jup}. However,

in practice exoplanets and brown dwarfs lie on a spectrum and cannot be differentiated by mass alone. The boundaries of this range are not exact, and can depend on the deuterium and helium abundances and metallicity of the object in question. Furthermore, distinguishing objects at the exoplanet/brown dwarf boundary is challenging and uncertainties on mass estimates sometimes substantially overlap both sides. For these reasons, the term 'exoplanet' is often used broadly to describe objects close to this boundary on either side. Indeed, several of the highest mass exoplanets in the NASA Exoplanet Archive have masses well above this $\sim$13M_{Jup} boundary. The more inclusive phrase 'substellar companion' is also common when describing any object in the exoplanet to brown dwarf regime that is gravitationally bound to a host object. This term is used to refer to many of the companion objects studied in this thesis, which span from high-mass exoplanets close to the brown dwarf boundary to high-mass brown dwarfs close to the stellar boundary.

Another proposed metric for separating exoplanets and brown dwarfs companions is that of formation mechanism. Most exoplanets are thought to have formed through core accretion, by which a solid core grows until it is massive enough to accrete a gaseous atmosphere (e.g. Pollack et al. 1996; Alibert et al. 2005; Mordasini et al. 2008). However, typical core accretion models struggle to explain the population of massive companions observed at extremely wide separations from their host stars, because the expected timescale to form such a core is longer than the typical lifetimes of the protoplanetary disks of material in which they form (Haisch et al. 2001; Lambrechts & Johansen 2012). An alternative formation mechanism suggested to explain these objects is disk instability, whereby material in a protoplanetary disk collapses to form a companion directly (e.g. Boss 1997; Boley 2009; Nero & Bjorkman 2009). There is evidence that both mechanisms can form objects with masses on either side of the typically-used $\sim$13M_{Jup} deuterium burning limit (e.g. Bodenheimer et al. 2013; Cadman et al. 2021). However, it can be argued that objects formed through disk instability are more akin to failed stars, and thus could be considered to be brown dwarfs (e.g. Kratter et al. 2010; Kratter & Lodato 2016). Indeed, a large fraction of the brown dwarf population likely instead formed directly from the fragmentation of protostellar molecular clouds, in a scaled-down form of another star formation mechanism (e.g. Luhman 2012; Chabrier et al. 2014; Bowler et al. 2020a). Regardless of formation mechanism, low mass brown dwarfs appear to share many of the same properties as giant exoplanets, such as temperature, surface gravity, and even weather (e.g. Faherty et al. 2013, 2016; Dupuy & Kraus 2013; Helling & Casewell 2014; Vos et al. 2022, 2023). Since brown dwarfs are often easier to observe, this makes them ideal analogues to help us better understand exoplanets.

An additional point to note is that substellar objects do not necessarily orbit a star; several systems have been identified in which exoplanets orbit brown dwarfs (e.g. Chauvin et al. 2004). There have also been numerous discoveries of field brown dwarfs and free-floating planetary-mass objects ('rogue planets'), which are believed to have either formed in situ like stars or been ejected from their original exoplanetary system by gravitational interactions (e.g. Luhman 2012; Scholz et al. 2022).

1.3 Searching for exoplanets

Exoplanets are extremely difficult to detect directly. This is because they are generally thousands or even millions of times fainter than their host stars, and the angular separations between exoplanets and their hosts are very small. The light from an exoplanet is often therefore almost entirely obscured by the light from its host star. In Figure 1.2, BT-Settl evolutionary models are plotted for objects of different masses, showing how their brightness changes as they get older (Allard et al. 2013). Stars ($\geq$80 M_{Jup}, in purple) initially get fainter as they contract after formation, but their luminosity levels off as they enter the main sequence and begin fusing hydrogen. Substellar objects below the hydrogen burning limit but above the deuterium burning limit (i.e. the brown dwarf mass regime, 13-80 M_{Jup}, in pink) initially remain bright while they fuse deuterium, but begin to cool and fade once this supply is exhausted. Planetary-mass objects ($\leq$13 M_{Jup}, in orange) begin to rapidly cool and fade immediately after they finish forming. This means that not only are exoplanets and other substellar companions much fainter than their host stars from their nascence, but that this vast difference in brightness (often referred to as contrast) becomes increasingly immense as a system ages. For these reasons, the vast majority of known exoplanets have not been detected directly, but instead are observed indirectly using a wide array of methods that measure their influence on their host star (e.g. Wright & Gaudi 2013). The work in these thesis is focused on the small number of substellar companions that have been imaged directly, as well as the techniques and instrumentation that we use to achieve this.

However, it is important to note that the properties of the exoplanets that are accessible to different approaches can be very different. Figure 1.3 shows the masses of all known exoplanets as a function of their separation from their host star, plotted in different colours that reflect the method by which they were detected. If we consider the transit method, for example, we see that most of the exoplanets discovered with this technique lie at close orbital separations ($<$1 au) to their host star. This method involves monitoring the flux of a target star. If the orbital path of an exoplanet around this star happens to take it in front of the star from the viewpoint of the observer, then a small fraction of the star's light will be blocked, causing it to appear fainter for the duration of the 'transit' of the exoplanet. Therefore, if repeated, periodic drops in brightness are detected for a star, we can infer that they are due to the presence of an orbiting companion (e.g. Charbonneau et al. 2000; Henry et al. 2000). The time between transits, the length of the transits, and the fraction of stellar flux blocked provide information about the orbital separation and radius of the companion. The success of this method in detecting companions in close orbits is because it is inherently more sensitive to them; a transit is more likely to be observed for a close-orbit companion, and the time between consecutive orbits will be far shorter. Similarly, each detection method has its own biases towards detecting exoplanets of certain masses and in certain orbits. Like the transit method, the radial velocity method (e.g. Mayor & Queloz 1995; Wright 2018) intrinsically favours massive companions in closer orbits, whereas most companions detected through microlensing lie at orbital separations $>$1 au but $<$10 au (e.g. Einstein 1936; Bond et al. 2004; Gaudi 2012).

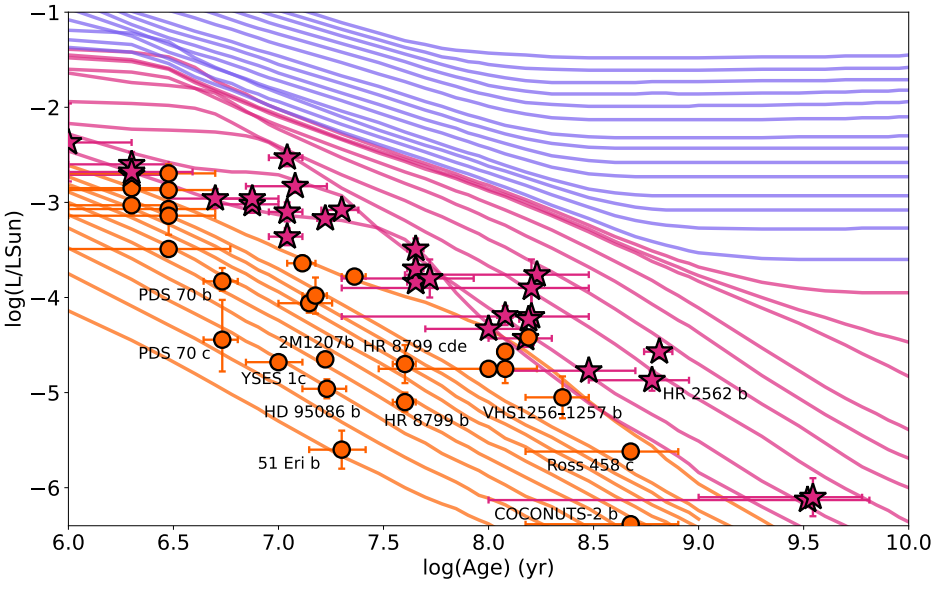

Figure 1.2: BT-Settl theoretical models from Allard et al. (2013) showing how the bolometric luminosities of objects of different masses change as a function of time. The purple, pink, and orange lines represent objects with masses $\geq$80 M_{Jup} (the hydrogen burning limit), 13-80 M_{Jup}, and $\leq$13 M_{Jup} (the deuterium burning limit), respectively. Directly imaged companions that are listed in the NASA Exoplanet Archive and have both age and bolometric luminosity measurements are shown for reference. Data obtained from the NASA Exoplanet Archive and the references therein. Based on a plot from Bowler (2016).

Some regions of the mass and orbital separation parameter space remain unexplored, as evidenced by the regions in Figure 1.3 where there are no detections of exoplanets. These gaps do not necessarily imply that exoplanets do not exist in these regions, but instead highlight the masses and orbital separations that current methods and technologies are unable to reach. To date, the only exoplanets discovered with masses less than that of Earth lie at separations $<$0.2 au, approximately half of the semi-major axis of Mercury in our own Solar System.

The direct imaging method probes a unique region of parameter space currently beyond the reach of indirect detection methods. Although the extreme contrasts between exoplanets and their host stars prohibit us from imaging the close-separation companions favoured by most indirect detection methods, this difference in brightness can be more easily overcome for massive companions at wider separations (e.g. Bowler 2016). In the following subsections, I discuss the challenges this involves and provide a description of the techniques and instrumentation that we use to successfully image substellar companions directly.

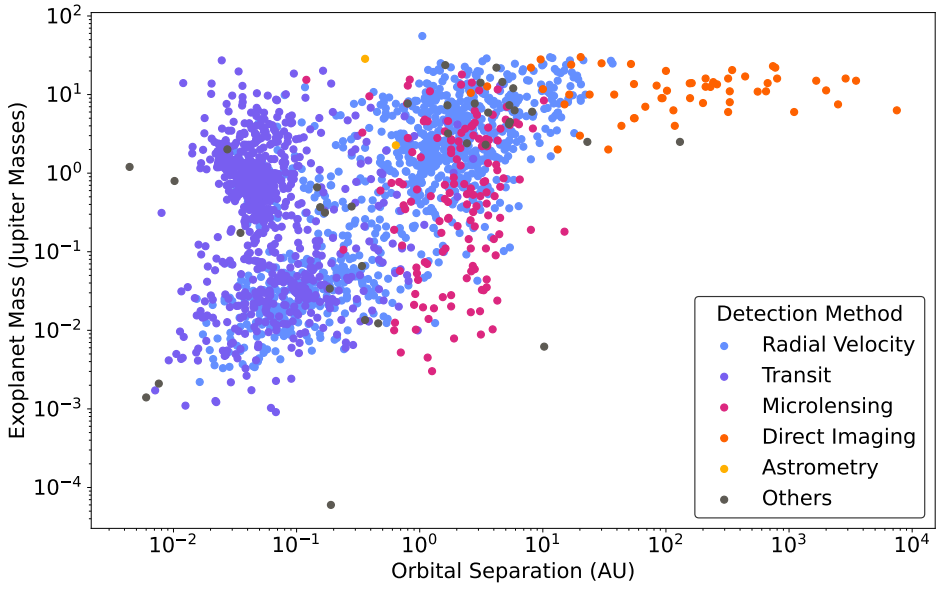

Figure 1.3: The masses of the 5235 exoplanets discovered as of 1st January 2023 as a function of the semi-major axis of their orbits, where these values exist in the NASA Exoplanet Archive. The colours reflect the method by which the exoplanets were discovered. The masses shown for many of the exoplanets discovered with the radial velocity method are their minimum possible mass ($M \sin i$) as their orbital inclinations are often unknown. Different detection methods probe different regions of parameter space; direct imaging allows us to detect high mass, widely separated companions that are inaccessible to indirect methods.

1.3.1 Direct imaging

The difficulty in observing exoplanets directly arises not only from the extreme difference in contrast between them and their host stars, but also from their close separations on the sky. The closer the angular separation of a companion's orbit, the more it is obscured by the glare from the star. Companions on the widest of orbits, hundreds or even thousands of au in separation (generally tens to hundreds of arcseconds separation on sky), can be observed largely unimpeded by stellar light (e.g. Rebolo et al. 1998; Faherty et al. 2010, 2021; Chinchilla et al. 2020; Zhang et al. 2021). Stellar systems closer to Earth are also easier targets for direct imaging searches, because a given physical separation will appear larger on sky (e.g. Bowler 2016).

The population of companions at closer separations that are most accessible to direct imaging are those for which the contrast ratio is the least extreme. If we again consider the models shown in Figure 1.2, the difference in brightness between stars and lower-mass objects is smallest for substellar objects with high masses and young ages. Furthermore, the contrast for a given system is smaller if the host object is of lower mass and therefore fainter (e.g. Chauvin et al. 2004, 2005a; Todorov et al. 2010; Dupuy et al. 2018; Fontanive et al. 2020). The contrast that needs to be achieved to detect a companion can be reduced further by observing at the optimal wavelength. If we assume that stars and companions radiate as black bodies, then the peak emissions of stars occur at much shorter wavelengths than those of cooler substellar companions. Substellar companions are extremely faint at optical wavelengths, so most exoplanet imaging studies are carried out in the longer near-infrared regime ($\sim$1–5 µm), where the contrast difference is more favourable yet companions still emit enough of their own light to be detected. Contrast ratios are even more favourable at longer mid-infrared wavelengths (>5 µm), but these wavelengths have remained out of reach for ground-based observatories thus far because of the high telluric background. JWST can now provide wavelength coverage up to 28 µm, opening a new window to detect and characterise directly imaged exoplanets (e.g. Hinkley et al. 2021; Currie et al. 2022a).

The exoplanets discovered through direct imaging to date are all 'super Jupiters', with masses greater than 2 M_{Jup}. Images of some of these exoplanets are shown in Figure 1.4, including the HR 8799 system in which multiple exoplanets have been detected. Imaging rocky 'Exo-Earth' planets around the nearest systems to Earth will require us to reach contrasts much deeper than 10^{-7} at close angular separations, compared to the 10^{-5}–10^{-6} contrasts reached by current state of the art instrumentation (e.g. Nielsen et al. 2019; Hinkley et al. 2021; Vigan et al. 2021; Currie et al. 2022a; Galicher & Mazoyer 2023).

In the future, high-contrast imagers on the upcoming extremely large telescopes, such as the Mid-infrared ELT Imager and Spectrograph (METIS) instrument on the Extremely Large Telescope (ELT), will achieve the deepest sensitivity yet, potentially enabling the first observations of exoplanetary Solar System analogues around nearby stars (e.g. Kasper et al. 2010; Brandl et al. 2008, 2021).

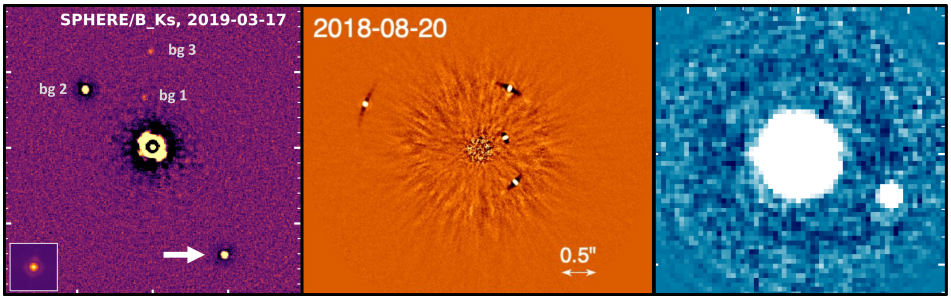

Figure 1.4: An image gallery of some of the substellar companions discovered through direct high-contrast imaging to date. **Left-hand panel:** the exoplanet YSES 1b, along with its host star (behind a coronagraph) and three background sources (Figure 1, Bohn et al. 2020a). **Centre panel:** the multi-planet system HR 8799 bcde, which contains four known planets and is approximately face-on as viewed from Earth (Figure 3, Biller et al. 2021). **Right-hand panel:** the host star HD 1160 A and its companion HD 1160 B, taken from Chapter 3 of this thesis (Sutlieff et al. 2023).

1.3.2 A recipe for ground-based high-contrast exoplanet imaging

The theoretical limiting angular resolution that a telescope can resolve is given by the Rayleigh criterion for the diffraction limit, $\theta \approx 1.22\ \lambda/\mathrm{D}$, where λ is the wavelength of the observations and D is the mirror diameter of the telescope. This means that resolving stars and companions with smaller angular separations requires ever larger telescopes. Although space-based telescopes benefit from increased sensitivity as a result of their environment, the sample of directly imaged companions that they can detect remains limited, as most lie at close angular separations within their inner working angles. Conversely, the largest ground-based telescopes have the mirror diameters necessary to detect these companions, but suffer from the sensitivity-degrading effects of Earth's atmosphere. As light passes through Earth's atmosphere, variations in pressure and refractive index induced by atmospheric turbulence lead to distortions in the incoming wavefront. This deterioration of image quality is often referred to as astronomical seeing. Ground-based observations therefore rarely reach the diffraction limit and are instead 'seeing-limited'. However, modern ground-based imaging systems are able to partially correct for the effects of atmospheric turbulence and suppress stellar flux, thereby obtaining diffraction-limited images at the contrasts required to detect close-separation, high-contrast companions (e.g. Guyon 2018). Such systems consist of several key components and techniques that work in combination to produce this effect, each of which I review here.

1.3.2.1 Adaptive Optics

A vital part of any high-contrast imaging system is an adaptive optics (AO) system which aims to measure the distortion of the incoming wavefront and correct it in real time (e.g. Babcock 1953; Rousset et al. 1990; Davies & Kasper 2012; Guyon 2018). The operating principle of a typical AO system is shown in Figure 1.5. First, a small fraction of the incoming, distorted light is redirected into a wavefront sensor using a beamsplitter. The wavefront

1

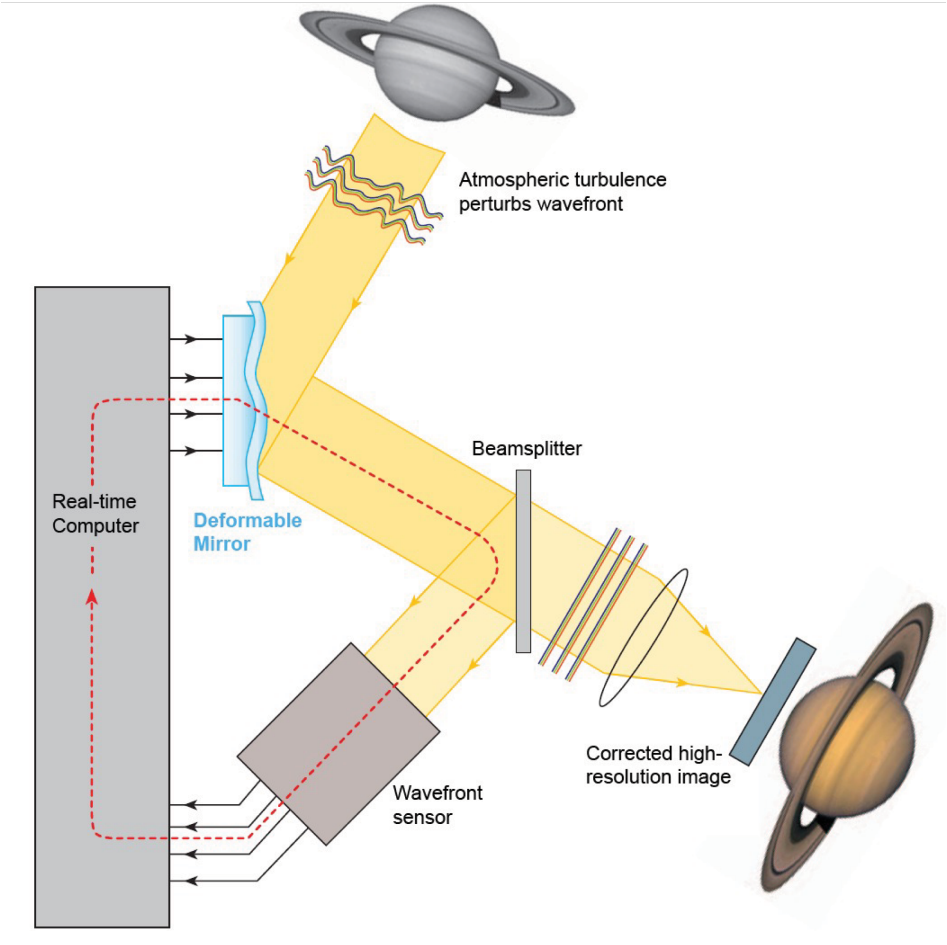

Figure 1.5: A schematic showing how a typical AO system operates. The closed feedback loop (red dotted line) is repeated hundreds of times per second to attempt to correct for atmospheric turbulence in real time. Figure used with permission of Annual Reviews, Inc., from Davies & Kasper (2012); permission conveyed through Copyright Clearance Center, Inc.

sensor then measures the shape of the wavefront (and hence the distortion) in one of two ways. A Shack-Hartmann wavefront sensor consists of an array of identical lenslets with the same size and focal length (e.g. Li et al. 2012). These lenslets focus the incoming light onto a detector, producing an array of spots that represent the local wavefront at each lenslet. The displacement of these spots from their expected positions for a flat wavefront corresponds to the local tilt of the wavefront at each lenslet, allowing the shape of the wavefront to be measured. Alternatively, a pyramid wavefront sensor splits the light into four images using a prism in the shape of a four-sided pyramid (e.g. Ragazzoni 1996). These images are identical for a flat wavefront, so variations in their intensity reflect the distortion of the wavefront. The wavefront sensor sends the measurements to a real-time control system, which uses a wavefront control algorithm to calculate the correction required to return the light to a flat wavefront. A deformable mirror, consisting of thousands of small actuators located behind a thin optical surface, is then used to apply the correction to the incoming wavefront (e.g. Guyon 2018).

This entire loop is completed hundreds of times per second to correct for the aberrations induced by rapidly changing atmospheric turbulence. The degree to which the wavefront is corrected can be quantified using the Strehl ratio, where higher values reflect a better correction. Extreme adaptive optics systems such as those used by the Gemini Planet Imager (GPI, Macintosh et al. 2014) and the Spectro-Polarimetric High-contrast Exoplanet REsearch (SPHERE, Beuzit et al. 2019) are able to achieve Strehl ratios of $>90\%$ in the infrared H-band. However, residual aberrations can still cause difficulties for observations of companions. Furthermore, aberrations introduced to the wavefront on the optical path leading to the detector (i.e. after the splitting by the beamsplitter) are not seen by the wavefront sensor, and so cannot be corrected. These are known as non-common path aberrations (NCPAs, e.g. Sauvage et al. 2007).

1.3.2.2 Coronagraphy

Although AO is able to correct for the effects of Earth's atmosphere to a high degree, the issue of the extreme difference in brightness between a substellar companion and its host star still remains. The level of stellar flux at the close angular separations at which these companions reside completely overwhelms the flux of any companions. To mitigate this problem, we use instruments known as coronagraphs that suppress the light from a target star, allowing faint companions to be detected. The coronagraph was originally designed by Bernard Lyot to enable observations of the solar corona to be carried out beyond the occasional total solar eclipse (Lyot 1932, 1939). Prior to this, astronomers could only observe the solar corona when the Sun was completely blocked by the Moon, and as such could only observe for the short duration of an eclipse and were required to travel to specific locations to do so. In Figure 1.6, I show the operating principle behind a simple Lyot coronagraph and how it can be used to observe high-contrast companions. First, the telescope is aligned such that the stellar flux arrives on-axis and centred in the field of view. The incoming starlight is then focused such that most of its light is blocked by an opaque coronagraphic mask in the focal plane. When the pupil is then reimaged by another lens, the remaining, diffracted

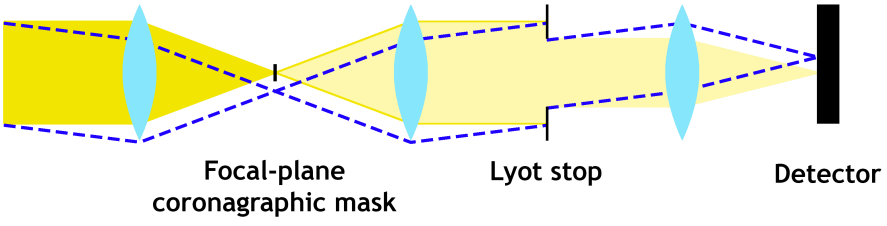

Figure 1.6: A schematic of the simplest form of Lyot coronagraph. Incoming on-axis starlight (in yellow) is blocked by the focal plane mask and the Lyot stop, reducing its flux significantly, while off-axis light from a faint companion (blue dashed lines) reaches the detector largely unimpeded.

stellar light is concentrated at the outer edges of the pupil. Most of this residual light is then absorbed by a device known as a Lyot stop, thereby further reducing the stellar flux that reaches the detector. Importantly, the incoming light from any companions arrives at a slight angle (off-axis) instead and therefore misses the coronagraphic mask and mostly passes through the centre of the Lyot stop.

Today, more advanced focal-plane coronagraphs that build on this original design are installed on ground-based telescopes worldwide as well as space telescopes such as the Hubble Space Telescope and JWST (e.g. Ruane et al. 2018; Galicher & Mazoyer 2023). Large ground-based coronagraphic imaging surveys routinely achieve high-contrasts at close angular separations (10^{-5}–10^{-6} at 0.4–0.5″ after data processing), allowing faint companions to be detected (e.g. Nielsen et al. 2019; Langlois et al. 2021; Vigan et al. 2021). However, focal-plane coronagraphs do have some key disadvantages. The target star must be centred in the field of view to a high degree of accuracy such that the coronagraphic mask is able to effectively block its light. They are therefore inherently sensitive to tip/tilt instabilities that result from telescope vibrations and residual seeing effects and can limit their ability to reach deeper contrast ratios (e.g. Fusco et al. 2014; Otten et al. 2017; Doelman et al. 2021).

Conversely, pupil-plane coronagraphs are inherently immune to these instabilities. These coronagraphs have a different working principle to focal-plane coronagraphs and, as the name suggests, reside in the pupil-plane of the telescope (e.g. Ruane et al. 2018; Galicher & Mazoyer 2023). Rather than blocking the light from the target star, pupil-plane coronagraphs modify its point spread function (PSF) to produce a ‘dark hole’ of deep flux suppression in which faint companions can be observed. As this modification is applied in the pupil plane, it affects all sources including companions equally and is therefore not impacted by tip/tilt instabilities. In this thesis, I present observations obtained using coronagraphs belonging to a class of pupil-plane coronagraphs known as vector Apodizing Phase Plates (vAPPs), which I describe in the following subsection.

1.3.2.3 The vector Apodizing Phase Plate (vAPP) coronagraph

The Apodizing Phase Plate (APP) coronagraph is a pupil-plane coronagraph that applies a phase modification to incoming light (Codona et al. 2006; Kenworthy et al. 2007). It consists of a single optic, a piece of glass with a high refractive index, and as such can be installed on a telescope simply by placing it in the filter wheel of the instrument. The thickness of the APP varies across the pupil, such that light passing through the APP travels different distances and therefore receives a varying degree of phase delay (Otten 2016). The destructive interference arising from this adjustment of phase causes a dark hole to be produced on one side of the PSF of the target star, allowing companions to be observed. However, this means that companions at position angles on the opposite side of the star remain obscured by the stellar flux. Furthermore, the phase delay applied by the APP is highly chromatic and so can only achieve optimal contrasts at certain wavelengths and is ineffective for broad-band observations.

The vector APP coronagraph, or vAPP, is the successor to the APP and overcomes many of its drawbacks (Snik et al. 2012; Otten et al. 2014a,b). The main component in the vAPP is a patterned half-wave retarder that induces geometric phase, or Pancharatnam-Berry phase, for incoming light (Pancharatnam 1956; Berry 1987). Unpolarised incoming light can be considered to be composed of both left-handed and right-handed circular polarisation states, each orthogonal to the other. When such light passes through the half-wave retarder of the vAPP, the handedness of the light in each polarisation state is flipped and a phase delay is applied. However, the sign of the phase delay (positive or negative) is dependent on the handedness, so the two polarisation states receive an opposite phase delay. Whereas the phase of the APP is encoded as physical differences in the optical path (i.e. the thickness of the glass optic), the phase applied by the vAPP is determined by the orientation of the fast axis of its half-wave retarder. The phase pattern of the APP is reproduced for the vAPP by setting the orientation of this fast axis to half of the APP phase, which ensures that incoming light is given the required phase delay to produce the same PSF shape as the APP. If the light were allowed to proceed directly from the half-wave retarder to the detector, a single PSF with no dark hole would be produced. It is therefore necessary to split the light according to its circular polarisation state. First, a quarter-wave plate (QWP) is used to convert the two circular polarisation states into two orthogonal linear polarisation states. A Wollaston prism is then used to split the beam according to these states, resulting in two beams of opposite phase and therefore two complementary PSFs of the target star on the detector, each with a dark hole on the opposite side (Snik et al. 2012; Otten et al. 2014a,b). This 360° coverage (180° per PSF) means that companions can be observed regardless of their position angle. A schematic of the operating principle of the vAPP coronagraph is shown in the top panel of Figure 1.7.

The vAPP coronagraph is manufactured by using an ultraviolet laser to write the desired phase pattern directly onto a liquid crystal layer positioned on a substrate. By adding additional layers of self-aligning birefringent liquid crystals, a stack known as a multi-layered twisted retarder (MTR) is produced. The layers in the MTR can be combined in a specific way to make

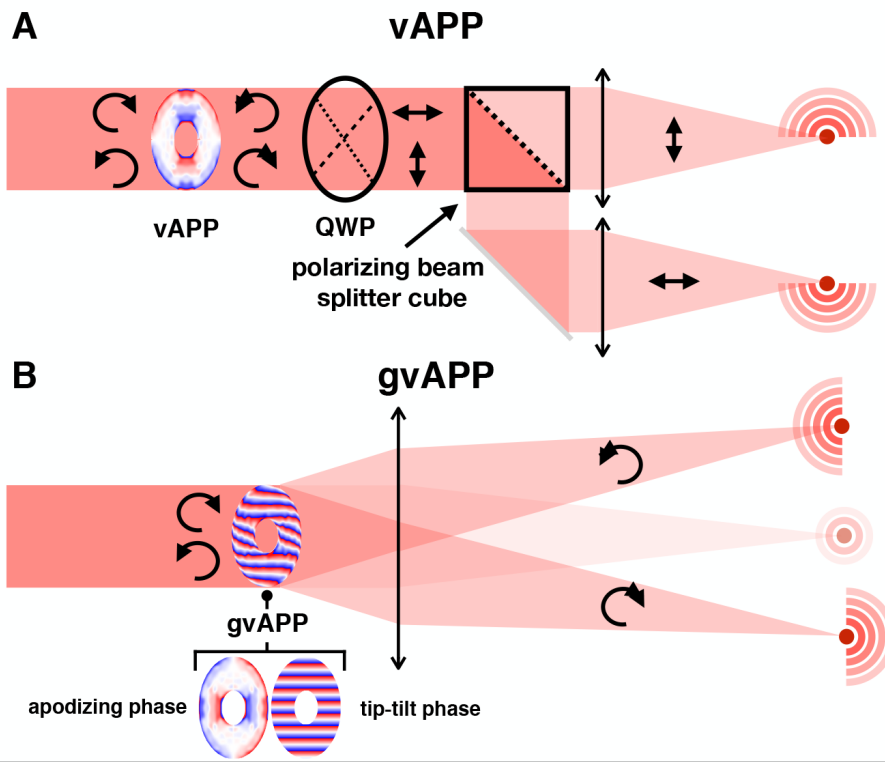

Figure 1.7: Schematics of the vAPP and gvAPP coronagraphs and the PSFs that they produce. Both coronagraphs produce two modified PSFs of all sources in the field of view, each with a 180° dark hole of deep flux suppression on opposite sides. The gvAPP also produces an additional unmodified PSF, known as the leakage term, positioned between the two coronagraphic PSFs. This is an entirely separate image of the target at a fraction of its full brightness and is therefore ideal for photometric referencing. Figure adapted from Bos et al. (2018); Doelman et al. (2021).

the vAPP achromatic, unlike the APP, and therefore highly effective over a wide wavelength range (e.g. Komanduri et al. 2013; Miskiewicz & Escuti 2014; Otten et al. 2014b; Doelman et al. 2021).

The simplicity of the vAPP design makes it very straightforward to install, and as such there are now vAPPs available on high-contrast imagers around the world. The first of the two specific vAPPs that are the focus of this thesis is the grating vAPP (gvAPP) installed on the Magellan Adaptive Optics (MagAO) system on the 6.5-m Magellan Clay Telescope at Las Campanas Observatory, Chile (top panel, Figure 1.8) (Close et al. 2012; Morzinski et al. 2014; Otten et al. 2017). A gvAPP is a variant of the vAPP for which a tip-tilt phase ramp is applied to its phase pattern, allowing the two circularly polarised beams to be split without a QWP and Wollaston prism. The phase ramp deflects the light at a different angle depending on the circular polarisation (Otten et al. 2014b). This can be seen in the bottom panel of Figure 1.7. When light passes through a vAPP, slight imperfections in the optic mean that a

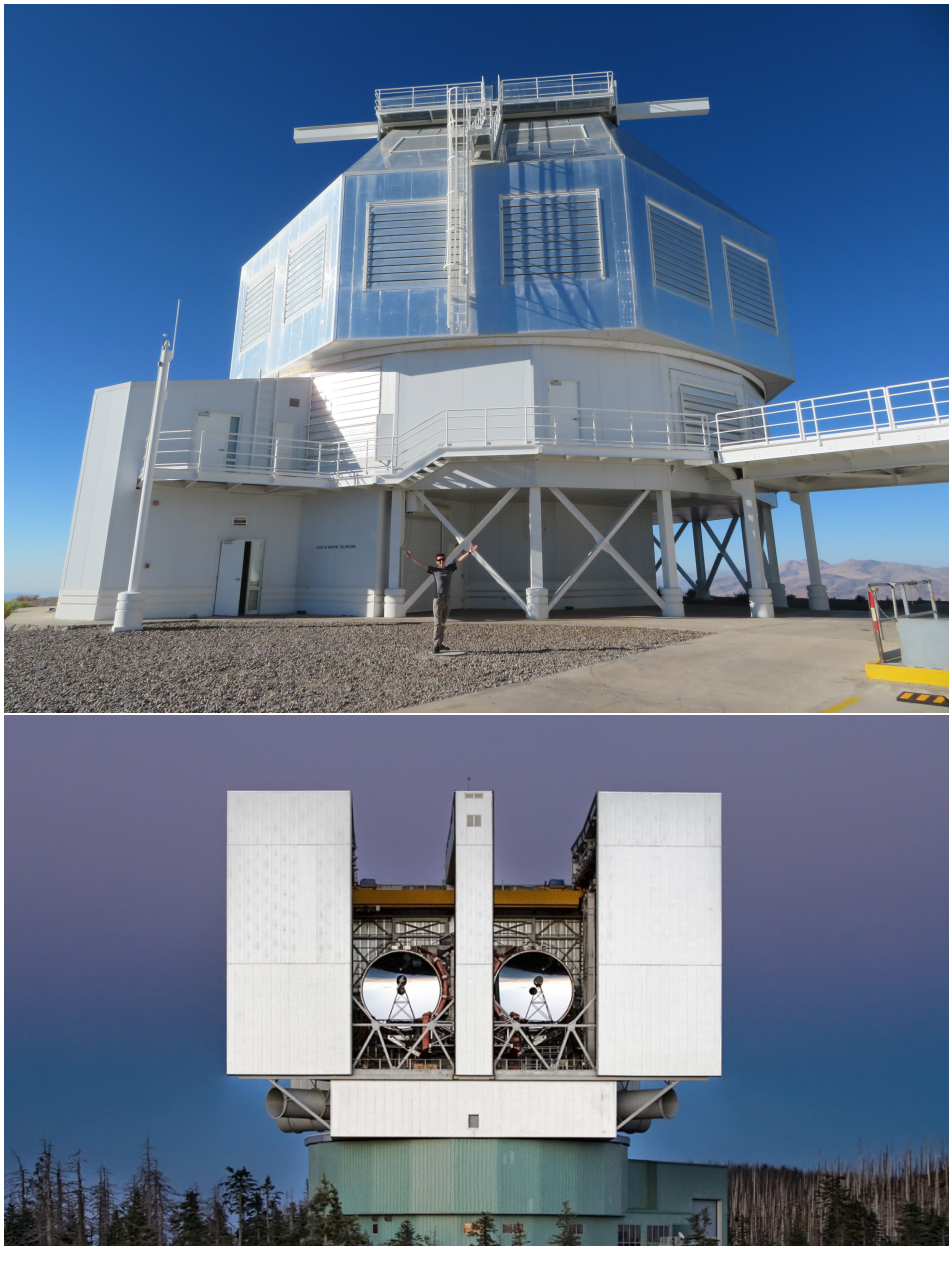

Figure 1.8: The two telescopes used to obtain the observations presented in this thesis. **Top panel:** The 6.5-m Magellan Clay Telescope at Las Companas Observatory, Chile, with an exoplanet observer shown for scale. This telescope hosts the MagAO system and a 180° vAPP coronagraph. Image credit: Jayne Birkby. **Bottom panel:** The Large Binocular Telescope (LBT) at Mount Graham International Observatory, Arizona, USA. The ALES IFS and a dgvAPP360 coronagraph are installed at LBT. Image credit: Large Binocular Telescope Observatory (LBTO), University of Arizona.

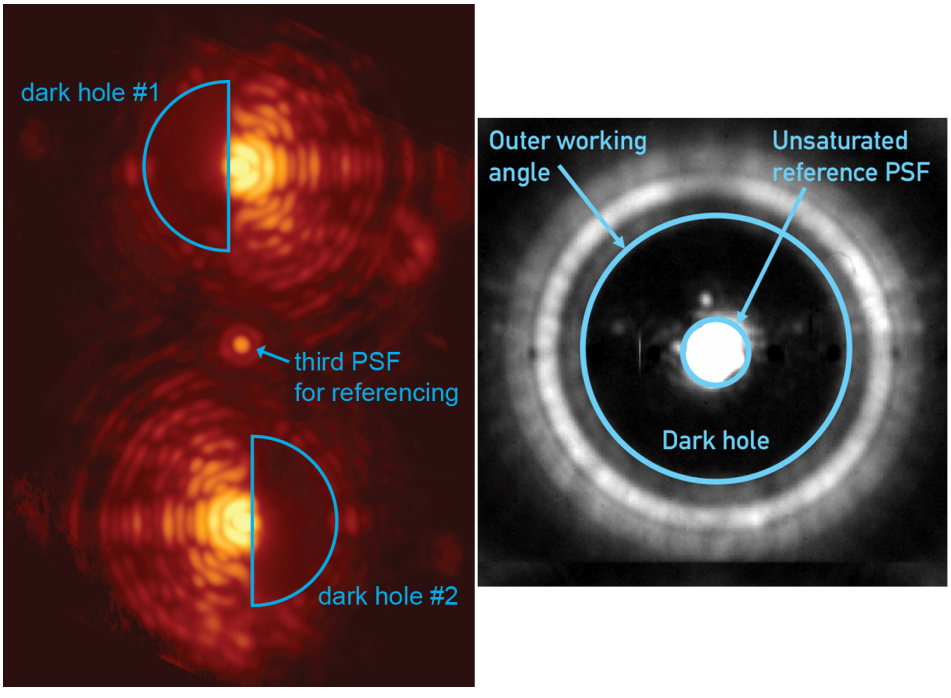

Figure 1.9: Example images of stars observed with a gvAPP (left-hand panel) and dgvAPP360 (right-hand panel). The gvAPP produces three PSFs of the target. The dgvAPP360 instead produces a 360° dark hole around an unsaturated PSF of the target in the centre. Credit: Leiden University; University of Arizona (left-hand panel), Sutlieff et al. (2023); Chapter 3 (right-hand panel).

very small fraction of light, known as the polarisation leakage, does not receive the required phase pattern. For the normal vAPP, this leakage can contaminate coronagraphic PSFs and therefore limit the contrast that can be achieved in the dark holes. However, the leakage is unaffected by the phase ramp of the gvAPP and so continues in a straight line, producing a third PSF of the target that is physically separated from the others. This 'leakage term' PSF does not have a dark hole, and typically consists of $\sim$1% of the flux of the target (Doelman et al. 2021). Although this PSF is the result of optical defects, it provides a highly useful photometric reference for observations of high-contrast companions. An on-sky example image obtained with the MagAO gvAPP is shown in the left-panel of Figure 1.9. The two coronagraphic PSFs with 180° dark holes are clearly seen, with the leakage term visible in the centre. The MagAO gvAPP operates over a 2-5 µm wavelength range and has a dark hole that covers 2-7 λ/D (Otten et al. 2017; Doelman et al. 2021).

The other vAPP used for the observations presented in this thesis is the 360° double-grating vAPP (dgvAPP360) on the 2 x 8.4-m Large Binocular Telescope (LBT) at Mount Graham International Observatory, Arizona, USA (bottom panel, Figure 1.8) (Doelman et al. 2017, 2020, 2021). The dgvAPP360 has a dark hole spanning 2.7 - 15 λ/D and operates in conjuc-

tion with the Arizona Lenslets for Exoplanet Spectroscopy (ALES) integral field spectrograph (IFS) to provide R∼40 spectroscopy over a 2.8-4.2 µm wavelength range (Skemer et al. 2015; Hinz et al. 2018; Stone et al. 2018). The dgvAPP360 differs from the gvAPP in two key ways. Firstly, an additional phase ramp is used to deflect the two beams back on axis such that they are recombined and a single PSF is produced in the image. Secondly, the phase pattern is designed such that the resulting PSF has a dark holes covering a full 360° around the target. This is advantageous compared to the gvAPP in that the flux of a potential companion is no longer split between two PSFs, yet an image of the host star is maintained in the centre of the dark hole. An on-sky image obtained with the LBT/NALES+dgvAPP360 setup is shown in the right-hand panel of Figure 1.9.

In addition to these vAPPs, there are a number of complementary vAPPs on other telescopes. Although LBT/ALES is the only instrument that can obtain integral field spectroscopy in the L and M bands, there is a gvAPP available for use with the SCExAO/CHARIS IFS on the 8.2-m Subaru Telescope, which provides spectroscopic coverage in the near-infrared (1.13-2.39 µm, Groff et al. 2016; Doelman et al. 2017). The gvAPP on MagAO-X enables coronagraphic observations at optical wavelengths (0.55-0.9 µm, Miller et al. 2019; Close et al. 2020a), as did the vAPP on the Leiden EXoplanet Instrument (LEXI) at the William Herschel Telescope (WHT) (Haffert et al. 2016, 2018). The newly-commissioned Enhanced Resolution Imager and Spectrograph (ERIS) instrument on the Very Large Telescope (VLT) also has a gvAPP, covering 2-5 µm (Boehle et al. 2021; Kenworthy et al. 2018b). A gvAPP has even been flown to Earth's stratosphere aboard a high-altitude balloon gondola as part of the High-Contrast Imaging Balloon System (HiCIBaS, Côté et al. 2018; Allain et al. 2018; Thibault et al. 2019), which was designed to test high-contrast imaging technology at an altitude of ∼40 km, simulating a space-like environment. Although astrophysical targets were not observed during this mission due to a mechanical failure, the PSFs of an internal source observed in-flight appeared similar to those obtained on the ground, providing an early indication that the gvAPP could be suitable for use on future space missions (Doelman et al. 2021).

There are also vAPPs planned for the upcoming METIS and Multi-AO Imaging CamerA for Deep Observations (MICADO) instruments on the ELT, which will obtain unprecedented sensitivity to exoplanetary companions with its 39-m mirror (Clénet et al. 2018; Kenworthy et al. 2018a; Perrot et al. 2018; Brandl et al. 2021, 2022).

An overview of the locations and statuses of all vAPPs produced to date and currently in production is shown in Figure 1.10. To date, all vAPPs have been designed at Leiden Observatory in the Netherlands and manufactured by ImagineOptix and North Carolina State University in the United States of America. Each of these vAPPs, their specific phase designs, and the underlying technology are described in detail in the review paper of Doelman et al. (2021).

1

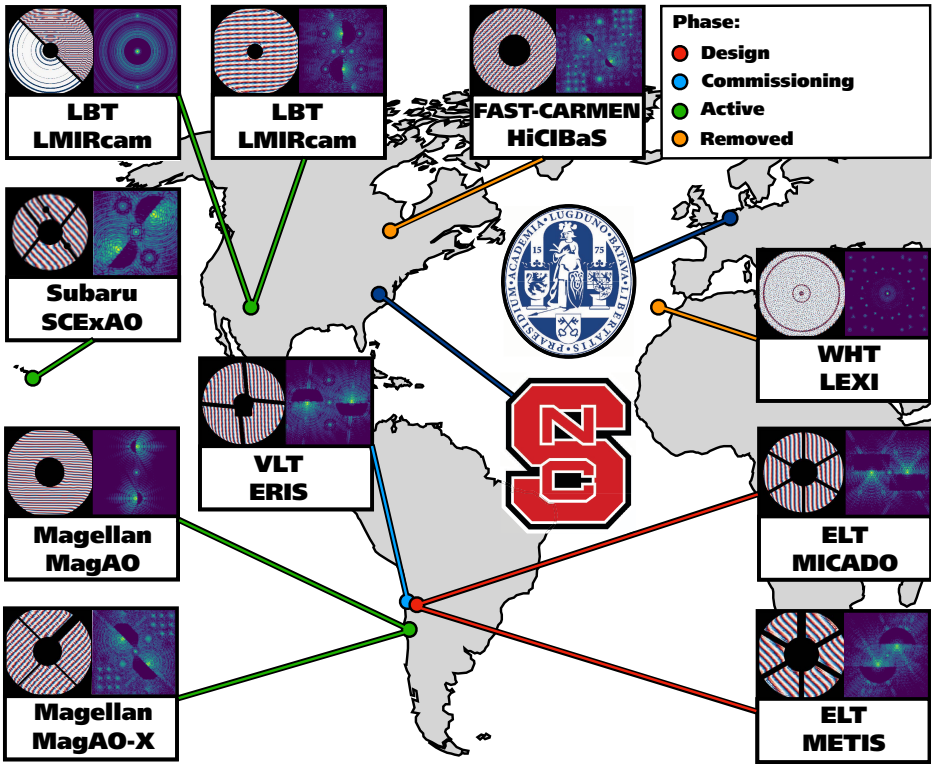

Figure 1.10: A map showing the location and status of vAPP coronagraphs around the world to date. The vAPPs were designed at Leiden Observatory in the Netherlands and manufactured by ImagineOptix and North Carolina State University in the USA, both of which are indicated by their respective logos. Credit: Doelman et al. (2021).

1.3.2.4 Speckle suppression

No AO system is able to perfectly correct for atmospheric turbulence, and no coronagraph is capable of eliminating all of the stellar flux at the location of a faint companion. High-contrast imaging observations are often limited by quasistatic 'speckles' of residual starlight that hamper the detection of companions at the closest angular separations, as well as a smoothly-varying halo effect produced when atmospheric turbulence varies too quickly for the AO to correct (e.g. Racine et al. 1999; Hinkley et al. 2007; Cantalloube et al. 2018; Madurowicz et al. 2019; Males et al. 2021). As the field of high-contrast imaging has developed, a wide variety of observing strategies and post-processing algorithms have been devised to tackle these effects (Cantalloube et al. 2020b). These algorithms make use of distinguishing properties, known as diversities, that differentiate the signal of a companion from speckle noise and hence allow deeper star-companion contrasts to be reached (e.g. Samland et al. 2021).

The simplest and most commonly used of these methods is classical Angular Differential Imaging (cADI, Marois et al. 2006a), which relies on spatial diversity between a host star and a companion. Many ground-based observatories have a field derotator, a device that ensures that the field of view remains fixed relative to the telescope when following a target. If instead the sky is allowed to rotate while images are being collected, with the pupil stabilised, companions and other off-axis sources will appear to rotate around the image centre while residual structure such as speckles will remain fixed. A reference PSF that models the residual starlight is then created by taking the median (or mean) of the obtained images. The signal of a companion will contribute minimally to this reference PSF, as long as the degree of field rotation is sufficient. This reference PSF can then be subtracted from each of the images in the observing sequence, removing the residual starlight and thereby improving the contrast at the locations of any companions. The images can then be derotated to align them relative to each other and combined to further improve the signal-to-noise of a companion.

Many more complex post-processing algorithms have since built on the concept of cADI by constructing the reference PSF for pupil-stabilised data in different ways. For example, Principal Component Analysis (PCA, Amara & Quanz 2012; Soummer et al. 2012; Meshkat et al. 2014) can be used to produce a bespoke reference PSF for each frame, thereby accounting for the quasistatic evolution of the residual starlight. Similarly, the Locally Optimized Combination of Images (LOCI, Lafrenière et al. 2007) algorithm also creates reference PSFs for each frame, by optimising the linear combination of the images used to create the reference PSFs. Some algorithms such as the ANgular Differential OptiMal Exoplanet Detection Algorithm (ANDROMEDA, Mugnier et al. 2009; Cantalloube et al. 2015) use a maximum likelihood approach to estimate the position and flux of candidate companions in pupil-stabilised data.

While most post-processing algorithms to date rely on the spatial diversity of data to remove stellar speckles, other diversities can also be used. If a dataset was obtained with an IFS, Spectral Differential Imaging (SDI, Racine et al. 1999; Sparks & Ford 2002) can be used. This technique makes use of the fact that the stellar PSF scales as a function of wavelength. As the position of a companion in the data instead remains fixed with changing wavelength, images at different wavelengths can be used to distinguish bona fide companions from

speckles. Other approaches, such as Temporal Reference Analysis of Planets (TRAP) and PAtch COvariances (PACO), instead rely on temporal diversity to eliminate speckle noise or retrieve information about a companion (e.g. Flasseur et al. 2018; Samland et al. 2021; Gebhard et al. 2022; Lewis et al. 2023, Liu et al. submitted).

The post-processing algorithm that achieves the best result for a given companion is dependent on the properties of both the specific data set and of the companion. Different post-processing algorithms can be more effective at different angular separations from the target star. It is therefore common to apply a range of different post-processing strategies to a data set to compare the results. In recent years, many of these algorithms have been integrated into generalised end-to-end data reduction pipelines for high-contrast imaging data, such as Vortex Image Processing (VIP, Gomez Gonzalez et al. 2017), Python Karhunen-Loève Image Processing (pyKLIP, Wang et al. 2015), and PynPoint (Amara & Quanz 2012; Stolker et al. 2019).

In Chapter 2 of this thesis, I make use of the cADI and PCA algorithms described above and present a new post-processing algorithm specifically designed for data obtained with gvAPP coronagraphs. In Chapters 3, 4, and 5, I choose not to apply post-processing algorithms to data obtained with the dgvAPP360 in order to maintain the stellar PSF for use as a photometric reference.

1.4 What can we learn about directly imaged companions?

1.4.1 Atmospheric characterisation

The recipe for high-contrast imaging described in the previous section enables the direct detection of faint exoplanets at close angular separations, and thus provides a unique avenue to characterise exoplanets through direct spectroscopic observations. This means that not only can we retrieve information about their physical properties and atmospheric compositions, but begin to answer the questions of their formation mechanisms and occurrence rates.

The most common characterisation approach for directly imaged companions is that of low-resolution spectroscopy, which can reveal the presence of specific molecules in a companion's atmosphere. For example, the J- and H-band spectrum of low-mass ($\sim$2 M_{Jup}) exoplanet 51 Eri b shows strong methane and water vapour absorption (Macintosh et al. 2015; Whiteford et al. 2023). Both water and carbon monoxide lines can be seen in the J-band spectrum of HR 8799 c, which together can be used to deduce the carbon-to-oxygen ratio (Konopacky et al. 2013). Chemical abundancies such as these are invaluable for breaking the degeneracies between formation mechanisms described in Section 1.2, which is an active area of research (e.g. Öberg et al. 2011; Barman et al. 2015; Skemer et al. 2016b; Wilcomb et al. 2020; van der Marel et al. 2021; Khorshid et al. 2022). Near-infrared spectral characterisations have also found that the young exoplanet companions found through direct imaging often have far redder colours than older field brown dwarfs of similar effective temperatures, highlighting that low surface gravity can have an important effect on their atmospheric structure (e.g. Macintosh et al. 2015; Chauvin et al. 2017; Biller & Bonnefoy 2018; Currie et al. 2022a).

The comparison of atmospheric models to their spectra further allows values for their physical properties to be inferred, such as temperature, surface gravity, metallicity, and luminosity (e.g. Morzinski et al. 2015; De Rosa et al. 2016; Samland et al. 2017; Stone et al. 2020; Ward-Duong et al. 2021). By fitting models based on different starting assumptions, such as cloudy or cloud-free, we can empirically test these assumptions (e.g. Currie et al. 2011; Skemer et al. 2012, 2014b; Ingraham et al. 2014; Rajan et al. 2017). Although the mass of an exoplanet cannot be inferred directly through the fitting of atmospheric models, it is possible to obtain an estimate, if its age is known, by evaluating model isochrones at the luminosity of the exoplanet for a given age (e.g. Allard 2014; Baraffe et al. 2015). This can also be done using the temperature or surface gravity instead of the luminosity. However, luminosity is significantly less model dependent (Bonnefoy et al. 2016).

Comparisons to empirical observed template spectra of field objects can further be used to estimate the spectral type of a companion, but it is important to note these generally only cover shorter wavelengths (e.g. 0.8–2.5 μm, Burgasser 2014). Moreover, some studies have found that no empirical template is a perfect match to their substellar companion spectra, and that satisfactory matches can only be found to individual wavebands separately (e.g. Konopacky et al. 2016; Mesa et al. 2018). One explanation for this can be the wavelength-dependent time variability due to atmospheric features rotating in and out of view (see next section).

1.4.2 Variability

The planets of our Solar System possess cloud structures and weather systems with a wide diversity of lifetimes and sizes (e.g. Gelino & Marley 2000; Simon et al. 2016; Ge et al. 2019; Stauffer et al. 2016; Coulter et al. 2022). Here on Earth, we experience small, short-lived storms, as well as hurricanes that can last for several days (Figure 1.11). Jupiter is famous for its distinct latitudinal cloud bands, and its gigantic 'Great Red Spot' storm that has lasted for centuries. These features induce variability in the total brightness of a planet as they rotate in and out of view over the planet's rotation period. The brightness of specific features can also be highly wavelength-dependent. For example, Jupiter's Great Red Spot is dark at visible wavelengths, but very bright in the 889 nm methane band, and Neptune's storms are far more prominent in the infrared (Gibbard et al. 2002; Ge et al. 2019). By measuring similar variations in brightness for directly imaged exoplanets and brown dwarfs, we therefore directly probe the dynamics and structure of their atmospheres, as well as their physical appearances (e.g. Kostov & Apai 2013; Crossfield et al. 2014; Karalidi et al. 2015, 2016; Apai et al. 2017; Manjavacas et al. 2021, 2022; Plummer & Wang 2022). Variability in these substellar objects can arise not only from inhomogeneous cloud cover and weather systems, but also from aurorae, magnetic spots, and the effects of radiative convection (e.g Goulding et al. 2012; Radigan et al. 2014; Hallinan et al. 2015; Tan & Showman 2019; Vos et al. 2023).

High cadence, time-resolved photometric monitoring with space-based telescopes has detected such variability in the light curves of several substellar companions (e.g. Manjavacas et al. 2018, 2019a; Zhou et al. 2018, 2019, 2020a, 2022; Miles-Páez et al. 2019), consistent

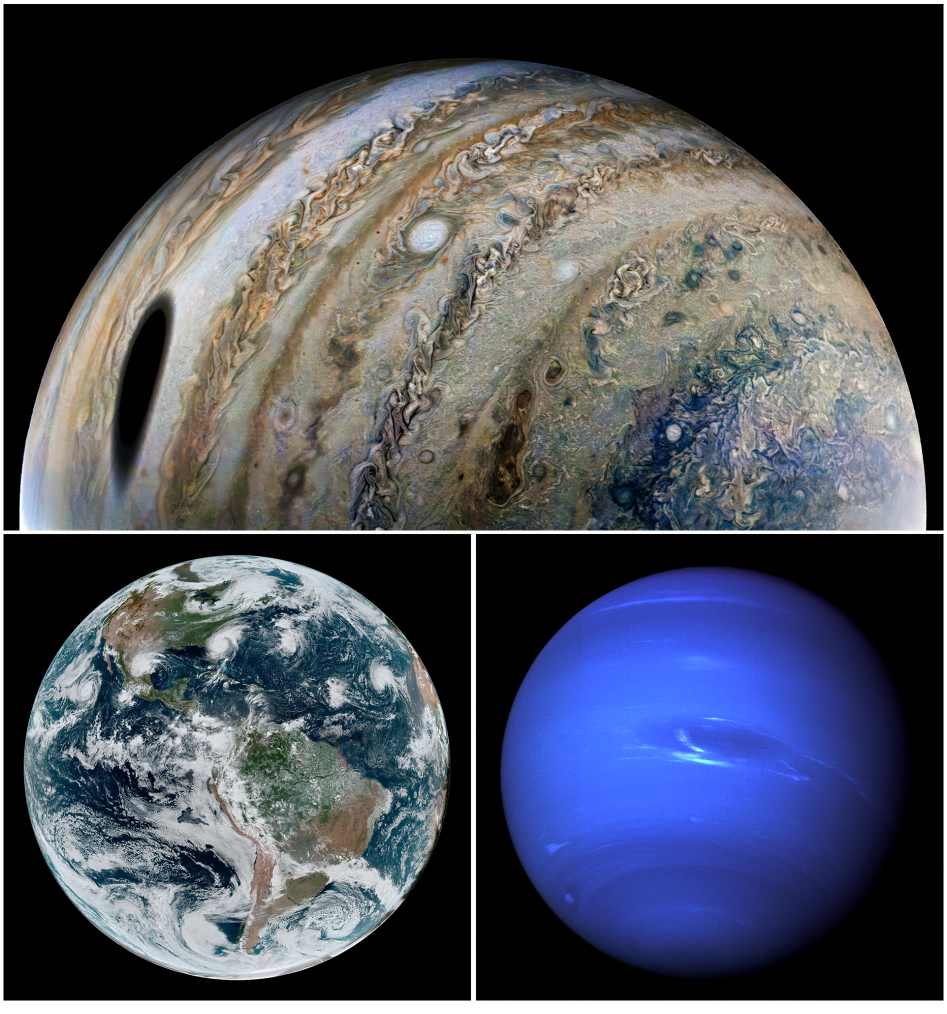

Figure 1.11: The Solar System planets have a wide variety of weather systems. **Top panel:** A close view of Jupiter taken by NASA's Juno spacecraft. Large storms and atmospheric turbulence can be seen at the interfaces between Jupiter's latitudinal cloud bands. The dark spot is a shadow cast by Ganymede, one of Jupiter's Galilean moons. Credit: NASA/JPL-Caltech/SwRI/MSSS, image processing by Thomas Thomopoulos. **Bottom-left panel:** A loose chain of four tropical cyclones in Earth's Western Hemisphere, taken in 2019 by a geostationary satellite. Credit: NASA Earth Observatory/Joshua Stevens; NOAA National Environmental Satellite, Data, and Information Service. **Bottom-right panel:** A full disk view of Neptune taken by the Voyager 2 spacecraft. Neptune's Great Dark Spot is visible in the centre, and a bright cloud band can be seen to the north. Credit: NASA/JPL

with both ground- and space-based studies of isolated brown dwarfs and planetary mass objects (e.g. Radigan 2014; Wilson et al. 2014; Biller et al. 2018; Vos et al. 2018, 2020, 2022; Lew et al. 2020a). This variability is seen at a wide range of amplitudes. Metchev et al. (2015) conducted a large survey of L and T dwarfs with the Spitzer Space Telescope, and found that $\geq$0.2% variability arising from photospheric spots is ubiquitous at wavelengths of 3-5 µm. Far stronger variability at the >10% level has also been detected for a handful of objects, with one planetary-mass companion showing peak-to-valley variations of 38% in the J-band (Radigan et al. 2012; Biller et al. 2015; Eriksson et al. 2019; Bowler et al. 2020b; Zhou et al. 2022). However, it is important to note that the intrinsic variability amplitude of a companion can be modulated by its viewing angle; the highest variability amplitudes tend to be detected for objects that are viewed equator-on (Vos et al. 2017; Biller et al. 2021). Moreover, the surface features and atmospheric dynamics that give rise to variability signals can evolve over time, leading to measurable changes in the observed variability. Variability evolution has been measured in the light curves of a number of substellar objects, including both rapid evolution between consecutive rotation periods and longer-term trends between epochs obtained months or years apart (e.g. Artigau et al. 2009; Gillon et al. 2013; Karalidi et al. 2016; Apai et al. 2021; Zhou et al. 2022). Much like multi-wavelength observations of the planets in our own Solar System, the light curves of substellar companions at different wavelengths probe different pressure levels and hence different layers in their atmospheres. This can give rise to discrete phase offsets between variability signals observed at different wavelengths (e.g. Buenzli et al. 2012; Biller et al. 2013; Yang et al. 2016; Manjavacas et al. 2019a).

The rotation periods of substellar companions as derived from their variability are typically short, ranging from $\sim$1 hour to $\gtrsim$20 hours (e.g. Metchev et al. 2015; Tannock et al. 2021). Bryan et al. (2018) and Vos et al. (2022) found that companion rotation rates and periods are consistent with those of analagous isolated objects, indicating that these populations share similar angular momentum histories.

Although variability has been successfully measured for numerous substellar companions using space-based telescopes, it is highly challenging to obtain precise photometric measurements for the population of close-separation, high-contrast companions only accessible to ground-based observatories. The larger mirror diameters and high-contrast imaging systems of ground-based telescopes allow us to detect these companions, but any intrinsic variability signal in their light curves is overwhelmed by non-astrophysical variability introduced by Earth's atmosphere and instrumental systematics. This contaminant variability can be removed by dividing the light curve of the companion by a simultaneous photometric reference; a separate source that is also contaminated by these systematics but is otherwise non-variable, observed simultaneously to the companion. Variability studies of stars or isolated substellar objects will often use known non-variable field stars for this purpose (e.g. Gelino et al. 2002; Biller et al. 2013; Girardin et al. 2013; Vos et al. 2019; Manjavacas et al. 2021, 2022). However, the fields of view of ground-based high-contrast imaging systems are generally narrow, so field stars are rarely available for use as photometric references.

Furthermore, as described in Section 1.3.2.2, the focal-plane coronagraphs used by these systems block the target star to achieve the necessary contrast to observe companions.

One option that is available for high-contrast imaging systems is to use satellite spots as the necessary photometric references. Satellite spots are off-axis PSFs, produced either by placing a diffractive grid in the telescope pupil, or by adding a modulation to the deformable mirror of an adaptive optics system (e.g. Marois et al. 2006b; Sivaramakrishnan & Oppenheimer 2006; Jovanovic et al. 2015a). These methods produce multiple bright spots at certain locations in the images, which can then be used as photometric references. Several studies have attempted to use satellite spots to measure the variability of the multiple exoplanets in the HR 8799 system (Apai et al. 2016; Biller et al. 2021; Wang et al. 2022). Although no variability was detected, these studies successfully placed variability upper limits; >5% for HR 8799 b (Biller et al. 2021), and >10% and >30% for HR 8799 c and d, respectively (Wang et al. 2022). However, they also showed that satellite spots can themselves vary under certain conditions, potentially limiting their suitability as photometric references.

As described in Section 1.3.2.3, vAPP coronagraphs do not block the light from the host star, but rather enable detections of high-contrast companions by modifying its phase. One of the main goals of this thesis is therefore to explore whether the stellar PSFs provided by the vAPP coronagraph could be used as photometric references for measuring the variability of directly imaged companions.

To further improve the stability, I adapt a technique from the transiting exoplanet community by combining the vAPP with an IFS to disperse the light into spectra (e.g. Diamond-Lowe et al. 2018, 2020a, 2022; Todorov et al. 2019; Wilson et al. 2020; Arcangeli et al. 2021; Panwar et al. 2022b,a). This has several advantages. When an exoplanet transits in front of its host star, a small fraction of the stellar light passes through the atmosphere of the exoplanet (Seager & Sasselov 2000; Charbonneau et al. 2002). Certain wavelengths of this light are absorbed by the atmosphere, depending on the molecules that are present. A 'transmission spectrum' of the atmosphere of the exoplanet can then be obtained by observing its transit at different wavelengths simultaneously and measuring how the transit depth, and hence the apparent radius of the exoplanet, changes with wavelength. It is also then possible to recombine the individual wavelengths into a 'white-light' curve, with the advantage that this smooths out wavelength-dependent flat-fielding errors and hence improves the stability and precision of the light curve. Moreover, problematic wavelengths that suffer from telluric or instrumental systematics can be excluded from the combination. The transit light curve can then be divided by the light curve of a photometric reference (i.e. a non-variable comparison star) to remove systematics introduced by Earth's atmosphere or the instrumentation. In Chapter 3 of this thesis, I emulate this principle for IFS observations of directly imaged companions, where the host star acts as the photometric reference.

1.4.2.1 Exomoons

Another possible source of variability in directly imaged companions could be satellites in orbit around the companion, such as exomoons or binary planets. Much like exoplanets that

transit in front of their host star, such a satellite may cause periodic drops in the brightness of a companion if its orbit happened to be aligned with the line of sight of the observer (e.g. Heller 2016; Lazzoni et al. 2022). To date, no exomoons have been conclusively detected around a substellar companion using any method, but several candidates have been identified (e.g. Teachey & Kipping 2018; Rodenbeck et al. 2018; Heller et al. 2019; Kreidberg et al. 2019; Lazzoni et al. 2020; Limbach et al. 2021). Snellen et al. (2014) found that a Ganymede-like exomoon orbiting directly imaged exoplanet β Pic b (11 ± 5 $M_{Jup,}$ Snellen et al. 2014) could produce a transit depth of 0.15%, beyond the reach of current techniques. However, larger binary-like satellites could produce far greater transit depths >10%, and so in principle could be detectable with observations covering a long enough baseline to confirm the periodicity (Biller et al. 2021; Lazzoni et al. 2022). Multi-wavelength variability monitoring would be key to distinguishing between atmospheric variability and variability due to satellite transits, as the former is often wavelength-dependent while transits are expected to be approximately achromatic (Limbach et al. 2021, 2023).

1.5 This thesis

In this thesis, entitled *Bringing Exoplanets Into Sharper View: Storm Chasing on Distant Worlds*, I use observations obtained with vAPP coronagraphs to characterise the atmospheres of substellar companions and search for photometric variability in their light curves. I also use these datasets to further develop new, bespoke techniques with which to do this.

In Chapter 2, I present observations of brown dwarf HR 2562 B with the 180° gvAPP coronagraph and the MagAO system on the 6.5-m Magellan Clay telescope at Las Campanas Observatory, Chile. These are the first reported observations of a substellar companion obtained with a vAPP coronagraph. I process the data using three different post-processing techniques to test which approach recovers the companion at the highest signal-to-noise. One of these is Flipped Differential Imaging (FDI), a new algorithm I developed to take advantage of the symmetry of the two complementary PSFs of the vAPP. I combine my complementary 3.94 µm narrow-band photometry of HR 2562 B with literature SPHERE and GPI data, and compare its spectrum to atmospheric models and template spectra to derive values for its physical properties.

In Chapter 3, I present a novel, ground-based approach for constructing light curves of high-contrast companions directly by combining the technique of differential spectrophotometric monitoring with the vAPP coronagraph. This allows me to search for variability arising from clouds and other features in the atmospheres of exoplanets and brown dwarfs. I test this approach using 2.8-4.2 µm observations of substellar companion HD 1160 B obtained with the dgvAPP360 and the Arizona Lenslets for Exoplanet Spectroscopy (ALES) integral field spectrograph (IFS) on the Large Binocular Telescope in Arizona. I develop a new data reduction pipeline to process this data and extract aperture photometry, producing a differential white-light curve for the companion. I then use a linear regression approach to fit and remove residual systematics from the light curve. I explore which systematics impact the precision most, and characterise the variability of HD 1160 B by searching for periodic

trends. Lastly, I discuss the advantages and disadvantages of this new approach compared to other techniques and make recommendations for how it can be used in future studies.

In Chapter 4, I present further observations of HD 1160 B with the LBT dgvAPP360 and ALES. I use the differential spectrophotometry approach described in the previous chapter to aim to confirm the variability of this companion over the course of a second night of observations. I also confirm the repeatability of this technique by testing whether the same precision can be achieved at multiple epochs under varying systematic trends. Additionally, I combine each night of data to carry out a spectral characterisation of HD 1160 B in the 2.8-4.2 µm range using BT-Settl atmospheric models. I further present high-resolution spectroscopy of host star HD 1160 A obtained with the PEPSI instrument at LBT, with which I characterise its properties and re-evaluate its spectral type.

Finally, in Chapter 5 I inject artificial companions with both non-varying and varying signals to real data obtained with the LBT dgvAPP360 and ALES. I process the data and extract photometry for each companion to explore how well their known variability signals can be recovered in their differential light curves, and hence the level to which telluric and other systematics contaminate such light curves. I also produce a simulated data set and introduce a range of systematics arising from atmospheric turbulence, such as NCPAs described by Zernike modes. Using these simulations, I investigate how different aberrations impact the relative aperture photometry of a star and substellar companion over the course of a time series when different size apertures are used for each object.

Combined, these chapters investigate the feasibility of using adaptive optics, state of the art high-contrast imaging techniques, and integral field spectrographs to create light curves of exoplanets directly. In the future, this will enable the mapping of their storms and features, and searches for their exomoons. I show that with the new techniques that I have developed we can reach 4% precision levels, repeatable on separate nights, and I highlight that improvements in wavefront sensing and systematics detrending could provide even greater precision, which will ultimately bring the features of distant worlds into sharper view.

That brown dwarf that you mentioned before...
it's, uh, pretty much a gas giant, right?
Captain Christopher Pike, Star Trek: Strange New Worlds

Chapter 2

High-contrast observations of brown dwarf companion HR 2562 B with the vector Apodizing Phase Plate coronagraph

Ben J. Sutlieff, Alexander J. Bohn, Jayne L. Birkby, Matthew A. Kenworthy, Katie M. Morzinski, David S. Doelman, Jared R. Males, Frans Snik, Laird M. Close, Philip M. Hinz, and David Charbonneau

Adapted from *Monthly Notices of the Royal Astronomical Society, 2021, Volume 506, Issue 3, pp. 3224-3238*

Abstract

The vector Apodizing Phase Plate (vAPP) is a class of pupil plane coronagraph that enables high-contrast imaging by modifying the Point Spread Function (PSF) to create a dark hole of deep flux suppression adjacent to the PSF core. Here, we recover the known brown dwarf HR 2562 B using a vAPP coronagraph, in conjunction with the Magellan Adaptive Optics (MagAO) system, at a signal-to-noise of S/N = 3.04 in the lesser studied L-band regime. The data contained a mix of field and pupil-stabilised observations, hence we explored three different processing techniques to extract the companion, including Flipped Differential Imaging (FDI), a newly devised Principal Component Analysis (PCA)-based method for vAPP data. Despite the partial field-stabilisation, the companion is recovered sufficiently to measure a 3.94 μm narrow-band contrast of $(3.05 \pm 1.00) \times 10^{-4}$ ($\Delta m_{3.94\mu m} = 8.79 \pm 0.36$ mag). Combined with archival GPI and SPHERE observations, our atmospheric modelling indicates a spectral type at the L/T transition with mass $M = 29 \pm 15$ M_{Jup}, consistent with literature results. However, effective temperature and surface gravity vary significantly depending on the wavebands considered ($1200 \leq T_{eff}(K) \leq 1700$ and $4.0 \leq \log(g)(dex) \leq 5.0$), reflecting the

challenges of modelling objects at the L/T transition. Observations between 2.4 and 3.2 µm will be more effective in distinguishing cooler brown dwarfs due to the onset of absorption bands in this region. We explain that instrumental scattered light and wind-driven halo can be detrimental to FDI+PCA and thus must be sufficiently mitigated to use this processing technique. We thus demonstrate the potential of vAPP coronagraphs in the characterisation of high-contrast substellar companions, even in sub-optimal conditions, and provide new, complementary photometry of HR 2562 B.

Key words: instrumentation: high angular resolution – planets and satellites: atmospheres – planets and satellites: detection – brown dwarfs – stars: individual: HR 2562 – infrared: planetary systems

2.1 Introduction

The detection and characterisation of planetary-mass and brown dwarf substellar companions through high-contrast imaging is reliant on coronagraphs that suppress the diffraction haloes of their host stars. A combination of innovative coronagraph design and optimal post-processing strategy is required to achieve deep contrast ratios at the smallest angular separations currently accessible to ground-based astronomy, where the companion flux can be dominated by quasistatic speckles of residual starlight (Racine et al. 1999; Hinkley et al. 2007; Martinez et al. 2013). The ever-growing sample of imaged planetary-mass (e.g. Marois et al. 2008; Lagrange et al. 2010; Macintosh et al. 2015; Chauvin et al. 2017; Keppler et al. 2018; Haffert et al. 2019; Janson et al. 2019; Bohn et al. 2020b) and brown dwarf (e.g. Chauvin et al. 2005b; Hinkley et al. 2015; Mawet et al. 2015; Mesa et al. 2016; Janson et al. 2019; Wagner et al. 2020a; Currie et al. 2020) companions highlights the success of the technique. However, many of the instruments involved in these discoveries use focal-plane coronagraphs (Soummer 2005; Mawet et al. 2012; Ruane et al. 2018) which are inherently susceptible to tip/tilt instabilities, primarily resulting from telescope vibrations, that limit their ability to reach deeper contrast ratios (Fusco et al. 2014; Otten et al. 2017). Conversely, vector Apodizing Phase Plate (vAPP) coronagraphs reside in the pupil plane and are therefore inherently insensitive to these tip/tilt instabilities. This intrinsic stability also facilitates beam-switching, which is advantageous in the thermal infrared for the removal of background flux. By adjusting the phase of the incoming wavefront, the vAPP modifies the Point Spread Functions (PSFs) of all objects in the field of view to create a 'dark hole', a region of deep flux suppression, adjacent to the PSF core (Otten et al. 2014a; Doelman et al. 2017; Por 2017; Bos et al. 2020a). The 6.5-m Magellan Clay telescope at Las Campanas Observatory (LCO) hosts a vAPP coronagraph for use in combination with the Magellan Adaptive Optics (MagAO) system (Close et al. 2012; Morzinski et al. 2014). This vAPP (described by Otten et al. 2017) uses a polarization grating to split incoming light according to its circular polarization, resulting in two complementary coronagraphic PSFs each with a 180° D-shaped dark hole on the opposing side, enabling a full view of the region around a target star in a single image (Snik et al. 2012; Otten et al. 2014b). The size of these dark holes is wavelength dependent, with inner and outer working angles of 2 - 7 λ/D. A faint and unmodified 'leakage' PSF also appears halfway between the two coronagraphic PSFs. These three PSFs are shown in Figure 2.1, with the centres of the PSF cores indicated by black crosses. The centres of these PSFs were found by fitting the PSF core with a 2D Gaussian and identifying the location of the peak flux. The leakage term collates the polarization leakage (i.e. the small fraction of light that does not receive the phase adjustment, Doelman et al. 2020), and can be useful for photometric monitoring of companions or other objects detected in the dark hole (Sutlieff et al., in preparation), depending on the phase design of the vAPP in question. The deep speckle suppression is highly advantageous, but comes at the expense of a few factors. For example, a companion will only be visible in the dark hole of one coronagraphic PSF, hence a loss of overall companion flux of $\sim$50% (Doelman et al. 2020). Further, due to the use of a polarization grating to split the coronagraphic PSFs, their separation is wavelength-dependent and all three PSFs are laterally smeared across the detector (Otten et al. 2017). However, narrow-band filters with a full width at half maximum

(FWHM) of $\frac{\Delta\lambda}{\lambda} \leq 0.06$ can limit the smearing to $< 1\lambda/D$, albeit at the expense of a lower total flux compared to when broad-band filters are used. The deep flux suppression of the vAPP can be further augmented by bespoke data reduction and post-processing strategies designed to remove residual speckles while handling the unique PSF shape, achieving optimal sensitivity to substellar companions in the dark hole. To date, the vAPP at the Large Binocular Telescope has been used to image a protoplanetary disc (Wagner et al. 2020b), and Apodizing Phase Plate coronagraphs (APPs; the predecessor technology to the vAPP, Codona et al. 2006; Kenworthy et al. 2007) were successfully used to detect substellar companions at high contrasts (Meshkat et al. 2015a,b; Quanz et al. 2010, 2015). However, observations of substellar companions using vAPPs have yet to be reported.

HR 2562 (HD 50571; HIP32775) is an F5V star with an estimated mass of 1.368±0.018 $M_\odot$ (Mesa et al. 2018) at a distance of 34.007±0.048 pc (Gaia Collaboration et al. 2018; Bailer-Jones et al. 2018). The key properties of the star are summarised in Table 2.1. As is common for F-type stars without known membership of a moving group or cluster, the age of the system is not well constrained, with the strongest constraints on the age (450^{+300}_{-250} Myr) arriving from measurements of the stellar lithium-temperature relationship (Mesa et al. 2018). HR 2562 has a circumstellar debris disc at an inclination of 78.0±6.3°and position angle of 120.1±3.2°, with an inner radius of 38±20 au and an outer radius of 187±20 au (Moór et al. 2006, 2015). Using the Gemini Planet Imager (GPI, Macintosh et al. 2014) in the J-, H-, and K-band Konopacky et al. (2016) identified a 30±15 M_{Jup} substellar companion to HR 2562, with an estimated spectral type of L7±3 at a projected separation of 20.3±0.3 au (0.618±0.003″), orbiting coplanar to the debris disc and within the inner gap of the disc. This companion is one of only two detected brown dwarfs orbiting interior to its host debris disc, alongside HD 206893 B (Milli et al. 2017). Mesa et al. (2018) and Maire et al. (2018) conducted a further study of the system with the Spectro-Polarimetric High-contrast imager for Exoplanets REsearch (SPHERE, Beuzit et al. 2019) instrument at the Very Large Telescope (VLT), completing an extensive spectrophotometric and astrometric characterisation of the companion through spectral observations in the Y- to J- band range plus broad-band imaging in the H-band. They derive a similar mass of 32±14 M_{Jup} but an early T spectral type. HR 2562 is an ideal target for the MagAO vAPP as the companion separation is at the centre of the dark hole of the vAPP at 3.94 µm (which covers a working angle of 261 - 912 mas at this wavelength) at an achievable contrast ($\Delta K2 = \sim 10.4$ mag, Konopacky et al. 2016). It is therefore optimal for developing and testing procedures for data reduction and post-processing. Furthermore, photometry of the companion at a wavelength longer than those in previous studies can further constrain physical properties of HR 2562 B, such as effective temperature and surface gravity, and help to resolve the tension in its spectral classification.

In this paper we present the first reported images of a substellar companion using a vAPP coronagraph. In Section 2.2 of this paper we describe the observations performed on HR 2562, and in Section 2.3 we outline the data reduction and new post-processing methodology we developed for data obtained with a vAPP. In Section 2.4 we explain how we obtained our photometric measurements, and fit spectral models and empirical templates to the data to

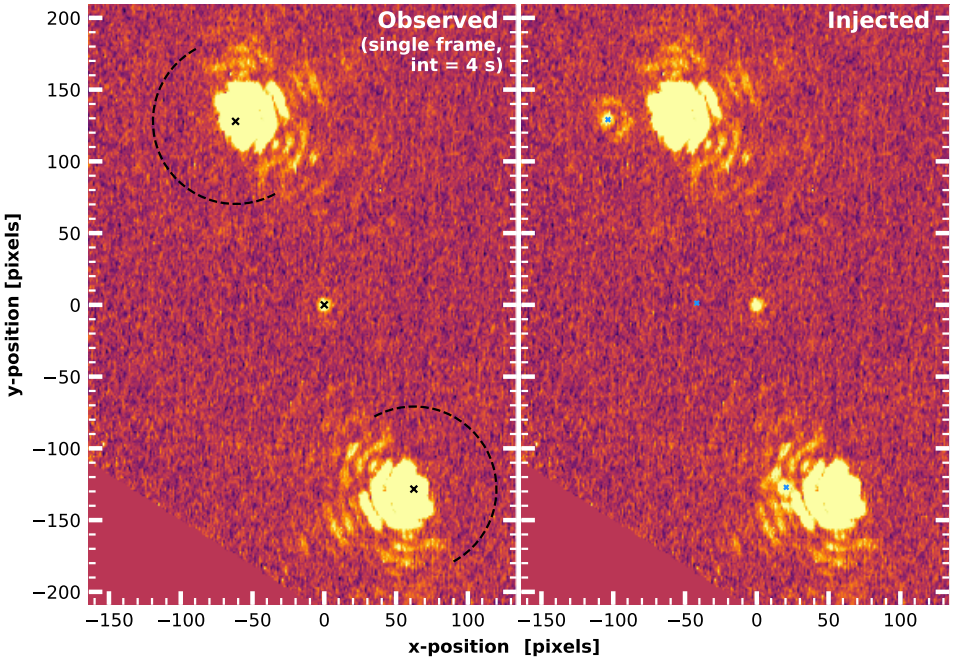

Figure 2.1: HR 2562 as it appears in a single science frame from the MagAO vAPP coronagraph after pre-processing (left-hand panel). The three PSFs characteristic of the vAPP are visible, with the centres of the PSF cores indicated by black crosses. At the top and bottom of the image are the coronagraphic PSFs with complementary D-shaped dark holes of deep stellar flux suppression (bounded by black dashed arcs), and the unmodified leakage PSF appears at the origin. The spatial scale shows the differential offsets (in pixels) of the coronagraphic PSFs on the detector with respect to the leakage term, however all three PSFs represent the same position on sky. On the right is the same frame with an artificial companion injected at a contrast of 4.0×10^{-2} ($\Delta m_{3.94\mu m} = 3.5$ mag) and separation of 41 pixels. The companion PSFs (indicated by blue crosses) have the same shape and structure as the three stellar PSFs. The injected companion can therefore be seen both in the dark hole of the top coronagraphic stellar PSF and, when compared to the left-hand panel, obscured by the flux of the bottom one. The leakage term corresponding to the companion is also present to the left of the stellar leakage term, but is too faint to be visible. Both images are presented with an arbitrary logarithmic colour scale. The frame is not aligned to north, and the lower left-hand corner is masked due to bad pixels.

obtain values for the physical parameters of the companion. We then discuss these results in Section 2.5, and compare them to previous results from the literature. We also discuss the effectiveness and limitations of our post-processing strategy. The conclusions of the paper are presented in Section 2.6.

2.2 Observations

We observed the star HR 2562 and its substellar companion (separated by 643.8±3.2 mas, Maire et al. 2018) on the nights of 2017 February 06 (02:47:39 - 05:16:11 UT) and 2017 February 07 (02:08:32 - 07:34:34 UT), with the vAPP coronagraph and the MagAO (Close

Table 2.1: Properties of host star HR 2562.

Parameter	Value	Reference(s)
Spectral Type	F5V	(1)
Right Ascension (J2000)	06:50:01.02	(2)
Declination (J2000)	-60:14:56.92	(2)
Age (Myr)	450^{+300}_{-250}	(3)
Parallax (mas)	29.3767±0.0411	(2)
Distance (pc)	34.007±0.048	(2, 4)
Proper motion (RA, mas yr^{-1})	4.663±0.084	(2)
Proper motion (Dec, mas yr^{-1})	108.377±0.089	(2)
Mass ($M_\odot$)	1.368±0.018	(3)
Radius ($R_\odot$)	1.334±0.027	(3)
T_{eff} (K)	6597±81	(5)
log(g) (dex)	4.3±0.2	(3)
[Fe/H]	0.10±0.06	(3)
V (mag)	6.098±0.010	(6)
G (mag)	5.9887±0.0005	(2)
J (mag)	5.305±0.020	(7)
H (mag)	5.128±0.029	(7)
K (mag)	5.020±0.016	(7)

References: (1) Gray et al. (2006); (2) Gaia Collaboration et al. (2018); (3) Mesa et al. (2018); (4) Bailer-Jones et al. (2018); (5) Casagrande et al. (2011); (6) Høg et al. (2000b); (7) 2MASS (Cutri et al. 2003)

et al. 2012; Morzinski et al. 2014) system on the 6.5-m Magellan Clay telescope at LCO, Chile. We used the Clio2 Narrow near-IR camera, which has a plate scale of 15.85 mas pixel^{-1} and an array of 1024 x 512 pixels, giving a field of view of 16″x 8″ (Sivanandam et al. 2006; Morzinski et al. 2015). The vAPP was positioned in the pupil stop wheel of Clio2 as described in Otten et al. (2017), such that three PSFs of the star appeared in a sequence across the short axis of the detector (as shown in Figure 2.1), leaving significant room on the long axis for background subtraction by nodding. We used a λ =3.94 µm narrow-band filter with a width of 90 nm for these observations, which placed the companion at the centre of the dark hole of the top coronagraphic PSF. With this filter, $\frac{\Delta\lambda}{\lambda} = 0.023$, so wavelength-dependent radial smearing is limited to $< 0.4\lambda$/D. Furthermore, the MagAO system achieves a high Strehl ratio (>90%) at this wavelength (Otten et al. 2017). Atmospheric conditions were clear throughout the observations. On the first night, seeing was measured at 0.6″ at the beginning of observations. At the start of the second night seeing was poor (1.3″) with no wind, and improved to 0.5-0.6″ seeing by midnight, but with ∼13 m s^{-1} winds. Observations were obtained in a continuous sequence on each night (interrupted only when the adaptive optics loop opened). We obtained 362 and 403 data cubes on the first and second nights, respectively. Each cube contains 10 sub-frames, where each sub-frame represents an integration time of 2 s on the first night and 4 s on the second. The total on-target integration time across both nights is thereby $(362 \times 10 \times 2 + 403 \times 10 \times 4) = 23360$ s (∼6.5 h). The increased exposure time for the second night was chosen as a compromise to minimize the effect of readout noise without obtaining excessive flux due to the high sky background at 3.94 µm. For background subtraction, we used an ABBA nodding pattern. Dark frames were also obtained at the corresponding exposure times for the science frames at the end of the night. The majority of the data was obtained in field-stabilised mode with the derotator switched on and the companion position fixed in the dark hole. Although this is non-standard for high-contrast imaging, our original intention for these observations was to characterise the stability of the MagAO vAPP over time by identifying fluctuations that correspond to instrumental systematics, hence we wanted to keep sources stationary on the same pixels (Sutlieff et al., in preparation). However, the derotator malfunctioned part way through each night (at 05:01:08 UT on the first night, and 04:44:34 UT on the second), causing the field to rotate during the remainder of the observing sequence. The field rotation when the derotator was off was 4.36° and 42.29° on the first and second nights, respectively. This mix of field-stabilised and pupil-stabilised data is not the most optimal approach for high-contrast imaging. Nonetheless, in the latter case, the high field rotation was sufficient enough that we were able to use the Angular Differential Imaging (ADI, Marois et al. 2006a) technique to reduce quasistatic speckle noise in the data from the second night (as discussed in Section 2.3.2), and determine a flux for the companion in the L-band regime for the first time. All three of the PSFs remained unsaturated in the core. By coincidence, HR 2562 was also observed with SPHERE on the night of 2017 February 07, the second night of our observations (Mesa et al. 2018; Maire et al. 2018), providing an exact known position of the companion in our observations.

2.3 Data reduction

2.3.1 Pre-processing

To handle the unique PSFs of the vAPP images, we used both standard tools in the literature and bespoke techniques. First, we discarded 10 data cubes from the first night and 49 cubes from the second night that were unusable due to the adaptive optics loop opening during detector exposure. We then corrected non-linear pixels and bad pixels using the formulae and maps described in Morzinski et al. (2015). The linearity correction is capable of correcting measured counts up to 45,000 data numbers (DN), where counts above 27,000 DN are considered non-linear. On average, ∼0.7% of pixels in each frame were in this non-linearity regime prior to correction and of these, none were present in the vAPP dark holes except for a small cluster of bad pixels in the top dark hole at the 'A' nod position, which were later corrected. Although the bad pixel map did not cover all of the bad pixels in our data, most of the remainder did not lie within or close to the vAPP dark hole. A master dark frame was created for each night by median combining five dark frames with the same array size, integration times, and input offset voltage as our data. The master dark frame was then subtracted from every raw science frame. We created an 'A' nod position sky flat and a 'B' nod position sky flat by median combining all of the dark-subtracted science frames at the opposite nod position. We normalised each of these sky flats by dividing them by the median number of counts in a region of the frame away from the PSFs. These normalised sky flats were then divided out of the dark-subtracted science frames, removing variations caused by the response of the detector and long-term sky structure throughout the observations. After these calibrations, background subtraction was carried out using the data from the opposing nod positions of the ABBA pattern. For each data cube obtained in the A position, we subtracted the corresponding B position data cube obtained closest in time to the A position cube, and vice versa. To remove any residual background offset, we then subtracted the median of a clean region of the data from each frame. A number of instrumental ghosts and other optical effects resulting from internal reflection within the refractive optics of the setup are visible in the data (see Section 2.5.2).

2.3.2 Post-processing

Additional post-processing of the data is required to further augment the deep flux suppression of the vAPP and achieve the sensitivity needed to detect HR 2562 B. To do this, we used custom modules based on version 0.6.2 of the PynPoint package for high-contrast imaging data (Stolker et al. 2019). First, we cropped each of the two coronagraphic PSFs separately and fit their cores with 2D Gaussians to align the data from both nod positions together, making an image cube for each coronagraphic PSF covering the full sequence. This placed the two nod positions at the same location and removed a linear drift in position across the full observing sequence. Regions inside the inner working angle of the vAPP and beyond the outer expanse of the vAPP PSF were then masked and the two opposing dark holes were joined together. At this stage, we separately applied three different post-processing techniques to the joined dark holes, designed to subtract speckle noise and other residual

starlight not suppressed by the vAPP, producing three final images.

Classical ADI (cADI): The first of these techniques was classical ADI (cADI, Marois et al. 2006a). We constructed a reference PSF by taking the median combination of the data. This reference PSF was then subtracted from the data. After subtraction of the reference PSF, we aligned the images to north according to their parallactic angles and median combined them. Unsurprisingly, as cADI is reliant on the field rotation of the observations to prevent the inclusion of flux from the companion in the reference PSF, we do not detect HR 2562 B in the data from the first night. However, in the final cADI image from the second night (which covered significantly more field rotation), the companion is detected at the expected position in the centre of the right-hand (after north alignment) vAPP dark hole and is shown in the left-hand panel of Figure 2.2. This is a marginal detection with a signal-to-noise ratio (S/N) of 3.04. Although this is not at the S/N = 5 level commonly accepted for a detection in a blind search, it is reinforced by its presence at the known position of the companion measured by Maire et al. (2018), in data obtained on the same night using SPHERE.

Principal Component Analysis (ADI+PCA): The second post-processing technique we applied to the joined dark holes was speckle subtraction via Principal Component Analysis (ADI+PCA; Amara & Quanz 2012; Soummer et al. 2012; Meshkat et al. 2014). We used PCA to construct and subtract a reference PSF consisting of 3 principal components, selected as the number that best removed the visible speckle structure and residuals of the vAPP PSF. The residual images were then aligned to north and median combined as above. As above, this technique did not produce a detection in the data from the first night, as the lack of field rotation led to companion self-subtraction. We again marginally detect HR 2562 B in the final image when ADI+PCA was applied to the second night of data, this time with an S/N of 2.38 (centre, Figure 2.2).

Flipped Differential Imaging (FDI+PCA): The third algorithm we used to construct and subtract a reference PSF was a new technique relying on the symmetry of the coronagraphic vAPP PSFs (hereafter Flipped Differential Imaging, FDI+PCA). With FDI+PCA, the reference PSF to be subtracted from one coronagraphic PSF is produced by applying the PCA algorithm to the opposing coronagraphic PSF after it has been rotated by 180 degrees. This was recommended by Otten et al. (2017) and builds upon a similar approach in the same paper, which uses the opposing vAPP coronagraphic PSF as a reference directly (without applying PCA). It is also similar to the technique used by Dou et al. (2015), who applied the ADI+PCA concept using a single non-coronagraphic PSF under 180° rotation as a self-reference. As with ADI+PCA, the reference PSF that we created consisted of 3 principal components. We subtracted then north aligned and median combined to produce the final images. In this case, we do not detect HR 2562 B in the images from either night of data. The final FDI+PCA processed image for the second night of data is shown in the right panel of Figure 2.2. The symmetry-breaking factors that have affected the performance of the FDI+PCA algorithm, including instrumental ghosts and wind-driven halo, are discussed in Section 2.5.2. As FDI+PCA is not inherently reliant on field rotation like cADI and ADI+PCA, in principle we would expect it to be more effective when applied to the first night of data compared to these techniques. However, it was clear from pre-processing that the asymmetric features would have an even stronger effect without field rotation, and that the increased

effect of readout noise due to the shorter exposure time on the first night further inhibits detection of the companion.

As we only detect the companion in the data from the second night of observations (which covers a total integration time of 14,160 s), we continue with the data from this night only for the remainder of our analysis. In each of the final images, contamination is seen where the edges of the dark holes were joined together, visible as structured bright and dark patches in the north-east and south-west regions (see segments indicated by blue dotted lines in Figure 2.2). However, the region surrounding the expected companion location (based on the concurrent SPHERE observations, Maire et al. 2018) is unaffected by this as it is positioned centrally in the vAPP dark hole.

2.4 Results

The cADI reduction, using observations from the second night only, gives the highest S/N for the companion in the final images (see Figure 2.2), so we proceed with this technique for the remainder of our analysis, noting that it contains a mix of field- and pupil-stabilised data. The companion was not detected in the first night of data, which was primarily obtained in field-stabilised mode. Either greater photon collecting power or targets with lower contrasts are required to successfully detect companions in field stabilised mode.

2.4.1 Photometric measurement

We measured the contrast ratio of HR 2562 B by injecting scaled negative template companions into the data after pre-processing at the known position of HR 2562 B, following the approach of Bonnefoy et al. (2011); Galicher et al. (2011); Lagrange et al. (2010). The PSFs of companions observed using a vAPP coronagraph have the same shape and structure as the stellar PSFs, i.e., two coronagraphic PSFs and a leakage PSF, all offset from the stellar PSF. However, typically only the coronagraphic PSF in the dark hole is seen, while the other is obscured by the bright coronagraphic stellar PSF, and the companion's leakage PSF is too faint to be detectable (right-hand panel, Figure 2.1). Template companion injection is therefore only required around the coronagraphic stellar PSF where the companion resides in the dark hole, as only this companion PSF contributes to the detection. We produced this PSF template by median combining the corresponding unsaturated coronagraphic PSF of the star in the pre-processed images and cropping to the first Airy ring. We then scaled the flux of the template relative to the coronagraphic stellar PSF and subtracted it at the location of the companion in the pre-processed data, iterating over different values for the contrast ratio in a grid ranging from contrasts of $8.4 \leq \Delta m_{3.94\mu m}(\text{mag}) \leq 9.4$ with a step size varying from 0.1 to 0.01 as the value was refined. For each injection, we applied cADI as described in Section 2.3.2. The contrast measurement was then taken as the value which minimized the root mean square in an aperture at the companion location after the negative injection. We also iterated over a grid of possible positions for the companion and found a companion separation of 665.4 ± 24.0 mas and position angle of $297.3 \pm 2.3°$. These values are consistent with those of Maire et al. (2018) to within 1σ, who observed HR 2562

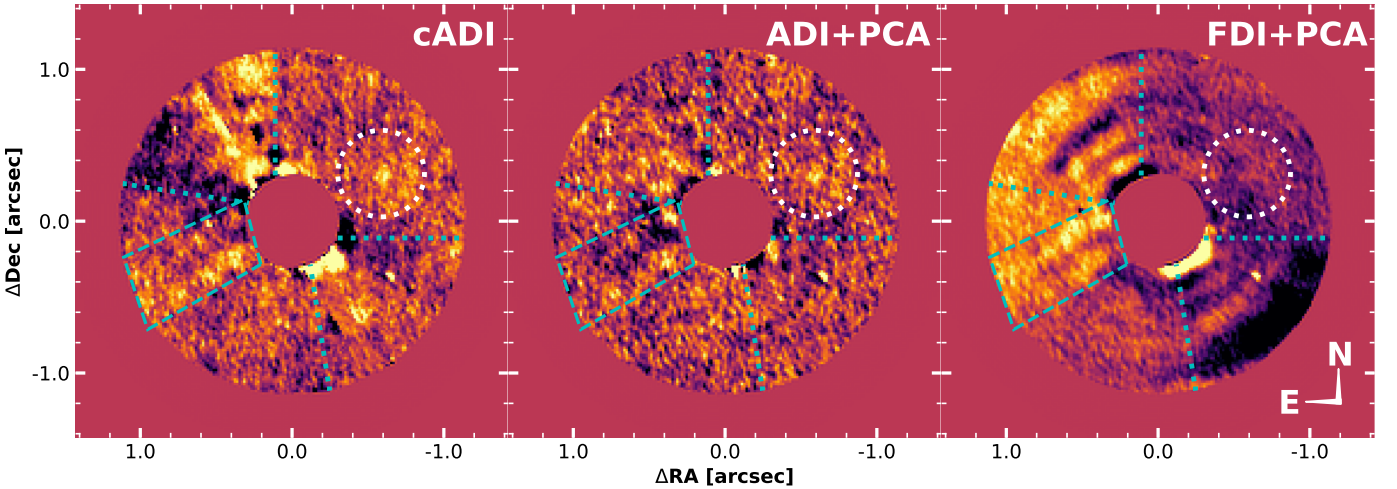

Figure 2.2: The final post-processed images obtained with MagAO+vAPP, as processed using the cADI (left-hand panel), ADI+PCA (middle), and FDI+PCA (right-hand panel) algorithms, and covering a total integration time of 14,160 seconds. The two D-shaped dark holes have been stitched together around their common centre. Residual contamination is visible where the dark holes were joined together in the form of bright and dark regions in the north-east and south-west (segments indicated by blue dotted lines). Regions inside the inner working angle of the vAPP and beyond the outer expanse of the vAPP PSF have been masked. The expected location of the companion from concurrent SPHERE observations (Maire et al. 2018) is indicated by a dotted white circle in each image. HR 2562 B is detected in the cADI and ADI+PCA images, but not in the FDI+PCA image. The non-detection in the FDI+PCA image is due to symmetry-breaking factors such as instrumental ghosts and wind-driven halo, and is discussed in Section 2.5.2. The characteristic butterfly pattern of wind-driven halo can be seen in the FDI+PCA image as extended bright and dark patches immediately and diagonally either side of the masked inner region. A bright spike caused by instrumental scattered light is indicated in the blue dashed box. The bright patch in the south-west is a persistent detector defect that was not removed during the data reduction process. All three images use an arbitrary logarithmic colour scale.

with SPHERE on the same night as these observations and found a companion separation of 643.8±3.2 mas and position angle of 297.51±0.28°. The relatively large uncertainties on our position measurements can likely be attributed to the photometric extraction process, which is intrinsically less accurate in the low S/N regime of our measurement. Despite this, the difference between the SPHERE position and our position affects the contrast measurement at the millimagnitude level only. We measure the 3.94 µm contrast to be $(3.05\pm1.00) \times 10^{-4}$ ($\Delta m_{3.94\mu m}$ = 8.79±0.36 mag). We calculated the measurement error on this value following Morzinski et al. (2015), which uses the S/N of the companion in the final image. We measured an S/N of 3.04 for the companion by dividing the Gaussian-smoothed peak height of the companion by the standard deviation in an annulus centred on the companion location with inner and outer radii of 1 × FWHM and 2 × FWHM wide, respectively. The uncertainty can primarily be attributed to the quasistatic speckle noise throughout the observations. This error bar is relatively large compared to literature measurements of companion contrast, again reflecting the photometric extraction process in the low S/N regime of the detection. The causes of this low S/N are discussed in Section 2.5.1.

The star does not have flux calibrated observations in the 3.94 µm filter. To convert our contrast value to a measurement of the physical flux of the companion, we used the Virtual Observatory SED Analyzer (VOSA, Bayo et al. 2008) to fit the Spectral Energy Distribution (SED) of the host star and calculate the stellar flux at 3.94 µm. We included literature photometry of HR 2562 from Gaia (Gaia Collaboration et al. 2018), 2MASS (Skrutskie et al. 2006) and WISE (Wright et al. 2010) catalogues, and fitted a grid of BT-Settl models (Allard et al. 2012) using a chi-square test, assuming a distance of 34.01 pc (Gaia DR2) and an extinction of A_V = 0.07 mag from the extinction map of Morales Durán et al. (2006). The best fit model had T_{eff} = 6600 K, log(g) = 4 dex, and [Fe/H] = 0.5, which are in good agreement with the values derived by Mesa et al. (2018). Evaluating this model in the 3.94 µm filter profile of MagAO/Clio2 and multiplying by our contrast measurement of $(3.05 \pm 1.00) \times 10^{-4}$, we obtain a physical flux of $F_{3.94\mu m} = (1.3 \pm 0.4) \times 10^{-13}$ erg s^{-1} cm^{-2} micron^{-1} for HR 2562 B at 3.94 µm. This value is shown in Figure 2.3 alongside the GPI spectrum from Konopacky et al. (2016) in the J, H, K1, and K2 bands; as well as the Y,J SPHERE IFS spectrum and SPHERE IRDIS H-broad-band datapoint from Mesa et al. (2018). The SPHERE IFS and GPI spectra are comparable where they overlap in the J-band, with a small systematic offset within the 1σ error bars at ∼1.28 µm. Mesa et al. (2018) note the possibility of systematic offsets between GPI and SPHERE photometry, likely caused by differences in the algorithms used for processing data, extracting spectra and calibrating the flux (Rajan et al. 2017; Samland et al. 2017). We nonetheless include the data from both instruments in our analysis of the companion SED, considering theoretical model and empirical template fits to both the entire SED, and subsets that exclude individual instruments (see Sections 2.4.2.1 - 2.4.2.2).

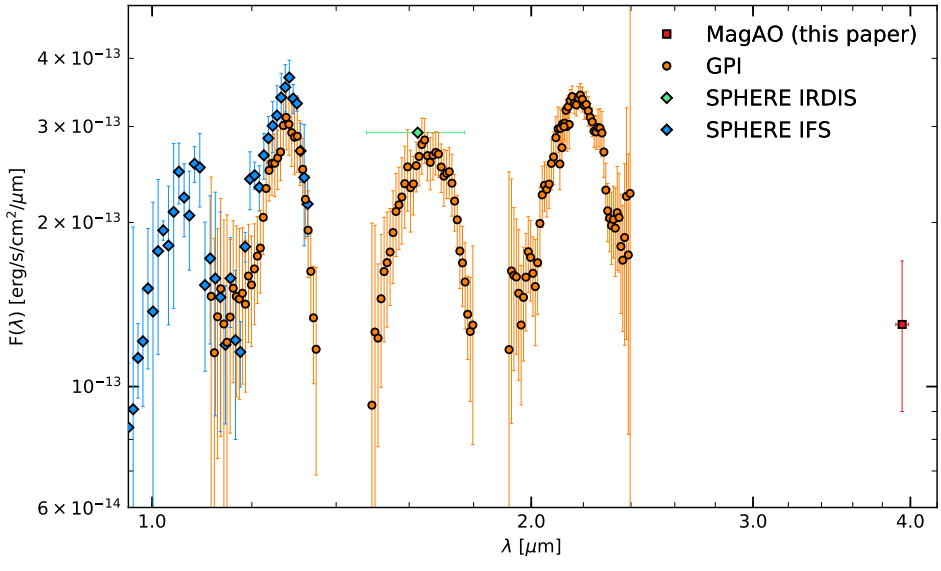

Figure 2.3: The spectrum of HR 2562 B including our 3.94 µm observation with MagAO+vAPP (red square) alongside all previous photometric data: SPHERE IRDIS photometry using the H broad-band filter (turquoise diamond), SPHERE IFS data in the Y and J bands (blue diamonds), and GPI spectral data in the J, H, K1, and K2 bands (orange circles). The errorbars in the wavelength direction correspond to filter width, or in the case of the IFS and GPI spectral data points, Gaussian widths corresponding to the resolution of the respective spectrograph in the relevant band (see 2.4.2.1). The width of the MagAO 3.94 µm narrow-band filter is 90 nm. Some errors are smaller than the symbols.

2.4.2 Spectral fitting

2.4.2.1 Theoretical atmospheric models

To determine the physical properties of HR 2562 B, we followed the approach of Bohn et al. (2020a), using a linear least squares approach to fit grids of theoretical spectra to the photometric data. We selected a grid of BT-Settl models[1] (Allard et al. 2012) limited to effective temperatures between 400 K and 2500 K with a step size of 100 K, surface gravities between 0.0 dex and 5.5 dex with a step size of 0.5 dex, and metallicity [Fe/H] = 0. We then integrated the flux of each model in the grid over the spectral response curves of each observed filter to find the scaling parameter that best matched the model to the SED of the companion, characterised as the value that minimizes the Euclidean norm of the residual vector between the two. The overall best fit model is then identified as the one that results in the minimum residual compared to the SED. In lieu of spectral response curves for the SPHERE IFS and GPI spectral data, we treated the spectral response of each wavelength channel as a Gaussian corresponding to the resolution of the spectrograph in the relevant band (Samland et al. 2017). When the fitting procedure described above was performed on the full spectrum of HR 2562 B, the minimum residual is given by a model with T_{eff} = 1700 K and log(g) = 5.0 dex, shown alongside the SED as a purple line in Figure 2.4. As the MagAO and SPHERE photometry were obtained concurrently on the same night, we also performed the fitting procedure to this subset of the data. On the other hand, as the GPI data were not obtained concurrently with the MagAO data, we did not apply the fitting procedure to that subset of data. The best fit model to the subset of concurrent MagAO and SPHERE photometry alone instead has T_{eff} = 1200 K and log(g) = 4.0 dex, shown as a green line. The reduced chi-square values of the fits to the full spectrum of HR 2562 B and to the MagAO + SPHERE-only subset of data are 4.40 and 3.86, respectively, suggesting that neither model is a particularly satisfying match for the corresponding data. Indeed, while the T_{eff} = 1700 K model is statistically the best fit to the full SED and is a closer match to the amplitude of the peaks in the GPI spectrum, it is almost flat in the K-band and visibly fails to capture the wide absorption bands seen in the SED of HR 2562 B. Conversely, while the T_{eff} = 1200 K model does show these absorption features, the amplitudes of the peaks miss those of the GPI spectrum. We attempt to explain these differences between the synthetic spectra and the observational data, and the corresponding absence of a strong best fit result, in Section 2.5.3.1. We assess the effect of the photometric measurement errors on the outcome of this fitting procedure by iterating 10^5 times, varying the data flux values across Gaussian distributions centred on the original value, where the uncertainty on the original value is used as the standard deviation of the sampling. This statistical error on the derived physical properties of the companion is given by the 2.5 and 97.5 percentiles of the corresponding distribution of models (Bohn et al. 2020a). We then use the largest of either the statistical error or the BT-Settl model grid spacing of $\pm$100 K in temperature and $\pm$0.5 dex in surface gravity as our reported uncertainties on these physical parameters. By integrating over the full wavelength range of the models and accounting for the distance to

[1] Models downloaded from: http://perso.ens-lyon.fr/france.allard/

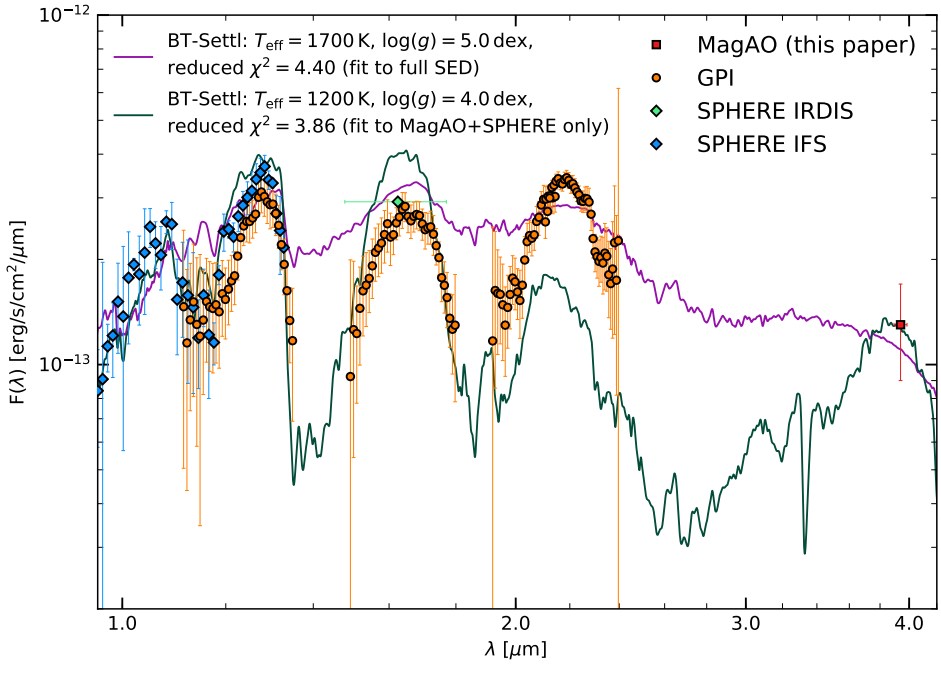

Figure 2.4: The best fit BT-Settl models to the photometry of HR 2562 B. The purple line shows the best fit to the full SED of HR 2562 B, with T_{eff} = 1700 K and log(g) = 5.0 dex, whereas the green line shows the best fit to the MagAO + SPHERE-only subset of data, with T_{eff} = 1200 K and log(g) = 4.0 dex. Both models have a metallicity of [Fe/H] = 0. Significantly different best fit models are found depending on the wavelength range considered, with very different physical parameters allowed while still providing an equally good fit. Note the large difference in the models between 2.4-3.2 µm.

the system, we further infer the companion luminosity in each case. The estimates provided by the procedure described above, considering the full SED and separately the MagAO + SPHERE-only subset of data, are given in Table 2.2. The scaling parameter is equivalent to R^2/D^2, where R is companion radius and D is the distance to the system (where D is well constrained), so we are further able to infer radius estimates for each best fit case. The fit to the full SED yields a radius of $R = 0.56^{+0.02}_{-0.01}$ R_{Jup}, whereas in the MagAO + SPHERE-only case we find $R = 0.89^{+0.14}_{-0.27}$ R_{Jup}. The reported uncertainties on the luminosity and radius estimates are the statistical errors. These results and the differences between those derived in each fitting case are discussed further in Section 2.5.3.1, where we note the likely unphysical radius derived from the full SED.

Table 2.2: Estimated physical properties of HR 2562 B. The reported errors on the effective temperature and surface gravity are the largest of either the statistical error or the BT-Settl model grid spacing. The errors on the luminosities are the statistical errors. Derived values for the mass of HR 2562 B are found by evaluating the derived values of $\log(L/L_\odot)$ with BTSettl and AMES-Dusty isochrones across the 200-750 Myr age range of the system, and the corresponding mass ratio with respect to the primary, q (see Section 2.5.3.3). The error on the age of the system dominates the errors on the mass and q.

Data	$T_{\rm eff}$ (K)	log(g) (dex)	$\log(L/L_\odot)$	Mass ($M_{\rm Jup}$)		Mass ratio q	
				BT-Settl	AMES-Dusty	BT-Settl	AMES-Dusty
Full SED	1698^{+100}_{-100}	$4.98^{+0.5}_{-0.5}$	$-4.60^{+0.03}_{-0.01}$	$30.7^{+9.7}_{-12.1}$	$33.3^{+10.0}_{-11.3}$	$0.021^{+0.007}_{-0.008}$	$0.023^{+0.007}_{-0.008}$
MagAO+SPHERE	1168^{+132}_{-100}	$4.22^{+0.78}_{-0.5}$	$-4.87^{+0.10}_{-0.11}$	$25.1^{+9.9}_{-10.9}$	$26.3^{+10.7}_{-12.2}$	$0.018^{+0.007}_{-0.008}$	$0.018^{+0.007}_{-0.008}$

2.4.2.2 Empirical templates

Noting the differences between synthetic spectra and the observations, we further performed the fitting procedure described in Section 2.4.2.1 using empirical template spectra of field L and T dwarfs from the SpeX Prism Spectral Libraries (Burgasser 2014). These templates are limited in wavelength range to 0.65 - 2.56 µm, and so do not extend to the 3.94 µm position of our MagAO datapoint for the required spectral types. Nonetheless, we proceeded with a comparison to these templates to further investigate the differences between fits to the SPHERE and GPI data, as well as to determine a spectral type for HR 2562 B. We find the best fit template to the combined SPHERE and GPI data to be that of 2MASSW J2244316+204343 (McLean et al. 2003; Looper et al. 2008), which has a spectral type of L7.5±2, plotted in Figure 2.5 as a pink line. The same best fit template is obtained when the fitting procedure is performed for the GPI data alone, but fitting to the SPHERE data alone instead best matches the spectrum of SDSS J151643.01+305344.4 (spectral type T0.5±1, Chiu et al. 2006; Burgasser et al. 2010a). This template is shown in Figure 2.5 as a grey line. We therefore consider HR 2562 B to have a spectral type at the L/T transition, and discuss this interpretation further in 2.5.3.2.

2.5 Discussion

2.5.1 Photometry

In Section 2.4.1, we report a marginal detection of HR 2562 B with an S/N of 3.04 in the final image produced by cADI at a position which matches that measured by Maire et al. (2018) and Mesa et al. (2018), who observed this companion on the same night using SPHERE. However, this value is notably lower than the S/N reported by Mesa et al. (2018), who detected HR 2562 B at an S/N of ∼20 in their final SPHERE IRDIS image, and ∼30 in their final SPHERE IFS image. Although Konopacky et al. (2016) do not provide the S/N of the detections of HR 2562 B in their final GPI images, it is clear that these are on a similar order to the SPHERE detections. This difference can primarily be explained by comparing the bandwidths of each set of observations. For our MagAO+vAPP observations, we used a 3.94 µm narrow-band filter with a width of 90 nm. This is significantly narrower than the H broad-band SPHERE IRDIS filter, which has a width of 290 nm. and the wavelength ranges covered by the final SPHERE IFS and GPI images, which are composed of spectral datacubes collapsed across their respective wavebands. Our lower S/N is therefore unsurprising. The flux measurement error of our MagAO datapoint is comparable to those of the individual spectral datapoints of SPHERE IFS and GPI. The use of a broad-band filter may be preferable if one were to conduct a blind search for undiscovered companions, where the position is not already known, as the wider wavelength coverage will enable the capture of greater companion flux and hence a stronger initial detection. However, the polarization grating of the MagAO vAPP causes wavelength-dependent smearing of the PSFs across the detector when broad-band filters are used. An additional processing step is therefore required to either extract the resulting low-resolution spectra or recombine the PSFs along the axis of

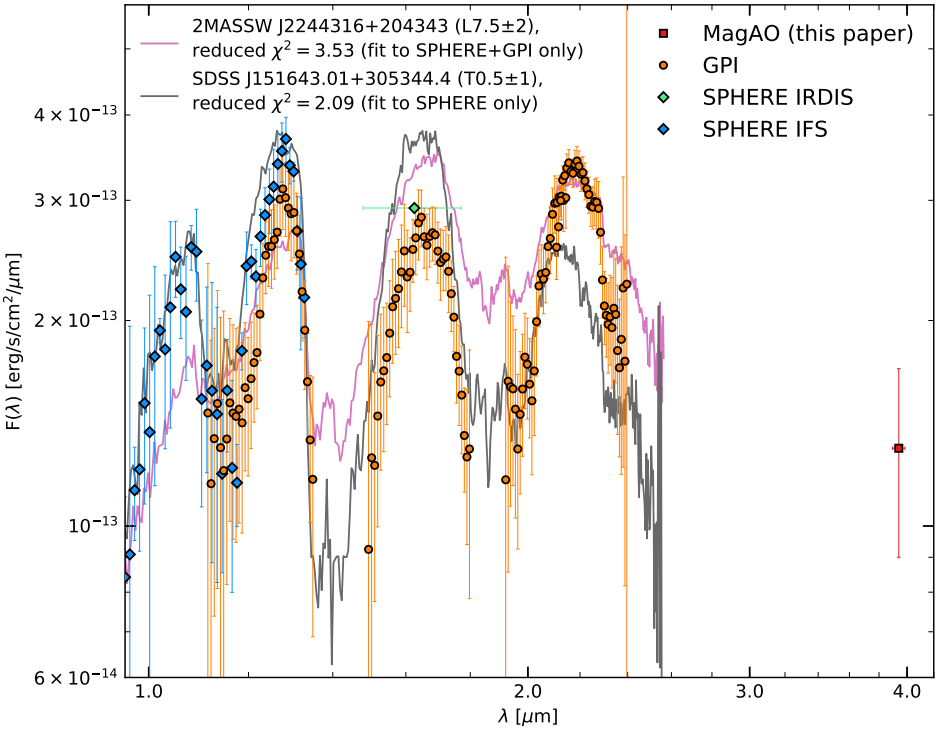

Figure 2.5: The best fit empirical template spectra to the photometry of HR 2562 B, from a set of L and T dwarf templates taken from the SpeX Prism Spectral Libraries (Burgasser 2014). The pink line shows the best fit to the combined SPHERE + GPI data, while the grey line shows the best fit model to the SPHERE data only. These templates only extend to $\lambda = 2.56$ µm, and so do not reach the 3.94 µm wavelength of the MagAO datapoint, which is shown for reference.

the vAPP. Alternatively, broad wavelength coverage can be achieved without lateral smearing by using a vAPP in combination with an integral field spectrograph, or a vAPP with a 360° dark hole, which is not affected by such smearing as a second polarization grating is used to recombine the beams on axis (Doelman et al. 2020). Another factor affecting the strength of our companion recovery is the thermal background flux arising from both the sky and the instrumentation itself, which is far greater at 3.94 µm than at the shorter wavelengths used to observe HR 2562 in previous studies (Lloyd-Hart 2000). The difference in the size of the telescopes used in these observations further contributes to the lower S/N reported in this work; the 6.5-m Magellan Clay Telescope used for these observations is slightly smaller than the 8.1-m Gemini South telescope, on which GPI is installed, and the 8.2-m VLT Unit Telescope, where SPHERE is installed. Lastly, the combination of field-stabilised and pupil-stabilised observations composing this dataset may also have had some impact on the S/N, as the field-stabilised parts may contribute some companion signal to the reference PSF removed by cADI.

Due to the small angular coverage of the dark holes, residual noise structure from the vAPP PSFs in the contaminated regions, and the non-standard combination of field and pupil-stabilised observations comprising this dataset, it is not possible to produce a meaningful assessment of the detection limits reached by each algorithm in this particular case. In the final images, not enough space remains to place the number of photometric apertures required to validly estimate the noise term, especially at small separations (Jensen-Clem et al. 2018). Furthermore, these detection limits will vary significantly not only with angular separation from HR 2562, but also depending on the position angle being considered. In lieu of such measurements of the detection limits, we include an alternative, if limited, comparison of the performance of the three algorithms applied to this data. Figure 2.6 shows the S/N at the location of HR 2562 B in the final images, as produced by each algorithm, as a function of the number of principal components removed in each case. As stated in Section 2.3.2, cADI produces the image with the highest S/N recovery of HR 2562 B (S/N=3.04). Although ADI+PCA is far more effective than cADI at reducing noise, even succeeding in removing the residual contamination from the vAPP PSF between the dark holes (dotted segments, Figure 2.2), its performance is limited by oversubtraction which reduces the signal of the companion. This can again be attributed to the non-standard combination of field and pupil-stabilised data, due to which the companion is fixed in the same location for a significant fraction of the observing sequence. It is unsurprising that some degree of companion self-subtraction occurs when our data is processed with ADI+PCA as the first component of this algorithm is simply the mean combination of the input images orthogonalised with respect to the PCA basis. While this effect likely also impacts the signal of the cADI detection, the reference PSF in this case is constructed using a median combination of the data, which will capture a lesser degree of companion flux when the majority of the observations are pupil-stabilised. Removing additional PCA components gradually suppresses the companion signal further, increasingly homogenising the image. In the case of FDI+PCA, with which the companion is not detected, the variation of the noise is greater than the peak flux at the companion location when a small number of principal components are applied, leading to an S/N smaller than one. As with PCA, this variation is gradually suppressed with additional components.

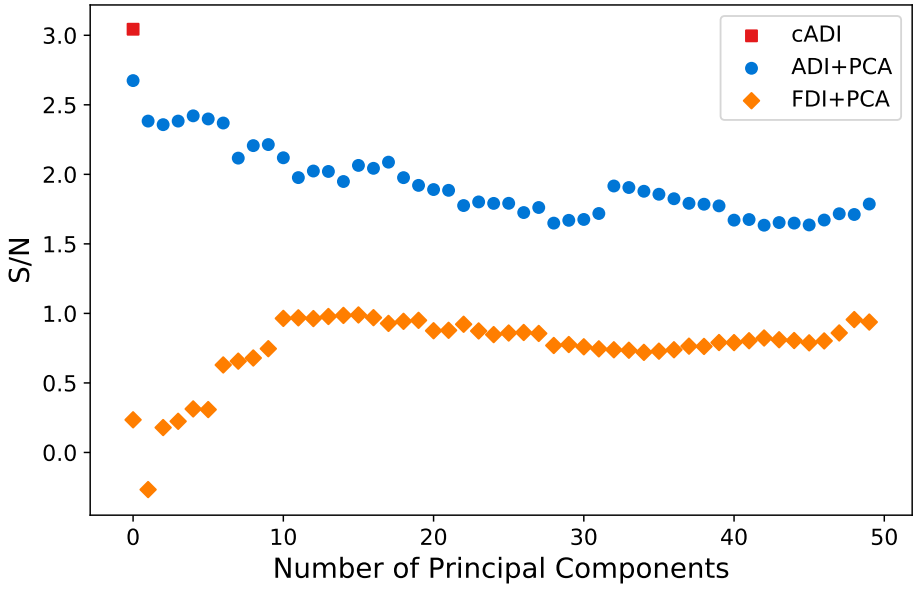

Figure 2.6: The S/N at the companion location in the final images produced by each algorithm, as a function of the number of principal components removed in each case. Although ADI+PCA is more effective at removing noise than cADI (see Figure 2.2), its performance is negatively impacted by oversubtraction which reduces the signal of the companion. As HR 2562 B is not detected in the FDI+PCA images, the variation of the noise is greater than the peak flux at the companion location, leading to an S/N smaller than one. Removing additional principal components has the effect of increasingly homogenising the image, causing the S/N at the companion location to tend towards one.

2.5.2 Flipped Differential Imaging (FDI)

Although HR 2562 B is visible in the final cADI- and ADI+PCA-processed images, we are unable to detect it in the image resulting from the PCA-based FDI procedure. As FDI+PCA is inherently reliant on the symmetry of the PSFs along the axis of the vAPP (and by extension, the response of the detector to incoming flux), artefacts such as reflection ghosts can have a significant effect on the ability of the algorithm to achieve optimal flux suppression in the vAPP dark holes (Otten et al. 2017). Long et al. (2018) characterised many such artefacts on the Clio2 camera, including some that are only visible following a background subtraction, and several that scale with increased incoming flux, such as amplifier crosstalk (Morzinski et al. 2015). A number of these effects and their impact on the vAPP dark holes can be seen in Figure 2.7. In particular, a bright spike of scattered light passes directly through the dark hole of the bottom coronagraphic PSF while the top remains unaffected. Furthermore, this artefact does not appear in the same way when the vAPP is positioned in the alternate nod position. The symmetry of the coronagraphic PSFs was likely further impacted by the wind-driven halo effect described by Cantalloube et al. (2018, 2020a) and Madurowicz et al. (2018, 2019), which results when atmospheric turbulence above the telescope pupil, primarily in the jet stream layer, varies at a rate faster than can be corrected for by the deformable mirror of the adaptive optics system. Indeed, the characteristic 'butterfly pattern' of wind-driven halo can be seen in the final FDI+PCA image of Figure 2.2 as the extended bright and dark patches on either side of the masked inner region. Even if the butterfly pattern were perfectly aligned along the axis of the vAPP, interference between scintillation effects and the lag in adaptive optics correction gives rise to an asymmetry in the butterfly pattern itself. This asymmetry is wavelength-dependent, growing stronger at longer wavelengths. As these instrumentational and atmospheric effects all negatively impact the symmetry between the two coronagraphic stellar PSFs, it is likely that the reference PSF constructed using FDI+PCA on our HR 2562 data was a poor match for the opposing coronagraphic stellar PSF, thus explaining the non-detection of the companion in the final image. Companion detection using the first night of observations was further inhibited by the increased effect of readout noise resulting from the shorter exposure time. Although successful photometric extraction via FDI+PCA was not possible within the limitations of the data presented here, it could be a potentially effective strategy for future observations if a high enough degree of symmetric precision can be reached between the two coronagraphic PSFs of the vAPP. FDI+PCA is built on the approach of Otten et al. (2017), who use the opposing vAPP coronagraphic PSF as a reference directly, without PCA. When applied to MagAO+vAPP observations obtained under excellent atmospheric conditions, they find that this technique reaches contrasts up to 1.46 magnitudes deeper than cADI. They further cite the case of Dou et al. (2015), who apply ADI+PCA to a non-coronagraphic PSF under 180° rotation to create a reference PSF, and achieve an order of magnitude improvement in contrast at small separations (compared to when the Locally Optimised Combination of Images algorithm, LOCI, is applied to ADI data, Lafrenière et al. 2007). Considering these results, Otten et al. (2017) conclude that a PCA-based algorithm such as FDI+PCA should produce an improved reference PSF and achieve even deeper contrasts compared to when the opposing vAPP PSF is used as a reference without PCA. However, as the observations here are not fully optimised for high-contrast

imaging, and further contain the symmetry-breaking artefacts described above, they serve to highlight where this technique can break down. An analysis using better optimised data is required to fully determine the potential of FDI+PCA and to compare its performance to that of other post-processing algorithms. Coronagraphic simulations could further be used to assess the extent to which different symmetry-breaking factors limit the performance of FDI+PCA and establish mitigation strategies for the most significant contributors. Although instrumental artefacts such as reflection ghosts may be challenging to remove completely, asymmetries arising from effects such as wind-driven halo vary between observations, and will be increasingly manageable with ongoing advancements in wavefront sensing and predictive control (Guyon & Males 2017; Miller et al. 2018, 2021; Jovanovic et al. 2018; Bos et al. 2019; van Kooten et al. 2020). A number of 180° coronagraphs are currently installed on instruments at other telescopes, including SCExAO/CHARIS on the 8.2-m Subaru Telescope (Doelman et al. 2017) and LMIRcam/ALES on the 8.4-m Large Binocular Telescope (Otten et al. 2014a), and several are planned for future instruments, such as MagAO-X on Magellan (Miller et al. 2019), ERIS on the VLT (Boehle et al. 2018; Kenworthy et al. 2018b), and METIS on the ELT (Carlomagno et al. 2016; Brandl et al. 2018). A thorough evaluation and comparison of the different post-processing algorithms that can be applied to vAPP data is essential if observations using vAPP coronagraphs are to be used to their full potential. While the effectiveness of FDI+PCA has not yet been demonstrated, it is an alternate processing pathway uniquely available to the vAPP and thus could prove advantageous if the limiting factors can be overcome.

2.5.3 Companion characterisation

2.5.3.1 Theoretical atmospheric models

The fitting of BT-Settl atmospheric models to the full SED and separately to the MagAO + SPHERE-only subset of data produces substantially different physical parameters for HR 2562 B (see Table 2.2). Our values for the concurrent MagAO + SPHERE data are in good agreement with Mesa et al. (2018), who found $T_{\rm eff}$ = 1100±200 K and log(g) = 4.75±0.41 dex by fitting several atmospheric models to the SPHERE data only, including the BT-Settl models used in this work. Konopacky et al. (2016), whose analysis of the GPI spectra by way of evolutionary models produces $T_{\rm eff}$ = 1200±100 K and log(g) = 4.7±0.32 dex, is also in good agreement. Our calculated radius from the MagAO + SPHERE-only case is $R = 0.89^{+0.14}_{-0.27}$ $R_{\rm Jup}$, which is consistent within 1σ to Konopacky et al. (2016), who estimated a radius of R = 1.11±0.11 $R_{\rm Jup}$ using the evolutionary models from Saumon & Marley (2008). However, the temperature and surface gravity values produced by fitting the full SED with BT-Settl are notably higher, and $T_{\rm eff}$ = 1698±100 K is inconsistent with the literature. Furthermore, the sub-Jupiter value for the radius derived from this analysis ($R = 0.56^{+0.02}_{-0.01}$ $R_{\rm Jup}$) is unphysically small due to the pressure of degenerate electrons in the interior of brown dwarfs (Chabrier et al. 2009). We also note that neither of the best fit models resulting from our analysis is a strongly compelling match for the SED of the companion when inspected visually. The $T_{\rm eff}$ = 1700 BT-Settl model, although statistically the best fit to the full SED, does not feature

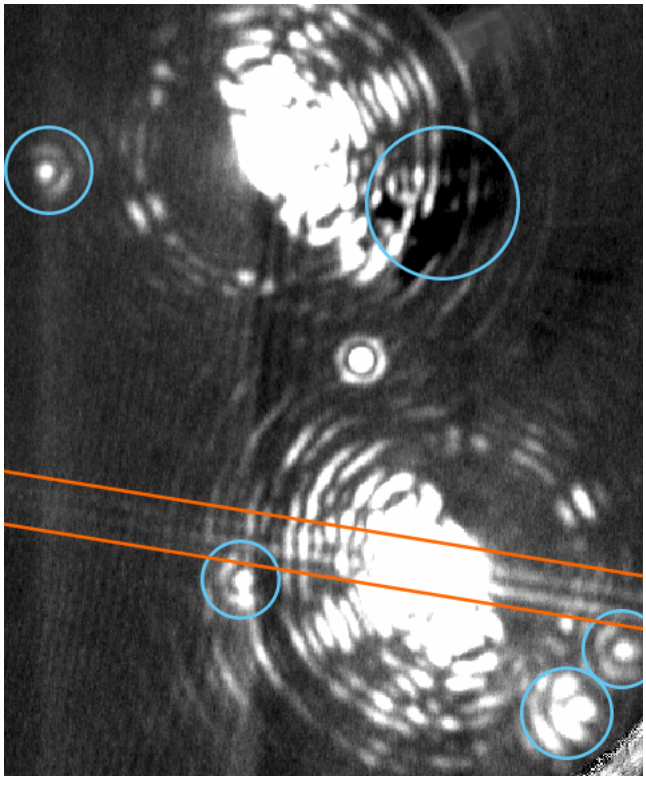

Figure 2.7: A background-subtracted and median combined frame from the 3.94 µm MagAO+vAPP observations of HR 2562, cropped around the vAPP PSFs. A number of PSF symmetry-breaking artefacts are visible, including reflection ghosts (highlighted in blue) and a bright spike of scattered light that passes directly through the dark hole of the bottom PSF (in orange). The frame is not aligned to north.

the wide absorption bands visible in the companion SED. While these bands are seen in the T_{eff} = 1200 BT-Settl model, this model instead fails to match the absolute fluxes of the GPI observations. In both cases, the reduced chi-square values of the fits suggest that a good fit is not achieved, although arguably one might favour the models that produce physically plausible radii. Such wide-ranging best fit parameters and low radii estimates resulting from fits of atmospheric grid models to observations of substellar objects with L/T spectral types have been reported previously, with an apparent dependence on both wavelength range and the specific wavebands included in the fit, as well as the models used (Ward-Duong et al. 2021; Stone et al. 2020; Wilcomb et al. 2020; Rajan et al. 2017; Morzinski et al. 2015). Manjavacas et al. (2014) found that although the BT-Settl models are largely successful at reproducing the SEDs of L-type objects, they do not always match the redness of the spectral slope in the near-infrared, suggesting that the cloud models do not include enough dust at high altitudes. Indeed, despite accounting for non-equilibrium chemistry and aiming to reproduce the L/T transition in brown dwarfs, Bonnefoy et al. (2016) demonstrated that the BT-Settl models can struggle to simultaneously produce good matches for both the shape and absolute fluxes of the SEDs of the highly red HR8799 planets, leading to underestimated radii (Marois et al. 2008; Marley et al. 2012). The challenge in fitting these models to the SED of HR 2562 B (and the resulting wide range of physical parameters) could therefore be due to the slightly enhanced flux in the K-band compared to the J- and H-bands, potentially caused by the presence of dust in the high altitude cloud layer. Although HR 2562 B is not so strongly red as HD 206893 B (the reddest substellar object observed to date, and a system with remarkably similar architecture to HR 2562 (Milli et al. 2017; Ward-Duong et al. 2021)), Mesa et al. (2018) show that it is slightly redder than other objects at the L/T transition, such as HN Peg B (which is of comparable mass and age (Luhman et al. 2007)). We also consider the possibility that the model fit to the full SED could be impacted by systematic differences between the SPHERE and GPI photometry. Although the SPHERE IFS and GPI spectra are comparable where they overlap in the J-band, it could be argued that there is a small difference between the two, due to differences in the flux calibration or otherwise. However, a constant offset applied to bring the two level would still fail to bring the GPI K-band data to match the best fit models in either case. Brown dwarfs are known to vary in time, and that such variability can manifest differently at different wavelengths (Biller et al. 2013; Vos et al. 2017, 2018; Manjavacas et al. 2018; Bowler et al. 2020b). This could influence the shape and absolute fluxes of the SED of HR 2562 B, including any difference between the SPHERE and GPI photometry, although the SPHERE and MagAO+vAPP data are concurrent. A large Spitzer survey of isolated brown dwarfs concluded that photometric variability is ubiquitous for L and T dwarfs, with some exhibiting up to ∼5% amplitude variations (Metchev et al. 2015). Recent studies have provided further evidence that brown dwarfs close to the L/T transition present the most variability, attributing the variations to patchy clouds (or clouds of varying thickness) rotating in and out of view throughout the rotation periods of the objects (Karalidi et al. 2016; Charnay et al. 2018; Vos et al. 2019; Zhou et al. 2020a). The 3.94 µm MagAO+vAPP measurement matches the T_{eff} = 1200 K, log(g) = 4.0 dex best fit model to the MagAO + SPHERE data, but the error bar spans a wide range of BT-Settl models with different physical parameters, including the T_{eff} = 1700

K, log(g) = 5.0 dex best fit model to the full SED. Although this datapoint alone is therefore unable to further constrain the physical parameters of HR 2562 B, we can conclude that its flux at this wavelength is not unusual for an object of the range of temperatures and surface gravities previously derived for HR 2562 B in the literature and lend additional weight to these values. It is clear from Figure 2.4 that complementary observations in the 2.4-3.2 µm region would be most effective in distinguishing models due to the onset of significant absorption bands in this region for cooler objects. To overcome telluric bands in this window, this will likely require space-based instruments such as the JWST (Gardner et al. 2006; Perrin et al. 2018), or ground-based high resolution spectroscopy (Birkby et al. 2013; Snellen et al. 2014; Schwarz et al. 2016; Hoeijmakers et al. 2018). JWST/MIRI will further provide characterisation at wavelengths longer than ∼5 µm, with observations of HR 2562 B already planned as part of Cycle 1 GTO Program 1241 (PI: M. Ressler).

2.5.3.2 Empirical templates

The fitting of empirical template spectra to the SPHERE + GPI data together gave a best fit object with a spectral type of L7.5±2, while the best fit to the SPHERE data alone was an object with a spectral type of T0.5±1, suggesting that HR 2562 B has a spectral type within the L/T transition regime. These results are consistent with those previously reported. For example, Mesa et al. (2018) compared their extracted spectrum to a range of template spectra between L5 and T5.5 and concluded that an early T (T2-T3) spectral type was the best match overall, but that their SPHERE IRDIS H broad-band datapoint was better described by a late L spectra. Similarly, Konopacky et al. (2016) found that the GPI SED in full is not matched perfectly by the empirical spectra of any other object but that objects with spectral types between L3.5 and T2 do offer good fits to individual wavebands, concluding a spectral type of L7±3 while noting that brown dwarfs can have very different colours while possessing similar spectral features (Leggett et al. 2003a; Cruz et al. 2018). This also reflects the issue described in Section 2.5.3.1, where fitting atmospheric models to different wavelength ranges or individual wavebands can produce different results. One might further consider that brown dwarf companions and field brown dwarfs could have different properties, and that the spectra of field brown dwarfs may therefore not be the ideal comparison to those of bound substellar companions. While Liu et al. (2016) found evidence that young brown dwarf companions with late-M and L spectral types may form distinct sequences on infrared colour-magnitude diagrams compared to the field dwarf population, their analysis suggests that the two populations are broadly consistent in the L/T transition regime (noting however, that the L/T transition lies beyond the spectral type and colour range of their fits). Mesa et al. (2018) stated that observations on a wider wavelength range would be needed to completely disentangle the spectral classification of HR 2562 B. While the 3.94 µm MagAO datapoint can potentially assist with this, there remains a lack of L and T dwarf empirical template spectra in the literature that cover the wavelength range up to and including 3.94 µm. Without such benchmark spectra for comparison, attaining a model-independent classification of the spectral type of HR 2562 B remains a challenge.

2.5.3.3 Mass estimation

To derive a range of possible values for the mass of the companion, we evaluated our inferred luminosities with BT-Settl (Allard et al. 2012; Baraffe et al. 2015) and AMES-Dusty (Allard et al. 2001; Chabrier et al. 2000) isochrones across the system age range of 450^{+300}_{-250} Myr range found by Mesa et al. (2018). Although this process could also be performed using our derived values for effective temperature or surface gravity, luminosity is generally much less model dependent (Bonnefoy et al. 2016). The two different sets of models account for atmospheric dust formation in different ways; the BT-Settl models do so by way of a parameter-free cloud model whereas the AMES-Dusty models assume that dust is formed in equilibrium with the gas phase. The results of this mass evaluation are presented in Table 2.2, alongside the corresponding values of mass ratio with respect to the primary, q. Considering the spread of these results, we report a weighted average value of 29 ± 15 M_{Jup} as our final mass estimate with a corresponding mass ratio q of 0.020 ± 0.011. This is consistent with the range of values found by Mesa et al. (2018) by comparing evolutionary models to the SPHERE photometry in each band individually using the same age range, as well as their final reported value of 32 ± 14 M_{Jup}. A similar estimate of 30 ± 15 M_{Jup} was found by Konopacky et al. (2016), who assumed a slightly higher and wider age range of 300-900 Myr. As previously noted by Mesa et al. (2018), these values are consistent with those of a brown dwarf with a late-L/early-T spectral type when compared to the dynamical mass measurements of ultracool M7-T5 objects by Dupuy & Liu (2017), matching the spectral classification in Section 2.5.3.2. The wide uncertainties on these estimates are dominated by the uncertainty on the age of the system, which is not well constrained for HR 2562, and reflect the strong dependence of substellar companion mass measurements on system age. Either a dynamical mass measurement or improved constraints on the age of the system are therefore crucial if the mass of HR 2562 B is to be constrained further.

2.6 Conclusions

We present an S/N=3.04 recovery and tentative characterisation of a companion in the lesser studied L-band regime using a vector Apodizing Phase Plate coronagraph in observations obtained with MagAO+vAPP, recovering the known brown dwarf companion to HR 2562 previously studied with GPI (Konopacky et al. 2016) and concurrently with SPHERE (Mesa et al. 2018; Maire et al. 2018). We processed our 3.94 µm images using cADI, ADI+PCA, and a newly-developed algorithm, FDI+PCA. We measure the companion 3.94 µm contrast to be $(3.05 \pm 1.00) \times 10^{-4}$ relative to the host star, which is equivalent to a physical flux of $(1.3 \pm 0.4) \times 10^{-13}$ erg s^{-1} cm^{-2} micron^{-1}. The companion is visible in images produced by applying cADI and ADI+PCA to the observations from the second night. The highest S/N (= 3.04) is produced by cADI. Although this S/N is low, the companion recovery is further supported by its position, which matches that measured by Maire et al. (2018) in observations obtained on the same night. This S/N is lower than those of literature detections of HR 2562 B, but this can primarily be attributed to the significantly narrower filter used in this work and the higher thermal background at 3.94 µm. We do not detect HR 2562 B

in the final images produced from the first night of observations, which did not cover sufficient field rotation to prevent self-subtraction when applying post-processing algorithms. Performing observations in pupil-stabilised mode, with the field of view rotating, is therefore likely necessary to detect high-contrast systems like HR 2562 B with this instrument setup. We describe FDI+PCA, a new post-processing algorithm that uses the symmetry of the vAPP PSFs to construct a reference PSF for subtraction from the data, removing quasistatic speckle noise. Although we were unable to recover the companion in our FDI+PCA processed image, we explain the impact of instrumental scattered light and wind-driven halo which degrade the symmetry of the vAPP and consequently reduce the effectiveness of the algorithm. FDI+PCA may still prove effective for future datasets that use a 180° vAPP, obtained under more optimal atmospheric conditions or on instruments with fewer scattered light artefacts, but further analysis is required to assess its potential. Broad-band filters may be preferred for MagAO+vAPP observations conducting blind searches for undiscovered companions as wider wavelength coverage will enable stronger detections, despite the lateral smearing of the PSFs that occurs when such filters are used. This wavelength dependent smearing can be handled through additional processing to either extract the resulting low-resolution spectra or collapse the PSFs along the axis of the vAPP. This wavelength-dependent smearing can alternatively be avoided by using a 360° vAPP coronagraph, which does not have such smearing even when broad-band filters are used (Doelman et al. 2020). Wide wavelength coverage can also be achieved when vAPPs are combined with integral field spectrographs (Otten et al. 2014a). Nonetheless, MagAO+vAPP still allowed a measurement in the lesser studied L-band regime. We fit BT-Settl atmospheric models to our 3.94 µm flux in combination with literature spectral data from GPI (Konopacky et al. 2016) and SPHERE (Mesa et al. 2018), and find different results depending on the wavebands included in the fit. We do not find a single model that is a convincing match to the SED, and instead find a wide range of allowable values, including $1200 \leq T_{eff}(K) \leq 1700$ and $4.0 \leq \log(g)(dex) \leq 5.0$ for the companion; dependent on which wavelength regions are fitted. Although we were therefore unable to significantly further constrain the physical parameters of the companion, the consistent measurements lend additional weight to those derived in the literature and highlight the degeneracies that arise from fitting atmospheric models to brown dwarf atmospheres. Complementary observations at 2.4-3.2 µm will help distinguish cooler brown dwarfs due to the onset of absorption bands at this wavelength region. Comparing the SED of the companion to empirical template spectra, we conclude that HR 2562 B has a spectral type at the L/T transition. However, the unavailability of templates with 3.94 µm coverage precluded us from including our MagAO datapoint in this fit. We also evaluate the inferred luminosities using BT-Settl and AMES-Dusty isochrones across the system age range of 450^{+300}_{-250} Myr, deriving a mass estimate for HR 2562 B of 29 ± 15 M_{Jup}, in good agreement with the values found by (Konopacky et al. 2016) and (Mesa et al. 2018) and consistent with the mass of a late-L/early-T type brown dwarf. As companion mass is highly dependent on system age, either a precise dynamical mass measurement or improved constraints on the age of the system are crucial if the mass of HR 2562 B is to be constrained further.

Acknowledgements

The authors thank Quinn Konopacky and Dino Mesa for sharing the GPI and SPHERE IRDIS + IFS[1] spectra of HR 2562 B, respectively. The authors would also like to thank Gilles Otten, Jos de Boer, Sebastiaan Haffert, and Steven Bos for valuable discussions that improved this work. We thank our anonymous referee whose comments helped to improve this manuscript, and for their timely response in these unusual times. We are especially grateful to France Allard for providing the community access to the PHOENIX and BT-Settl model database for so many years. It has been enormously impactful and we hope that her legacy continues long in her absence.

BJS is fully supported by the Netherlands Research School for Astronomy (NOVA). JLB acknowledges funding from the European Research Council (ERC) under the European Union's Horizon 2020 research and innovation program under grant agreement No 805445. This work was performed in part under contract with the Jet Propulsion Laboratory (JPL) funded by NASA through the Sagan Fellowship Program executed by the NASA Exoplanet Science Institute. KMM's work is supported by the NASA Exoplanets Research Program (XRP) by cooperative agreement NNX16AD44G. The research of DD and FS leading to these results has received funding from the European Research Council under ERC Starting Grant agreement 678194 (FALCONER). This paper includes data gathered with the 6.5 meter Magellan Telescopes located at Las Campanas Observatory, Chile. This paper uses observations obtained at the Gemini Observatory, which is operated by the Association of Universities for Research in Astronomy, Inc., under a cooperative agreement with the NSF on behalf of the Gemini partnership: the National Science Foundation (United States), the National Research Council (Canada), CONICYT (Chile), the Australian Research Council (Australia), Ministério Ciência, Tecnologia e Inovação (Brazil) and Ministerio de Ciencia, Tecnología e Innovación Productiva (Argentina). This publication makes use of VOSA, developed under the Spanish Virtual Observatory project supported by the Spanish MINECO through grant AyA2017-84089. VOSA has been partially updated by using funding from the European Union's Horizon 2020 Research and Innovation Programme, under Grant Agreement №776403 (EXOPLANETS-A). This publication makes use of data products from the Two Micron All Sky Survey, which is a joint project of the University of Massachusetts and the Infrared Processing and Analysis Center/California Institute of Technology, funded by the National Aeronautics and Space Administration and the National Science Foundation. This publication makes use of data products from the Wide-field Infrared Survey Explorer, which is a joint project of the University of California, Los Angeles, and the Jet Propulsion Laboratory/California Institute of Technology, funded by the National Aeronautics and Space Administration. This work has made use of data from the European Space Agency (ESA) mission *Gaia* (https://www.cosmos.esa.int/gaia), processed by the *Gaia* Data Processing and Analysis Consortium (DPAC, https://www.cosmos.esa.int/web/gaia/dpac/consortium). Funding for the DPAC has been provided by national institutions, in particular the institutions participating in the *Gaia* Multilateral Agreement. This research has benefitted from the SpeX Prism Spectral Libraries, maintained by Adam Burgasser at http://pono.ucsd.edu/~adam/browndwarfs/spexprism. This research has

[1] Based on observations collected at the European Southern Observatory under ESO programme(s) 198.C-0209(D).

made use of NASA's Astrophysics Data System. This research has made use of the SIMBAD database, operated at CDS, Strasbourg, France (Wenger et al. 2000). This research made use of ds9, a tool for data visualization supported by the Chandra X-ray Science Center (CXC) and the High Energy Astrophysics Science Archive Center (HEASARC) with support from the JWST Mission office at the Space Telescope Science Institute for 3D visualization (Joye & Mandel 2003). This work makes use of the Python programming language[1], in particular packages including NumPy (Oliphant 2006; Van Der Walt et al. 2011), Astropy (Astropy Collaboration et al. 2013, 2018), SciPy (Virtanen et al. 2020), scikit-image (van der Walt et al. 2014), Photutils (Bradley et al. 2017), and Matplotlib (Hunter 2007).

Data Availability

The data from the MagAO observations underlying this article are available in the Research Data Management Zenodo repository of the Anton Pannekoek Institute for Astronomy, at https://doi.org/10.5281/zenodo.4333200.

[1] Python Software Foundation; https://www.python.org/

...one must work with time and not against it.
Ursula K. Le Guin, The Dispossessed

Chapter 3

Measuring the variability of directly imaged exoplanets using vector Apodizing Phase Plates combined with ground-based differential spectrophotometry

Ben J. Sutlieff, Jayne L. Birkby, Jordan M. Stone, David S. Doelman, Matthew A. Kenworthy, Vatsal Panwar, Alexander J. Bohn, Steve Ertel, Frans Snik, Charles E. Woodward, Andrew J. Skemer, Jarron M. Leisenring, Klaus G. Strassmeier, and David Charbonneau

Adapted from *Monthly Notices of the Royal Astronomical Society, 2023, Volume 520, Issue 3, pp. 4235–4257*

Abstract

Clouds and other features in exoplanet and brown dwarf atmospheres cause variations in brightness as they rotate in and out of view. Ground-based instruments reach the high contrasts and small inner working angles needed to monitor these faint companions, but their small fields-of-view lack simultaneous photometric references to correct for non-astrophysical variations. We present a novel approach for making ground-based light curves of directly imaged companions using high-cadence differential spectrophotometric monitoring, where the simultaneous reference is provided by a double-grating 360° vector Apodizing Phase Plate (dgvAPP360) coronagraph. The dgvAPP360 enables high-contrast companion detections without blocking the host star, allowing it to be used as a simultaneous reference. To further reduce systematic noise, we emulate exoplanet transmission spectroscopy, where the light is spectrally-dispersed and then recombined into white-light flux. We do this by combining the dgvAPP360 with the infrared ALES integral field spectrograph on the Large Binocular

Telescope Interferometer. To demonstrate, we observed the red companion HD 1160 B (separation ∼780 mas) for one night, and detect 8.8% semi-amplitude sinusoidal variability with a ∼3.24 h period in its detrended white-light curve. We achieve the greatest precision in ground-based high-contrast imaging light curves of sub-arcsecond companions to date, reaching 3.7% precision per 18-minute bin. Individual wavelength channels spanning 3.59-3.99 µm further show tentative evidence of increasing variability with wavelength. We find no evidence yet of a systematic noise floor, hence additional observations can further improve the precision. This is therefore a promising avenue for future work aiming to map storms or find transiting exomoons around giant exoplanets.

Key words: infrared: planetary systems – instrumentation: high angular resolution – planets and satellites: detection – brown dwarfs – planets and satellites: atmospheres – techniques: imaging spectroscopy

3.1 Introduction

Planets do not have a homogeneous appearance. When we look at the planets in our own solar system, we see distinct cloud structures and giant storms that show great diversity in size, shape, lifetime, and brightness (e.g. Simon et al. 2016, 2021; Stauffer et al. 2016; Ge et al. 2019; Coulter et al. 2022). These features rotate in and out of view throughout the planet's rotation period, modulating its overall brightness and thus allowing us to map out its atmosphere (e.g. Kostov & Apai 2013; Karalidi et al. 2015, 2016; Fletcher et al. 2016; Apai et al. 2017; Plummer & Wang 2022). Beyond the solar system, variations in the light curves of stars deliver information on the distribution of features such as star spots (Barnes et al. 2002; Jeffers et al. 2007; Frasca et al. 2009; Strassmeier 2009; Morales et al. 2010; Goulding et al. 2012; Herbst 2012; Nielsen et al. 2013; Park et al. 2021; Thiemann et al. 2021). By measuring the photometric variability of exoplanets and brown dwarfs in the same way, we can gain not only an insight into their visual appearance, but also key information on the distribution of condensate clouds that strongly affect the infrared spectra of directly imaged companions, allowing degeneracies between atmospheric models to be broken (e.g. Yang et al. 2016; Rajan et al. 2017; Charnay et al. 2018; Zhou et al. 2019; Zhang 2020; Tan & Showman 2021; Ward-Duong et al. 2021). Space-based photometric monitoring with the Hubble Space Telescope (HST) has already shown that giant planetary-mass and brown dwarf companions do exhibit such variability, at a range of amplitudes and periods (Apai et al. 2013; Buenzli et al. 2014, 2015b,a; Zhou et al. 2016, 2020a; Manjavacas et al. 2018, 2019a; Miles-Páez et al. 2019; Bowler et al. 2020b; Lew et al. 2020b). These results are in good agreement with observations of isolated brown dwarfs and giant exoplanet analogues (Biller et al. 2018; Vos et al. 2018, 2020; Lew et al. 2020a; Ashraf et al. 2022), including a large Spitzer survey by Metchev et al. (2015) who found that photospheric spots causing $\geq$0.2% variability at 3-5 µm are ubiquitous. Several studies have identified objects with much stronger variability, at the >10% level, with some even varying with peak-to-peak amplitudes as high as 26% (e.g. Radigan et al. 2012; Wilson et al. 2014; Biller et al. 2015; Eriksson et al. 2019; Bowler et al. 2020b). Vos et al. (2022) further found that young, low-mass brown dwarfs with similar colours and spectra to directly imaged exoplanetary companions are highly likely to display variability in the L2-T4 spectral type range, with an enhancement in maximum amplitudes compared to field dwarfs.

The rotation periods of brown dwarf and planetary-mass companions are consistent with those of the isolated low-mass brown dwarf population, suggesting that they may share similar angular momentum histories (Bryan et al. 2018; Vos et al. 2022). These periods are generally short, ranging from $\sim$1 hour to $\gtrsim$20 hours (e.g. Radigan et al. 2014; Metchev et al. 2015; Apai et al. 2021; Tannock et al. 2021), within the range expected when evolutionary models and the age- and mass-dependent breakup velocities are considered (Leggett et al. 2016; Vos et al. 2020). These periods, derived from photometric measurements, are complementary to measurements of companion spin obtained from their spectra (Snellen et al. 2014; Schwarz et al. 2016; Bryan et al. 2018, 2020b; Xuan et al. 2020; Wang et al. 2021b). When combined, rotation period and spin measurements can be used to constrain companion obliquities (Bryan et al. 2020a, 2021). However, the population of directly imaged compan-

ions accessible to space-based facilities such as HST remains small as most companions lie at close angular separations within the inner working angles of these facilities.

Equipped with coronagraphs and extreme adaptive optics (AO) systems operating in the infrared, large ground-based observatories have the resolution and photon collecting power needed to overcome the glare of the host star and reach the high contrasts and close angular separations of substellar companions currently inaccessible to space telescopes (Bowler 2016; Hinkley et al. 2021; Currie et al. 2022a). Although this provides the opportunity for variability studies of such companions, precise photometric monitoring is difficult as the companion light curve is contaminated by variability arising from Earth's atmosphere and other systematics. Therefore, a simultaneous, unsaturated photometric reference is required to remove this contaminant variability from the companion light curve. For non-coronagraphic, ground-based observations of isolated brown dwarfs and planetary-mass objects, nonvariable stars present in the field of view have often been used as photometric references to enable many successful measurements of variability (e.g. Gelino et al. 2002; Biller et al. 2013, 2015; Girardin et al. 2013; Radigan et al. 2014; Wilson et al. 2014; Naud et al. 2017; Eriksson et al. 2019; Vos et al. 2019; Manjavacas et al. 2021, 2022). However, the typically narrow field of view of ground-based coronagraphic imagers generally precludes the use of field stars as photometric references for observations of companions, and widely used focal-plane coronagraphs block the host star to enable the detection of the companion (Soummer 2005; Mawet et al. 2012; Ruane et al. 2018).

One solution to this problem is to use off-axis satellite Point Spread Functions (PSFs), or satellite spots, which can act as simultaneous photometric references even when a host star is blocked by a coronagraph (Marois et al. 2006b; Sivaramakrishnan & Oppenheimer 2006). Satellite spots can be created by adding a periodic modulation to the deformable mirror of an AO-equipped telescope or by placing a square grid in the pupil plane to produce spots through diffraction of starlight (Langlois et al. 2013; Wang et al. 2014; Jovanovic et al. 2015a). The former approach has been used by Apai et al. (2016), Biller et al. (2021), and Wang et al. (2022) for observations of the multi-planet HR 8799 system (Marois et al. 2008, 2010b). The first two of these studies observed HR 8799 with the Spectro-Polarimetric High-contrast imager for Exoplanets REsearch (SPHERE; Beuzit et al. 2019) instrument at the Very Large Telescope (VLT), and the latter used the CHARIS integral field spectrograph (IFS) in combination with the Subaru Coronagraphic Extreme Adaptive Optics instrument at the Subaru Telescope (Jovanovic et al. 2015b; Groff et al. 2017). Biller et al. (2021) used the satellite spots with a broadband-H filter to successfully constrain their sensitivity to variability to amplitudes $>$5% for HR 8799b for periods $<$10 hours, and amplitudes $>$25% for HR 8799c for similar periods, noting that the observed amplitude of any variability would be muted by the likely pole-on viewing angle of these planets (Vos et al. 2017; Wang et al. 2018; Ruffio et al. 2019). They also rule out non-shared variability between HR 8799b and HR 8799c at the $<$10-20% level over a 4-5 hour timescale by using one planet as a photometric reference for the other. Using a spectrophotometric approach, Wang et al. (2022) further constrained the variability amplitudes of HR 8799c to the 10% level, and HR 8799d to the 30% level, and found that there was no significant variability in the planet's colours. However, all three

studies found that satellite spots are anti-correlated with each other and can demonstrate individual variations of their own, potentially setting a limit to the precision that can be achieved with this technique (although Biller et al. (2021) and Wang et al. (2022) note that the satellite spot light curves can be flat in their most stable epochs).

3.1.1 Ground-based differential spectrophotometry

In this paper we present a novel, alternative ground-based approach for constructing light curves of high-contrast companions directly through the technique of differential spectrophotometric monitoring, akin to that used highly successfully to study exoplanet transmission spectra (e.g. Kreidberg et al. 2014; Stevenson et al. 2014; Wilson et al. 2020; Arcangeli et al. 2021; Panwar et al. 2022b,a). We use a double-grating 360° vector Apodizing Phase Plate (dgvAPP360) coronagraph (Doelman et al. 2017, 2020, 2021; Wagner et al. 2020b), which enables high-contrast companions to be detected without blocking the host star, hence leaving an unsaturated image of the host star available for use as a simultaneous reference. The more widely used grating vector Apodizing Phase Plate (gvAPP) coronagraph adjusts the phase of the incoming wavefront to modify the PSFs of all objects in the field of view, creating two images of the target star each with a 180° D-shaped 'dark hole', a region of deep flux suppression in which high-contrast companions can be observed, on opposing sides (Snik et al. 2012; Otten et al. 2014a, 2017; Bos et al. 2020a; Doelman et al. 2021; Sutlieff et al. 2021). The dgvAPP360 instead creates a 360° dark hole surrounding each of the two images of the target star, and then uses an additional grating to overlap the images to produce a single image of the star (Doelman et al. 2022). An example image obtained with the dgvAPP360 is shown in Figure 3.1, with the target star in the centre and the dark hole surrounding it.

In addition, we combine the dgvAPP360 with an IFS, enabling us to use differential spectrophotometry for high-contrast directly imaged companions. The incoming light is first dispersed into individual spectra, and then recombined into a single 'white-light' data point. This has the advantage of smoothing out wavelength-dependent flat-fielding errors and allows wavelength regions with instrumental absorption or highly variable telluric bands to be excluded, meaning systematic effects can be significantly reduced, thus yielding greater stability and precision in the final white-light curve.

3.1.2 The HD 1160 system

We test this approach using observations of the HD 1160 system, which is located at a distance of 120.4±0.6 pc (Gaia Collaboration et al. 2016, 2021; Bailer-Jones et al. 2021) and consists of host star HD 1160 A (spectral type A0V; Houk & Swift 1999) and two high-contrast companions, HD 1160 B and C (Nielsen et al. 2012). HD 1160 B and C lie at separations of ∼80 au (∼0.78″) and ∼530 au (∼5.1″), respectively. Several key properties of HD 1160 A are listed in Table 3.1. HD 1160 A is bright (K = 7.040±0.029 mag, Cutri et al. 2003), and the contrast ratio between HD 1160 A and HD 1160 B is $\Delta L' = 6.35 \pm 0.12$ mag (Nielsen et al. 2012). This makes it an ideal target for demonstrating our technique, as a high signal-

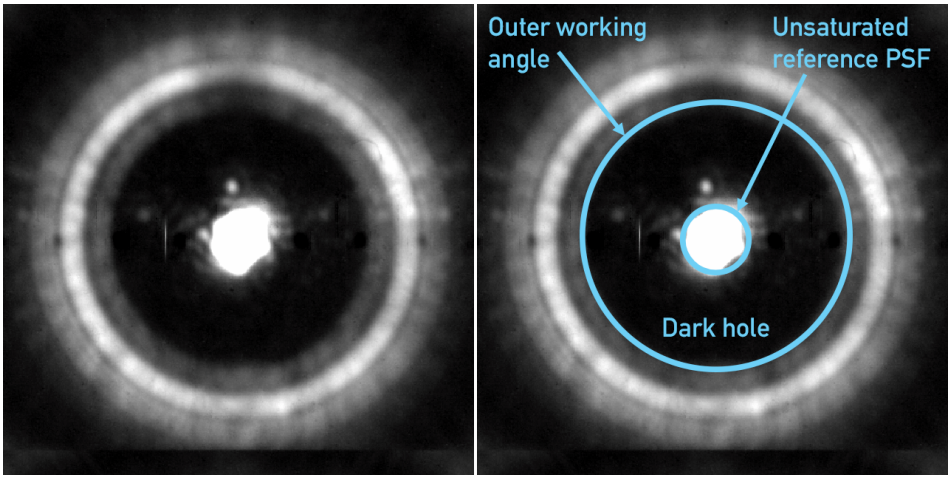

Figure 3.1: An on-sky example image of a $K \sim 7$ mag target observed with the dgvAPP360 coronagraph on the Large Binocular Telescope (LBT), copied and annotated on the right. The dgvAPP360 produces a dark hole of deep flux suppression, seen here surrounding the target star, allowing high-contrast companions to be detected in this region. The star itself remains unsaturated in the middle, allowing it to be used as a simultaneous reference PSF when making a differential light curve for a companion. The outer edge of the dark hole lies beyond the field of view in the LBT observations used in this work.

to-noise detection of the companion allows high cadence monitoring and a deep investigation into any residual systematic effects. A-type stars such as HD 1160 A generally vary below the millimagnitude level, which corresponds to variability amplitudes comfortably below the ∼1% level (Ciardi et al. 2011). We assess the variability of the host star in Section 3.4.2 using observations from the Transiting Exoplanet Survey Satellite (TESS) mission. The age of the system is poorly constrained, with estimates ranging from 50^{+50}_{-40} Myr (Nielsen et al. 2012) to 100^{+200}_{-70} Myr (Maire et al. 2016). The HD 1160 system may be a member of the Pisces-Eridanus stellar stream, which would place its age at ∼120 Myr, but this has yet to be confirmed (Curtis et al. 2019).

HD 1160 B has a spectral type close to the brown dwarf/stellar boundary; Nielsen et al. (2012) found a spectral type of ∼L0, but more recent papers suggest that it lies between M5-M7 (Maire et al. 2016; Garcia et al. 2017; Mesa et al. 2020). However, Mesa et al. (2020) found its spectrum to be highly peculiar and that no spectral model or template in current libraries can produce a satisfactory fit. Although the cause of this peculiarity has not yet been explained, Mesa et al. (2020) hypothesise that possible causes could include a young system age, dust in the photosphere of HD 1160 B, or ongoing evolutionary processes. The mass of HD 1160 B also remains unclear, primarily due to the poorly constrained age of the system, with estimates ranging from that of a low mass brown dwarf (∼20 M_{Jup}, Mesa et al. 2020) to decisively in the stellar mass regime ($0.12 \pm 0.01 M_{\odot} \approx 123 M_{Jup}$, Curtis et al. 2019) if the system is indeed a member of the Pisces-Eridanus stellar stream. HD 1160 C is a low-mass

Table 3.1: Properties of host star HD 1160 A.

Parameter	Value	Reference(s)
Spectral Type	A0V	(1)
Right Acension (J2000)	00:15:57.32	(2)
Declination (J2000)	+04:15:03.77	(2)
Age (Myr)	10-300	(3, 4)
Parallax (mas)	8.2721±0.0354	(2)
Distance (pc)	120.4±0.6	(2, 5)
Proper motion (RA, mas yr^{-1})	20.150±0.040	(2)
Proper motion (Dec, mas yr^{-1})	-14.903±0.034	(2)
Mass ($M_\odot$)	∼2.2	(3)
T_{eff} (K)	9011±85	(6)
$\log(L/L_\odot)$	1.12±0.07	(6)
log(g) (dex)	∼4.5	(7)
[Fe/H]	∼solar	(7)
V (mag)	7.119±0.010	(8)
G (mag)	7.1248±0.0004	(2)
J (mag)	6.983±0.020	(9)
H (mag)	7.013±0.023	(9)
K (mag)	7.040±0.029	(9)

References: (1) Houk & Swift (1999); (2) Gaia Collaboration et al. (2016, 2021); (3) Nielsen et al. (2012); (4) Maire et al. (2016); (5) Bailer-Jones et al. (2021); (6) Garcia et al. (2017); (7) Mesa et al. (2020); (8) Tycho-2 (Høg et al. 2000b); (9) 2MASS (Cutri et al. 2003; Skrutskie et al. 2006)

star (spectral type M3.5), and its separation of ∼530 au (∼5.1″) places it beyond the field of view of most vAPPs currently in use (Maire et al. 2016; Doelman et al. 2021).

The observations carried out on the HD 1160 system are described in Section 3.2, and in Section 3.3 we describe the spectral extraction and data reduction processes. In Section 3.4 we produce and present our differential spectrophotometric light curves of HD 1160 B. We then examine various factors that may be correlated with the light curves and detrend them in Section 3.5. These results and their implications are then discussed in Sections 3.6 and 3.7. Lastly, the conclusions of the work are summarised in Section 3.8.

3.2 Observations

We observed the HD 1160 system on the night of 2020 September 25 (03:27:31 - 11:16:14 UT) with the double-grating 360° vector Apodizing Phase Plate (dgvAPP360) coronagraph (see Section 3.1.1) and the Arizona Lenslets for Exoplanet Spectroscopy (ALES) IFS (Skemer et al. 2015; Hinz et al. 2018; Stone et al. 2018). ALES is integrated inside the Large

Binocular Telescope Interferometer (LBTI) (Hinz et al. 2016; Ertel et al. 2020), which works in conjunction with the LBT mid-infrared camera (LMIRcam), on the 2 x 8.4-m LBT in Arizona (Skrutskie et al. 2010; Leisenring et al. 2012). For these observations, ALES was in single-sided mode and was therefore fed only by the left-side aperture of LBT. Atmospheric turbulence was corrected for by the LBTI adaptive optics (AO) system (Bailey et al. 2014b; Pinna et al. 2016, 2021). We used the ALES L-band prism, which covers a simultaneous wavelength range of 2.8-4.2 µm with a spectral resolution of R∼40 (Skemer et al. 2018). The plate scale is ∼35 mas spaxel^{-1}. The other LBT aperture was used to feed the Potsdam Echelle Polarimetric and Spectroscopic Instrument (PEPSI), which obtained R = 50,000 combined optical spectra of HD 1160 A and B in the 383-907nm wavelength range (Strassmeier et al. 2015, 2018c), which is subject to analysis in other forthcoming works.

Conditions were exceptionally clear and stable throughout the night, with no time lost to weather, and seeing ranged from 0.7-1.4″. We acquired 2210 on-target ALES frames, with an integration time of 5.4 s per frame, giving a total on-target integration time of 11934.0 s (∼3.32 h) spread over ∼7.81 h once readout time, nodding, and wavelength calibrations are included. The integration time was chosen such that the stellar PSF remained unsaturated in the core so that it can be used as the photometric reference for the companion. We used an on/off nodding pattern to enable background subtraction, nodding to a position 5″ away for the off-source nod position. As HD 1160 C is located at a similar separation (∼5.1″), we nodded in a direction away from this companion to prevent it from contaminating the frames obtained in the off-source nod position. Beam-switching in this way is possible because of the intrinsic stability provided by the dgvAPP360 coronagraph's placement in the pupil plane. We obtained dark frames with the same exposure time at the end of the night, and 6 wavelength calibrations were acquired at irregular intervals during the night. LBTI operates in pupil-stabilized mode, such that the field of view was rotating throughout the observations. The total field rotation across the observing sequence was 109.7°. The HD 1160 system was observed from an elevation of 29.4° at the start of the night to a maximum elevation of 61.7°, and then back down to an elevation of 27.5°. The dgvAPP360 creates an annular dark hole around the target PSF, with an inner radius close to the PSF core and an outer radius at the edge of the 2.2″ field of view of the detector (2.7 - 15 λ/D in ALES mode) (Doelman et al. 2020, 2021). For these observations, this meant that HD 1160 B was located in the dark hole of HD 1160 A across the entire wavelength range covered by the ALES L-band prism. HD 1160 C (separation ∼5.1″) remained beyond the ALES field of view.

3.3 Data reduction

The raw ALES images contain the spectra that have been projected onto the detector. Ultimately, we are aiming to produce a light curve for the companion that is made from the 'white-light', i.e. combined in the wavelength dimension. To do this, we must first extract the spectra from the raw data along with bad pixel correction and flat-fielding. We can then extract the photometry of the star and the companion at each wavelength before collapsing the data in the wavelength dimension to obtain white-light fluxes. A light curve for the companion is then obtained by dividing the companion flux by the stellar flux to remove

systematic trends shared by both. In the following subsections we describe the methods used to carry out each of these steps and obtain the white-light curve of the companion.

3.3.1 Spectral data cube extraction

Raw ALES data consists of a two-dimensional grid of 63×67 micro-spectra over a 2.2″x 2.2″ field of view, which must be extracted into three-dimensional data cubes of x-position, y-position, and wavelength λ (Stone et al. 2022). To do this, we first performed a background subtraction using the sky frames obtained in the off-source nod position. For each ALES image, we subtracted the median combination of the 100 sky frames closest in time. We then extracted the micro-spectra into cubes using optimal extraction, which is an inverse variance and spatial profile weighted extraction approach (Horne 1986; Briesemeister et al. 2018; Stone et al. 2020). The extraction weights were obtained by measuring the spatial profile of each micro-spectrum in the dark-subtracted sky frames. As there is no significant change in the spatial profile as a function of wavelength, we average the spatial profile of each micro-spectrum over wavelength to obtain higher signal-to-noise (S/N). The wavelength calibration of the raw ALES data was then obtained using four narrow-band photometric filters at 2.9, 3.3, 3.5, and 3.9 µm, positioned upstream of the ALES optics. These filters are each of a higher spectral resolution $\frac{\lambda}{\Delta\lambda}\sim$100 than ALES, so are therefore unresolved and provide four single-wavelength fiducial spots with which each micro-spectra can be calibrated (Stone et al. 2018, 2022). For each micro-spectrum, we performed this calibration by fitting a second-order polynomial to the calculated pixel positions of these four spots, therefore mapping pixel position to wavelength. Each of the 63×67 micro-spectra was thereby converted into a corresponding spaxel in the three-dimensional data cube (Briesemeister et al. 2019; Doelman et al. 2022). The resulting data cube contained 100 channels in the wavelength dimension ranging from 2.8-4.2 µm.

The primary wavelength calibration used to process this data set was obtained at 08:25:00 UT on the night of observations, i.e. 4 hours 57 minutes into the observing sequence. To test whether a wavelength calibration obtained at a different point in the night has a significant effect on the photometry of the target star and the companion, we also separately processed the data using an alternative wavelength calibration obtained at 04:54:00 UT, 1 hour 26 minutes into the observing sequence. We compare and discuss the results of the two wavelength calibrations in Section 3.4.3.

3.3.2 Data processing

Once the spectra were extracted into background-subtracted three-dimensional cubes of images for each exposure, we applied several data reduction steps to remove systematics and improve the S/N at the location of the companion. We first removed 8 time frames from the data in which the AO loop opened while the data was being collected. Next, we identified bad pixels using a 6σ filter and replaced them with the mean of the neighbouring pixels. We then applied a flat-field correction to calibrate the data against the response of the detector. For each wavelength channel, the corresponding flat was a time-average of the

frames obtained in the 'off' nod position, which had then been corrected for bad pixels in the same way as the science frames and smoothed over using a Gaussian filter. These flats were then divided by the maximum value in the frame such that the value of every pixel was between zero and one. We then divided the science frames by these smoothed, normalised sky flats. This flat-fielding process was also repeated separately using a median filter instead of a Gaussian filter as a means to test the robustness of this step in our method. We proceed with the Gaussian filter and discuss the impact of the choice of flat frame on the photometry of the star and companion in Section 3.4.3.

Doelman et al. (2022) previously identified that background-subtracted, flat-fielded ALES images contain residual structure that cannot be described by purely Gaussian noise, in the form of time-varying row and column discontinuities (faintly visible in the top panel of Figure 3.2). Such discontinuities are expected and arise from the way in which the micro-spectra lie across multiple channels of the LMIRcam detector (Doelman et al. 2022). We followed the method of Doelman et al. (2022) to characterise and remove these discontinuities by fitting a third-order polynomial to each row and column in each frame (Figure 3.2). Removing these systematics is important as they could impact the precision of our differential light curve, or even generate a false variability signal if the target moves over them throughout the observing sequence. Prior to fitting, we applied circular masks at the locations of the star and the companion in each frame such that their flux did not contaminate the fit. To find the position of the star in each time frame, we selected a wavelength channel with a high stellar flux per frame (channel 52, $\lambda \approx 3.69$ µm) and fit the PSF core with a 2D Gaussian. The position of the companion in each time frame was then identified using its separation and position angle relative to the star and accounting for the effect of the field rotation over time. We then masked the star and the companion across all wavelength channels using circular masks with diameters of 18 pixels and 5 pixels, respectively, before fitting the third-order polynomials to each column. The resulting values were then subtracted from the data to remove the column discontinuities. This process was then repeated for each row in the resulting image to remove the row discontinuities.

In addition to removing these systematic discontinuities, this process has the effect of removing residual background flux not eliminated by earlier processing steps. This is indicated by the histograms in Figure 3.2, which show that the noise distribution of the data was offset from zero prior to the removal of the discontinuities (in blue) but is approximately consistent with zero after this process has been applied (in orange). We then used the position of the star in each frame, found when applying the masks in the previous step, to spatially align the data such that the star was in the centre of each frame. Finally, we rotationally aligned the images by applying an anticlockwise rotation corresponding to their parallactic angles.

We did not use any further post-processing methods that reduce quasistatic speckle noise through the subtraction of reference PSFs, such as Angular Differential Imaging (ADI, Marois et al. 2006a). Although the field rotation over the night of observations was sufficient enough to use these to remove noise with minimal companion self-subtraction, doing so would also remove the unsaturated stellar reference PSF, which is required to eliminate systematics in the companion photometry. It would not be possible to use the host star PSF prior to

ADI subtraction as a photometric reference for the companion PSF after ADI subtraction, as the two would no longer share the same systematic trends. Furthermore, HD 1160 B is sufficiently bright that it can be detected at ample S/N for our purposes without further noise reduction.

3.3.3 Wavelength channel selection

Although the final processed cubes contain data from 100 wavelength channels across the observed wavelength range of 2.8-4.2 µm, not all of these channels are suitable for further analysis. The first 3 and final 10 channels contain flux from the adjacent spaxel in the dispersion direction as an oversized spectral length is required to extract the spectrum at each position, so the extracted data overlaps slightly in the wavelength dimension (Stone et al. 2022). Furthermore, the dgvAPP360 contains a glue layer that causes up to 100% absorption between 3.15 and 3.55 µm (Otten et al. 2017; Doelman et al. 2021). As described in Section 3.1.1, one of the key advantages of a spectrophotometric approach is the option to exclude channels that are known to cause systematic variability in the 'white-light' curve, hence improving the companion S/N and stability in the combined image when compared to combining all wavelength channels without any selection. This is key to reducing large systematic effects that may otherwise dominate the variability signals that we are aiming to measure. For the purposes of this technique demonstration, we proceed using 30 sequential wavelength channels (45-74, spanning 3.59-3.99 µm) which all have a high throughput and do not lie in the regions affected by the dgvAPP360 glue absorption, significant telluric absorption, or the overlapping spectral traces. In the left panel of Figure 3.3 we show the median combination of these channels in both wavelength and time, while the centre and right panels respectively show example images from the median combined cubes in the time and wavelength dimensions only. The images shown are those processed using the flat frame that was smoothed using a Gaussian filter; the equivalent images as processed using the median-smoothed flat frame are visually indistinguishable from these.

3.4 Generating differential spectrophotometric light curves

Variability arising from instrumental systematics and the effects of Earth's atmosphere, such as airmass, seeing, and tellurics, contaminate the raw flux of the companion. Simultaneous flux measurements of a photometric reference are required to eliminate this contaminant variability and produce a differential light curve of the companion, relative to the photometric reference. Although suitable photometric references are generally absent when using coronagraphs (Section 3.1), the dgvAPP360 coronagraph uniquely provides an image of the host star simultaneously to the companion, allowing the star to be used as the photometric reference when it is not saturated. Its placement in the pupil plane also makes it inherently stable and insensitive to tip/tilt instabilities (Otten et al. 2017; Doelman et al. 2022).

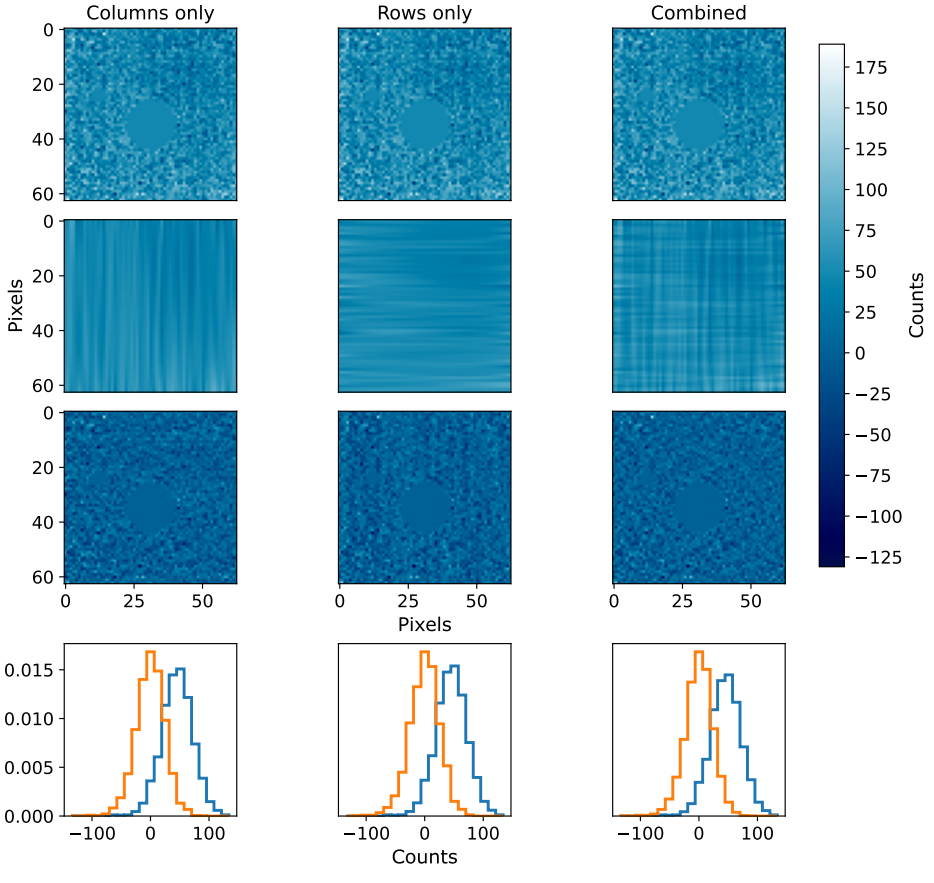

Figure 3.2: Demonstration of the process for removing systematic row and column discontinuities present in background-subtracted ALES images, as applied to a single frame of data in the 52nd ALES wavelength channel ($\lambda \approx 3.69$ µm). Top panels: input frame prior to the removal of the discontinuities, which are faintly visible as a chequered pattern. All three panels are the same. Both HD 1160 A and B are masked. Second row: results of the third-order polynomial fits individually to the columns (left panel) and rows (centre panel), and the combination of both (right panel). The combination of both was produced by first fitting and removing the column discontinuities, and then repeating the process on the resulting image to fit and remove the rows. We show row and column fits to the input frame separately here to highlight their individual contribution to the original systematics. The star and the companion were masked during this process, and the values to be removed at their locations were found through interpolation of the fits. Third row: data frame with the discontinuities removed by subtracting the fits. The histograms in the bottom row show the distributions of the counts in the unmasked regions of the third row images, with the original noise distribution in blue and the noise distribution after the discontinuities were removed in orange. The bottom right panel shows the version used in the analysis.

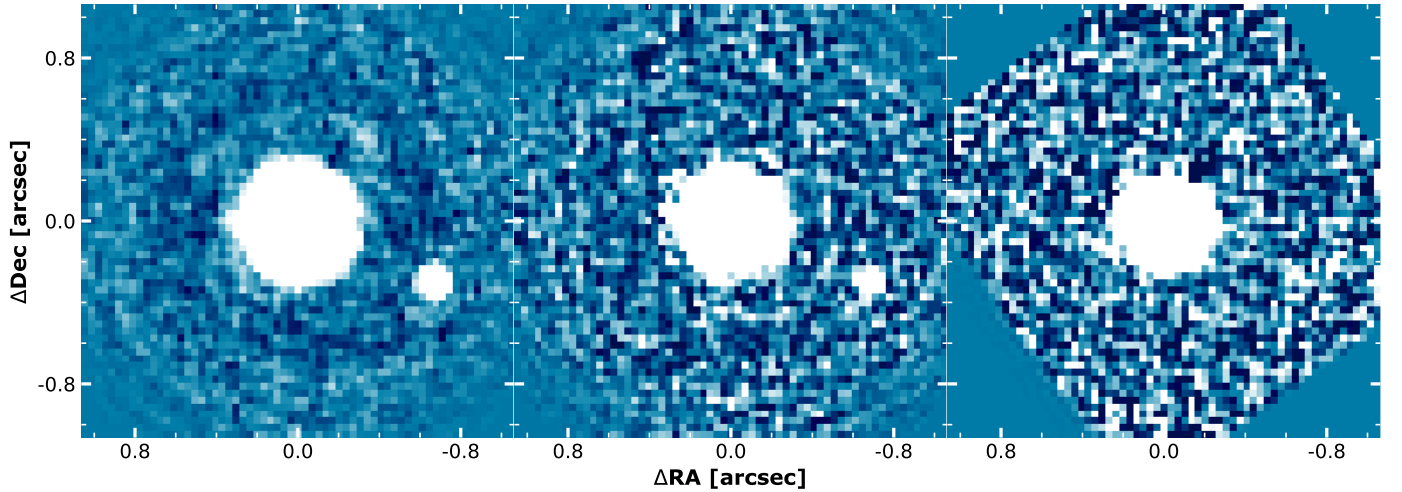

Figure 3.3: Reduced images of the HD 1160 system obtained with LBT/ALES and the dgvAPP360 coronagraph after all data processing steps and wavelength channel selection. Left: the median combination, in both wavelength and time, of all wavelength channels in the 3.59-3.99 µm range, covering a total integration time of 11891 s (∼3.31 h). Centre: example image from the same data cube but median combined only in the time dimension, along the 3.64 µm wavelength channel. Right: example time frame (integration time = 5.4 seconds) resulting from a median combination in wavelength over the 3.59-3.99 µm wavelength range. All three images use the same arbitrary logarithmic colour scale, and are aligned to north. North is up, and east is to the left.

3.4.1 Aperture photometry

We used version 1.4.0 of the Photutils Python package (Bradley et al. 2022) to simultaneously extract aperture photometry of HD 1160 A and B. We carried out this process for every individual frame in each of the 30 wavelength channels in the 3.59-3.99 µm range chosen in Section 3.3.3, with the aim of then combining these in the wavelength dimension to produce the white-light flux for each object. Circular apertures with radii of 9 pixels (3.1 λ/D) and 2.5 pixels (0.9 λ/D) were used for the host star and the companion, respectively. To estimate the background flux at the position of the star, we also extracted photometry in a circular annulus centred on the stellar location with inner and outer radii of 11 and 16 pixels, respectively. It was not possible to use this method to estimate the background flux at the position of the companion as the companion lies close to the edge of the field of view in some frames, limiting the space available to place an annulus that would be statistically wide enough. We therefore instead followed an approach used by Biller et al. (2021), estimating the background at the companion location by masking the companion and extracting flux in a circular annulus centred on the host star, with a width of 6 pixels at the radial separation of the companion. As most of the residual background in each frame was eliminated by the data processing steps in Section 3.3.2, these background values are close to zero. These apertures and annuli are shown in Figure 3.4, overlaid on a single processed time frame of data in the 52nd ALES wavelength channel ($\lambda \approx 3.69$ µm). We then removed the residual background from our stellar and companion flux measurements by multiplying the mean flux per pixel in the background annuli by the area of the corresponding apertures and subtracting the resulting values from the aperture photometry. We then produced single white-light measurements for both the companion and the star at each time frame by taking the median combination of the photometric measurements across the 30 wavelength channels. These raw time series, uncorrected for shared variations introduced by Earth's atmosphere (i.e. before division), are shown in grey in the top two panels of Figure 3.5. The discrete gaps in integration reflect time spent off-target due to the two-point on/off nodding pattern used to enable background subtraction. We also plot the data binned to 18 minutes of integration time. We binned the data by taking the median value in each time bin. The error on the binned fluxes are the Gaussian approximation of the root mean square (RMS) i.e. median absolute deviation (MAD) $\times$ 1.48 of the flux measurements inside each bin divided by $\sqrt{N-1}$, where N is the number of frames per bin. Next, we removed variability due to Earth's atmosphere and other systematics from the unbinned raw flux of the companion using the unbinned raw flux of the host star, which acts as a simultaneous photometric reference. By dividing the unbinned companion flux by the unbinned stellar flux, we eliminate trends common to both and produce a differential light curve that only contains non-shared variations. Assuming that the host star is not itself varying (see Section 3.4.2), the resulting differential light curve reflects the intrinsic variability of the companion plus any contamination arising from non-shared systematics. We show this raw differential light curve in the third panel of Figure 3.5. The bottom panel shows a zoomed-in view of the binned version, with tighter limits on the y-axis.

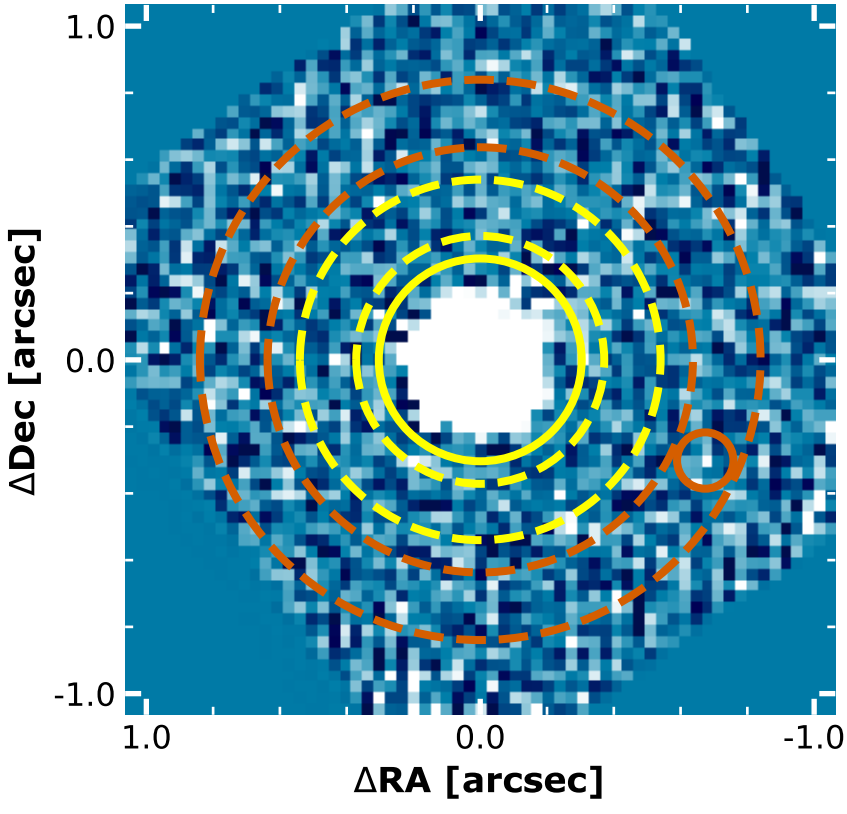

Figure 3.4: The apertures (continuous lines) and annuli (dashed lines) used to extract photometry and background measurements for host star HD 1160 A (in yellow) and companion HD 1160 B (in orange). The image is a single time frame from the 52nd ALES wavelength channel ($\lambda \approx 3.69$ µm). North is up, and east is left. The orange aperture is placed at the location of HD 1160 B, which is too faint to be visible in a single frame. The companion was masked when extracting photometry in the annulus for the companion background.

In the following sections we examine a number of physical, instrumental, and processing factors that may be correlated with non-astrophysical features in the differential white-light curve, and in Section 3.5 we model and remove non-shared variations arising from some of these factors.

3.4.2 TESS light curves of host star HD 1160 A

Although the vast majority of A-type stars generally vary well below the ∼1% level, a small fraction vary at a much higher level, showing up to ∼15% variations (Ciardi et al. 2011). To test our assumption that the host star HD 1160 A is not varying at a level that impacts our differential light curve, we used data from the TESS mission, which is publicly available on

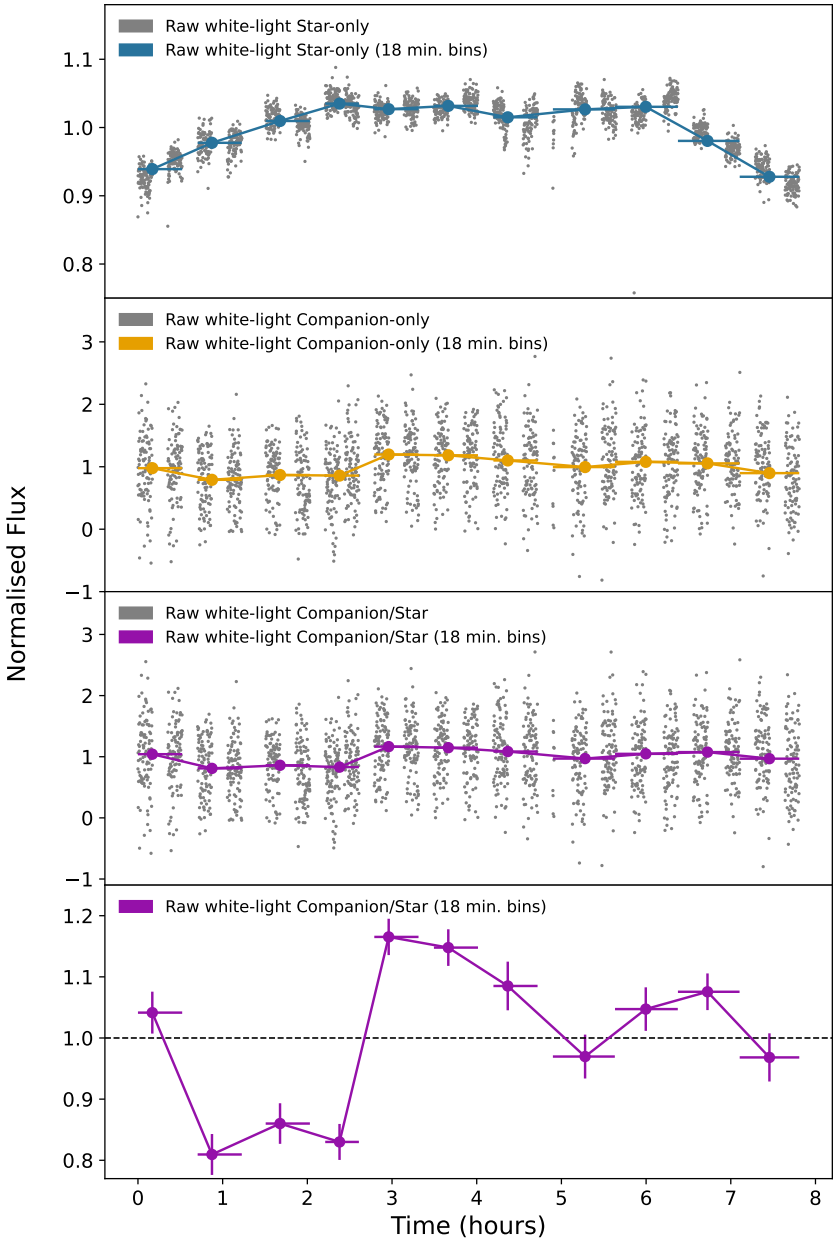

Figure 3.5: The top two panels show the normalised raw white-light flux (λ =3.59-3.99 µm wavelength range) of host star HD 1160 A (in grey, top panel) and companion HD 1160 B (in grey, second panel). The blue and orange lines are the same fluxes of the star and companion, respectively, binned to 18 minutes of integration time per bin. Each has been normalised by dividing by the mean value across the full sequence. The third panel shows, in grey, the resulting differential white-light curve when the white-light of the companion is divided by the white-light of the star to remove trends shared by both. The same data binned to 18 minutes of integration time per bin is shown in purple. The light curve in the bottom panel is the same as the third panel but zoomed in on the y-axis with a dashed line at normalised flux = 1 for clarity. Provided that there is no contamination from stellar variability, variations in this light curve are a combination of any intrinsic companion variability and trends arising from non-shared systematics. The gaps in the data are due to the two-point on/off nodding pattern used to collect sky frames for background subtraction.

the Mikulski Archive for Space Telescopes (MAST) data archive[1]. The TESS mission observed HD 1160 A for 25 days in Sector 42 (from 2021 August 21 to 2021 September 14) and for 26 days Sector 43 (from 2021 September 16 to 2021 October 11), 51 days in total, with 2 minute cadence. The TESS detector bandpass covers a broad-band wavelength range of 0.6-1.0 µm (Ricker et al. 2015), which does not overlap with our LBT/ALES observations in the 2.8-4.2 µm range. However, as stars are generally less variable in the infrared than in the optical regime, any variations in the TESS light curve of HD 1160 A should represent an upper limit for its variability at the wavelengths covered by ALES (e.g. Solanki & Unruh 1998; Unruh et al. 1999; Fröhlich & Lean 2004; Davenport et al. 2012; Goulding et al. 2012; Ermolli et al. 2013; Rackham et al. 2022). Each TESS pixel covers 21″ on sky. This means that HD 1160 A, HD 1160 B (at a separation of ∼0.78″), and HD 1160 C (at a separation of ∼5.1″) are not resolved separately in the TESS images and appear as a single object. However, as both HD 1160 B ($\Delta J = 8.85 \pm 0.10$ mag, $\Delta L' = 6.35 \pm 0.12$ mag) and C ($\Delta J = 6.33 \pm 0.04$ mag, $\Delta L' = 4.803 \pm 0.005$ mag) are far fainter than HD 1160 A, especially at shorter wavelengths, it is reasonable to assume that flux of HD 1160 A will dominate in the TESS data (Nielsen et al. 2012).

We first masked out any bad quality exposures using the one-hot encoded quality mask in the 'QUALITY' keyword in the header of the light curve files provided by the TESS Science Processing Operations Center (SPOC, Jenkins et al. 2016) on MAST. We then used the 'CROWDSAP' keyword in the header to get an estimate of the ratio of target flux to total flux in the optimal aperture used for the PDC SAP (Pre-search Data Conditioning Simple Aperture Photometry) flux (e.g. Panwar et al. 2022a). The 'CROWDSAP' value for sector 42 and 43 indicates that 0.17% and 0.2% flux is from dilution by nearby sources. We subtract the estimated diluted flux from each exposure in both the sectors. The resultant light curves for both the sectors are shown in Figure 3.6. Although the TESS observations are not contemporaneous with our LBT/ALES observations, we do not see variations above 0.03% in the light curve of HD 1160 A over the timescale covered by the two TESS sectors (51 days). As this is far smaller than the precision of our differential light curve, we proceed with the assumption the host star HD 1160 A is non-varying within the flux precision of our analysis of the variations in the light curve.

3.4.3 Impact of wavelength calibration and flat-field smoothing

In Section 3.3.1, we described the process used to perform the wavelength calibration of the raw data and to extract the micro-spectra into a three-dimensional image cube. This step was repeated separately using the wavelength calibration that was the most divergent of the 6 obtained throughout the observing sequence, i.e. the 3.9 µm fiducial spots for this wavelength calibration were the most significantly offset compared to the one that was originally used. Over the course of the night, the projection of the micro-spectra onto the detector drifts slightly. If this drift is significant then a particular wavelength calibration may not remain accurate for the entire observing sequence, potentially producing a false variability signal when the wrong part of the spectrum is assigned to a given channel. Repeating our

[1] MAST data archive portal: https://mast.stsci.edu/portal/Mashup/Clients/Mast/Portal.html

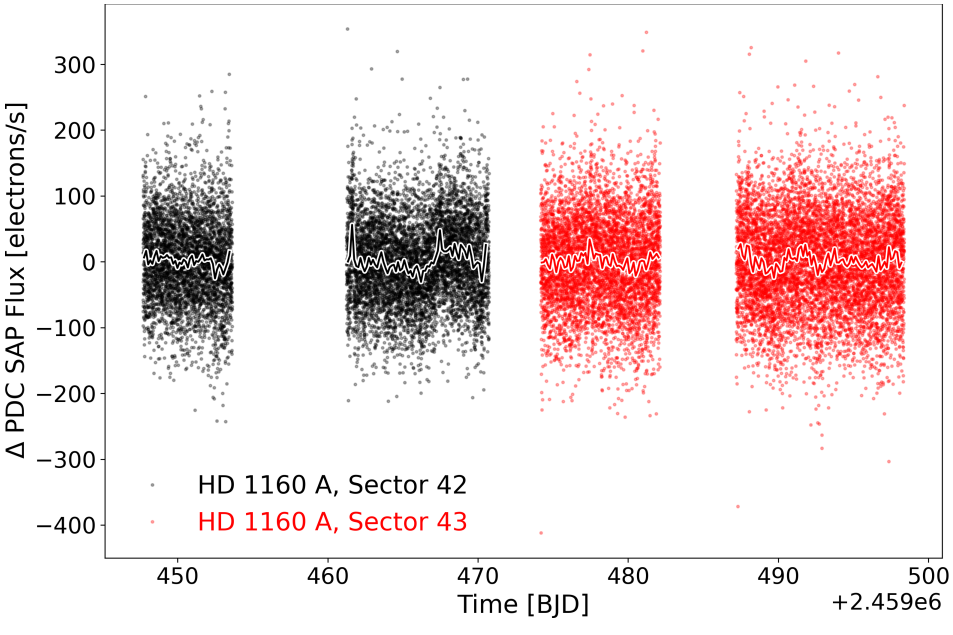

Figure 3.6: TESS 2 minute cadence PDC SAP light curve of HD 1160 A obtained from TESS sectors 42 (black points) and 43 (red points). Light curves from both sectors have been normalized to the median count level for the respective sector to remove the systematic change in the base flux level from one sector to the next. Overplotted is the binned TESS light curve for visual aid. The standard deviation of the stellar flux is 0.027% and 0.03% for sectors 42 and 43, respectively.

spectral extraction using a wavelength calibration obtained at a different point during the observations allows us to test whether this effect has a significant impact on the photometry of the target star and the companion. After extracting the micro-spectra using the alternative wavelength calibration, we then processed the data again in full to produce an alternative differential light curve. The original and alternative wavelength calibrations were obtained at 4 hours 57 minutes (08:25:00 UT) and 1 hour 26 minutes (04:54:00 UT) after the beginning of the observing sequence, respectively. We plot the resulting alternative stellar and companion fluxes, and the differential white-light curve (binned to 18 minutes) in Figure 3.7, alongside the originals from Figure 3.5 for comparison. The differential light curves in each case are consistent within 1σ, indicating that the extracted photometry is sufficiently robust to changes in the wavelength calibration and sub-pixel mis-registration of the spatial profiles for each microspectrum.

In Section 3.3.2, we described our method for applying a flat-field correction to the data to calibrate for the non-uniform response of the detector. Incorrect flat-fielding can lead to a false variability signal if the companion moves over regions of the detector with a non-uniform response that has not been properly calibrated. To test the robustness of our differential light curve to differences in the flat used we processed the data in two separate streams, using a flat that had been smoothed over using a Gaussian filter and a median filter, respectively. We plot the resulting differential light curves in Figure 3.8 for comparison. The two differential light curves are in close agreement and every binned data point lies well within their 1σ error bars, indicating that the method for producing the flat is robust and does not significantly affect the final images or extracted photometry of the star or companion.

3.5 Detrending through linear regression

Trends shared by the star and companion fluxes are removed in the differential light curve (see bottom panel of Figure 3.5), but any non-shared trends will still be present, including the intrinsic companion variability signal that we aim to measure. To improve our sensitivity to the companion's variability, we needed to remove the non-astrophysical residual trends in the differential light curve, which can arise from both telluric and instrumental sources. In the field of exoplanet transmission spectroscopy, such systematic trends are generally modelled and removed from light curves using either a polynomial model created by simultaneously fitting several decorrelation parameters (e.g. de Mooij & Snellen 2009; de Mooij et al. 2011; Brogi et al. 2012; Stevenson et al. 2014; Diamond-Lowe et al. 2018, 2020a; Todorov et al. 2019), or a non-parametric model produced using Gaussian processes (e.g. Gibson et al. 2012, 2013; Evans et al. 2013, 2015; Montet et al. 2016; Carter et al. 2020; Diamond-Lowe et al. 2020b; Panwar et al. 2022b,a). Unlike traditional transmission spectroscopy observations, our target is significantly fainter than the simultaneous reference that we use for detrending. Furthermore, the target was not pixel-stabilised for these observations and moved across the detector throughout the night, so we might predict that the measured light curves could be significantly correlated with the change in position of the companion and the star on the detector over time. Knowing how to remove these systematics is key to obtaining high-precision light curves in future observations of directly imaged exoplanets. For space-based

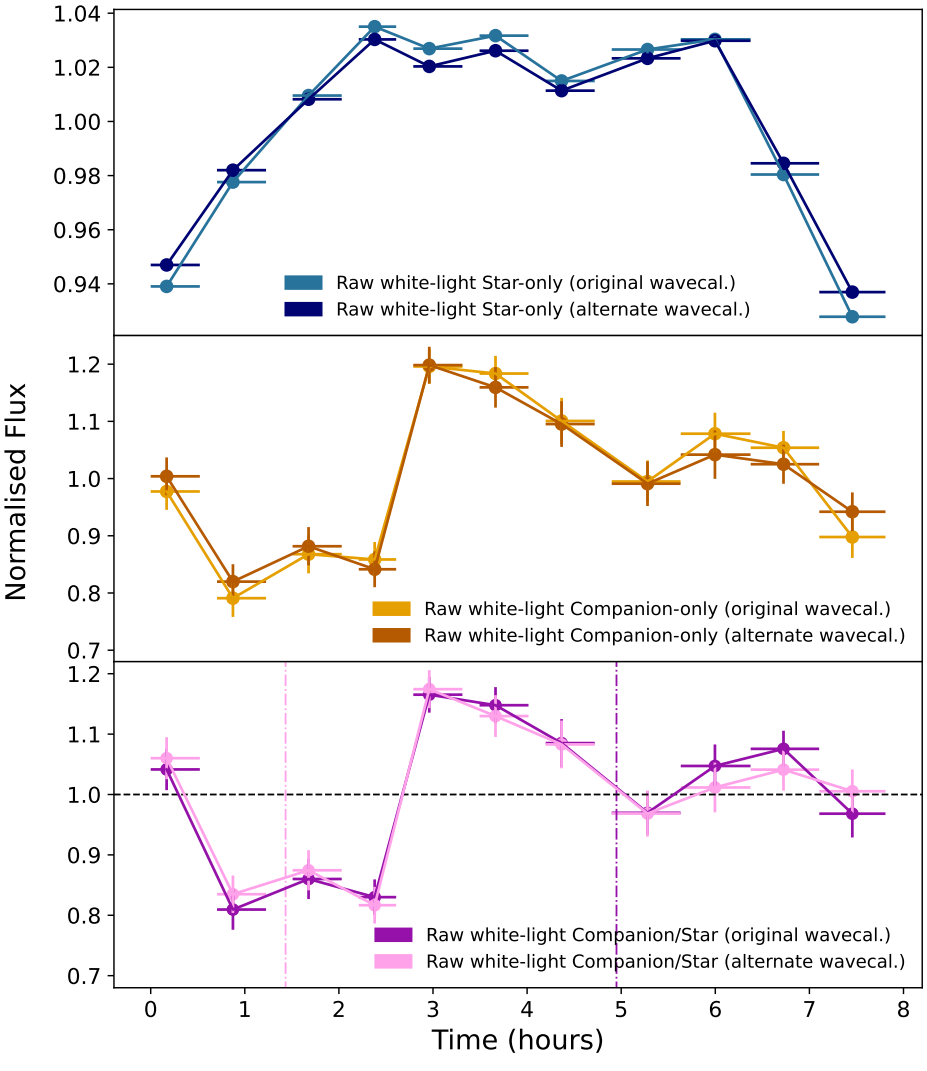

Figure 3.7: Impact of different wavelength calibrations on the star-only and companion-only fluxes, and the differential white-light curve, shown in 18 minute binning. The alternate wavelength calibration was chosen as the one that diverged most from the one originally used. The times at which the wavelength calibrations were obtained are indicated by vertical dashed lines in the same colours as the corresponding light curve.

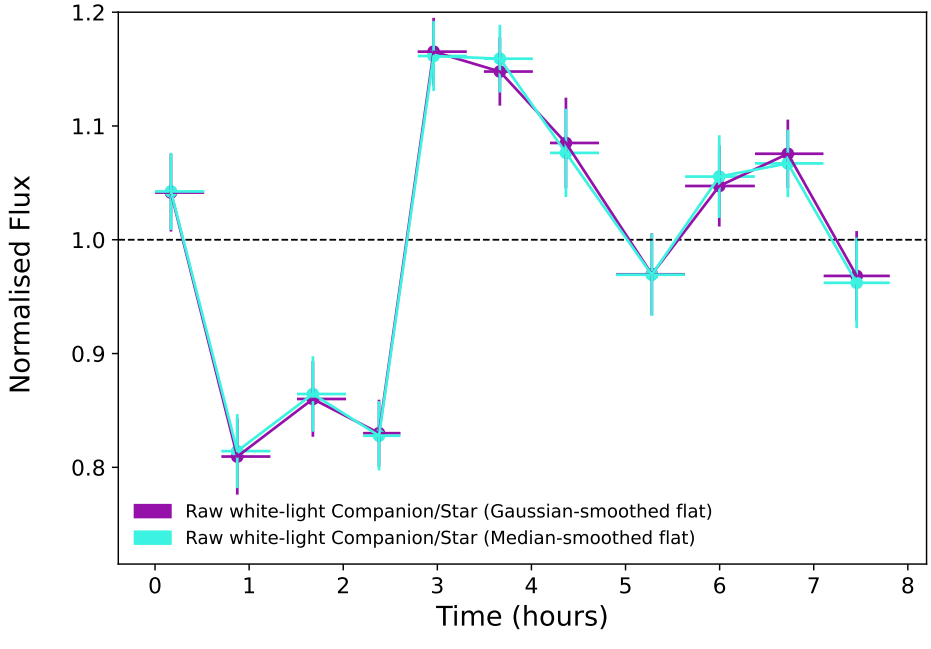

Figure 3.8: The raw differential companion/star white-light curves that are produced when the flat-field correction uses a flat that was smoothed using a median filter and a Gaussian filter, in turquoise and purple, respectively. The latter light curve is the same as that in the bottom panel of Figure 3.5, reproduced here for comparison.

observations the instrumentation is generally sufficiently stable such that the systematics are repeatable over time, allowing them to be well characterised. This is more challenging for ground-based observations, like those here, which are inherently less stable as Earth's atmosphere introduces systematics that can vary night by night.

As a basic demonstration of how to remove such residual trends from ground-based differential light curves of directly imaged planets, we here used a multiple linear regression approach to simultaneously fit several possible sources of systematics. This is not intended as a strictly rigorous statistical analysis of the trends in the light curve, but is done to perform an initial investigation into which parameters have the greatest impact and to illustrate an example approach of how to do this for future observations. As studies move towards increasing precision to measure smaller amplitude variability, one might instead consider approaches using Gaussian processes or similar.

An investigation of the LBT telemetry and white light images revealed eight physical and instrumental factors, shown plotted against time in Figure 3.9, that varied notably during the observing sequence and may be correlated with the residual trends in the differential light curve. We therefore included these parameters in the linear regression. The first three of these were air temperature, wind speed, and wind direction, shown in the three panels on the left-hand side of Figure 3.9. We also considered airmass, which is shown in the top-right panel. While the light from the companion and its host star pass through almost identical airmass (maximum difference $\sim 10^{-5}$), their significantly different colours mean that atmospheric extinction due to absorption and e.g. Rayleigh scattering can result in a differing airmass dependence, even when such scattering effects are reduced at our longer 2.8-4.2 µm wavelength range (Allen 1955; Broeg et al. 2005; Croll et al. 2015; Panwar et al. 2022b).

The remaining four parameters included in the linear regression were the x- and y- pixel positions of the star and the companion in the images prior to spatial and rotational alignment, shown in the centre-right and bottom-right panels of Figure 3.9. The dgvAPP360 is located in the pupil plane, meaning that drifts in the locations of the target PSFs on the detector do not affect its response and performance as it applies the phase modification to every source in the field of view (Otten et al. 2017; Doelman et al. 2022). However, systematics could still be introduced by such drifts if there are variations in the instrumentation or detector response. A number of sharp discontinuities in the y-position, and a singular discontinuity in the x-direction, can be seen in Figure 3.9. These discontinuities are the result of manual positional offsets applied during the observations to keep the star close to the centre of the small ($\sim 2.2''$x $2.2''$) ALES field of view. These offsets were always applied while in the off-source nod position, and always along one axis at a time. The largest discontinuities in the x- and y-positions correspond to shifts of $0.1''$ along the given axis. Neglecting the discontinuities, the drift of the stellar PSF in both the x- and y-directions follow arcs with turn-overs approximately 4.5 hours into the observing sequence. This slow drift is correlated with the pointing altitude of the telescope and arises from flexure of the ALES lenslet array as the telescope rotates. As the observations were obtained in pupil-stabilized mode such that the field of view was rotating over time, the change in position of the companion throughout

Table 3.2: The decorrelation parameters x_i used for the linear regression and the corresponding coefficients c_i and intercept c_0 of the resulting linear model fit to the raw differential light curve. The linear model fit is then given by $y = (\sum_{i=1}^{n} c_i x_i) + c_0$.

Parameter (x_i)	Value (c_i)
Airmass	0.28782524
Air temperature	0.10690617
Star x-position	0.04819219
Star y-position	-0.04368692
Companion x-position	-0.02608288
Companion y-position	0.02129148
Wind speed	0.00059976
Wind direction	0.00050927
Intercept (c_0)	-1.318553799

the data has an additional rotational component compared to the star. The drift arising from the flexure of the lenslet array therefore instead produces an inflection point ∼4.5 hours in the case of the companion.

We used the linear regression tools in version 1.0.2 of the scikit-learn Python package (Pedregosa et al. 2011) to simultaneously fit these input parameters and produce a model fit to our differential light curve. The coefficients of the linear model produced by the linear regression are shown in Table 3.2, and the model itself is shown in green in the top panel of Figure 3.10, relative to the raw differential white-light curve in grey. We then divided the raw differential light curve by this model to produce a detrended version, shown in red in the bottom panel of Figure 3.10. We also overplot the raw differential light curve from the bottom panel of Figure 3.5, prior to detrending, in purple to allow the two to be compared. We also repeated this detrending process to produce detrended differential light curves for each of the 30 individual wavelength channels over the 3.59-3.99 µm wavelength range that comprise the white-light curve. These are shown in Figure 3.11, again binned to 18 minutes. We note that while ALES has a resolution of R∼40, the raw data were spectrally extracted into 100 wavelength channels and so there is some correlation between wavelength channels.

3.6 Results

The detrended differential white-light curve (Figure 3.10) shows sinusoidal-like variability over a timescale of a few hours. In the binned light curve, the normalised flux ranges from a minimum of 0.91 at 0.874 hours to a maximum of 1.13 at 2.961 hours. To better allow us to estimate the differential precision that we achieve in our light curve, we fitted the variability and removed it from our light curve. As the variability signal appears periodic, we used the

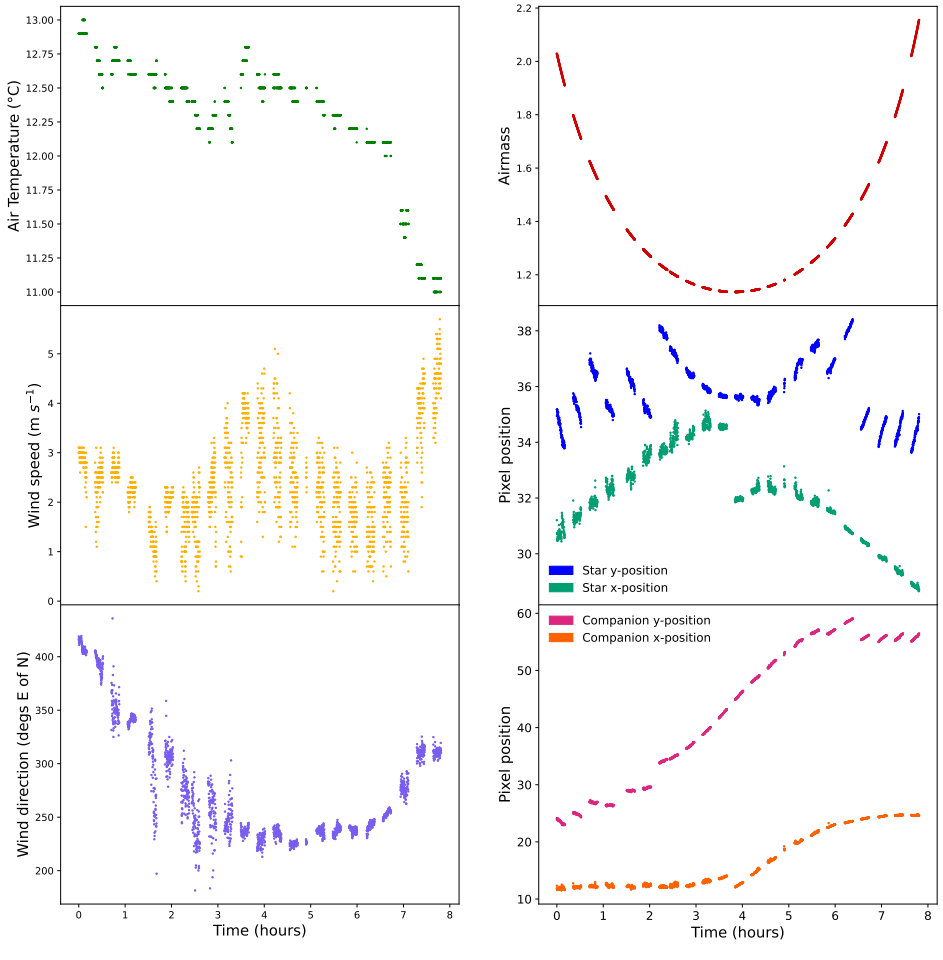

Figure 3.9: The decorrelation parameters used when detrending the differential light curve via linear regression. From top to bottom, the left panels show the air temperature (in), wind speed (in m s^{-1}), and wind direction (in degrees east of north) at the observatory as a function of time, as extracted from the FITS headers of the raw data. The panels on the right show airmass, the x- and y-positions of the star in pixels, and the x- and y-positions of the companion in pixels, as a function of time. The gaps in time reflect the on/off nodding pattern of the observations. The companion and star positions are those in the images prior to spatial and rotational alignment, and the sharp discontinuities in pixel position are due to manual offsets applied to keep the star close to the centre of the small field of view. The stellar positions follow arc-shaped trends aside from these discontinuities, which correlate with the pointing altitude of the telescope and arise from flexure of the ALES lenslet array as the telescope rotates throughout the night. The change in the companion position has an additional trend due to the 109.7° rotation of the field of view over the observing sequence.

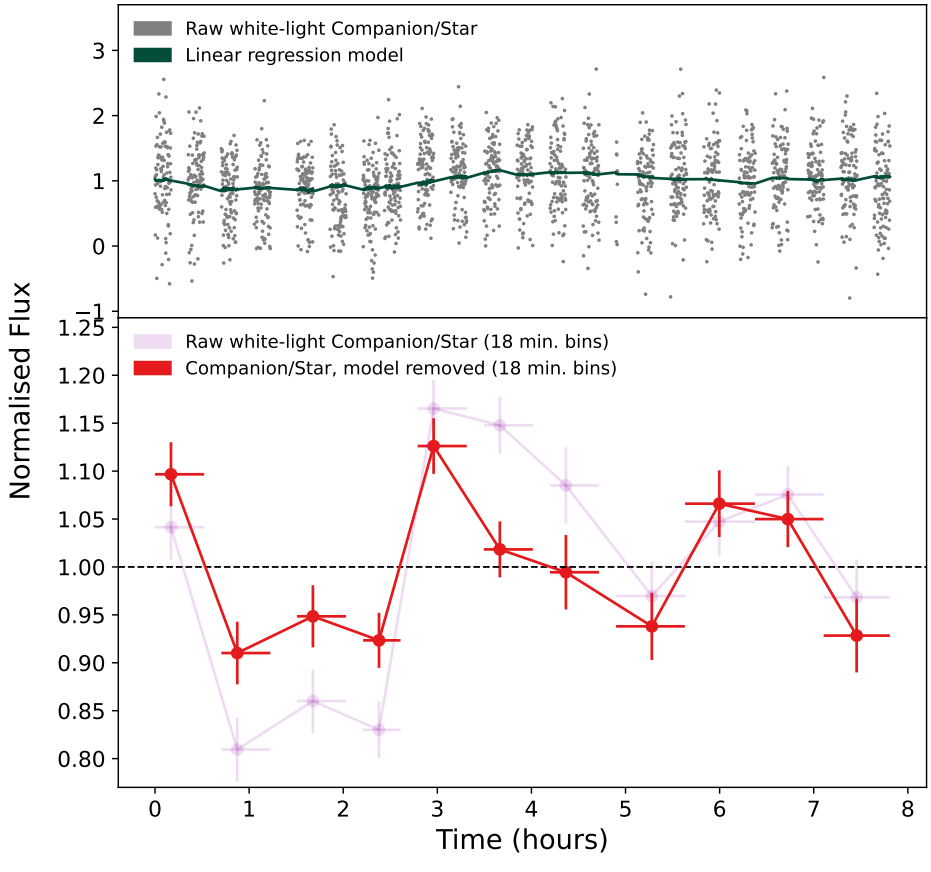

Figure 3.10: The model produced by the linear regression using the decorrelation parameter coefficients (in Table 3.2) is shown in the top panel in green alongside the raw differential light curve in grey. The bottom panel then shows in red the light curve produced when the raw differential light curve is divided by the linear regression model to remove the modelled trends that are not shared by the stellar and companion fluxes, binned to 18 minutes of integration time per bin. The raw differential light curve (i.e. prior to detrending) is also shown faintly in purple, reproduced for comparison from the bottom panel of Figure 3.5.

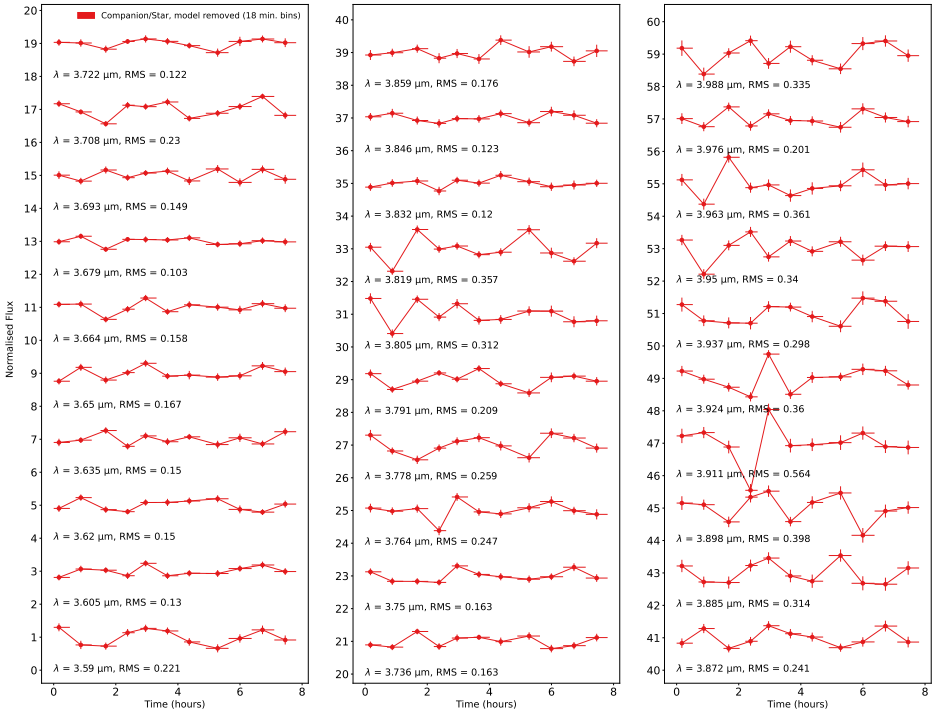

Figure 3.11: In red, we show the detrended versions of the individual differential light curves in each of the 30 wavelength channels that were combined to produce the white-light curve. These wavelength channels cover λ =3.59-3.99 μm, and are binned to 18 minutes of integration time per bin. An offset factor of 2 has been applied between each light curve to separate them from each other. Overall variability appears to increase with longer wavelength.

NASA Exoplanet Archive periodogram service[1] to apply the Lomb-Scargle algorithm to the unbinned detrended differential white-light curve and thereby search for sinusoidal periodic signals (Lomb 1976; Scargle 1982).

The strongest peak in the resulting periodogram (top panel, Figure 3.12) is at a period of 3.242 hours. We then fit a sinusoid to the light curve using this period as an initial guess, which returned a function with the same period (3.239), a semi-amplitude of 0.088, a phase shift of 0.228, and a y-offset of 0.993. This sinusoid is shown overplotted on the detrended light curve in the centre panel of Figure 3.12. The differential light curve was then divided by the fitted sinusoid to remove the variability signal to the first order (centre panel residuals, Figure 3.12). The bottom panel of this figure is the same as the panel above but with the data phase-folded to the period of the fitted sinusoid. Next, we followed the method of Kipping & Bakos (2011) to assess the degree of "red" (correlated) noise in our light curve. We binned our detrended differential white-light curve, with the sinusoid removed, to a range of bin sizes, before normalising and subtracting one to centre around zero. We then measured the RMS of each resulting binned light curve. These RMS values are plotted against bin size in Figure 3.13, alongside the expectation of independent random numbers as a function of bin size i.e. the white noise. For our chosen binning of 18 minutes of integration time per bin, which has a bin size of 200 frames per bin, we find an RMS of 0.037. For comparison, the RMS of the detrended differential white-light curve prior to the removal of the sinusoid, but with the same binning, is 0.073. We therefore conclude that the light curve of HD 1160 B shows variations with a semi-amplitude of $\sim$8.8% or peak-to-peak amplitude of $\sim$17.6%, and that the differential precision achieved in the binned light curve is at the 3.7% level. The amplitude of the variations is therefore above the measured precision. Furthermore, this estimate of the precision is likely a conservative one; the variability signal is unlikely to have been perfectly removed by the sine fit and so the measured RMS values may be higher than the true limiting precision. A caveat of this result is that the baseline of our observations is only $\sim$7.81 hours, so we only cover $\sim$2.4 periods. Additional data is therefore needed to confirm the periodicity and amplitude of the variability of HD 1160 B. We discuss these results further and compare the precision achieved to similar studies in the literature in Section 3.7.2.

3.7 Discussion

In this section we discuss the relative impact of the decorrelation parameters on our results, and the physical explanations of the systematics they introduce. We also compare the precision that we achieve to other variability studies in the literature that use different techniques, and discuss the potential application of differential spectrophotometry in future work.

3.7.1 Impact of decorrelation parameters

Using the linear regression coefficients of each parameter from Table 3.2, we can assess which parameters have the greatest impact on the light curve of HD 1160 B. The small

[1] https://exoplanetarchive.ipac.caltech.edu/cgi-bin/Pgram/nph-pgram

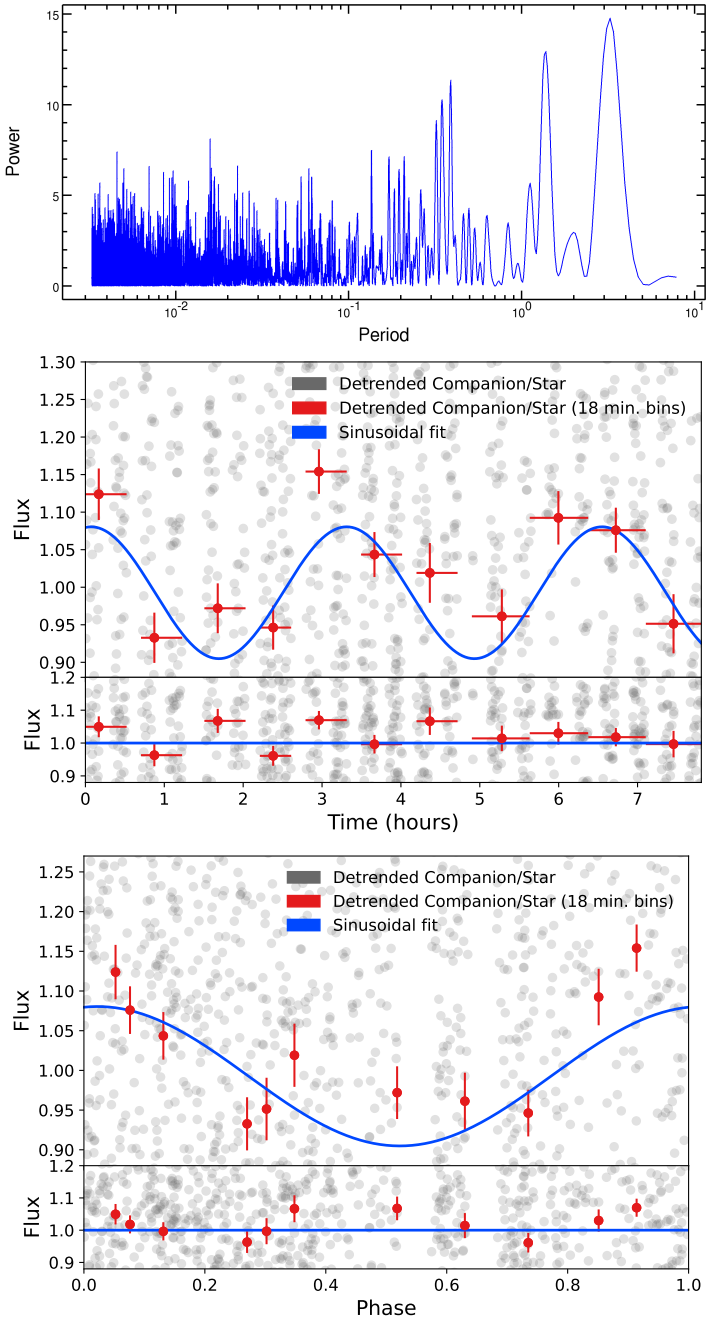

Figure 3.12: Top panel: the Lomb-Scargle periodogram for the unbinned detrended differential white-light curve. The strongest peak is at a period of 3.242 hours. Centre panel: the same detrended differential white-light curve from the bottom panel of Figure 3.10, unbinned in grey and binned to 18 minutes of integration time per bin in red. The blue line is the fitted sinusoid with a semi-amplitude of 0.088 and a phase shift of 0.228. The residuals when the fitted sinusoid is divided out from the light curves are shown underneath. Bottom panel: the same as the panel above, but phase-folded to a period of 3.24 hours.

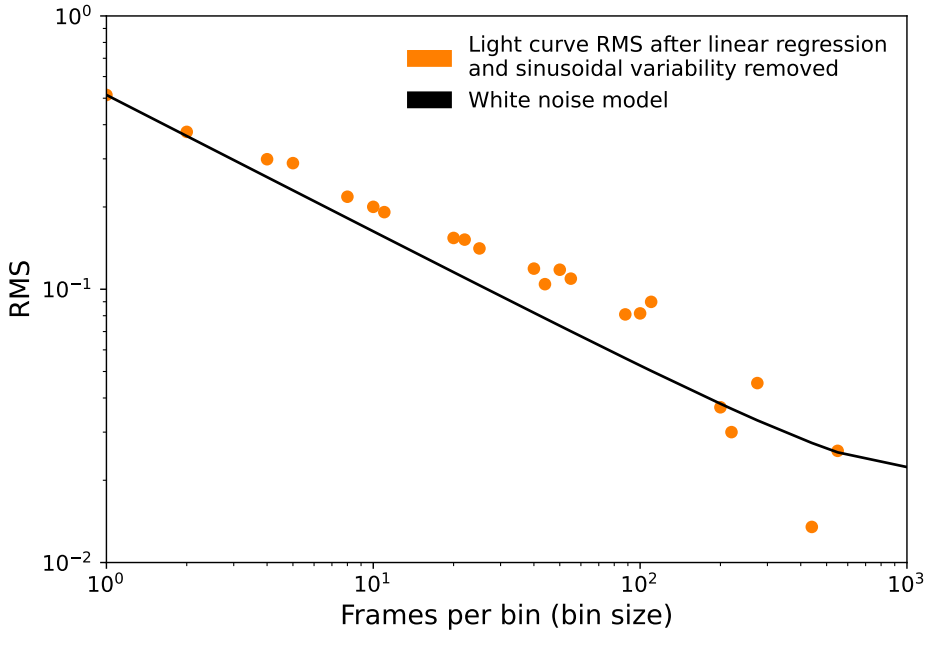

Figure 3.13: The RMS of the binned detrended differential white-light curve, after removing sinusoidal variability, is shown in orange as a function of bin size. The black line shows the theoretical white noise model, or the expectation of independent random numbers for a given bin size.

angular separation of the companion and star might suggest that the effect of airmass would be small. Airmass can be an important systematic for differential spectrophotometric observations where other stars are used as the simultaneous photometric reference as the angular separation between the target and the reference can be large, causing the light from the two objects to pass through different atmospheric columns (e.g. Broeg et al. 2005; Panwar et al. 2022b). However, in our case we use the companion's host star as the photometric reference, so the angular separation between the two is much smaller than is generally the case for observations using reference stars in the field. However, there is a significant colour difference between the star and the companion, which leads to different degrees of extinction at a given airmass. Therefore, we expect an airmass dependence and indeed it has the largest coefficient in the detrending model. Similar extinction effects are often seen in studies of transiting exoplanets, and can also exhibit a non-linear wavelength dependence (e.g. Panwar et al. 2022b).

We also find the air temperature at LBT to be one of the parameters that is most correlated with our differential light curve. As the air temperature changes, this can potentially cause slight changes in the optical path of the telescope or instrument that lead to this correlation.

We further predicted that the positions of the companion and the star could introduce significant non-shared systematics to our measurements; as HD 1160 A was not pixel-stabilised during our observations, we are sensitive to both intra- and interpixel variations as the star and the companion move across the detector. Both the star and the companion changed position on the detector due to flexure of the ALES lenslet array as the instrument moved and positional offsets applied intentionally to keep the target close to the centre of the field of view. We also nodded on and off of the target to enable background subtraction. While the process of nodding is itself relatively accurate, it is not repeatable at a sub-pixel pointing precision, introducing a slight offset error between nods. Furthermore, LBTI data is always pupil-stabilized, so the field of view was rotating throughout the night. Although it may have been optimal to fix the star and companion positions to the same detector pixels for the duration of the observations, this was not possible due to the effect of the lenslet array flexure and the lack of instrument derotator in the LBTI architecture (Doelman et al. 2022). However, we find that these positional changes are not the most correlated with our differential light curve. It is possible that this is because the light from the star and companion is spread out across multiple detector pixels when spectrally dispersed, reducing the impact of any systematic issues arising from any single pixel. The light of our target is dispersed across wavelength, similar to a technique often used for high-precision differential photometry whereby a telescope is intentionally defocused to disperse starlight over the detector (e.g. de Mooij et al. 2011, 2013; Crossfield et al. 2012; Croll et al. 2015). This has the effect of reducing systematics due to intrapixel variations and minimises the impact of any residual flat-field errors. The step of recombining our data into a white-light curve may therefore have helped to reduce systematic trends that would otherwise have been introduced by the positional movement of the targets throughout the night. The use of a spectrograph also has the additional benefit of allowing us to remove individual wavelength channels that are found to contain defects. For this dataset, this allowed us to leave out channels affected by

overlapping spectral traces, significant telluric absorption, and absorption by the glue layer of the dgvAPP360, as described in Section 3.3.3.

Lastly, we find that the wind speed and direction are the least correlated with our differential light curve, but note that the conditions on the night were exceptionally stable and so cannot rule out that these factors could have an impact in less optimal conditions.

For future observations, residual systematics in differential light curves of directly imaged companions could be removed using more advanced methods from the exoplanet transmission spectroscopy and high-precision secondary eclipse literature such as fitting the data using a Gaussian process regression (e.g. Gibson et al. 2012; Evans et al. 2017; Nikolov et al. 2018b,a; Diamond-Lowe et al. 2020a,b; Wilson et al. 2021). In general, methods used to identify trends in transmission spectroscopy data also include a model of the exoplanet transit itself, allowing the transit to be detected even when the strength of the signal is very low. However, this is possible because the expected shape of the signal is well understood. This is more difficult for searches for variability in directly imaged companions, where the expected shape of the variability signal is not necessarily well-known in advance. Furthermore, many of these methods assume a linear relationship between systematics and trends in the light curve, while the telluric and instrumental systematics present in time-series data can be complex and non-linear. In the future, an optimal approach should account for the functional form of the correlated parameters (Panwar et al. 2022b,a).

3.7.2 Differential light curves

3.7.2.1 Variability interpretation

In Section 3.6 we found that HD 1160 B shows variations with a semi-amplitude of ∼8.8% (or peak-to-peak amplitude of ∼17.6%). To compare this result to literature observations of similar objects, we must consider both spectral type and the wavelengths at which variability has been observed. Vos et al. (2022) found that virtually all L dwarfs are likely to be variable at the 0.05-3% range, and several studies have measured higher variability, up to 26% (e.g. Radigan et al. 2012; Radigan 2014; Lew et al. 2016; Biller et al. 2018; Bowler et al. 2020b). However, there is evidence that brown dwarf variability amplitude may have a strong wavelength dependence. For example, HST observations of highly variable L dwarf companion VHS 1256-1257 b identified a large variability amplitude of 24.7% at 1.27 µm, while Spitzer observations at 4.5 µm found a far lower amplitude of 5.76±0.04% (Bowler et al. 2020b; Zhou et al. 2020b; Miles et al. 2022). Zhou et al. (2020b) do note, however, that the HST and Spitzer observations were not obtained contemporaneously and so the atmosphere of VHS 1256-1257 b and hence its variability properties are likely to have changed substantially over the intervening timescale. Comparisons of large surveys also suggest that variability amplitudes are lower in the mid-infrared than in the near-infrared, although there is evidence for a weaker wavelength dependence and enhanced mid-infrared variability amplitudes for the young isolated brown dwarfs most similar to substellar companions (e.g. Radigan et al. 2014; Metchev et al. 2015; Biller et al. 2018; Vos et al. 2022).

The amplitude of the L-band variability we measure for HD 1160 B is quite extreme compared to literature results, but it is important to note that there have been very few variability studies for substellar companions in the mid-infrared, making direct comparison difficult. High-amplitude variability in brown dwarfs is generally attributed to heterogeneous surface features, such as spots or clouds of varying thickness, rotating in and out of view as the object rotates (e.g. Apai et al. 2013; Biller 2017; Artigau 2018). Some light curves show more complex features that cannot be modelled with a single atmospheric feature, or features that evolve over short or long timescales (e.g. Artigau et al. 2009; Metchev et al. 2015). These features and time evolution may arise from changing weather systems, or bands of clouds which rotate within the target's atmosphere and generate waves on a global scale (e.g. Apai et al. 2017; Tan & Showman 2021). For HD 1160 B, observations over a longer baseline are required to be able to characterise any time evolution in the variability signal.

However, the spectral type of HD 1160 B is unclear as it has a highly peculiar spectrum that cannot be satisfactorily fit with spectral models or templates in current libraries, and some studies suggest that it could instead be a late-M dwarf (Maire et al. 2016; Garcia et al. 2017; Mesa et al. 2020). If HD 1160 B is an M dwarf, its variability would most likely arise from cool star spots caused by magnetic activity in its photosphere, which are common in M-dwarfs and would rotate in and out of view in much the same way as the cloud features of lower mass objects (e.g. Barnes et al. 2002; Frasca et al. 2009; Scholz et al. 2009; Goulding et al. 2012; Ghosh et al. 2021; Johnson et al. 2021). The properties of such variability can be highly dependent on the spot distribution and fractional spot coverage of a given object; some M-dwarfs have a very high coverage with multiple starspots covering as much as 20-50% of their fractional surface area inhomogeneously (e.g. O'Neal et al. 2004; Morales et al. 2010; Irwin et al. 2011; Goulding et al. 2012; Jackson & Jeffries 2013). Spot-induced variability amplitudes for M-dwarfs generally range from the subpercent level up to around $\sim$5% (e.g. Rockenfeller et al. 2006; Charbonneau et al. 2009; Birkby et al. 2012; de Mooij et al. 2012; Nefs et al. 2013). Although observed far less often in the infrared compared to the optical, flaring events can induce far stronger variability in M-dwarfs at amplitudes ranging from the subpercent level up to tens of percent (e.g. Goulding et al. 2012; Tofflemire et al. 2012). Our measured variability amplitude for HD 1160 B is therefore also on the higher end of what has been observed for earlier spectral types such as late M- and early L-dwarfs, barring flares, although we again note the lack of literature studies of similar objects in the L-band.

While the variability observed for HD 1160 B appears high, another point to consider is its orbital inclination, which the latest orbital fits suggest is close to edge-on as viewed from Earth ($92.0^{+8.7}_{-9.3}$°; Bowler et al. 2020a). If the obliquity of HD 1160 B is aligned with its orbit such that we are viewing its rotation close to edge-on, the observed variability amplitude is likely to compose a much larger fraction of its true variability compared to if it were viewed face-on. Indeed, Vos et al. (2017) demonstrated that the highest variability amplitudes are seen for targets with close to edge-on viewing angles.

If we interpret the 3.24 h sinusoidal variation we observed as the true rotation period of HD 1160 B, we can further consider this within physical limitations. The breakup period of a rotating object is dependent on its radius, which is itself age-dependent, and mass. Both

age and mass are poorly constrained for HD 1160 B: literature results place the system's age in the 10-300 Myr range (Nielsen et al. 2012; Maire et al. 2016; Curtis et al. 2019), and mass estimates range from ∼20 M_{Jup} to 123 M_{Jup} (Curtis et al. 2019; Mesa et al. 2020). Vos et al. (2020) calculated the breakup periods of brown dwarfs as a function of age by equating equatorial velocity with the escape velocity, accounting for radial contraction over time. When we compare our measured HD 1160 B variability period of 3.24 hours to their results (their Figure 13), we find that this is a physically feasible rotation period for most possible combinations of mass and age from the literature, albeit very close to the breakup period in many cases. An alternative explanation is that the 3.24 hour variability signal that we see is produced by multiple features in the atmosphere of HD 1160 B, and that its rotation period is actually longer (Leggett et al. 2016). Additional observations of this variability over a longer baseline will help to further characterise its origin and confirm whether its periodicity reflects that of the companion's rotation.

The detrended differential light curves for each of the 30 individual wavelength channels over the 3.59-3.99 µm wavelength range that comprise the white-light curve (Figure 3.11) show increasing statistical errors at longer wavelengths, as expected as our S/N is lower here. Using the RMS of each light curve as a metric to compare the scatter in each channel, we do see tentative evidence of increasing variability towards longer wavelengths beyond the increase of RMS expected from the S/N. However, as the total baseline of our observations is only a single night, we see too few repetitions to be confident of variability patterns in individual wavelength channels. Additional spectrophotometric data will therefore be required to confirm this. Although we modelled the overall variability in our white-light curve with a single sinusoid, it is also possible that the phase and amplitude is different per wavelength channel as distinct atmospheric features at separate locations in the atmosphere of the companion may produce variability with a different wavelength dependence. Furthermore, although the overall wavelength range of these 30 channels is relatively small, different wavelengths probe different pressure levels in the companion's atmosphere, and hence different layers of the atmosphere (e.g. Buenzli et al. 2012; Biller et al. 2013; Apai et al. 2017; Ge et al. 2019).

3.7.2.2 Light curve precision

In Section 3.6, we found that after removing a single sinusoid from the data, we achieved a precision of 3.7% in the detrended differential light curve when it is binned to a bin size of 200 data points, corresponding to 11 bins of 18 minutes of integration time. There have been three previous studies searching for variability in substellar companion from the ground; Apai et al. (2016), Biller et al. (2021), and Wang et al. (2022) each conducted variability searches on the HR 8799 planets using satellite spots as photometric references. In a pilot variability study, Apai et al. (2016) reach a ∼10% planet-to-planet photometric accuracy for SPHERE observations of 25 minute cadence when data from different nights are combined for a total telescope time of 3.5 hours. Biller et al. (2021) goes further with SPHERE to conduct a longer (>4 hours) search, successfully constraining the sensitivity to variability to amplitudes >5% for HR 8799b and >25% for HR 8799c. More recently, Wang et al. (2022) used SCExAO/CHARIS to improve the variability constraints of HR 8799c to the 10%

level, and HR 8799d to the 30% level. They did this by combining the use of satellite spots with a spectrophotometric approach similar to the one we present in this paper, using the CHARIS IFS to disperse the light into individual spectra before recombining the channels into wider bands. At first glance, the sensitivity that we achieve for HD 1160 B here may appear to compare favourably with these results. However, it is important to consider a number of caveats that make direct comparison unjustified. All three of the HR 8799 studies were conducted at near-infrared wavelengths with 8.2-m telescopes, while ours was in the mid-infrared with an 8.4-m telescope. More significantly, the HR 8799 planets are fainter than HD 1160 B, with contrasts of $\Delta H = 8 - 10$ mag compared to their host star, which has a H-band magnitude of 5.28 mag (Marois et al. 2008, 2010b). HD 1160 B is brighter, with a contrast of $\Delta L' = 6.35$ mag compared to a host star with an L'-band magnitude of 7.06 mag (Nielsen et al. 2012). The lower sensitivity to variability achieved by these studies is therefore partially a reflection of the intrinsically lower fluxes of their targets, which leads to higher errors on their photometry.

However, each of the HR 8799 variability studies also found that the satellite spots can demonstrate individual variations of their own and are often anti-correlated with each other. This means that they may not always serve as appropriate photometric references with which to detrend the light curve of a companion. Wang et al. (2022) found that the flux ratio of the SCExAO satellite spots shows time variation with a scatter of $\sim$3% across a night, and can show even larger variations on a shorter timescale, up to 10%. This potentially sets a limit to the precision that can be achieved using satellite spots, particularly on nights where observing conditions are less stable.

A key advantage of the dgvAPP360 compared to satellite spots is its simplicity; the photometric reference it provides is simply an image of the host star, and so it does not suffer from the same correlated systematics as the satellite spots. Differential photometry between the companion and the star can be carried out directly. It may be possible to reach an even deeper precision through differential spectrophotometry with a dgvAPP360 than the 3.7% level that we achieve here. Indeed, if we compare the detrended light curve RMS as a function of bin size to the white noise expectation (Figure 3.13), it continues to follow the trend of the white noise and does not plateau implying that we have not yet reached any noise floor. This means that in principle the precision of the differential light curve would improve further if more data from additional epochs was added. This also indicates that this technique should remain usable for companions with less favourable contrasts than HD 1160 B, such as those in the planetary-mass regime. However, more data per bin will be required to achieve the same precision for a fainter companion, so the time-sampling in the binned light curves may be less fine in these cases.

Many transiting exoplanet studies make use of a region of the target light curve that is expected to be flat (i.e. an out-of-transit baseline) to test the degree to which systematics have been corrected. While we have shown here that key systematic trends are successfully removed in the detrended differential white-light curve of HD 1160 B, we do not have such a baseline to verify the level of impact of any remaining systematics. The possibility therefore remains that an unknown systematic could be present that has not been accounted for by

any of the processes that we have applied here, and could be responsible for the variability that we see in the light curve of HD 1160 B. However, this is also inherently the case for any study that explores the variability of isolated brown dwarfs and planetary-mass objects, stellar variability due to star spots or other sources, or transiting exoplanet studies where exoplanets transit variable stars (e.g. Gelino et al. 2002; Rockenfeller et al. 2006; Biller et al. 2013, 2015, 2021; Girardin et al. 2013; Radigan et al. 2014; Wilson et al. 2014; Naud et al. 2017; Eriksson et al. 2019; Vos et al. 2019; Manjavacas et al. 2021, 2022). A subsequent study is forthcoming in which we further investigate the precision that can be reached with this technique, and use injection-recovery tests to assess the extent to which known, simulated variability signals can be recovered (Sutlieff et al., in preparation, Chapter 5 of this thesis).

Nonetheless, ground-based differential spectrophotometry with the vAPP is highly complementary and advantageous to space-based approaches for measuring the variability of high-contrast companions. There have been many successful space-based measurements of companion variability using HST, detecting variability with amplitudes down to the 1-2% level in some cases (e.g. Manjavacas et al. 2018, 2019a; Bowler et al. 2020b; Zhou et al. 2020a,b). Zhou et al. (2016) was further able to detect sub-percent variability using HST observations of planetary-mass companion 2M1207b, which lies at roughly the same angular separation as HD 1160 B, albeit with a more favourable contrast. Furthermore, the first variability monitoring with JWST, which should reach an even greater precision, is currently underway as part of the Early Release Science Program (Hinkley et al. 2022a). However, while JWST has the sensitivity to image fainter, lower mass companions and measure their variability with great precision, its $\sim$6.5 m mirror is smaller than those of the largest ground-based telescopes, and thus is cannot outperform large ground-based telescopes with extreme AO at small separations $\lesssim 0.5''$ at $\sim$3.5 µm (Girard et al. 2022). This means that companions at the closest angular separations such as Jupiter analogues are for now likely only accessible with ground-based monitoring techniques, for all but the nearest stars (Carter et al. 2021; Kammerer et al. 2022). Ground-based telescopes also uniquely provide access to higher resolution spectrographs, such that line profile variability could be used in Doppler imaging to create 2D global maps of features in exoplanet atmospheres such as storms similar to Jupiter's Great Red Spot (e.g. Crossfield 2014).

3.7.3 Observing strategy

During the observing sequence, we obtained 6 wavelength calibrations at intervals throughout the night to allow us to test whether differences in the wavelength calibration used would lead to differences in the differential light curve. In Figure 3.7 in Section 3.4.3, we found that the differential light curve is robust to changes in the wavelength calibration. It is therefore preferable to acquire wavelength calibrations at the start or end of future observations, perhaps along with a single precautionary wavelength calibration at high elevation, and instead obtain additional data on target and minimise pixel offsets.

We also used an on/off nodding pattern to enable background subtraction. However, future studies may wish to consider alternative methods to remove the thermal background such that the amount of time spent on target can be doubled and the entire system stabilised.

For example, Doelman et al. (2022) developed an approach whereby 93% of the frames obtained were on-target and the thermal background was modelled and removed using the science frames themselves and a small number of background frames obtained before and after the observing sequence. As Figure 3.13 shows that we approach the photon noise limit, increased on-target time would therefore allow a greater differential light curve precision to be obtained in a single night of observations.

Lastly, the absence of an instrument derotator in the LBTI architecture meant that the field of view was rotating throughout the observing sequence. In addition to the drift due to lenslet flexure and the manual offsets applied to keep HD 1160 A centred in the field of view, this meant that HD 1160 A and B were not pixel-stabilised during our observations. However, the linear regression correlation coefficients of the positions of the star and the companion are small relative to those of airmass and air temperature. This suggests that that, when present, these factors dominate over any effect from HD 1160 A and B not being pixel-stabilised.

Understanding whether the host star of a given target is itself varying is important when interpreting the trends in a differential light curve. Most, if not all, potential targets for differential spectrophotometry will be present in at least the TESS full frame images available on the MAST archive. Even though this data will most likely not be contemporaneous with a particular set of observations, the total baseline of the coverage should be relatively long and therefore sufficient to check a host star for variability at the required precision, especially if the target appears in multiple TESS sectors. We therefore recommend this method as a good way to verify the level of variation shown by the host star of a target for differential spectrophotometry, and hence whether it is stable enough to act as a simultaneous photometric reference without requiring further analysis to account for stellar variability.

3.7.4 Outlook

In principle, the technique presented in this paper can be applied to any vAPP coronagraph used in combination with an IFS. Although ALES is currently the only IFS operating over the L and M bands (Doelman et al. 2021), a vAPP coronagraph is also available on SCExAO/CHARIS on the 8.2-m Subaru Telescope, offering R$\sim$19 spectrographic coverage over the J, H, and K bands (1.13-2.39 µm) (Groff et al. 2016; Doelman et al. 2017; Bos et al. 2019; Lozi et al. 2020; Miller et al. 2021). There will also be two different vAPPs on the Mid-infrared ELT Imager and Spectrograph (METIS) instrument on the upcoming 39-m Extremely Large Telescope (ELT), for which this work is a pathfinder. METIS will provide high spectral resolution spectroscopy (R$\sim$100,000) over the L and M bands (Carlomagno et al. 2016; Brandl et al. 2018, 2021; Kenworthy et al. 2018a). Variability measurements using a vAPP may even be possible for broad-band imaging data where an IFS is unavailable, although sensitivity will be inherently more limited without the benefits of using differential spectrophotometry to reduce the effects of systematics. There are several vAPPs currently available on such coronagraphic imagers, such as MagAO (Morzinski et al. 2016; Otten et al. 2017; Sutlieff et al. 2021) and MagAO-X (Miller et al. 2019; Close et al. 2020a) on the 6.5-m Magellan Clay Telescope, and the recently-commissioned Enhanced Resolution Imager and Spectrograph (ERIS) instrument on the VLT (Boehle et al. 2018, 2021; Kenworthy et al.

2018b; Dubber et al. 2022), with more planned, including for GMagAO-X on the GMT (Close et al. 2020b) and MICADO on the ELT (Clénet et al. 2018; Perrot et al. 2018). Using the vAPPs that will be available on larger telescopes, variability monitoring through differential spectrophotometry will be possible for fainter companions at closer angular separations, including those in the exoplanet mass regime. While this will be inherently more challenging for such companions at greater contrasts, these will remain accessible to this technique through the addition of data from multiple epochs as long as the systematic noise floor is not reached, albeit with a trade-off between light curve precision and time-sampling.

In the era of extremely large telescopes, high-contrast imaging combined with high resolution spectroscopy will provide access to fainter companions at lower masses and older ages and allow their orbital velocities and spin to be measured (e.g. Snellen et al. 2014, 2015; Schwarz et al. 2016; Birkby 2018; Wang et al. 2021b; Xuan et al. 2022). Measurements of how individual absorption lines change in depth and width as an exoplanet rotates will allow two-dimensional surface maps of exoplanet atmospheres and weather to be produced, through techniques such as Doppler imaging (e.g. Crossfield 2014; Crossfield et al. 2014; Luger et al. 2021; Plummer & Wang 2022). Further in the future, multi-wavelength variability measurements obtained in reflected light may even enable exo-cartography of directly imaged Earth-like exoplanets (e.g. Luger et al. 2019, 2022; Kawahara 2020; Kuwata et al. 2022; Teinturier et al. 2022).

A limitation of using the dgvAPP360 for variability measurements is that post-processing algorithms relying on angular diversity, such as ADI and PCA, cannot be used without also removing the central PSF of the star that we use as the simultaneous photometric reference. Furthermore, the stellar PSF must remain unsaturated throughout the observing sequence. This potentially limits the sample of targets with bright enough companions. Although HD 1160 B is bright enough that additional noise reduction techniques were not necessary to produce a detection of ample S/N, this may not be the case for fainter directly imaged companions in the exoplanet mass regime. However, it may be possible to use novel alternative algorithms to reach deeper contrasts.

For example, the Temporal Reference Analysis of Planets (TRAP; Samland et al. 2021, Liu et al., submitted) algorithm instead relies on temporal diversity. TRAP reconstructs the systematics in a given region in the data using reference pixels that share the same underlying noise sources. By simultaneously fitting the model of a companion signal 'transiting' over detector pixels and the light curves of the reference pixels, TRAP can then remove these systematics. It may be possible to leverage the information provided by TRAP to improve the companion S/N without removing the stellar PSF, or even to extract detrended light curves directly. Another option would be to use the gvAPP coronagraph, which is different from the dgvAPP360 in that it creates two images of the target star each with a 180° D-shaped dark hole on opposing sides, as well as an additional 'leakage term' positioned between the two (Snik et al. 2012; Otten et al. 2014b; Sutlieff et al. 2021). The leakage term is an entirely separate PSF of the star that appears at a fraction of its full brightness, making it ideal as a simultaneous photometric reference and enabling observations of systems with host stars that would otherwise be too bright. Post-processing algorithms can be applied to the main

PSFs to reach deeper contrasts without impacting the leakage term, enabling differential variability measurements provided that the impact of the algorithms on the photometry of the companion can be characterised precisely. However, the gvAPP coronagraph can suffer from wavelength-dependent smearing, which would make such measurements more complex than those obtained with a dgvAPP360 (Otten et al. 2017). In addition to the leakage term, some vAPPs (such as the VLT/ERIS gvAPP) produce other faint reference spots specifically for use as photometric references in situations where the core of the target star PSF is saturated (Doelman et al. 2021; Kravchenko et al. 2022).

In addition to probing the intrinsic variability of high-contrast companions, differential spectrophotometry could also be used to observe the transits of satellites such as exomoons or binary planets passing in front of these companions (e.g. Heller 2016; Lazzoni et al. 2022). Candidate satellites have been identified around transiting exoplanets, directly imaged companions, and isolated planetary-mass objects using a range of techniques, but none have yet been definitively detected (e.g. Teachey & Kipping 2018; Rodenbeck et al. 2018; Heller et al. 2019; Kreidberg et al. 2019; Lazzoni et al. 2020; Teachey et al. 2020; Limbach et al. 2021; Vanderburg & Rodriguez 2021; Kipping et al. 2022). For directly imaged companions, variability arising from transit events could be distinguished from that caused by inhomogeneous atmospheric features in similar ways to transiting exoplanets and star spots, by considering the companion light curves across the different wavelength channels. Transit signals are expected to be almost achromatic, while intrinsic variability is generally wavelength-dependent (Manjavacas et al. 2019b; Limbach et al. 2021, 2023; Lazzoni et al. 2022). Lazzoni et al. (2022) found using simulations that although the probability of successfully detecting smaller exomoons around a directly imaged companion is very low with current instrumentation and techniques, detections of larger binary planets are already within reach. New techniques to improve differential light curve precision for directly imaged companions, including differential spectrophotometry with the dgvAPP, will help to increase these probabilities further and potentially enable the first definitive detections of satellites around substellar companions.

3.8 Conclusions

We present a novel, ground-based approach for constructing differential light curves of high-contrast companions through direct differential spectrophotometric monitoring, using the double-grating 360° vector Apodizing Phase Plate coronagraph and the ALES integral field spectrograph. The dgvAPP360 allows high-contrast companions to be detected while also providing an image of the host star, which crucially can be used as a simultaneous photometric reference. We combine the dgvAPP360 with ALES to follow the highly successful technique of differential spectrophotometry used in exoplanet transmission spectroscopy, where light is spectrally-dispersed to reduce systematic effects that otherwise dominate the variability signal we aim to measure, and then recombined into white-light flux measurements.

We demonstrated this approach using a full night of observations of substellar companion HD 1160 B. The time-series fluxes of the companion and the star in each wavelength channel were extracted simultaneously using aperture photometry. We then produced white-light

measurements for both the companion and the star at each time frame by taking the median combination of the photometry in the wavelength dimension. The companion flux was then divided by that of the star to eliminate trends common to both, arising from Earth's atmosphere and other systematics, producing a differential white-light curve that only contains non-shared variations and covers a wavelength range of 3.59-3.99 µm. We find that the shape of the resulting light curve is robust against issues arising from instrumental flexure, as tested using calibration frames collected throughout the observation sequence. Using a multiple linear regression approach with eight decorrelation parameters, we modelled and removed non-shared trends from the differential white-light curve. We find that airmass and air temperature are the most correlated parameters with the light curve. We also analyse publicly available data from the TESS mission to check for variability in the host star HD 1160 A, and confirm that it is non-varying at the 0.03% level.

We find that the detrended differential white-light curve of HD 1160 B shows sinusoidal-like variability over a short timescale. By fitting the unbinned light curve with a sinusoid, we identify that the variability has a semi-amplitude of $\sim$8.8% and a period of $\sim$3.24 hours. When binned to 18 minutes of integration time per bin, we achieve a light curve precision at the 3.7% level. After thorough investigation and rejection of systematic noise sources, we attribute this variability as likely due to heterogeneous features in the atmosphere of the companion, rotating in and out of view as it rotates. We find that if the period of this variability reflects the rotation period of HD 1160 B, physical limitations suggest that it is rotating at close to its breakup period. Alternatively, the short period variability in the light curve of HD 1160 B may arise from multiple periodic features in its atmosphere with different phase offsets. Furthermore, light curves in the 30 individual wavelength channels in the 3.59-3.99 µm range show tentative evidence of an increase in variability amplitude at longer wavelengths. Further observations at additional epochs will help to confirm and characterise the variability of HD 1160 B and to determine its physical explanation.

The precision that we achieve in the detrended differential white-light curve is the greatest achieved from ground-based studies of sub-arcsecond high-contrast companions to date. However, direct comparisons to other ground-based studies that instead use satellite spots to search for variability in the light curves of high-contrast companions are not straightforward due to the different magnitude and contrast of the observed systems, with HD 1160 B having a more favourable contrast (Apai et al. 2016; Biller et al. 2021; Wang et al. 2022). The RMS of the detrended differential light curve for HD 1160 B as a function of bin size follows the same trend as the theoretical white noise expectation with no evidence of yet approaching a noise floor. This indicated that the single night of data analysed here is not yet systematic-limited, and that further observations from additional epochs could enable greater sensitivity to be reached. A deeper investigation of this type of data and its precision, including injection-recovery tests to test how effectively known variability signals can be recovered and which systematics have the greatest impact, is forthcoming (Sutlieff et al., in preparation, Chapter 5 of this thesis).

While JWST will measure the variability of fainter, lower mass companions from space with unprecedented precision, its comparatively smaller aperture means it cannot outperform the

largest AO-equipped ground-based telescopes at separations $\lesssim 0.5''$ at $\sim$3.5 µm (Girard et al. 2022), so companions such as Jupiter analogues at the closest angular separations, for all but the nearest stars, remain accessible only to ground-based monitoring techniques for the coming decade. Ground-based differential spectrophotometry with the vAPP is therefore highly complementary to space-based approaches for measuring the variability of high-contrast exoplanet and brown dwarf companions, and for searching for their transiting exomoons or binary planets. Moreover, ground-based telescopes can reach much higher spectral resolution, which then enables line profile variability studies to map atmospheric features, including storms and hurricanes like Jupiter's Great Red Spot, via Doppler imaging. These results are promising for further variability studies using vAPP coronagraphs on current and upcoming instruments and telescopes, which include ERIS on the VLT and METIS on the ELT.

Acknowledgements

The authors would like to thank Frank Backs and Elisabeth C. Matthews for valuable discussions that improved this work. We also thank our anonymous referee whose comments helped us to improve this manuscript. BJS is fully supported by the Netherlands Research School for Astronomy (NOVA). JLB acknowledges funding from the European Research Council (ERC) under the European Union's Horizon 2020 research and innovation program under grant agreement No 805445. This paper is based on work funded by the United States National Science Foundation (NSF) grants 1608834, 1614320, and 1614492. The research of DD and FS leading to these results has received funding from the European Research Council under ERC Starting Grant agreement 678194 (FALCONER).

We acknowledge the use of the Large Binocular Telescope Interferometer (LBTI) and the support from the LBTI team, specifically from Emily Mailhot, Jared Carlson, Jennifer Power, Phil Hinz, Michael Skrutskie, Travis Barman, Ilya Ilyin, and Ji Wang. The LBT is an international collaboration among institutions in the United States, Italy and Germany. LBT Corporation partners are: The University of Arizona on behalf of the Arizona Board of Regents; Istituto Nazionale di Astrofisica, Italy; LBT Beteiligungsgesellschaft, Germany, representing the Max-Planck Society, The Leibniz Institute for Astrophysics Potsdam, and Heidelberg University; The Ohio State University, representing OSU, University of Notre Dame, University of Minnesota and University of Virginia. We gratefully acknowledge the use of Native land for our observations. LBT observations were conducted on the stolen land of the Ndee/Nnēē, Chiricahua, Mescalero, and San Carlos Apache tribes.

This publication makes use of data products from the Two Micron All Sky Survey, which is a joint project of the University of Massachusetts and the Infrared Processing and Analysis Center/California Institute of Technology, funded by the National Aeronautics and Space Administration and the National Science Foundation. This work has made use of data from the European Space Agency (ESA) mission *Gaia* (https://www.cosmos.esa.int/gaia), processed by the *Gaia* Data Processing and Analysis Consortium (DPAC, https://www.cosmos.esa.int/web/gaia/dpac/consortium). Funding for the DPAC has been provided by national institutions, in particular the institutions participating in the *Gaia* Multilateral Agreement.

This paper includes data collected with the TESS mission, obtained from the Mikulski Archive for Space Telescopes (MAST) data archive at the Space Telescope Science Institute (STScI). Funding for the TESS mission is provided by the NASA Explorer Program. STScI is operated by the Association of Universities for Research in Astronomy, Inc., under NASA contract NAS 5–26555. Support for MAST for non-HST data is provided by the NASA Office of Space Science via grant NNX13AC07G and by other grants and contracts. This research has made use of the NASA Exoplanet Archive, which is operated by the California Institute of Technology, under contract with the National Aeronautics and Space Administration under the Exoplanet Exploration Program. This research has made use of NASA's Astrophysics Data System. This research has made use of the SIMBAD database, operated at CDS, Strasbourg, France (Wenger et al. 2000). This research made use of SAOImageDS9, a tool for data visualization supported by the Chandra X-ray Science Center (CXC) and the High Energy Astrophysics Science Archive Center (HEASARC) with support from the JWST Mission office at the Space Telescope Science Institute for 3D visualization (Joye & Mandel 2003). This work made use of the whereistheplanet[1] prediction tool (Wang et al. 2021a). This work makes use of the Python programming language[2], in particular packages including NumPy (Harris et al. 2020), Astropy (Astropy Collaboration et al. 2013, 2018), SciPy (Virtanen et al. 2020), HCIPy (Por et al. 2018), PynPoint (Amara & Quanz 2012; Stolker et al. 2019), scikit-image (van der Walt et al. 2014), scikit-learn (Pedregosa et al. 2011), statsmodels (Seabold & Perktold 2010), pandas (McKinney 2010; Reback et al. 2022), Photutils (Bradley et al. 2022), and Matplotlib (Hunter 2007).

Data Availability

The data from the LBT observations underlying this article are available in the Research Data Management Zenodo repository of the Anton Pannekoek Institute for Astronomy, at https://doi.org/10.5281/zenodo.5617572.

[1] http://whereistheplanet.com/
[2] Python Software Foundation; https://www.python.org/

Colour, the touchstone of reality. Colour to excite the mind.
The vivid, pulsating miracle that gives substance to shadow.
Public Service Broadcasting, ROYGBIV

Chapter 4

Exploring the directly imaged HD 1160 system through spectroscopic characterisation and high-cadence variability monitoring

Ben J. Sutlieff, Jayne L. Birkby, Jordan M. Stone, Frank Backs, Annelotte Derkink, David S. Doelman, Matthew A. Kenworthy, Alexander J. Bohn, Steve Ertel, Frans Snik, Charles E. Woodward, Ilya Ilyin, Andrew J. Skemer, Jarron M. Leisenring, Klaus G. Strassmeier, and David Charbonneau

To be submitted for publication in *Monthly Notices of the Royal Astronomical Society*

Abstract

The time variability and spectra of directly imaged companions provide insight into their physical properties and atmospheric dynamics. We present two nights of R∼40 spectrophotometric monitoring of substellar companion HD 1160 B at 2.8-4.2 µm using the double-grating 360° vector Apodizing Phase Plate (dgvAPP360) coronagraph and ALES integral field spectrograph on the Large Binocular Telescope Interferometer (LBTI). We use the recently developed technique of vAPP-enabled differential spectrophotometric monitoring to produce differential light curves for HD 1160 B. Although we recover the ∼3.2 h periodic variability seen previously on the first night, we do not detect periodic variability on the second night, potentially indicating rapid time evolution in the variability of HD 1160 B. We also extract complementary spectra of HD 1160 B for each night and find that the two are consistent at most wavelengths, but that the companion appears systematically fainter on the second night at 3.0-3.2 µm. Fitting atmospheric models to these spectra produces different values for physical properties depending on the night considered. We find an effective temperature $T_{eff} = 2804^{+152}_{-74}$ K on the first night, consistent with the literature, but a much cooler

$T_{\rm eff} = 2310^{+93}_{-82}$ K on the second night. We estimate the mass of HD 1160 B to be 16-81 $M_{\rm Jup}$, depending on the age of the system. We also present R = 50,000 high-resolution optical spectroscopy of host star HD 1160 A obtained simultaneously with the PEPSI spectrograph on the LBTI, with which we re-evaluate its spectral type to A1 IV-V and characterise its properties including a first estimate of its $v\sin i = 96^{+6}_{-4}$ km s^{-1}. We thus highlight that vAPP-enabled differential spectrophotometry can achieve a repeatable precision at the $\sim$4% level and does not currently reach a systematic noise floor, suggesting greater precision could be achieved with additional data or advanced detrending approaches such as Gaussian process regression.

Key words: infrared: planetary systems – instrumentation: high angular resolution – stars: individual: HD 1160 – planets and satellites: detection – brown dwarfs – planets and satellites: atmospheres

4.1 Introduction

With the aid of the latest advancements in adaptive optics and coronagraphic instrumentation, the technique of direct high-contrast imaging has uncovered numerous planetary-mass companions in wide orbits around their host stars (e.g. Marois et al. 2010b; Bailey et al. 2014a; Bowler et al. 2017; Keppler et al. 2018; Haffert et al. 2019; Bohn et al. 2020a,b, 2021; Currie et al. 2022c,b; Hinkley et al. 2022b). Furthermore, searches for such objects have also identified a population of higher mass substellar companions up to the brown dwarf/stellar boundary (e.g. Biller et al. 2010; Mawet et al. 2015; Konopacky et al. 2016; Milli et al. 2017; Rickman et al. 2020; Bonavita et al. 2022; Kuzuhara et al. 2022; Franson et al. 2023; Li et al. 2023). These brown dwarf companions are generally brighter than exoplanets and hence easier to observe, yet often appear to have similar properties to giant exoplanets, including effective temperatures, surface gravities, and weather (e.g. Dupuy & Kraus 2013; Faherty et al. 2013, 2016; Helling & Casewell 2014; Skemer et al. 2016a; Morley et al. 2018; Vos et al. 2019; Ashraf et al. 2022). Studies of brown dwarfs as exoplanet analogues may therefore also help us to understand the underlying processes in exoplanet atmospheres and to break degeneracies surrounding formation mechanisms.

While spectroscopic observations allow us to derive values for the physical parameters of brown dwarfs through comparisons of companion spectra to atmospheric models, high-cadence variability monitoring provides insight into the dynamics and structure of atmospheric features such as clouds and storms (e.g. Kostov & Apai 2013; Crossfield et al. 2014; Karalidi et al. 2016; Manjavacas et al. 2019a, 2021, 2022; Vos et al. 2022, 2023). Variability has now been detected in the light curves of numerous planetary-mass and brown dwarf companions using observations obtained with space-based telescopes (e.g. Zhou et al. 2016, 2020b, 2022; Miles-Páez et al. 2019; Miles-Páez 2021; Bowler et al. 2020b; Lew et al. 2020b). However, obtaining similar measurements using ground-based telescopes, which have the large diameters needed to resolve companions at close angular separations, has proven more challenging. Non-astrophysical variability induced by turbulence in Earth's atmosphere overwhelms any variability signal from the atmosphere of a faint companion. While the companion's host star would be an ideal photometric reference with which to divide out these systematics and recover its intrinsic variability, this is often obscured by the focal-plane coronagraphs used by most coronagraphic imagers (e.g. Ruane et al. 2018). Nonetheless, ground-based variability studies with coronagraphic imagers have been shown to be possible using satellite spots as photometric references for the companion light curve, with which upper limits for variability have been found for the exoplanets orbiting HR 8799 (Apai et al. 2016; Biller et al. 2021; Wang et al. 2022).

Another, more recently developed approach for exploring the variability of high-contrast companions from the ground is that of differential spectrophotometry used in combination with a vector Apodizing Phase Plate (vAPP) coronagraph (Sutlieff et al. 2023). Unlike focal-plane coronagraphs, vAPP coronagraphs enable observations of high-contrast companions at close separations while maintaining a Point Spread Function (PSF) of the target star that can be used as a simultaneous photometric reference (Snik et al. 2012; Otten et al. 2014a; Doelman et al. 2021; Sutlieff et al. 2021). To obtain differential spectrophotometry, a vAPP

can be combined with an integral field spectrograph (IFS) to spectrally disperse the light from the target. The spectra can then be recombined into white-light, reducing the impact of systematic errors in any single wavelength channel and therefore producing light curves with higher precision (Sutlieff et al. 2023). The light curve of the companion is then divided by the light curve of the photometric reference (in this case the host star) to remove systematic variability trends shared by both objects. This concept was also used for the satellite spot study of Wang et al. (2022), and is commonplace in the field of exoplanet transmission spectroscopy (Diamond-Lowe et al. 2018, 2020a, 2022; Todorov et al. 2019; Arcangeli et al. 2021; Panwar et al. 2022b,a). To demonstrate this technique, Sutlieff et al. (2023) observed HD 1160 B, a companion with a peculiar spectrum at the brown dwarf/stellar boundary, for one night with the double-grating 360° vector Apodizing Phase Plate (dgvAPP360, Doelman et al. 2017, 2020, 2021) coronagraph combined with the Arizona Lenslets for Exoplanet Spectroscopy (ALES) integral field spectrograph (IFS) on the Large Binocular Telescope. They detected significant sinusoidal variability in the differential white-light curve of this companion with a semi-amplitude of 8.8% and a period of ∼3.24 hours. Furthermore, they obtained a 3.7% precision in bins of 18 minutes, after a multiple linear regression approach was applied to the differential white-light curve to remove residual systematics arising from non-astrophysical sources such as airmass and detector position. This study found no evidence of having reached a systematic noise floor in their single epoch of observations, indicating that the data was not systematic-limited and that additional data could further improve the sensitivity to variability.

In this work, we further characterize HD 1160 B and its host star HD 1160 A using additional observations obtained with the Large Binocular Telescope (LBT). In addition to a further epoch of variability monitoring of HD 1160 B with ALES+dgvAPP360, we also conduct a complementary spectral characterisation of HD 1160 B using the 2.8-4.2 µm spectra from both epochs and separately of HD 1160 A using data obtained simultaneously with the PEPSI high resolution spectrograph. The differential spectrophotometry observations with ALES+dgvAPP360 also allow us to test the repeatability of the light curve precision achieved by Sutlieff et al. (2023) in their pilot study. In Section 4.2, we review the properties of the HD 1160 system. Our observations of this system are then described in Section 4.3, and in Section 4.4 we describe the methods used to reduce the data from each instrument and extract photometry of the targets. In Section 4.5, we investigate the variability of HD 1160 B by using the ALES+dgvAPP360 data to produce differential spectrophotometric light curves. We also use this data in Section 4.6 to produce and study the spectrum of HD 1160 B. The data obtained with PEPSI is analysed in Section 4.7, in which we explore the spectrum of HD 1160 A. The results found in each of these three sections are then discussed in Section 4.8. Finally, we summarise the conclusions of the paper in Section 4.9.

4.2 Target Properties

The HD 1160 system is located at a distance of 120.7±0.5 pc (Gaia Data Release 3, Gaia Collaboration et al. 2016, 2022). In Table 4.1, we summarize literature values for key properties of the stellar primary component HD 1160 A, for which Houk & Swift (1999) assigned

a spectral type of A0 V using photographic plates on the 0.61-m Curtis Schmidt telescope at the Cerro Tololo Inter-American Observatory (CTIO). Using observations from the Transiting Exoplanet Survey Satellite (TESS) mission, Sutlieff et al. (2023) found that HD 1160 A is non-variable at the 0.03% level, and Spitzer observations by Su et al. (2006) found no infrared excess, suggesting that there is not significant circumstellar dust present. Nielsen et al. (2012) identified two comoving companions to HD 1160 A at separations of ∼80 au (∼0.78″) and ∼530 au (∼5.15″), known as HD 1160 B and C, respectively, during the Gemini Near-Infrared Coronagraphic Imager (NICI) Planet-Finding Campaign (Liu et al. 2010). HD 1160 B has a contrast of $\Delta L' = 6.35 \pm 0.12$ mag relative to the $L' = 7.055 \pm 0.014$ mag of HD 1160 A, and its orbit is almost edge-on, with an inclination angle of $92^{+8.7}_{-9.3}$° (Leggett et al. 2003b; Nielsen et al. 2012; Bowler et al. 2020a). The wide angular separation of HD 1160 C places it beyond the fields of view of the data sets in this paper.

Nielsen et al. (2012) found HD 1160 B to be a L0±2 brown dwarf based on their near-infrared photometry, and that their near-infrared spectrum of HD 1160 C best matches that of an M3.5±0.5 low-mass star. They found that both companions are redder than similar objects, which combined with an apparent underluminosity of HD 1160 A suggests a young age of 50^{+50}_{-40} Myr. Combining this age range with the luminosity of HD 1160 B, they derived a value for its mass of 33^{+12}_{-9} M_{Jup}.

Using observations from the Spectro-Polarimetric High-contrast imager for Exoplanets REsearch (SPHERE, Beuzit et al. 2019) instrument on the Very Large Telescope (VLT), Maire et al. (2016) concluded that the 1.0-1.6 µm spectrum of HD 1160 B best matched that of a M6.0$^{+1.0}_{-0.5}$ dwarf. Unlike Nielsen et al. (2012), they did not find unusually red colours for either companion. They also found higher estimates for its mass; 79^{+65}_{-40} M_{Jup} based on its luminosity and 107^{+59}_{-38} M_{Jup} based on its effective temperature. The wide range of possible masses is driven by the uncertain age used, 100^{+200}_{-70}, which was chosen due to the lack of reliable age indicators with the upper limit given by the 300 Myr predicted main-sequence lifetime of an A0 star (Siess et al. 2000).

Garcia et al. (2017) also observed the HD 1160 system, using the Subaru Coronagraphic Extreme Adaptive Optics (SCExAO Jovanovic et al. 2015b) instrument and the Gemini Planet Imager (GPI, Macintosh et al. 2014). They too found that HD 1160 B has typical colours for a mid-M dwarf and assign it a spectral type of M5.5$^{+1.0}_{-0.5}$, in good agreement with Maire et al. (2016), and rule out earlier spectral types. Considering a range of different evolutionary models, they report two different possible system ages; 20-125 Myr if HD 1160 A is considered alone, and 80-125 Myr if HD 1160 A, B, and C are considered jointly. These lead to mass values for HD 1160 B of 35-90 M_{Jup} and 70-90 M_{Jup}, respectively. However, they note that the derived mass of HD 1160 B is highly dependent on its surface gravity and age. Garcia et al. (2017) further found that HD 1160 B likely has approximately solar metallicity, which is consistent with almost all systems in the solar neighbourhood (e.g. Dias et al. 2002).

Based on its Gaia kinematics, Curtis et al. (2019) found that the HD 1160 system could be part of the Pisces-Eridanus stellar stream, indicating an age on the order of ∼120-135 Myr if this were to be confirmed (Meingast et al. 2019; Röser & Schilbach 2020).

The most recent spectral characterisation of HD 1160 B was carried out by Mesa et al. (2020), who again observed the system with SPHERE and found it to have a peculiar spectrum that is not well matched by any spectra in current spectral libraries, but concluded a spectral type of M5-M7 based on the best fits to individual spectral bands. They propose that this peculiarity could be explained by the presence of dust in its photosphere, or if it has a young age and is not yet fully evolved. By fitting the spectrum of HD 1160 B with atmospheric models and considering alkali lines that become weaker at lower surface gravities, Mesa et al. (2020) found a low surface gravity of log(g) = 3.5-4.0 dex. This suggests that HD 1160 B may actually have a low age of 10-20 Myr, and a mass of $\sim$20 M_{Jup}, in contrast to previous results. However, they noted that they cannot rule out older ages.

While the studies above explored the spectrum of HD 1160 B, it was also the target of a variability monitoring search by Sutlieff et al. (2023). As described in Section 4.1, they found 8.8% semi-amplitude variability with a period of $\sim$3.24 hours in the differential white-light curve of HD 1160 B during a pilot study combining the technique of differential spectrophotometry with the dgvAPP360 coronagraph. They attribute this variability to heterogeneous features in the atmosphere of the companion, such as clouds or cool star spots, but conclude that additional data is needed to confirm its periodicity and establish its physical explanation.

4.3 Observations

We observed the HD 1160 system on the nights of 2020 September 25 (03:27:31 - 11:16:14 UT) and 2020 September 26 (03:20:16 - 10:46:09 UT) using the 2 x 8.4-m Large Binocular Telescope (LBT) at the Mount Graham International Observatory, Arizona. On the left-hand side aperture of the LBT, we used the dgvAPP360 coronagraph (see Section 4.1) in combination with the Arizona Lenslets for Exoplanet Spectroscopy (ALES) IFS (Skemer et al. 2015; Hinz et al. 2018; Stone et al. 2018). ALES is located in the focal plane of the LBT mid-infrared camera (LMIRcam, Wilson et al. 2008; Skrutskie et al. 2010; Leisenring et al. 2012) and mounted inside the LBT Interferometer (LBTI, Defrère et al. 2015; Hinz et al. 2016; Ertel et al. 2020), which uses the LBTI adaptive optics (AO) system to provide a Strehl ratio up to 90% at 4 µm (Hinz et al. 2012; Bailey et al. 2014b; Pinna et al. 2016, 2021). These observations were obtained using the ALES L-band prism, providing R$\sim$40 spectroscopy over a 2.8-4.2 µm wavelength range simultaneously, with a 2.2″x 2.2″ field of view and plate scale of $\sim$35 mas spaxel^{-1} (Skemer et al. 2018).

The first night of these LBT/ALES+dgvAPP360 observations has previously been described in Sutlieff et al. (2023). On the second night, we obtained 2000 ALES frames with 5.4 s of integration time per frame, ensuring that the stellar PSF remained unsaturated in each frame. The total time on-target was therefore 10800 s or 3 h (compared to $\sim$3.32 h on the first night, Sutlieff et al. 2023). However, this on-target integration time is spread out over $\sim$7.43 h due to time spent on nodding, wavelength calibrations, and readout time. When we combine both nights of data, the total on-target integration time is 22734 s (6.32 h) over a timescale of 112718 s ($\sim$31.31 h, $\sim$1.30 days). To enable background subtraction, we used

Table 4.1: Literature properties of host star HD 1160 A.

Property	Value	Ref.
Right Acension (J2000, hh:mm:ss.ss)	00:15:57.32	(1)
Declination (J2000, dd:mm:ss.ss)	+04:15:03.77	(1)
RA proper motion (mas yr^{-1})	20.150±0.040	(1)
Dec. proper motion (mas yr^{-1})	-14.903±0.034	(1)
Parallax (mas)	8.2721±0.0355	(1)
Radial velocity (km s^{-1})	13.5±0.5	(1)
Distance (pc)	120.7±0.5	(1)
Extinction A_V (mag)	0.16	(1)
Spectral Type	A0 V	(2)
	A1 IV-V	(3)
Mass ($M_\odot$)	∼2.2	(4)
T_{eff} (K)	9011±85	(5)
	9200^{+200}_{-100}	(3)
log(g) (dex)	∼4.5	(6)
	$3.5^{+0.5}_{-0.3}$	(3)
$v\sin i$ (km s^{-1})	96^{+6}_{-4}	(3)
log($L/L_\odot$)	1.12±0.07	(5)
[Fe/H]	∼solar	(6)
V (mag)	7.119±0.010	(7)
G (mag)	7.1248±0.0004	(1)
J (mag)	6.983±0.020	(8)
H (mag)	7.013±0.023	(8)
K (mag)	7.040±0.029	(8)
L′ (mag)	7.055±0.014	(9)
M′ (mag)	7.04±0.02	(9)
System age (Myr)	50^{+50}_{-40}	(4)
	100^{+200}_{-70}	(10)
	20-125	(5)
	∼120	(11)
	10-20	(6)

References: (1) Gaia Collaboration et al. (2016, 2022); (2) Houk & Swift (1999); (3) This work; (4) Nielsen et al. (2012); (5) Garcia et al. (2017); (6) Mesa et al. (2020); (7) Tycho-2 (Høg et al. 2000b,a); (8) 2MASS (Cutri et al. 2003; Skrutskie et al. 2006); (9) Leggett et al. (2003b); (10) Maire et al. (2016); (11) Curtis et al. (2019)

an on/off nodding pattern, switching position every 10 min except when interrupted by an open AO loop or to take wavelength calibrations. We also obtained 6 wavelength calibrations at irregular intervals throughout the night, and dark frames at the end of the night with the same exposure time as the science and calibration frames. At a separation of $\sim$0.78″, HD 1160 B remained in the coronagraphic dark hole of the dgvAPP360 at all wavelengths throughout the observations, while HD 1160 C was beyond the 2.2″$\times$ 2.2″ field of view of ALES at $\sim$5.1″.

On the right-hand side LBT aperture, we used the Potsdam Echelle Polarimetric and Spectroscopic Instrument (PEPSI), a fiber-fed white-pupil echelle spectrograph (Strassmeier et al. 2015, 2018c). We obtained high resolution (R = 50,000) optical spectra using the 300 µm diameter PEPSI fiber, which operates over a wavelength range of 383-907nm. This fiber has a diameter of 2.25″ which encompasses the angular separation of HD 1160 B from HD 1160 A ($\sim$0.78″), so the obtained PEPSI spectra are combined spectra of both objects. HD 1160 C was located outside of the fiber at a separation of $\sim$5.1″. Data were obtained with the first three and the sixth PEPSI cross dispersers (CDs), which cover wavelength ranges of 383.7-426.5 nm, 426.5-480.0 nm, 480.0-544.1 nm, and 741.9-906.7 nm, respectively, but not with the fourth and fifth CDs. We observed using two CDs at any given time; the sixth CD was always in use, and was paired with one of the other three on a rotating cycle. The total on-target integration times obtained with each CD were 14713 seconds, 14761 seconds, 14666 seconds, and 44723 seconds for CDs 1, 2, 3, and 6, respectively.

No time was lost to weather and the observing conditions were stable with no cloud cover. The seeing ranged from 0.7-1.5″. As LBTI does not use an instrument derotator, all data were obtained in pupil-stabilized mode such that the companion rotated in the field of view. The total field rotation over the course of the night was 108.2°. This is comparable to the 109.7° of field rotation on the first night, on which the observing conditions were similarly clear with a seeing of 0.7-1.4″ (Sutlieff et al. 2023).

4.4 Data reduction and spectral extraction

4.4.1 LBT/ALES+dgvAPP360 data processing

Our goal is to use the LBT/ALES+dgvAPP360 observations to characterise HD 1160 B by measuring both its spectrum and its time variability. We therefore need to make a flux-calibrated spectrum of the companion by summing the observations in the time dimension, and a 'white-light' curve of the companion by summing the observations in the wavelength dimension.

Several data processing steps are required to convert the raw ALES data from 2D grids of micro-spectra on the detector into 3D image cubes of x,y-position and wavelength and prepare them for our analyses (Briesemeister et al. 2019; Doelman et al. 2022; Stone et al. 2022). The data from the first night of LBT/ALES+dgvAPP360 observations was previously processed (for a time variability study only) in Sutlieff et al. (2023). We reprocessed this first night of data here following the same method as Sutlieff et al. (2023), and also used

this approach for the data from the second night to ensure consistency between the two epochs. We briefly summarise the steps in this process here. We first used the sky frames from the off-source nod position to subtract the background in each frame, before extracting the micro-spectra into 3D cubes through weighted optimal extraction, where the extraction weights were defined by the wavelength-averaged spatial profiles of the micro-spectra in the sky frames (Horne 1986; Briesemeister et al. 2018; Stone et al. 2020). Next, the data were wavelength calibrated using four narrow-band filters operating upstream of the ALES optics. Each of these filters produced a single-wavelength spot on the LMIRcam detector. We performed the wavelength calibration for the 63×67 micro-spectra in the ALES grid by fitting the positions of these four spots with a second-order polynomial to derive the necessary wavelength solution (Stone et al. 2018, 2022). This process produced 3D wavelength-calibrated data cubes of x- and y-position, and wavelength λ, with 100 wavelength channels spanning the 2.8-4.2 µm wavelength range of ALES.

Continuing to follow the data reduction method of Sutlieff et al. (2023), we removed 8 frames from the first night that were unsuitable as the AO loop opened during the exposure. No frames were removed from the dataset from the second night. We then performed a bad pixel correction for each frame and applied a flat-field correction using a flat frame created from images obtained in the off-source nod position. ALES images also contain systematic time-varying row and column discontinuities caused by the intersection of the ALES micro-spectra with the channels of the LMIRcam detector (Doelman et al. 2022). To correct for the column discontinuities, we first masked HD 1160 A and B in each frame before fitting third-order polynomials to each column. These values were then subtracted and the process was repeated for each row to remove the row discontinuities. The frames were then shifted using a spline interpolation to centre the star in each frame and derotated using their parallactic angles to align them to north. A final image from the second night, obtained by median-combining every frame in the 3.59-3.99 µm range in both time and wavelength, is shown in the top panel of Figure 4.1. Both HD 1160 A and B are clearly visible.

As the data were obtained in pupil-stabilized mode, we could have applied post-processing algorithms reliant on angular diversity (e.g. Angular Differential Imaging, Marois et al. 2006a) to further remove quasistatic speckle noise and increase the S/N of the targets. However, we chose not to do this so that we could make use of the stellar PSF provided by the dg-vAPP360 as a simultaneous photometric reference when characterising the variability of HD 1160 B in Section 4.5. If we had applied an ADI-based algorithm the stellar PSF would have been removed, meaning there would be no photometric reference with which to divide out time-varying systematics from the companion flux.

4.4.1.1 Photometric extraction

Once the data had been fully processed to correct for the systematic discontinuities we extracted simultaneous aperture photometry of HD 1160 A and B, again following the approach of Sutlieff et al. (2023). Although some of the 100 ALES wavelength channels are not suitable for analysis (see Sections 4.5.1 and 4.6.1), we nonetheless performed this step for

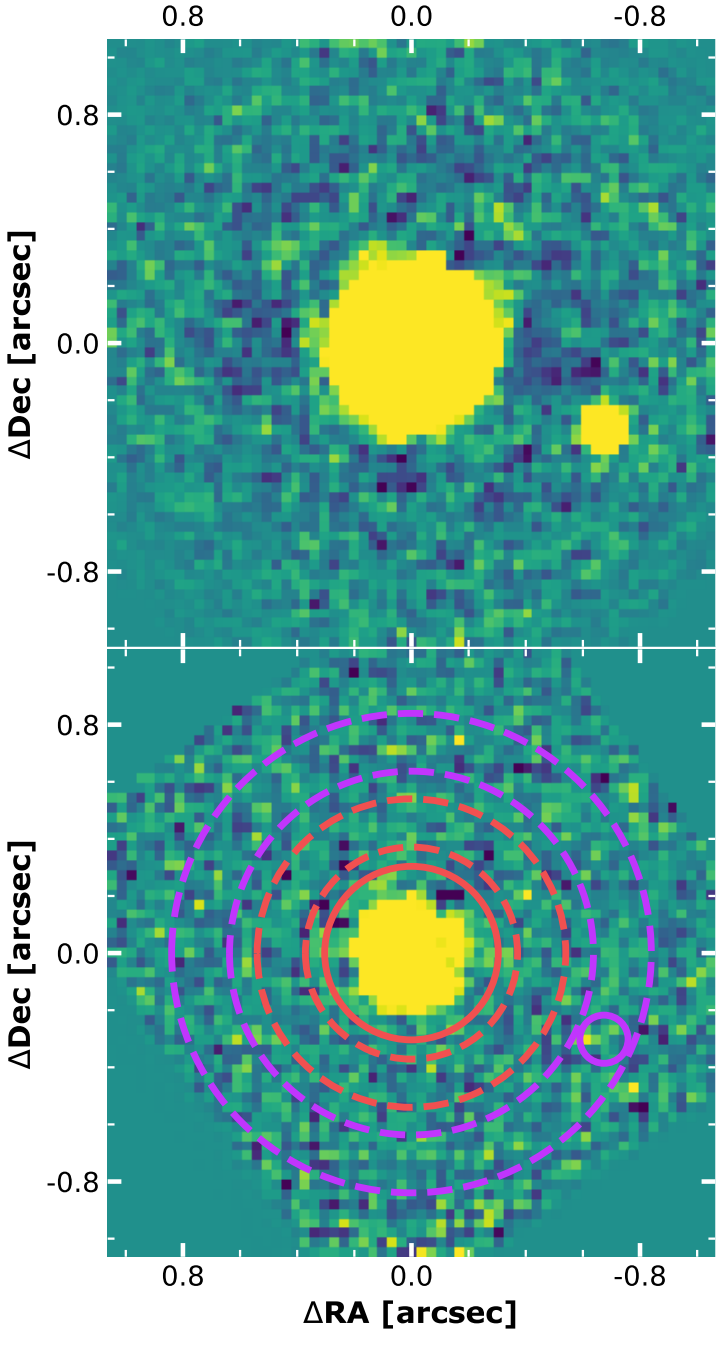

Figure 4.1: Top panel: the final LBT/ALES+dgvAPP360 image of the HD 1160 system from the second night, produced by taking the median combination of all frames in the 3.59-3.99 µm range over both time and wavelength. This image covers a total integration time of 10800 s (3 h). Bottom panel: A single frame of data from the 3.69 µm wavelength channel, overplotted with the apertures and annuli used to obtain flux and background measurements for the host star HD 1160 A (in orange) and companion HD 1160 B. Each image uses a different arbitrary logarithmic colour scale, and both are north-aligned, where north is up and east is to the left.

every frame in each of the 100 channels to allow a selection to be carried out at a later stage in the process. To do this, we extracted photometry in circular apertures with radii of 9 pixels (3.1 λ/D) for HD 1160 A and 2.5 pixels (0.9 λ/D) for HD 1160 B. The background flux was near zero following the removal of the row and column discontinuities in the previous section. However, we nonetheless estimated the residual background at the locations of the star and companion such that we could correct our flux measurements for any remaining offset. The background flux at the location of HD 1160 A was estimated by extracting photometry in a circular annulus with inner and outer radii of 11 and 16 pixels, respectively. The drift of the star combined with the rotation of the field over the course of the night means that HD 1160 B was close to the edge of the field of view in some frames, meaning that we could not use a similar annulus to estimate the background at its location. Instead, we did this by masking HD 1160 B and then extracting photometry in another annulus centred on the star, this time with a 6-pixel width around the radial separation of HD 1160 B (Biller et al. 2021; Sutlieff et al. 2023). We show these apertures and annuli overplotted on a single frame of data in the bottom panel of Figure 4.1. We then corrected our aperture photometry of the star and companion by subtracting the mean counts per pixel in the corresponding annulus multiplied by the area of the respective aperture.

This extracted spectrophotometry of HD 1160 A and B is used to investigate the time variability of HD 1160 B in Section 4.5 and its spectrum in Section 4.6.

4.4.2 PEPSI data processing

In this paper we aim to use the LBT/PEPSI observations to characterise the physical properties of host star HD 1160 A. The PEPSI data were reduced using the Spectroscopic Data Systems for PEPSI (SDS4PEPSI) generic package written in C++ under Linux and based on the 4A package for processing data from the SOFIN spectrograph on the Nordic Optical Telescope (Ilyin 2000; Strassmeier et al. 2018a,b; Keles et al. 2022). SDS4PEPSI applied a fully automated set of standardised data reduction steps to the raw data, including CCD bias removal, photon noise estimation, flat-field correction, and scattered light subtraction. It then performed a weighted optimal extraction of the spectral orders to maximise the S/N of the target, and wavelength calibration. The spectra were then normalised to the continuum by fitting the extracted spectral orders with a 2D smoothing spline on a regular grid of CCD pixels and echelle order numbers, and then shifted to the stellar rest frame. Each of these steps carried out by SDS4PEPSI is described in full detail in Strassmeier et al. (2018a). Finally, we combined the spectra from all of the exposures obtained with a given CD by interpolating them to the same wavelengths and summing them according to their weights.

4.5 Analysing the variability of HD 1160 B

In this section we use the aperture photometry of HD 1160 A and B obtained in Section 4.4.1.1 to explore the time variability of HD 1160 B via the technique of differential spectrophotometry. This method applied using the dgvAPP360 coronagraph was first described by Sutlieff et al. (2023). While we are interested in the intrinsic variability arising from the atmosphere

of the companion, the raw flux that we obtained through aperture photometry is inherently polluted by additional variability caused by Earth's atmosphere and systematics originating from the instrumentation. This unwanted variability can be mitigated using an independent, simultaneous photometric reference, but this is generally problematic for ground-based variability studies of high-contrast companions, as field stars are rarely available and focal-plane coronagraphs block the host star in order to allow companions to be detected (e.g. Mawet et al. 2012; Ruane et al. 2018). The dgvAPP360 coronagraph uniquely enables host stars and their companions to be imaged simultaneously, thus we can use the simultaneous aperture photometry of HD 1160 A as a photometric reference to remove variability arising from non-astrophysical sources external to HD 1160 B (Doelman et al. 2020, 2021; Sutlieff et al. 2023). As Sutlieff et al. (2023) previously found no evidence for variability in HD 1160 A above the 0.03% level in Transiting Exoplanet Survey Satellite (TESS) observations over a 51 day baseline, we proceed with the assumption that HD 1160 A does not have intrinsic variations of its own.

4.5.1 ALES wavelength channel selection

The first step in the process of making a differential white-light curve for HD 1160 was to select which wavelength channels should be included. A benefit of the spectrophotometric approach is that channels with low target S/N or issues that could introduce false variability signals can be excluded, allowing the light curve precision to be maximised. Our data cubes consist of 100 wavelength channels ranging from 2.8-4.2 µm. However, wavelength channels at the start and end of this range are unsuitable for analysis as the photometry is contaminated by flux from the neighbouring spaxel in the dispersion direction, and those in the ∼3.25-3.5 µm wavelength range are significantly impacted by absorption caused by the glue molecules in the dgvAPP360 (Otten et al. 2017; Doelman et al. 2021, 2022). Sutlieff et al. (2023) selected the 30 wavelength channels in the 3.59-3.99 µm range that had a high target S/N for inclusion in their time variability analysis of the first night of data. We therefore chose to use these same channels for our analysis in this paper such that we could directly compare the light curves from each night of data.

4.5.2 Differential spectrophotometric light curves

We produced our differential white-light curve of HD 1160 B following the technique presented by Sutlieff et al. (2023), using HD 1160 A as a simultaneous photometric reference. First, we separately prepared white-light time series for HD 1160 A and HD 1160 B. We did this by taking the median combination of the photometry for each object over the 30 wavelength channels chosen in the previous section, thereby obtaining a single white-light measurement for each object at each time. These are shown in grey in the top two rows of Figure 4.2, and binned to 18 minutes of integration time per bin in blue and yellow for the host star and companion, respectively. The time series shown here are plotted on the same axes and were normalised over the full sequence, including both epochs, to allow comparison between each night. Aside from the change in the normalisation, the data points

on the first night are identical to those in Sutlieff et al. (2023). The gaps in integration time in the unbinned data are due to the on/off nodding pattern used when observing. To produce a differential white-light curve, we then divided the unbinned, unnormalised flux of HD 1160 B by that of HD 1160 A. This raw differential light curve is plotted unbinned in grey, and binned in purple, in the third row of Figure 4.2. We also plot a closer view of the same binned light curve in the fourth row. We calculated the errors on the binned fluxes by taking the 1.48 $\times$ median absolute deviation (MAD) of the fluxes in each time bin, then dividing these values by $\sqrt{N-1}$, where N is the number of frames per bin. Dividing the two time series in this way has the effect of removing most of the variability due to shared systematics arising from the instrumentation or telluric effects. HD 1160 A is known to be non-varying to at least the 0.03% level (Sutlieff et al. 2023), so remaining variability trends in this differential light curve are therefore only those arising from HD 1160 B itself and from any contaminating systematics that are not shared by the star and the companion.

4.5.3 Detrending

In this section we attempt to fit and remove several residual (i.e. non-shared) systematic trends from the differential light curve, with the aim of producing a detrended differential light curve containing only the intrinsic variability of HD 1160 B. These residual systematics are likely due to differences in brightness, colour, or position of the companion and host star, and can arise from both instrumental and telluric sources (e.g. Broeg et al. 2005; Pont et al. 2006; Gibson et al. 2012; de Mooij et al. 2013; Diamond-Lowe et al. 2018; Panwar et al. 2022b,a). Here, we applied a multiple linear regression including six different possible sources of systematics as decorrelation parameters. These parameters are shown plotted against time in hours after midnight, for each epoch, in Figure 4.3. Sutlieff et al. (2023) found that airmass and external air temperature were the most parameters that were the most correlated with the differential light curve from the first night alone, so we chose to include both of these again here. We also again included the x- and y- pixel positions of HD 1160 A and B in the original images, before centering and rotational alignment were carried out. These parameters probe any remaining systematics arising from the response of the detector or other instrumental effects. The sharp jumps in position seen in Figure 4.3 arise from manual positional offsets performed during the observing sequence to ensure star did not drift too far from the centre of the small field of view. We further considered including wind speed and wind direction, but Sutlieff et al. (2023) found that wind speed and wind direction were not significantly correlated with the trends in the light curve from the first night. We found that this was also the case for the second night, so chose not include these as parameters in the linear regression here.

We used a multiple linear regression to simultaneously fit these six decorrelation parameters to the differential white-light curve of HD 1160 B. This process was carried out for the light curve on each night separately, in case the systematics induce different trends on each night. The resulting model fits are shown in dark green in the top panels of Figure 4.4, overplotted on the raw differential white-light curves (in grey). The corresponding coefficients and intercept of these two models are given in Table 4.2. We detrended the two differential white-

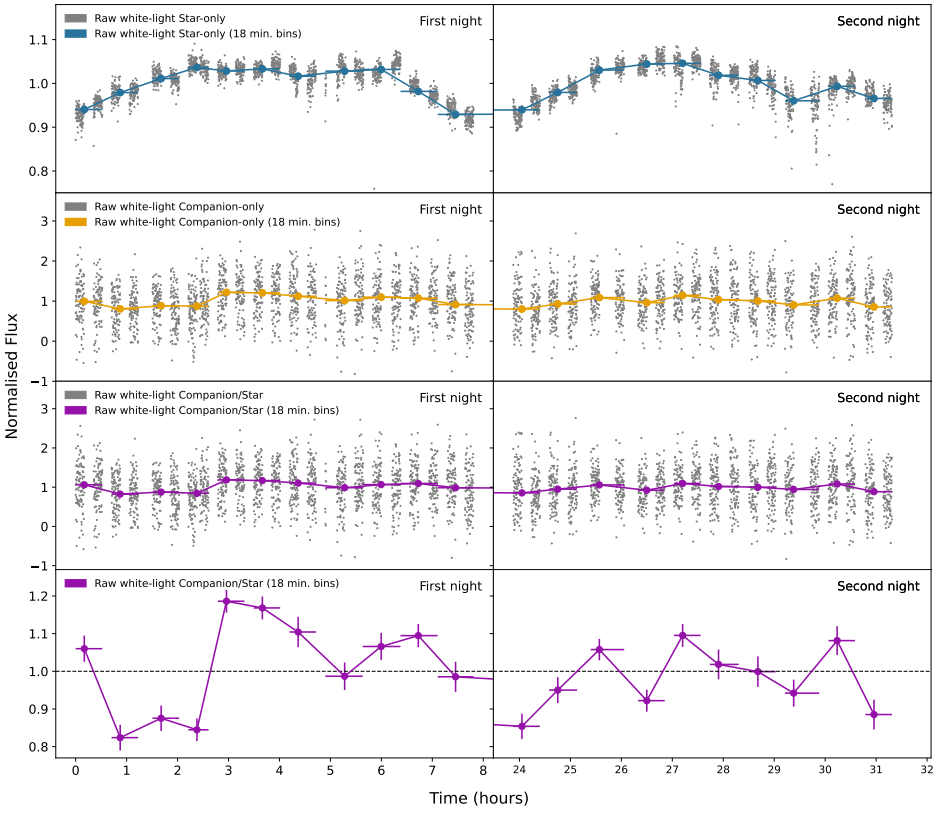

Figure 4.2: Top two rows: the raw white-light fluxes of host star HD 1160 A and companion HD 1160 B from both nights are plotted in grey, and binned to 18 minutes of integration time per bin in blue and yellow, respectively. The time series were normalised over the full time series covering both epochs, and consist of the data in the 3.59-3.99 µm wavelength range. The data from the first night is reproduced from Sutlieff et al. (2023), but the normalisation is different here. Bottom two rows: the raw differential white-light curve obtained by dividing the unnormalised, unbinned companion flux by that of the star, shown unbinned in grey and binned in purple. The bottom row shows a zoomed-in view of the binned version. This division removes variability shared by both the star and the companion from the companion flux, leaving a differential light-curve containing only variability arising from the companion's atmosphere and non-shared systematics.

Table 4.2: The decorrelation parameters x_i included in the linear regression used to detrend the differential white-light curve of HD 1160 B at each epoch. The resulting linear model fit was given by $y = (\sum_{i=1}^{n} c_i x_i) + c_0$, where c_0 is the intercept and c_i are the coefficients of each parameter. The parameters are ordered by the magnitude of the corresponding coefficients on the first night.

Parameter (x_i)	Value, 1st night (c_i)	Value, 2nd night (c_i)
Airmass	0.34590456	-0.46758893
Air temperature	0.11689032	-0.12725877
Star x-position	0.04596314	-0.08979261
Star y-position	-0.04426898	0.02947633
Companion x-position	-0.02499303	0.00674422
Companion y-position	0.01966123	-0.01849457
Intercept (c_0)	-1.23206397	5.45860550

light curves by dividing by these linear regression models, respectively. The final detrended differential white-light curves are plotted in the bottom panels of Figure 4.4, alongside the raw differential white-light curves for comparison (in light purple, reproduced from the bottom panel of Figure 4.2).

4.5.4 Period analysis and light curve precision

Sutlieff et al. (2023) identified sinusoidal-like variability in the first night of the detrended differential white-light curve of HD 1160 B and produced a periodogram to search for periodicity. They then fit a sinusoid to the light curve and measured the period of this variability as 3.239 hours. This trend is still present in the first night of our new light curve (Figure 4.4). However, while some individual data points appear to deviate from a flat line, it is not visually clear whether or not the detrended differential white-light curve from the second night is also variable. The maximum normalised flux is 1.07, but the RMS of the light curve is 0.035. We therefore carried out a similar analysis to Sutlieff et al. (2023) to search for periodic variability using periodograms.

We produced periodograms for the unbinned detrended differential white-light curve using the Lomb-Scargle algorithm (Lomb 1976; Scargle 1982). These are shown in Figure 4.5; the top panel was produced using both nights combined, while the centre and bottom panels show the periodograms produced using only the data from the first and second nights, respectively. Each of these power spectra has been normalised by dividing them by the variance of the data points in the light curve (Horne & Baliunas 1986). The blue dashed line is the power threshold that corresponds to a false-alarm probability of 0.1 (i.e. 10%), and the horizontal brown dotted line on the periodogram for the first night is the power threshold for a false-alarm probability of 0.01 (i.e. 1%).

We find that the strongest peak in the periodogram of the first night is at approximately the same period as Sutlieff et al. (2023), with a period of 3.227 hours, peak power of 14.67,

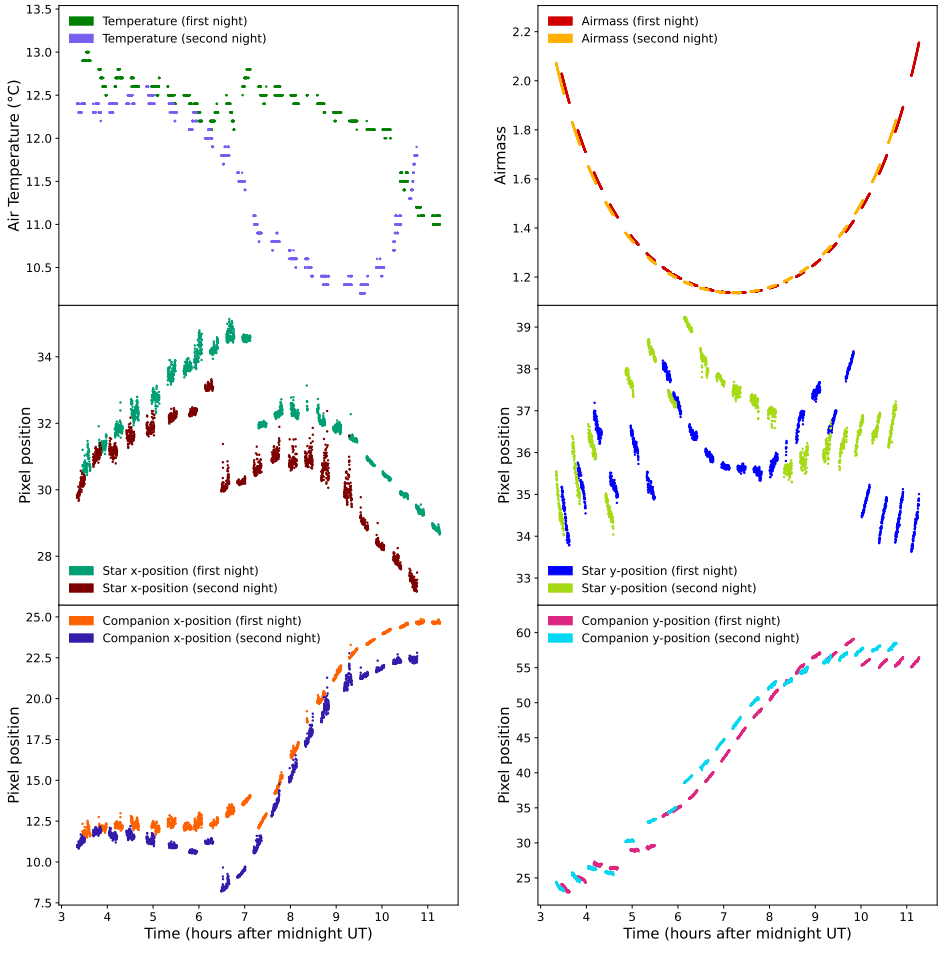

Figure 4.3: The six decorrelation parameters used in the linear regression to detrend the differential white-light curve of HD 1160 B, shown for both nights. To allow the trends at each epoch to be overplotted and compared, 24 hours has been removed from the x-axis for the second night. As with the time series photometry, the gaps in the data arise from the use of the on/off nodding pattern. The top two panels show the air temperature in and the airmass as a function of time. The remaining four panels show the x- and y-positions (in pixels) of host star HD 1160 A and companion HD 1160 B in the original 3D image cubes (i.e. before spatial and rotational alignment) as a function of time. The large jumps in these positions were caused by manual offsets applied to maintain the central location of HD 1160 A within the small field of view, and the slowly varying trends arise from lenslet array flexure as the telescope rotates. For HD 1160 B, the rotation of the field of view itself (109.7° and 108.2° for the first and second nights, respectively) induces an additional component to its positional trends.

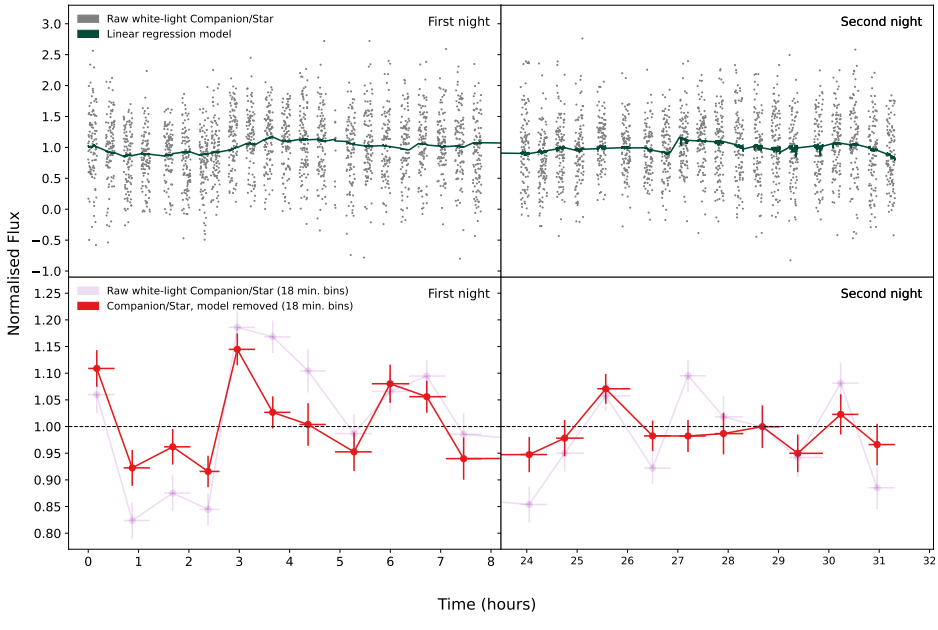

Figure 4.4: Top panel: the model, in dark green, produced when a multiple linear regression is applied to the raw white-light differential light curves from each night using the decorrelation parameters from Figure 4.3. The corresponding coefficients and intercept of each model are given in Table 4.2. The raw differential white-light curve is shown in grey, reproduced from the third panel of Figure 4.2. Bottom panel: the detrended differential white-light curve, in red and binned to 18 minutes of integration time per bin, obtained by dividing the raw differential light curve by the linear regression models above. The binned version of the raw differential white-light curve from the bottom panel of Figure 4.2 is also shown for comparison in purple.

and false-alarm probability of 0.009. This slight difference in period is due to the different normalisation used here and the different linear regression model produced by not including wind speed and wind direction as decorrelation parameters. The second strongest peak in this periodogram, with a period of 1.370 hours, peak power of 13.26, and false alarm probability of 0.035, does not appear to be harmonic with the strongest peak. However, there are no significant peaks present in the periodograms of the second night or of both nights combined. All of the features in these periodograms have false-alarm probabilities greater than 0.5. When the light curves are combined, the periodicity in the first night appears to be diluted by an absence of constructive addition from periodicity in the second night, causing there to be no significant peaks in the combined periodogram.

We also carried out a comparative analysis of the precision achieved in each detrended differential white-light curve. When estimating the precision achieved for the first night, Sutlieff et al. (2023) fitted and removed the observed periodic variability signal from the light curve. They did this using a non-linear least squares approach, assuming that it followed a sinusoidal trend and using the period of the highest peak in the periodogram as an initial guess for the fit. They then measured the precision using the residual light curve. As we do not detect a clear periodicity in the light curve from the second night, we could not do this here if we wished to compare the precision achieved on each night. We therefore instead performed our assessment of the precision using the detrended differential white-light curves from each night, and both nights combined, noting that any variations intrinsic to HD 1160 B would make these values appear higher and therefore above the true limiting precision. We did this by following the approach used by Kipping & Bakos (2011) and Sutlieff et al. (2023) for assessing the impact of correlated noise on time-series data. First, we binned our detrended differential white-light curves into a range of different bin sizes. We then renormalised the resulting binned light curves and subtracted one to centre them around zero, before measuring the root mean square (RMS) of each one. We plot these values as a function of bin size for each light curve in Figure 4.6. The black line shows the expectation of independent random numbers with increasing bin size. If we take the RMS values at each night for the bin size that we used for our binned white-light curves in Figures 4.2 and 4.4 (i.e. 200 frames per bin, or 18 minutes of integration time), we find RMS values of 0.075 and 0.035 for the first and second nights, respectively. The RMS value at this bin size for the light curve covering both nights combined is 0.060. The higher RMS for the first night (and both nights combined) reflects the higher variability that we see here compared to the second night. We discuss these results further in Section 4.8.1.

4.6 Spectral analysis of HD 1160 B

In addition to investigating the brightness fluctuations of HD 1160 B, we also extracted its spectrum on each night to allow us to characterise its physical properties through the fitting of atmospheric models.

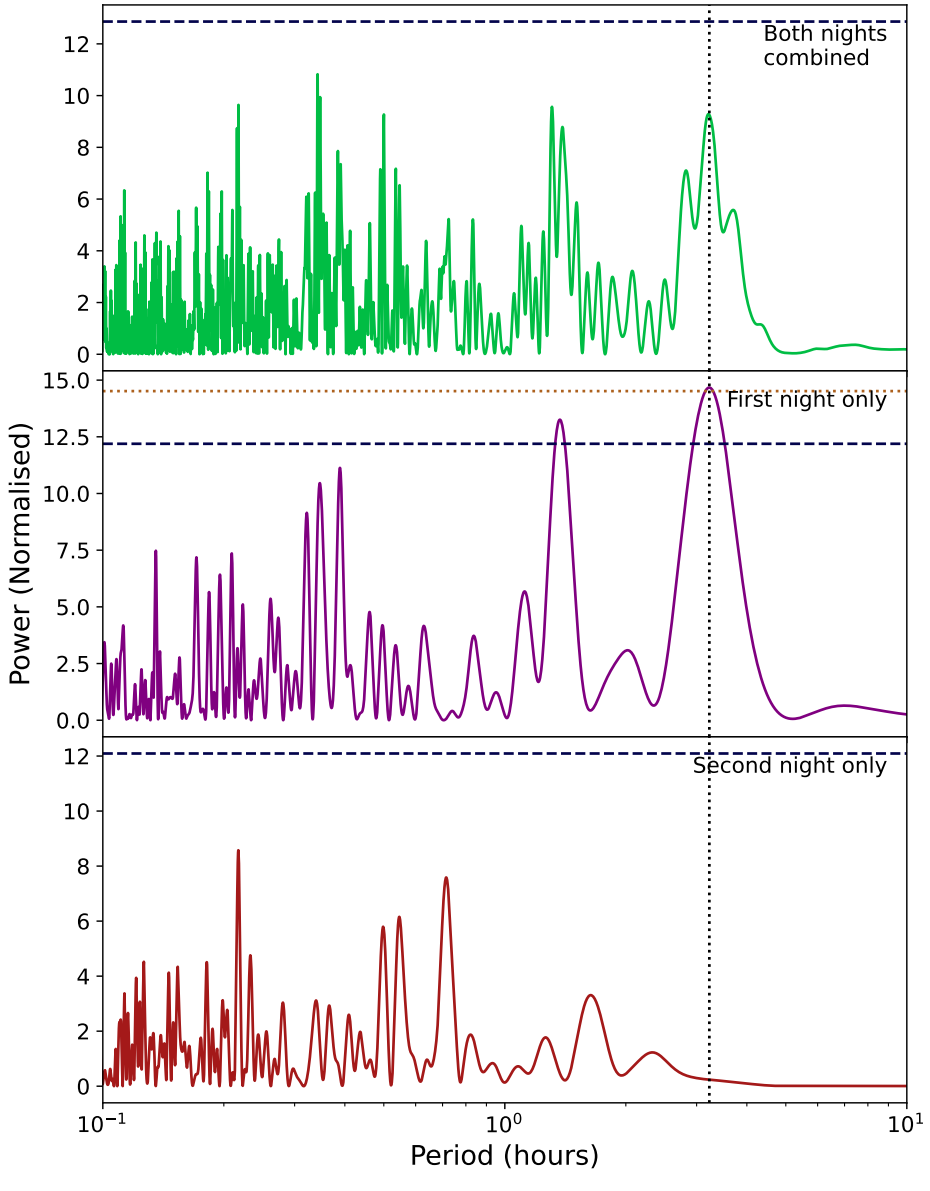

Figure 4.5: Lomb-Scargle periodograms produced using the unbinned, detrended differential white-light curves from Figure 4.4. The top panel shows the periodogram for the full light curve over both nights, whereas the centre and bottom panels are those for the light curves of the first and second nights only, respectively. The blue dashed lines indicate the power threshold corresponding to a false-alarm probability of 0.1 (10%), and the horizontal brown dotted line is that for a false-alarm probability of 0.01 (1%). The vertical dotted line highlights the 3.227 h period of the strongest peak in the periodogram for the first night.

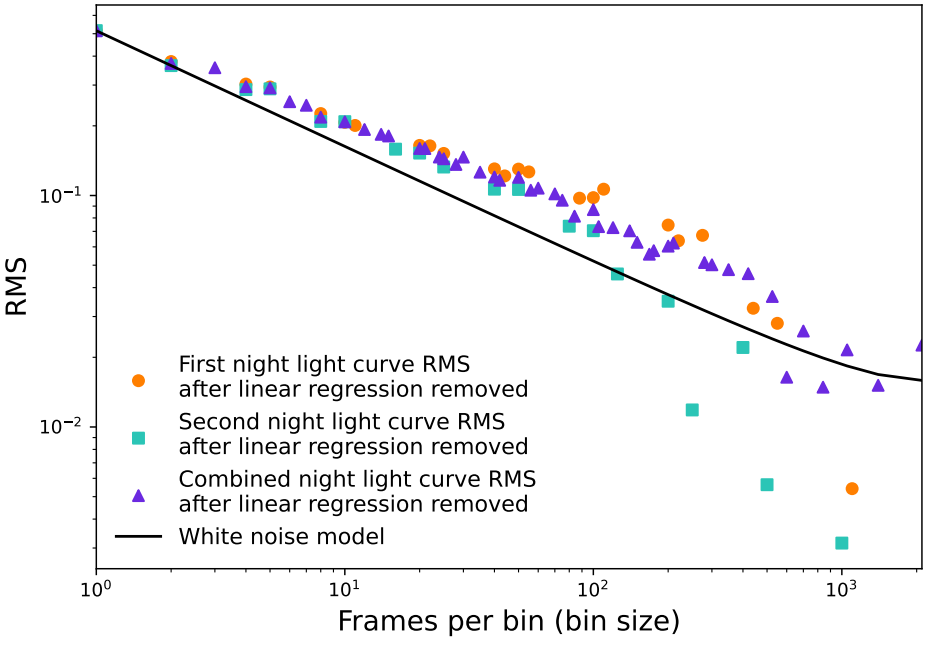

Figure 4.6: The RMS of the binned detrended differential white-light curve of HD 1160 B for the first and second nights, respectively, without the removal of any periodic variability. The theoretical white noise model as a function of bin size is also shown. This was calculated using the bin sizes used for the both nights combined light curve.

4.6.1 Spectral extraction

We measured the contrast between host star HD 1160 A and companion HD 1160 B in each wavelength channel using the aperture photometry of each object obtained in Section 4.4.1.1. To do this, we took the median combination of these flux measurements over the time sequence, producing single flux measurements for the companion and the star at each wavelength. As with the time-dependent fluxes obtained in Section 4.5.2, the errors on each measurement were calculated as the 1.48 $\times$ MAD of the fluxes in each wavelength channel (bin), divided by the square root of the number of frames per channel minus one. Next, we divided the companion flux at each wavelength by that of the star to produce a contrast spectrum. We carried out this process separately for each night of data.

We then converted our contrast spectra of HD 1160 B on each night to physical flux units by multiplying them by a flux calibrated spectrum of HD 1160 A. To do this, we used the Virtual Observatory SED Analyzer (VOSA, Bayo et al. 2008) to plot the Spectral Energy Distribution (SED) of HD 1160 A, including literature data from the 2MASS (Skrutskie et al. 2006), Tycho-2 (Høg et al. 2000b,a), and WISE (Wright et al. 2010) catalogues. We assumed a distance of 120.7 pc and an extinction of $A_V = 0.16$ mag (Gaia Collaboration et al. 2016, 2022). The SED was dereddened using the extinction law of Fitzpatrick (1999) and Indebetouw et al. (2005). Using a chi-square test to fit the SED with a grid of BT-Settl models (Allard et al. 2011, 2012), we selected a model with effective temperature $T_{eff} = 9200$ K, surface gravity $\log(g) = 4.5$ dex, metallicity [Fe/H] = 0.0, and alpha element abundance $\alpha = 0.0$, consistent with that found by Mesa et al. (2020) using the same approach. The literature photometry of HD 1160 A and this model are shown in Figure 4.7. We then convolved this model to the resolution of ALES (R$\sim$40, Skemer et al. 2018) and evaluated it at the wavelengths of our observations, before multiplying it by our contrast measurements to produce a flux calibrated spectrum of HD 1160 B on each night. These spectra are shown in Figure 4.8, with the flux measurements from the first and second nights in blue and orange, respectively. The shaded areas indicate regions in the observed 2.8-4.2 µm wavelength range where the data is unreliable and excluded from our analysis, due to contamination from the neighbouring spaxels or the dgvAPP360 glue absorption.

We note that while the spectra from each night are in good agreement in the wavelength region redward of the dgvAPP360 glue absorption, there appears to be a slight offset between the two nights at 3-3.2 µm, which we discuss further in Section 4.8.2.

4.6.2 Spectral fitting

Once we had obtained a flux calibrated spectrum of HD 1160 B for each night, we fit this data with atmospheric models to characterise its physical properties. We used a set of BT-Settl grid models (Allard et al. 2011, 2012, 2013) which were downloaded from the Spanish Virtual Observatory (SVO) Theory Server[1]. We restricted the models to those with effective temperatures between 400 K and 4600 K, surface gravities between 3.5 and 5.0 dex, metallicities between -0.5 and 0.5, and an α-enhancement of 0. The grid step sizes

[1] http://svo2.cab.inta-csic.es/theory/newov2/

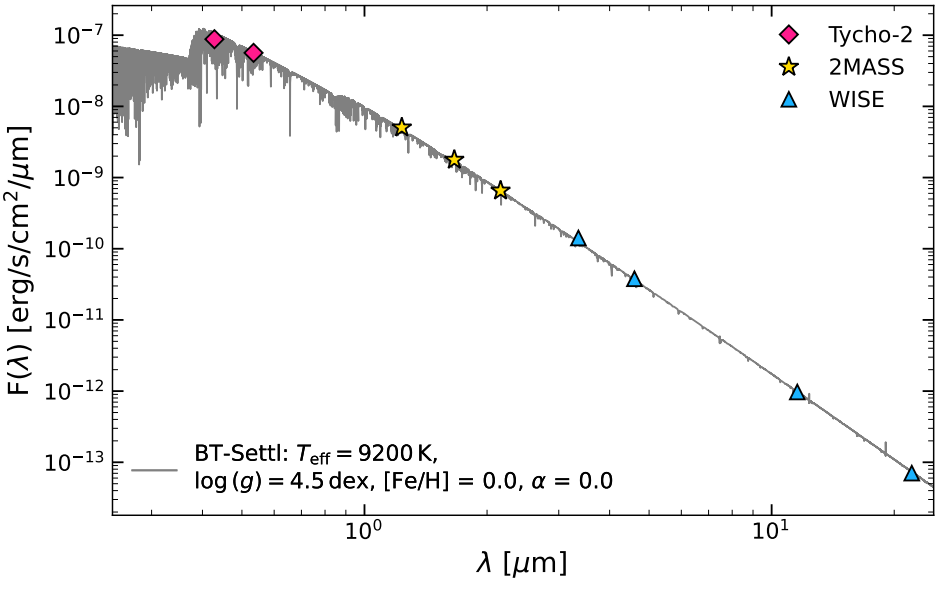

Figure 4.7: Literature photometry of the host star HD 1160 A from the Tycho, 2MASS, and WISE catalogues. The grey line shows the model fit to this photometry. The model has been convolved to a resolution of R = 100,000 for visual purposes. The uncertainties are shown but are much smaller than the symbols.

for temperature and surface gravity were 100 K and 0.5 dex, respectively, and metallicity could have values -0.5, 0, 0.3, or 0.5. We chose to restrict the range of possible surface gravities to these values based on the predicted physical limitations of objects with ages and masses within the ranges found for HD 1160 B in the recent literature, which are 10-125 Myr and ∼20 M_{Jup} to 123 M_{Jup}, respectively (Garcia et al. 2017; Curtis et al. 2019; Mesa et al. 2020). According to the isochrones and evolutionary tracks of the BT-Settl models, the surface gravities of objects with ages and masses within these constraints should always be ≥3.5 and ≤5.0 (Baraffe et al. 2015; Stone et al. 2016). Maire et al. (2016) did previously use a higher age upper limit of 300 Myr for the HD 1160 system, which would allow a HD 1160 B surface gravity of up to log(g) = ∼5.2, but Garcia et al. (2017) later found that such high ages were not consistent with the properties of the host star.

Each model was convolved to the R∼40 spectral resolution of ALES and sampled at the wavelengths of our spectral data points. By fitting each model to the data, we then determined the scaling factor that minimises the Euclidean norm of the residual vector between the two i.e. the value multiplied by each model to best match it to the companion spectrum, and calculated the χ^2 value for each fit accounting for the errors on each data point (e.g. Bohn et al. 2020a; Sutlieff et al. 2021). The model that produced the smallest χ^2 value was then taken as the best-fitting model to the data. When performing this fitting procedure we excluded the data points in the shaded regions of Figure 4.8, which were not suitable for analysis as described in Section 4.6.1. We performed the fitting process three times; once

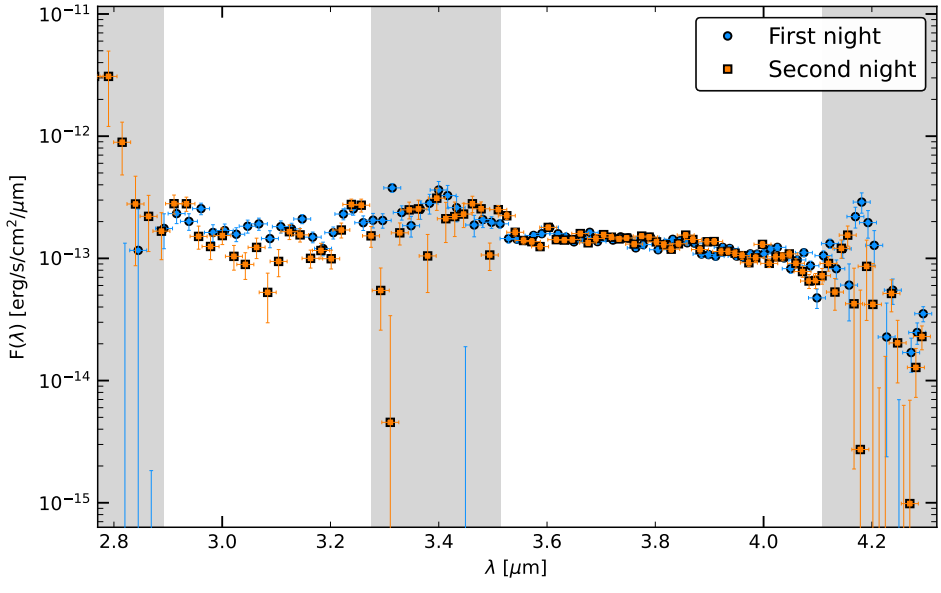

Figure 4.8: The flux calibrated spectrum of HD 1160 B obtained with LBT/ALES. Data points from the first and second nights are shown in blue and orange, respectively. The shaded regions indicate data points which are not suitable for analysis due to contamination arising from overlapping spectral traces or absorption caused by the carbon-carbon bonds in the glue layer of the dgvAPP360. The wavelength channels used for the variability analysis are those in the 3.59-3.99 μm wavelength range.

Table 4.3: The physical properties of HD 1160 B as derived by fitting BT-Settl models to its spectrum from the first night, the second night, and both nights combined. These values are the weighted means calculated based on the chi-square values of each model fit. The uncertainties reported here are only the statistical errors based on sided variance estimates. Where the fitting procedure tends to prefer models at the edge of the allowed parameter range, we instead report upper/lower limits. The bottom part of the table shows the estimated mass ranges for HD 1160 B and the corresponding mass ratios q relative to HD 1160 A, as found in Section 4.8.2.1 by evaluating BT-Settl isochrones at our luminosity values. These ranges are wide due to the wide age range considered, 10-125 Myr.

Property	First night	Second night	Both nights
T_{eff} (K)	2804^{+152}_{-74}	2310^{+93}_{-82}	2597^{+12}_{-98}
log(g) (dex)	$\geq$4.27	$\geq$4.48	$\geq$4.50
Metallicity	$\leq$0.18	$0.00^{+0.40}_{-0.00}$	$\leq$0.00
Radius (R_{Jup})	$1.46^{+0.05}_{-0.06}$	$1.75^{+0.05}_{-0.06}$	$1.57^{+0.02}_{-0.01}$
log($L/L_{\odot}$)	$-2.91^{+0.03}_{-0.02}$	$-3.08^{+0.04}_{-0.03}$	$-2.97^{+0.01}_{-0.01}$
Mass (M_{Jup})	18.2-81.2	15.9-66.7	17.6-72.6
Mass ratio q	0.008-0.038	0.007-0.031	0.008-0.034

each for the spectra from the first and second nights separately, and a third time considering both nights of data together. The best-fitting model in each case is shown overplotted on the companion spectrum in Figure 4.9. The best-fitting model to the first night of data alone has T_{eff} = 2800 K, log(g) = 4.5 dex, and metallicity [Fe/H] = -0.5 (purple line, Figure 4.9). When the second night of data is considered alone, the best-fitting model instead has solar metallicity and is slightly cooler, with T_{eff} = 2300 K, log(g) = 5.0 dex (red line). This is likely due to the lower flux recorded in the 3-3.2 μm region of the spectrum on this night. The effective temperature of the best-fitting model to both nights of data then lies between the two, as would be expected, with T_{eff} = 2600 K, log(g) = 4.5 dex, and metallicity [Fe/H] = -0.5 (green line). Using the χ^2 values of each model fit as weights, we also calculated the weighted means and sided variance estimates (i.e. statistical errors) of these atmospheric parameters using the approach of Burgasser et al. (2010a,b); Stone et al. (2016). These results are presented in Table 4.3. The weighted means and their uncertainties are biased in some cases, where the preferred model fits lie at the edge of the allowed parameter range. We therefore instead report upper/lower limits in these instances.

We further inferred estimates of the radius and luminosity of the companion using the scaling factor for each model, which is equal to the squared ratio of the companion's radius and distance. As the distance to the HD 1160 system is well-known (120.7±0.5 pc Gaia Collaboration et al. 2016, 2022), we are able to solve for radius. The luminosity can then be inferred by integrating each model over its full wavelength range and multiplying by 4π times the radius squared. These values are also shown in Table 4.3, where the reported uncertainties are again the statistical errors. These results are discussed further in Section 4.8.2.

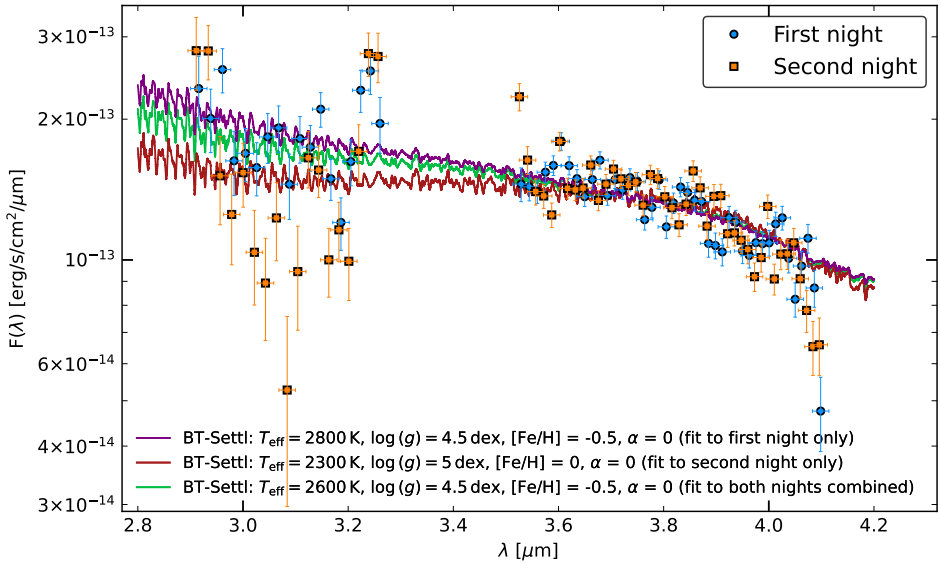

Figure 4.9: The best-fitting models to the flux-calibrated ALES spectrum of HD 1160 B. The large difference in the temperatures of the best-fitting models appears to arise from the difference in flux between the two nights in the 3.0-3.2 µm region. Data points in the shaded regions in Figure 4.8 were not included in these fits and are therefore not shown.

4.7 Characterising HD 1160 A with PEPSI

In addition to characterising HD 1160 B using the data obtained with ALES+dgvAPP360, the simultaneous high resolution PEPSI spectrum of the HD 1160 system in the optical (383-542 nm) further allows us to assess the properties of the host star HD 1160 A, which was originally classified as an A0 V star by Houk & Swift (1999). Although HD 1160 C lies at an angular separation far beyond the 2.25″ diameter of the PEPSI fiber, HD 1160 B lies within this fiber diameter at a separation or ∼0.78″, so the obtained PEPSI spectrum contains the spectra of both HD 1160 A and B. However, the contrast between the two is very large: 7.72±0.01 mag in the 1.25 µm J-band, and even larger at the shorter wavelengths covered by PEPSI (Garcia et al. 2017). We therefore assumed that the contribution of HD 1160 B to the PEPSI spectrum was negligible and treated the PEPSI spectrum as solely that of HD 1160 A (see Figure 4.10).

To estimate the properties of HD 1160 A, we compared the spectrum to BT-NextGen atmospheric models, which are computed with the use of the PHOENIX code (Hauschildt et al. 1999; Allard et al. 2012). The input parameters for the model spectra were effective temperature (T_{eff}), surface gravity (log(g)), and metallicity, the latter of which was taken as solar for HD 1160 A. The models were convolved to the resolution of the PEPSI instrument and broadened by the rotation of the star (vsin$i$). We identified the best fit values for these parameters by determining the χ^2 values for a grid of models, varying T_{eff} (9200-9800 K in steps of

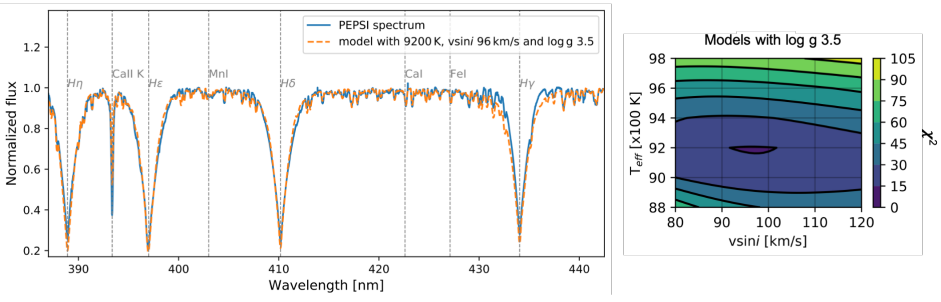

Figure 4.10: The left panel shows the PEPSI spectrum of the host star HD 1160 A in blue, overplotted with the best-fitting model from BT-Nextgen in orange. The contour plot in the right panel shows the χ^2 distribution for several temperatures and $v\sin i$ at fixed log(g) of 3.5.

4

200 K), log(g) (1.5-4.5 in steps of 0.5), and vsin$i$ (80-120 km s^{-1} in steps of 1 km s^{-1}). The ranges of these parameters were chosen based on an initial visual inspection of the PEPSI spectrum using the digital spectral classification atlas of Gray (2000). The model grid spectra were normalised with splines fitted at similar (continuum) points for a given T_{eff}. The same continuum points are used for a re-normalisation of the PEPSI spectrum with a spline to match the normalisation of the grid spectra. However, the shape of the Balmer lines appears to be inconsistent between lines, which is hard to explain with any intrinsic properties for this type of star (Gray 2000). We interpret this as a systematic error arising from the order merging and initial normalisation performed by the automated data reduction pipeline, and therefore excluded the region around the Hβ and Hγ lines from the fitting procedure.

The errors on the PEPSI data points given by the automated pipeline are on average 0.0003% of the flux, which corresponds to an extremely high S/N of $\sim$3300 that we interpret as implausible since the PEPSI exposure time calculator requires $\sim$120000 s while exposure times were $\sim$14800 s. Furthermore, the spectrum seems to contain a low level sinusoidal-like structure, which most likely arises from systematics introduced by the unusually long duration of the observations. We therefore recalculated the error on each data point using the S/N instead measured from the normalised spectrum by taking the inverse of the standard deviation of the flux in the continuum, which gives S/N = $\sim$500 (or $\sim$0.2% of the normalized flux). This value is then weighted by $\sqrt{F_i}$, where F_i is the flux for a given wavelength point i, to calculate the observed errors for each wavelength point.

We found that the resulting best fit model, taken as that with the lowest χ^2 value (= 14.46), has $T_{eff} = 9200^{+200}_{-100}$ K, $v\sin i = 96^{+6}_{-4}$ km s^{-1} and log(g) $= 3.5^{+0.5}_{-0.3}$ dex. This corresponds to an A1 IV-V classification for HD 1160 A. This best-fitting model is shown overplotted on the PEPSI spectrum of HD 1160 A in the left panel of Figure 4.10. The right panel then shows the χ^2 distribution for models with a log(g) of 3.5 over temperature and $v\sin i$. The relatively high χ^2 values, even for the best fit model, are due to normalisation differences between the model and the spectrum, the very small errors on the flux, and the large grid separation for T_{eff} and log g for BT-Nextgen models. We discuss these results further in Section 4.8.3.

4.8 Discussion

4.8.1 HD 1160 B light curves

4.8.1.1 The variability of HD 1160 B

In Section 4.5.4, we recovered the high-amplitude ∼3.2 h periodic variability signal identified by Sutlieff et al. (2023) in the first night of the detrended differential white-light curve of HD 1160 B. We also found that some data points in the light curve from our additional night deviate from equilibrium flux, albeit with a smaller amplitude. However, we do not identify any periodic signals in the light curve from this second night, nor in the full light curve covering both epochs. In both of these cases, all peaks in their respective periodograms lie well below the 1σ level.

Let us first consider the case that HD 1160 B is variable. There are several physical mechanisms that could potentially explain the decrease or absence of variability that we see on the second night. Variability in substellar objects arises from clouds or other atmospheric features, such as magnetic spots if the object is of higher mass, rotating in and out of view over their rotation periods (e.g. Ackerman & Marley 2001; Morales et al. 2010; Goulding et al. 2012; Radigan et al. 2014; Metchev et al. 2015; Tan & Showman 2019; Vos et al. 2022). Where multiple such features with different sizes are present in the atmosphere of a companion at different locations, the resulting variability signal can appear irregular in amplitude, phase, and/or periodicity (e.g. Tackett et al. 2003; Leggett et al. 2016). It is possible that we are seeing this effect in the full light curve of HD 1160 B; if its true rotation period is in fact longer than ∼3.2 h (and perhaps even longer than the baseline of a single epoch), then we could be viewing it at a different phase in its rotation on the second night. In this case, additional observations would be required to cover the full rotataion period of HD 1160 B and verify whether or not these trends repeat. Another possibility is that the difference in the level of variability is due to evolution in the surface features and atmospheric dynamics that cause the variability (e.g. Tan & Showman 2021). Many studies have identified changing variability in the light curves of brown dwarfs and planetary-mass objects, including both long-term trends over hundreds of rotation periods and rapid light curve evolution from one night to the next or even between consecutive rotations (e.g. Gelino et al. 2002; Artigau et al. 2009; Radigan et al. 2012; Gillon et al. 2013; Karalidi et al. 2016; Apai et al. 2017, 2021; Zhou et al. 2022). If the rotation period of HD 1160 B is ∼3.2 h, it would have completed ∼5 rotations between the end of the observing sequence on the first night and the start of observations on the second night, which may be long enough for rapid evolution to have occurred.

Several studies exploring the variability of substellar objects in different wavebands have further found that light curves can have similar shapes at different wavelengths, but with an offset in phase as different wavelengths probe different atmospheric pressures (Buenzli et al. 2012; Yang et al. 2016; Biller et al. 2013, 2018; Ge et al. 2019). Since our differential light curve of HD 1160 B is a white-light curve integrated over a wide wavelength range, such wavelength-dependent phase offsets could lead to a ‘cancelling out’ effect if they were

of certain magnitudes. This effect could impact the light curve of HD 1160 B if its variability has different periods at different wavelengths, such that their phases mismatch at certain times.

Sutlieff et al. (2023) highlighted that if HD 1160 B is a low-mass M-dwarf, a short-lived flaring period could be the cause of its ∼8.8% semi-amplitude variability on the first night. If this is indeed the case for HD 1160 B, this would be consistent with both the high-amplitude variability seen on the first night and its decrease or absence on the second night. However, while flaring events of this magnitude have been observed in the infrared, they are expected to be rare (e.g. Davenport et al. 2012; Goulding et al. 2012; Tofflemire et al. 2012).

We must now also consider the possibility that one or more unknown systematics could be responsible for the high-amplitude periodic variability that we see on the first night. However, it is not clear what systematic effect could induce such high-amplitude periodic variations on one night and not do so on the following night, given that the same methodology was applied to each epoch. The observing conditions were very similar and highly stable on both nights. If we consider the decorrelation parameters used in the detrending procedure (Figure 4.3), we see that the airmass, companion position, and stellar position all follow approximately the same trends on each night. This would appear to rule out residual systematics arising from these parameters as the source of the light curve differences between each night. The air temperature does differ slightly in the second half of each night but is otherwise broadly similar, and any correlation arising from this difference is unlikely to be significant enough to explain what we see, particularly after the detrending process has been applied. One possibility could be that there is an additional systematic connected to the flexure of the ALES lenslet array as the telescope rotates. However, any such effects should already be accounted for by the inclusion of the pixel positions of HD 1160 A and B in the detrending process. An alternative parameter probing this flexure would be the pointing altitude of the telescope, which again follows the same trend on each night (and follows an inverse relationship to airmass). Furthermore, Sutlieff et al. (2023) found that the shape of the raw light curves is robust against issues arising from lenslet flexure by comparing data processed using wavelength calibration frames obtained at different pointing altitudes.

Although the nature of the variability of HD 1160 B remains unclear, the additional night of variability monitoring presented here shows that this variability does not follow a simple periodic trend and highlights the complexities of interpreting the light curves of high-contrast substellar companions. Future ground-based observations will help to shed light on the trends in the light curves of HD 1160 B through additional epochs that provide a longer baseline, and the greater photometric precision provided by space-based facilities such as JWST could further help to constrain its variability amplitudes.

4.8.1.2 Precision of vAPP differential spectrophotometric monitoring

Our additional night of variability monitoring through differential spectrophotometric monitoring combined with the dgvAPP360 allows us to test whether this recently-developed technique can achieve the same precision at multiple epochs. Sutlieff et al. (2023) found

that this technique did not reach a systematic noise floor on the first night, suggesting that the precision would continue to improve with a longer baseline and increasing bin size. In Section 4.5.4, we measured the RMS as a function bin size for the detrended differential white-light curves on each night and both nights combined (Figure 4.6). As noted previously, the RMS trends for the first night and both nights combined cases do sit at a slightly higher level than on the second night, but this is expected as no variability signal has been removed from either night and the variability is of higher amplitude on the first night. Aside from this offset, we see that the RMS follows the same trend on both nights; both decrease according to the trend of the white noise and do not level off. This is also the case for the light curve covering both nights combined. This suggests that the data possesses similar noise properties at both epochs and therefore that the precision reached with this technique can be reliably repeated. Since we do not appear to reach the photon noise limit with these observations, future observations may be able to achieve a greater precision by using more complex methods to detrend the differential light curve of the companion, such as approaches using Gaussian processes (e.g. Gibson et al. 2012; Evans et al. 2013; Nikolov et al. 2018a; Carter et al. 2020; Diamond-Lowe et al. 2020a,b; Panwar et al. 2022b). However, we note that robustly assessing the true deviation of these trends from the white noise model is difficult due to the possible astrophysical variability.

4.8.2 Spectral characterisation of HD 1160 B

In Section 4.6.1, we presented the extracted spectra of HD 1160 B for each night and noted an offset in the spectra of HD 1160 B from each night in the 3-3.2 µm wavelength region, where the data points from the second night appear to lie slightly lower than those from the first night. The cause of this offset is unclear. A possibility is that this feature is astrophysical and arises from the intrinsic variability of HD 1160 B, with it appearing fainter in this wavelength region on the second night. In addition to this feature, the scatter of the datapoints at longer wavelengths (e.g. 3.6-4.0 µm) is also larger than would be expected from the fitted models. If our uncertainties are correctly estimated, then this may also be due to the effects of variability; a greater scatter in the spectrum of HD 1160 B would be expected if its variability has different properties at different wavelengths. However, we cannot rule out that this scatter is a systematic effect.

Regardless of the origin of the offset at 3-3.2 µm, it has a significant impact on the results of the atmospheric model fitting described in Section 4.6.2. This process produced significantly different values for the physical properties of HD 1160 B depending on whether the models were fit to the spectra from the first night alone, the second night alone, or both nights combined (Table 4.3). The values for effective temperature $T_{\rm eff}$ cover a particularly large range, from 2310^{+93}_{-82} K for the fit to the second night to 2804^{+152}_{-74} K on the first night (a $>1\sigma$ difference). The effective temperatures derived from the second night and both nights combined spectra are much cooler than those in the literature, but the higher temperature from the first night is consistent with previous measurements to within 1σ. Maire et al. (2016) determined a $T_{\rm eff}$ for HD 1160 B of 3000±100 K through atmospheric modeling, consistent with the 3000-3100 K value found by Garcia et al. (2017), although the latter

study noted that they could not rule out slightly cooler temperatures. Our value derived from the spectrum from the first night also overlaps with the 2800-2900 K range estimated by Mesa et al. (2020).

All three of our constraints for surface gravity log(g) are consistent with the 4.0-4.5 dex range estimated by Garcia et al. (2017) (who also could not rule out slightly higher values), and consistent within 2σ with Mesa et al. (2020), who estimated a lower log(g) of 3.5-4.0 dex. Maire et al. (2016) were not able to constrain the surface gravity in their study. However, we note that surface gravity is not strongly constrained by our atmospheric model fitting. Our inferred radii from the fits to the first night and both nights spectra are consistent with the 1.55 ± 0.1 R_{Jup} radius inferred by Garcia et al. (2017), but our radius for the second night spectrum is slightly larger. Finally, all three of our inferred luminosities $\log(L/L_{\odot})$ are lower than the -2.76 ± 0.05 dex value measured by Garcia et al. (2017). However, our luminosity from the first night is consistent within 1σ with that found by Maire et al. (2016), $\log(L/L_{\odot}) = -2.81\pm0.10$ dex.

If we consider these results in full, the spectrum of HD 1160 B on our second night of observations does not appear to be consistent with the literature. If the differences between the spectra from each night at bluer wavelengths are due to astrophysical variability in the atmosphere of HD 1160 B, this highlights the impact that this can have on the results of fitting models to the atmospheres of substellar companions. Difficulties in fitting the spectrum of HD 1160 B have also been noted previously. When analysing the SPHERE spectra in the Y, J, and H bands, Mesa et al. (2020) found that HD 1160 B has a spectrum that is not well matched by any spectra in current spectral libraries, and were only able to obtain good fits by considering the Y+J and H bands separately. Several studies of other substellar companions have also reported such issues when trying to fit their spectra, sometimes finding wide-ranging results depending on the wavebands considered (e.g. Stone et al. 2020; Ward-Duong et al. 2020; Sutlieff et al. 2021; Whiteford et al. 2023).

Simultaneous observations over a broad wavelength range with facilities such as JWST may help to break these degeneracies between wavebands and further identify whether the differences in the spectrum of HD 1160 B between epochs are due to time variability (Gardner et al. 2006; Hinkley et al. 2022a; Kammerer et al. 2022). Ground-based high-resolution spectroscopy may further help us to determine its nature by resolving specific molecular lines that constrain effective temperature, surface gravity, and other physical properties (Birkby et al. 2013; Birkby 2018; Hoeijmakers et al. 2018; Brogi & Line 2019; van Sluijs et al. 2022).

4.8.2.1 The mass of HD 1160 B

It is further possible to infer estimates for the mass of HD 1160 B using our luminosity estimates from Section 4.6.2 and values for the age of the HD 1160 system. We used the BT-Settl (Allard 2014; Baraffe et al. 2015) isochrones for this purpose, which are valid for brown dwarfs and low mass stars. To obtain mass estimates, we first interpolated over the model grid of each isochrone and then evaluated them at our luminosity values. As the

resulting mass estimates are highly age-dependent and the age of the HD 1160 system is not well-constrained, we carefully considered the range of age estimates in the literature and chose to use a 10-125 Myr range. This is a combination of the 20-125 Myr age range found by Garcia et al. (2017) considering the properties of HD 1160 A and a range of evolutionary models, and the lower 10-20 Myr ages favoured by the results of Mesa et al. (2020) (the former study also produced a range based on HD 1160 ABC together, but this was narrower 80-125 Myr). Our chosen range also covers the ∼120 Myr age that the HD 1160 system would be expected to have if it is a member of the Psc-Eri stellar stream, as suggested by Curtis et al. (2019). Maire et al. (2016) did allow ages up to 300 Myr in their study, but ages this old appear to be ruled out by Garcia et al. (2017).

The resulting estimated mass ranges are shown in Table 4.3. We also include the corresponding values for the mass ratio relative to HD 1160 A, q, assuming a stellar mass of 2.05 $M_\odot$ (A1 V, Pecaut & Mamajek 2013). Our full range of allowable values covers 16-81 M_{Jup}. This places HD 1160 B comfortably above the deuterium burning limit (∼11-16.3 M_{Jup}, Spiegel et al. 2011), but does not rule out the possibility that it is a low mass star above the hydrogen burning limit (78.5 M_{Jup}, Chabrier et al. 2022). This is fully consistent with mass estimates in the literature, as we might expect given the broad age range assumed. Nielsen et al. (2012) estimated the mass of HD 1160 B to be 33^{+12}_{-9} M_{Jup} upon its discovery, and Maire et al. (2016) found a mass range of 39-166M_{Jup} based on their wider range of allowable system ages. Garcia et al. (2017) later found a mass range of 35-90 M_{Jup}. Finally, Mesa et al. (2020) estimated a mass of ∼20 M_{Jup} for HD 1160 B, which falls at the lower end of our range.

Our ability to precisely estimate the mass of HD 1160 B is severely limited by the highly uncertain age of the HD 1160 system, thus it will be difficult to further constrain the mass of this companion without either tighter constraints on its age or a dynamical mass measurement (e.g. Konopacky et al. 2010; Crepp et al. 2012; Dupuy et al. 2016; Dupuy & Liu 2017; Brandt et al. 2019; Biller et al. 2022; Rickman et al. 2022).

4.8.3 PEPSI characterisation of HD 1160 A

In Section 4.7, we fitted BT-NextGen models to the PEPSI data of HD 1160 A and estimated its physical properties, finding $T_{eff} = 9200^{+200}_{-100}$ K, $v\sin i = 96^{+6}_{-4}$ km s^{-1} and log(g) $= 3.5^{+0.5}_{-0.3}$ dex. If we compare these physical properties to those of the best-fitting model found by using VOSA to fit the literature SED of HD 1160 A for the flux calibration process in Section 4.6.1, the temperature and metallicity have the same values but the surface gravity here is lower than that of the log(g) $= 4.5$ dex model found with VOSA. This difference in surface gravity does not significantly impact the flux calibration of the spectra of HD 1160 B in Section 4.6.1, as the best-fitting model found with VOSA is convolved to the R∼40 resolution of ALES prior to being used for this purpose. At this resolution, the two stellar models are indistinguishable and do not lead to differences in the HD 1160 B spectral fitting results.

If we assume the BT-Settl model grid spacing for log(g), 0.5 dex, as the uncertainty on the VOSA result, the two values are consistent within 1σ. We note that surface gravity is

difficult to constrain with atmospheric models, and similarly good fits to the PEPSI data could also be obtained with slightly higher surface gravities. However, if HD 1160 A does have log(g) = 3.5, this may be an indicator of youth, as older objects are likely to have higher surface gravities (e.g. Baraffe et al. 2015).

Our derived values for the physical properties of HD 1160 A from the PEPSI spectrum correspond to an A1 IV-V spectral type. This is a slightly later spectral type than the A0 V classification found by Houk & Swift (1999) using photographic plates. Nielsen et al. (2012) previously noted that HD 1160 A is underluminous for its position on the HR diagram, based on it being an A0 V star, and interpreted this as a sign of youth (e.g. Jura et al. 1998). But if HD 1160 A is an A1 V star, this may partially account for this apparent underluminosity. As we also measured the $v\sin i$ of HD 1160 A, we further considered the alternative possibility that gravity darkening could help to explain this. If a star rotates rapidly it becomes oblate, leading to a greater radius and hence lower temperature and brightness at its equator compared to its poles (Monnier et al. 2007; Espinosa Lara & Rieutord 2011; Lipatov et al. 2022). As HD 1160 A has an almost edge-on inclination angle ($92^{+8.7}_{-9.3}$°, Bowler et al. 2020a), rapid rotation would therefore lead to an apparent decrease in its luminosity as viewed from Earth. However, a typical A-type star has a much faster rotation (e.g. ∼190 km s^{-1} for an A0 star) than our rotational velocity measurement $v\sin i = 96^{+6}_{-4}$ km s^{-1} (McNally 1965; Nielsen et al. 2013). This indicates that gravitational darkening cannot explain any underluminosity of HD 1160 A, and that this is better accounted for by it being of a later spectral type than previously thought.

4.9 Conclusions

We present here a new study of the HD 1160 system using two nights of observations obtained with the Large Binocular Telescope. This work is divided into three parts: variability monitoring of substellar companion HD 1160 B with the dgvAPP360 coronagraph and the ALES IFS; a R∼40 spectral characterisation of HD 1160 B using the same data; and lastly a spectral characterisation of host star HD 1160 A using R = 50,000 high resolution spectroscopy obtained with the PEPSI spectrograph.

The variability analysis of HD 1160 B was conducted following the technique of vAPP-enabled differential spectrophotometric monitoring recently presented by Sutlieff et al. (2023), who demonstrated this approach with the first night of observations used here. We first processed the LBT/ALES+dgvAPP360 data and extracted aperture photometry of both HD 1160 A and B, before combining the data in the wavelength dimension and dividing the companion flux by that of the star to produce a differential white-light curve for HD 1160 B spanning both nights. We then further detrended the light curve using a multiple linear regression approach. We find that we recover the high-amplitude ∼3.2 h periodic variability identified by Sutlieff et al. (2023) in the first night, but that the second night light curve does not contain significant periodic variability, potentially indicating rapid time evolution in the atmosphere of HD 1160 B and highlighting the complexity of interpreting the light curves of high-contrast substellar companions. We also analysed the precision achieved in the detrended differential

white-light curve on each night and found that the noise properties were similar. This suggests that vAPP-enabled differential spectrophotometric monitoring achieves a repeatable precision at the ∼4% level over multiple epochs and that we do not reach the photon noise limit. Thus, a greater precision could be achieved in future studies if residual systematics in the differential light curves can be further mitigated using more advanced detrending approaches such as those using Gaussian processes (e.g. Gibson et al. 2012; Panwar et al. 2022b).

We conducted our spectral characterisation of HD 1160 B by instead combining the LBT/ALES+dgvAPP360 observations over the time sequence for each night, thereby producing 2.8-4.2 µm spectra of the companion. These spectra are the first for this target in the mid-infrared and are therefore highly complementary to previous studies in the literature. We find that the spectrum of HD 1160 B from the second night is systematically fainter in the 3.0-3.2 µm wavelength range than on the first night, which could be due to the intrinsic variability of the companion if this difference is astrophysical. We then fit these spectra with BT-Settl atmospheric models, considering each night separately and both nights together, and found that the results differ considerably depending on the data being fitted. Our effective temperature T_{eff} estimates range from 2310^{+93}_{-82} K for the second night spectrum to 2804^{+152}_{-74} K on the first night. This first night T_{eff} is consistent with the literature, but those derived from the second night and both nights combined spectra are cooler. Our inferred luminosities are lower than those in the literature, but our radius estimates are mostly consistent. Overall, we conclude that the spectrum of HD 1160 B on the second night of our observations is not consistent with the literature. The differences in the results obtained for each spectrum highlights the impact that variability can have on atmospheric model fitting for substellar companions. Simultaneous observations over a broad wavelength range with facilities such as JWST may help to break the degeneracies arising from these model fits and determine whether the differences in the spectrum of HD 1160 B between epochs are due to time variability.

By evaluating our luminosity estimates with BT-Settl isochrones over an age range of 10-125 Myr, we also estimated the mass of HD 1160 B. We report a 16-81 M_{Jup} mass range, consistent with previous estimates in the literature. This places HD 1160 B comfortably above the deuterium burning limit, but also allows the possibility that it is a low mass star above the hydrogen burning limit.

Lastly, we performed a new characterisation of host star HD 1160 A by comparing the R∼50,000 high resolution spectrum obtained with PEPSI to BT-NextGen atmospheric models. We found values for the physical properties of HD 1160 A; $T_{eff} = 9200^{+200}_{-100}$ K, $\log(g) = 3.5^{+0.5}_{-0.3}$, and $v\sin i = 96^{+6}_{-4}$ km s^{-1}, the first $v\sin i$ estimate obtained for this target. This model corresponds to a spectral type of A1 IV-V, which is slightly later than the literature A0 V classification found by Houk & Swift (1999) using photographic plates. This may explain the apparent underluminosity of HD 1160 A previously noted by Nielsen et al. (2012). By considering our rotational velocity $v\sin i$ measurement alongside the known near edge-on inclination angle of the HD 1160 system, we find that HD 1160 A rotates slower than the typical A-type star, and hence rule out gravitational darkening as the cause of any underluminosity.

Tighter limits on the age of the HD 1160 system or dynamical mass measurements of each component are key if the physical properties of HD 1160 A and B are to be constrained further. Observations over a broad wavelength range or at a high spectral resolution will also help to break the degeneracies in the spectrum of HD 1160 B, while additional epochs of ground-based differential spectrophotometric monitoring or high-precision space-based monitoring will shed light on its variability.

Acknowledgements

The authors would like to thank the exoZoo team for valuable discussions that improved this work. BJS is fully supported by the Netherlands Research School for Astronomy (NOVA). JLB acknowledges funding from the European Research Council (ERC) under the European Union's Horizon 2020 research and innovation program under grant agreement No 805445. This paper is based on work funded by the United States National Science Foundation (NSF) grants 1608834, 1614320, and 1614492. The research of DD and FS leading to these results has received funding from the European Research Council under ERC Starting Grant agreement 678194 (FALCONER).

We acknowledge the use of the Large Binocular Telescope Interferometer (LBTI) and the support from the LBTI team, specifically from Emily Mailhot, Jared Carlson, Jennifer Power, Phil Hinz, Michael Skrutskie, Travis Barman, and Ji Wang. The LBT is an international collaboration among institutions in the United States, Italy and Germany. LBT Corporation partners are: The University of Arizona on behalf of the Arizona Board of Regents; Istituto Nazionale di Astrofisica, Italy; LBT Beteiligungsgesellschaft, Germany, representing the Max-Planck Society, The Leibniz Institute for Astrophysics Potsdam, and Heidelberg University; The Ohio State University, representing OSU, University of Notre Dame, University of Minnesota and University of Virginia. We gratefully acknowledge the use of Native land for our observations. LBT observations were conducted on the stolen land of the Ndee/Nnēē, Chiricahua, Mescalero, and San Carlos Apache tribes.

This publication makes use of VOSA, developed under the Spanish Virtual Observatory (https://svo.cab.inta-csic.es) project funded by MCIN/AEI/10.13039/501100011033/ through grant PID2020-112949GB-I00. VOSA has been partially updated by using funding from the European Union's Horizon 2020 Research and Innovation Programme, under Grant Agreement №776403 (EXOPLANETS-A). This work has made use of data from the European Space Agency (ESA) mission *Gaia* (https://www.cosmos.esa.int/gaia), processed by the *Gaia* Data Processing and Analysis Consortium (DPAC, https://www.cosmos.esa.int/web/gaia/dpac/consortium). Funding for the DPAC has been provided by national institutions, in particular the institutions participating in the *Gaia* Multilateral Agreement. This publication makes use of data products from the Wide-field Infrared Survey Explorer, which is a joint project of the University of California, Los Angeles, and the Jet Propulsion Laboratory/California Institute of Technology, funded by the National Aeronautics and Space Administration. This publication makes use of data products from the Two Micron All Sky Survey, which is a joint project of the University of Massachusetts and the Infrared Processing and Analysis

Center/California Institute of Technology, funded by the National Aeronautics and Space Administration and the National Science Foundation. This research has made use of the SIMBAD database and the VizieR catalogue access tool, operated at CDS, Strasbourg, France (Wenger et al. 2000; Ochsenbein et al. 2000). This research has made use of the NASA Exoplanet Archive, which is operated by the California Institute of Technology, under contract with the National Aeronautics and Space Administration under the Exoplanet Exploration Program. This research has made use of NASA's Astrophysics Data System. This research made use of SAOImageDS9, a tool for data visualization supported by the Chandra X-ray Science Center (CXC) and the High Energy Astrophysics Science Archive Center (HEASARC) with support from the JWST Mission office at the Space Telescope Science Institute for 3D visualization (Joye & Mandel 2003). This work made use of the whereistheplanet[1] prediction tool (Wang et al. 2021a). This work makes use of the Python programming language[2], in particular packages including NumPy (Harris et al. 2020), SciPy (Virtanen et al. 2020), Astropy (Astropy Collaboration et al. 2013, 2018, 2022), HCIPy (Por et al. 2018), PyAstronomy (Czesla et al. 2019), PynPoint (Amara & Quanz 2012; Stolker et al. 2019), Photutils (Bradley et al. 2022), scikit-learn (Pedregosa et al. 2011), scikit-image (van der Walt et al. 2014), statsmodels (Seabold & Perktold 2010), pandas (McKinney 2010; Reback et al. 2022), and Matplotlib (Hunter 2007).

Data Availability

The data from the LBT/ALES+dgvAPP360 and LBT/PEPSI observations underlying this article will be available in the Research Data Management Zenodo repository of the Anton Pannekoek Institute for Astronomy shortly after publication, at https://doi.org/10.5281/zenodo.7051242.

[1] http://whereistheplanet.com/
[2] Python Software Foundation; https://www.python.org/

Into all lives a little turbulence must fall.
Nicola Yoon

Chapter 5

Investigating the application of adaptive optics and high-contrast imaging techniques in the production of precise exoplanet light curves

Ben J. Sutlieff, David S. Doelman, Jayne L. Birkby, Matthew A. Kenworthy, Jordan M. Stone, Frans Snik, Steve Ertel, and Alexander J. Bohn

To be submitted for publication in *Monthly Notices of the Royal Astronomical Society*

Abstract

Substellar companions such as exoplanets and brown dwarfs exhibit changes in brightness arising from surface inhomogeneities, providing insights into their atmospheric structure and dynamics. This variability can be measured in the light curves of faint companions from the ground by combining the technique of differential spectrophotometric monitoring with high-contrast imaging. However, ground-based observations are inherently sensitive to the effects of turbulence in Earth's atmosphere, and while extreme adaptive optics (AO) systems and bespoke data processing techniques help to mitigate these, residual systematics can limit photometric precision. Here, we inject artificial companions to data obtained with an AO system and a vector Apodizing Phase Plate coronagraph to test the level to which telluric and other systematics contaminate such light curves, and thus how well their known variability signals can be recovered. We find that varying companions can be distinguished from non-varying companions, but that variability amplitudes and periods cannot accurately be recovered when observations cover only a small number of periods. Based on how the root mean square values of the differential light curves vary with binning, we find that there are still residual systematics but that we do not reach a noise floor, thus the precision can be improved further with increased bin sizes. We also simulate observations to assess

how specific systematic sources, such as non-common path aberrations and AO residuals, can impact aperture photometry as a companion moves through pupil-stabilised data. We show that only the lowest-order aberrations are likely to affect flux measurements, and that thermal background noise is the dominant source of scatter in raw companion photometry. Predictive control and focal-plane wavefront sensing techniques will help to further reduce systematics in data of this type.

Key words: planets and satellites: atmospheres – exoplanets – methods: observational – techniques: imaging spectroscopy – atmospheric effects – software: simulations

5.1 Introduction

Periodic variations in the brightness of exoplanets and brown dwarfs provide a unique avenue to explore their atmospheric structures and how they change over time. Such variations can arise from a range of sources, including inhomogeneous cloud cover, magnetic spots, aurorae, and temperature fluctuations caused by radiative convection, and can have different amplitudes and phases at different wavelengths (e.g. Goulding et al. 2012; Apai et al. 2013, 2017; Radigan et al. 2014; Hallinan et al. 2015; Tremblin et al. 2016, 2020; Yang et al. 2016; Tan & Showman 2019; Vos et al. 2023). Thus, the variability properties of substellar objects yield valuable information about the underlying physical processes that govern their atmospheres. Time-resolved photometric monitoring has now identified variability in the light curves of many substellar companions and isolated objects (e.g. Metchev et al. 2015; Cushing et al. 2016; Biller et al. 2018; Manjavacas et al. 2019a, 2021; Miles-Páez et al. 2019, 2023; Vos et al. 2022; Lew et al. 2020b,a; Tannock et al. 2021; Zhou et al. 2016, 2022). The large diameters, coronagraphic imagers, and adaptive optics (AO) systems of ground-based telescopes allow us to resolve substellar companions at close angular separations that are otherwise inaccessible to space-based observatories with smaller mirrors. However, achieving the photometric precision required to measure the variability of these companions can be challenging, as ground-based observations inherently suffer from systematics caused by turbulence in Earth's atmosphere. High-contrast imaging data are often limited by quasi-static speckles of residual starlight at the smallest separations, as well as the wind-driven halo effect that arises when atmospheric turbulence varies faster than the AO system can correct for it (e.g. Hinkley et al. 2007; Cantalloube et al. 2018, 2020a; Madurowicz et al. 2019; Males et al. 2021). Non-common path aberrations (NCPAs), introduced by differences in the optical paths that lead to the wavefront sensor of the AO system and the detector, further give rise to changes in the shapes and sizes of the Point Spread Function (PSF) of the target (e.g. Sauvage et al. 2007; N'Diaye et al. 2013, 2014; Miller et al. 2018; Bos et al. 2019; Menduiña-Fernández et al. 2020; Vigan et al. 2019, 2022; Skaf et al. 2022). Although extreme AO systems and optimised data processing strategies help to significantly reduce these effects, remaining systematics can produce non-astrophysical variability in the light curves of companions.

For observations of isolated objects that are observed without a coronagraph, non-variable comparison stars are often used as simultaneous photometric references to divide out this systematic variability from the photometry of the target (e.g. Artigau et al. 2009; Wilson et al. 2014; Biller et al. 2015; Naud et al. 2017; Vos et al. 2019). However, there are often no comparison stars available in the small fields of view of the coronagraphic imagers used to observe faint companions, and the companion's host star is typically obscured by the coronagraph itself (e.g. Ruane et al. 2018). Nonetheless, differential light curves of close-separation companions can be produced using the technique of differential spectrophotometry when combined with a vector Apodizing Phase Plate (vAPP) coronagraph (Sutlieff et al. 2023, Sutlieff et al. in prep.). Uniquely, the vAPP coronagraph preserves an image of the target star for use as a photometric reference, while simultaneously producing a coronagraphic dark hole in which high-contrast companions can be detected (Snik et al. 2012; Otten et al. 2014a,b;

Doelman et al. 2021). By further combining the vAPP with an integral field spectrograph (IFS), the light from both the host star and the companion are dispersed into spectra, which can then be extracted through aperture photometry and recombined to obtain a white-light time series for each object. This step helps to minimise the impact of any wavelength-specific flat-fielding errors, improving the precision of the light curves compared to broad-band photometric observations. A differential light curve for the companion can then be produced by dividing the companion flux by that of the host star, thereby eliminating trends arising from systematics shared by both objects, leaving behind only non-shared variations. However, while this includes the intrinsic variability of the companion, any remaining systematics not shared by the star and companion also remain. These can be further corrected to some extent, where their sources are known; in a pilot study of this technique, Sutlieff et al. (2023) used a parametric linear regression approach to fit and remove residual trends from sources such as airmass, achieving a 3.7% precision per 18-minute bin in their differential light curve of substellar companion HD 1160 B. Similar studies of transiting exoplanet transmission spectroscopy and secondary eclipses often correct for non-shared systematics using more comprehensive polynomial models or Gaussian processes (e.g. de Mooij et al. 2011; Gibson et al. 2012; Diamond-Lowe et al. 2018, 2022; Todorov et al. 2019; Diamond-Lowe et al. 2022; Panwar et al. 2022b,a). Yet, understanding the sources and magnitudes of the systematics that impact light curves obtained through ground-based differential spectrophotometry is key to accurately estimating the precision achieved with this method, and for devising new approaches to mitigate these systematics and hence reach greater precision in the future.

In this paper, we assess the extent to which telluric and instrumental systematics contaminate the differential light curves obtained with the technique of vAPP-enabled ground-based differential spectrophotometry. We do this by injecting artificial companions with and without variability to real data to test the shapes of the recovered light curves, and by producing simulated data to explore the impact of specific systematics. Artificial companion injection is an ideal way to assess the extent to which unknown systematics limit the precision that we achieve with this technique, while simulated data allows us to measure the strength of some of the systematics that we are aware of, such as those caused by Zernike modes. In Section 5.2, we describe the methods used to inject the artificial companions, process the data, and produce differential white-light curves for each companion. The simulated data is described in Section 5.3. In Section 5.4, we test how well the injected variability signals are recovered. We discuss these results and their implications for the light curve precision in Section 5.5, and lastly summarise the conclusions of this work in Section 5.6.

5.2 Artificial companion injection

By injecting artificial companions with simulated variability signals into real observational data, we can assess the level of variability that can be recovered in this type of data and whether it can be recovered consistently at different locations in the data. Furthermore, injecting companions with no variability (i.e. a flat signal) allows us to test the extent to which the differential light curves are affected by systematics. Such tests are not possible using real companions, as their level of variability is usually not known a priori, and itself can

change over time (e.g. Zhou et al. 2022). In this section, we inject artificial companions with and without variability signals into an observational dataset, reduce the data, and produce differential light curves for these companions following the standard method used for real companions by (Sutlieff et al. 2023, Sutlieff et al. in prep.). We then compare the recovered variability signal to that which was originally injected.

5.2.1 Ground-based differential spectrophotometry dataset

The vAPP-enabled differential spectrophotometric monitoring dataset used here for our artificial planet injection and recovery tests is that presented by Sutlieff et al. (2023), who conducted a variability study of substellar companion HD 1160 B. This dataset was obtained with the left-side aperture of the 2 x 8.4-m Large Binocular Telescope (LBT) in Arizona, using the double-grating 360° vector Apodizing Phase Plate (dgvAPP360; Doelman et al. 2017, 2020, 2021) coronagraph. The Arizona Lenslets for Exoplanet Spectroscopy (ALES) IFS was used with an L-band prism to spectrally disperse the light from the target over a 2.8-4.2 µm wavelength range with an R∼40 spectral resolution (ALES; Skemer et al. 2015, 2018; Hinz et al. 2018; Stone et al. 2018, 2022). ALES works alongside the LBT Mid-InfraRed Camera (LMIRcam) as part of the LBT Interferometer (LBTI), providing a 2.2″x 2.2″ field of view with a ∼35 mas spaxel^{-1} plate scale (Skrutskie et al. 2010; Leisenring et al. 2012; Hinz et al. 2016; Ertel et al. 2020). Sutlieff et al. (2023) obtained ∼3.32 hours of integration time on the HD 1160 system over ∼7.81 hours using an on/off nodding pattern, with 109.7° of field rotation and stable weather conditions. Importantly, companion host star HD 1160 A has been shown to be non-variable, making it suitable for use as a simultaneous photometric reference (Sutlieff et al. 2023). To avoid any issues arising from micro-spectra overlap and the dgvAPP360 glue absorption feature at ∼3.25-3.5 µm, we chose to use a subset of this data set covering a wavelength range of 3.59-3.99 µm for our analysis (Otten et al. 2017; Doelman et al. 2021).

To enable artificial companions to be injected to the data easily, the raw ALES micro-spectra grids were first converted into 3D image cubes of spatial position and wavelength according to the procedure described by (Sutlieff et al. 2023); once the sky background had been subtracted using the data obtained in the off-source nod position, the micro-spectra were extracted using weighted optimal extraction (Horne 1986; Briesemeister et al. 2018, 2019; Stone et al. 2020). Wavelength calibration of the micro-spectra was carried out using four four fiducial spots provided by narrow-band filters located upstream of ALES which were fitted using a second-order polynomial, allowing pixel position to be mapped to wavelength (Stone et al. 2018, 2022). The final image cube consisted of 30 wavelength channels, with 2200 frames per channel.

5.2.2 Injecting artificial companions

Artificial companion injection is widely used in high-contrast imaging studies as a method for obtaining photometric measurements of bona fide companions (e.g. Lagrange et al. 2010; Marois et al. 2010a; Bonnefoy et al. 2011; Apai et al. 2016). This is generally done using an

unsaturated PSF of the host star, obtained separately, which acts as the artificial companion. The brightness of the real companion is then measured by subtracting the artificial companion at its location in the images, while iteratively scaling the artificial companion's brightness until the residuals at this location are minimised. Here, we instead apply the concept of artificial planet injection to insert additional companions into the images. Furthermore, we use the instantaneous PSF of host star HD 1160 A provided by the dgvAPP360 in each frame as the template for the artificial companion in that frame. This is usually not possible for high-contrast imaging data as the host star is often blocked by a focal-plane coronagraph in such observations (e.g. Mawet et al. 2012; Ruane et al. 2018). However, this novel frame-dependent approach is advantageous because the template PSFs will reflect frame-to-frame changes, caused by time-varying systematics, in the shapes and sizes of the PSFs of real companions and their host stars.

We produced the artificial companion template PSF for each frame by first duplicating the frame, then dividing it by a flat frame produced by combining off-source frames from the same wavelength channel. We then cropped the template to a 12-pixel radius, and shifted it to the image coordinates where we wished to inject an artificial companion. Both the rotation of the field and drifts in the position of the star on the detector were taken into account in calculating these coordinates, such that the companion was injected at the desired separation and position angle relative to the star. Next, we set all pixels less than 1% of the peak flux to zero, and scaled the flux to the required star-companion contrast. Where we wanted to simulate a variability signal, we did this by further multiplying the template by a sinusoidal function with the corresponding amplitude, period, and phase. Finally, we multiplied the template by the flat frame again and added it to the original data frame to inject the companion.

We injected six companions, three with no variability and three with simulated sinusoidal variability. Only one companion was injected per iteration. We did not attempt to remove the real companion HD 1160 B from the data, but ensured that the artificial companions were physically separated from it by choosing position angles at 90°, 180°, and 270° offset from that of HD 1160 B. We used the physical separation of HD 1160 B ($\sim$0.78″) for the separation of the artificial companions, as this placed them centrally in the coronagraphic dark hole of the dgvAPP360. We also used the flux of HD 1160 B as a baseline flux for many of the injected companions, assuming an L'-band contrast of contrast of $\Delta L' = 6.35$ mag (Nielsen et al. 2012). Sutlieff et al. (2023) found sinusoidal-like variations in their light curve of HD 1160 B and fitted them with a 8.8% semi-amplitude sinusoid with a period of 3.239 h, phase shift of 0.228, and y-offset of 0.993. To enable a comparison to their results, we simulated this variability signal for the time-varying artificial companions.

5.2.3 Data processing and extracting spectrophotometry

Once an artificial companion had been injected to the data, we followed the standard steps for processing data of this type and extracting photometry of the targets, as described by Sutlieff et al. (2023).

Firstly, we corrected for errors in the response of the detector by dividing each frame by the flat frame previously used in the preparation of the artificial companion templates. We then masked the host star HD 1160 A, the companion HD 1160 B, and the artificial companion, before fitting and removing a third-order polynomial from each image column and then repeating this process for each row. This was done to correct for systematic discontinuities that exist in ALES data, arising from the overlap of the micro-spectra with different LMIRcam detector channels (Doelman et al. 2022). We then shifted the frames to align the star to the centre of each frame, and derotated them to account for the field rotation and align the data to north. Examples of the final images are shown in the left-hand and centre panels of Figure 5.1, median combined in time and wavelength to highlight the companions by increasing their signal-to-noise ratio (S/N). The left-hand panel shows the final image with no artificial companions; the real companion, HD 1160 B, can be clearly seen. This is the same as the left-hand panel of Figure 3 in Sutlieff et al. (2023). The centre panel then additionally contains three artificial companions with the same contrast as HD 1160 B, but located at positions offset from it by intervals of 90° in position angle. This image is a composite; in practice, only one artificial companion was injected into the data at a time, but we show multiple artificial companions per frame here to demonstrate the relative locations at which they were injected.

Next, we extracted aperture photometry for the host star and each artificial companion in each frame in both wavelength and time. We used the same aperture radii as Sutlieff et al. (2023), which were 9 pixels (3.1 λ/D) and 2.5 pixels (0.9 λ/D) for the star and artificial companions, respectively. We also subtracted any residual background flux in these apertures using the annuli to estimate the background at their locations. For the star, we did this using an annulus centred on the star with an inner radius of 11 pixels and an outer radius of 16 pixels. For the companions, we also used an annulus centred on the star, but with a width of 6 pixels at the radial separation of the companion. Both the artificial companion and HD 1160 B were masked for this process, so that they did not contaminate our estimate of the background. An example of these apertures and annuli for an artificial companion 180° offset from HD 1160 B can be seen in the right-hand panel of Figure 5.1, superimposed on a single frame of data.

5.2.4 Companion light curves

Once we had extracted photometric measurements for the host star and each artificial companion in each wavelength channel, we applied the steps of Sutlieff et al. (2023) to create detrended differential white-light curves for each companion. We first took the median combination of the photometric measurements over the 3.59-3.99 µm range, producing single white-light flux measurements for each object at each time. For each companion, we then divided these white-light flux measurements by the white-light flux measurements of the host star. This step has the effect of removing any systematic trends shared by the time series of both objects from the flux of the companion, leaving behind a differential light curve containing non-shared variations only. This includes both the simulated variability signal of the injected companion and any residual systematic trends. Such systematics can

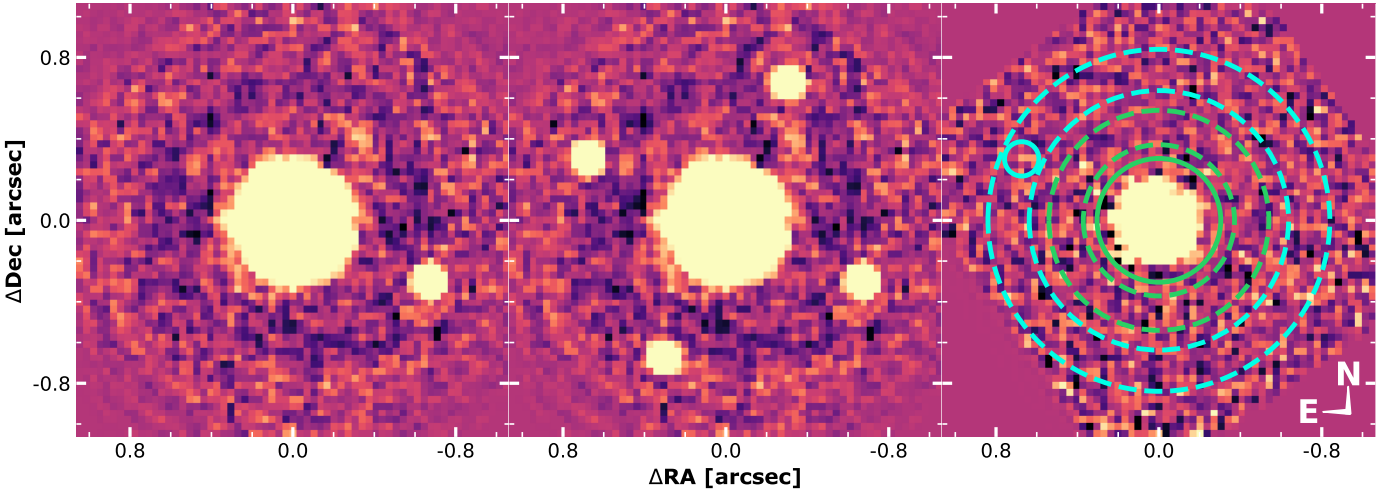

Figure 5.1: The left-hand and centre panels are examples of the final processed LBT/ALES+dgvAPP360 images produced when the data were median-combined in both time and wavelength. Left: the case where no artificial companions were injected to the data, so only the bright host star HD 1160 A and its bona fide companion HD 1160 B is visible. Centre: similar to the left-hand panel, but three artificial companions have been injected at 90° intervals in position angle from HD 1160 B. All three artificial companions were injected with contrasts of 6.35 mag relative to the host star. This image is a composite; for the purposes of the analysis, only one companion was injected at a time. Right: A single frame of data highlighting examples of the apertures and annuli used to extract photometry and background measurements for the host star (in green) and artificial companions (in blue). The left-hand and centre panels use the same arbitrary logarithmic colour scale while the right-hand panel uses a different one, and all three panels are aligned to north, where north is up and east is to the left.

arise from the effects of Earth's atmosphere, as well as from the instrumentation and data reduction process, and many of them will be the result of differences in the properties of the star and companion (e.g. Broeg et al. 2005; Pont et al. 2006). However, we note that while the artificial companions that we inject here do differ from the host star in brightness and position in the data, they do not reflect the difference in colour that would exist for a real companion because their template PSFs were constructed using the PSF of the star. In this regard, the artificial companions are not perfectly reflective of true companions and thus these residual systematics may differ slightly.

Nonetheless, we proceeded to detrend the differential white-light curves of each artificial companion further using a multiple linear regression approach with the same decorrelation parameters used by Sutlieff et al. (2023), thereby partially mitigating any residual systematics from these known sources. These decorrelation parameters were airmass, air temperature, wind speed, wind direction, and the x,y-positions of both the star and companion in the original data cubes. We produced a linear regression model for each artificial companion using these parameters, and then divided the model out of the light curve of the corresponding companion. The final, detrended, differential white-light curves for each artificial companion are shown in Figure 5.2, binned to 18 minutes of integration time per bin. The left-hand panels are those that were injected with no variability signal, and the right-hand panels are those that were injected with the variability signal found by Sutlieff et al. (2023) for HD 1160 B. The raw differential white-light curves, prior to detrending and again in 18 minute bins, are also shown overplotted in lighter colours for comparison. The error bars are the median absolute deviation (MAD) $\times$ 1.48 of the data points in each bin divided by $\sqrt{N-1}$, where N is the number of frames in each bin. We analyse the detrended differential white-light curves in Section 5.4.

5.3 Simulations

Artificial planet injection and recovery allows us to characterise the overall effect of systematics present in the data on differential light curves produced through the process described in Section 5.2. In this section, we take an additional step to understand the individual contributions of known sources of systematic errors: non-common path aberrations (NCPAs) and residual wavefront errors generated by the correction of atmospheric turbulence using adaptive optics (AO), i.e. AO residuals. Both effects can generate varying speckles at the location of a companion, influencing the flux measured with aperture photometry.

We used the Python package HCIPy (Por et al. 2018) to produce simulated LBT/ALES+dgvAPP360 data including NCPA and AO residuals, allowing us to test their impact on variability measurements obtained using vAPP-enabled differential spectrophotometric monitoring. HCIPy is capable of generating both static wavefront errors and dynamic turbulence phase screens, simulating adaptive optics systems, propagating aberrations through the coronagraph to the focal plane, and simulating realistic camera images from the resulting PSF. We simulated the LBT/ALES+dgvAPP360 system in HCIPy by propagating an unpolarized wavefront through the dgvAPP360 optic to the focal plane. This input wavefront had an

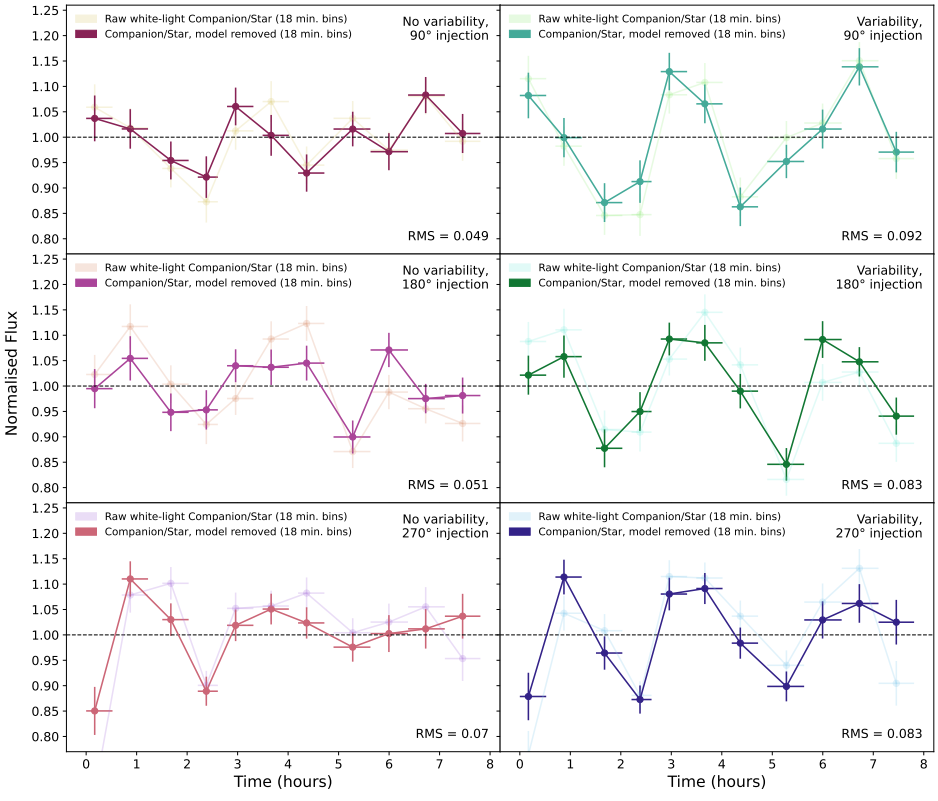

Figure 5.2: The raw differential white-light curves for each of the injected artificial companions are shown in lighter colours in each panel, binned to 18 minutes of integration time per bin. The detrended differential white-light curves, after division by the multiple linear regression model to remove the modelled systematic trends, are then overplotted in darker colours. The left-hand panels show the light curves for the artificial companions injected without variability, whereas the right-hand panels are those injected with a simulated sinusoidal variability signal. The root mean square (RMS) shown are those of the detrended light curves.

amplitude given by the LBT pupil without secondary support and with no phase aberrations. We downsampled the dgvAPP360 design by a factor of 4.3 using matrix Fourier transforms to improve the simulation speed while minimizing the impact on the performance of the coronagraph. The focal plane sampling was chosen to closely match that of a single wavelength channel of LBT/ALES data after it has been extracted into a 3D cube of 63 x 63 pixel images. We directly compared our simulations to the background-subtracted images of the HD 1160 system described in Section 5.2.1, allowing us to match this sampling to real data to the sub-pixel level. These simulations are monochromatic at a wavelength of 3.75 µm.

We then simulated a companion using the same steps, except that the input wavefront was given an additional tip and tilt phase ramp to place the source off-axis at the desired companion location. The location of the companion was matched with the photometric mask (i.e. aperture) used by Sutlieff et al. (2023) to extract the flux of HD 1160 B. We also scaled the companion flux level to match that of HD 1160 B, assuming an L'-band contrast of contrast of $\Delta L' = 6.35$ mag (Nielsen et al. 2012). We did not provide the simulated companion with a variability signal. As the simulated and real data were closely matched in this way, we were able to perform aperture photometry for the simulated star and companion using the same focal plane aperture masks used for the original analysis (see right-hand panel of Figure 5.2). However, we first injected the desired aberrations (e.g. NCPA and AO-residual wavefront aberrations) to the data to simulate their effect on the photometric measurements. These are described in the following subsections.

5.3.1 Impact of low-order aberrations

NCPAs are aberrations generated by the optical system after the beam splitting of incoming light into the two paths that lead to the AO wavefront sensor and to the detector, respectively. These aberrations also vary in time due to effects such as atmospheric turbulence, thermal drifts, and vibrations in the instrumentation, with timescales ranging from a few seconds to several hours (e.g. Sauvage et al. 2007; N'Diaye et al. 2014; Vigan et al. 2019, 2022; Skaf et al. 2022). In principle, slowly varying NCPAs could induce a false variability signal in differential light curves obtained using differential spectrophotometry, if they impact the extracted photometry of the star and the companion differently. To the first order, the dgvAPP360 coronagraph is insensitive to these aberrations as the impact on the Strehl ratio is the same for both the star and the companion. However, changes in the shapes and the sizes of the companion and star PSFs over time can impact the ratio of their fluxes, particularly if different aperture sizes are used for each object. The companion may also move over stellar speckles caused by NCPAs as the field rotates, contaminating its flux. Mitigating NCPAs is challenging, as they are introduced after the incoming light is split by the beam splitter and therefore cannot be corrected even by the most powerful AO systems. Furthermore, the properties of NCPAs cannot be inferred from observational data itself as the photon noise from the thermal background is too high. Here, we used HCIPy to investigate which aberrations have the largest effect on companion and stellar photometry and whether or not a realistic distribution of NCPAs can have a significant impact on variability measurements obtained through vAPP-enabled differential spectrophotometry.

We added simulated NCPAs to our simulated data using the first 100 Zernike modes, a series of polynomials that describe wavefront aberrations in optical systems (Zernike 1934; Noll 1976; Niu & Tian 2022). We added one mode per iteration, allowing us to measure their individual impact on the companion flux over the observing sequence. The Zernike modes were scaled to 120 nm RMS in the pupil. We varied the companion location by rotating it according to the 109.7° of field rotation of the real data set described in Section 5.2.1. However, the aberrations remained static with respect to the pupil as the observations were pupil-stabilised. We show the impact of three low-order aberrations (defocus, coma and quadrafoil) on the star and companion PSFs at three different observing times in Figure 5.3. These images highlight how even a static aberration can affect the observed flux of a companion over an observing sequence as it moves over the spatially-varying structure of the stellar PSF. Symmetric modes will inherently induce less systematic variability, while asymmetric modes will have a greater impact. For example, variability induced by the quadrafoil aberration will have a higher frequency than that of the coma aberration. We also note that all variability induced by static modes is a direct function of the angular rotation rate, and is thus observatory dependent for a given object (and vice versa).

We then derotated the data by the rotation angles and extracted stellar and companion photometry for each of the 100 simulated Zernike modes, where the modes were all scaled to the same 120 nm RMS wavefront error. The time-averaged normalised fluxes of each object are shown as a function of Zernike mode (represented by its Noll index, Noll 1976) in the top panel of Figure 5.4. The error bars indicate the minimum and maximum measured fluxes (i.e. the peak-to-peak variability amplitude) over the observing sequence covering the 109.7° of field rotation. The error bars for the star are too small to be visible. For the stellar flux, we find a decrease in flux and larger differences per mode for higher Noll indices. This is the direct result of scaling by RMS wavefront error, as higher-order modes will have a larger peak-to-valley error for the same RMS wavefront error. Interestingly, the measured companion fluxes do not match the same pattern as the stellar fluxes. Dividing the companion flux by the stellar flux therefore does not improve the photometric stability.

In this scenario, where the wavefront error is 120 nm RMS for a single mode, the offset of the companion flux from a normalised flux of one is on the order of a few percent for most Zernike modes. The speckles generated by a single Zernike mode dominate the measured companion flux for this $\Delta L'$. The level of variability in the measured flux of the companion, arising from the changing rotation angle, also changes significantly between modes. We find that most modes induce $\sim$1% variability over the observing sequence, most likely due to rotation and derotation interpolation effects which could also be present in real data of this type. However, the change in companion flux is much higher for some modes, up to $\sim$10%.

At first glance, this paints a worrisome picture for the determination of companion variability in the presence of static NCPAs. However, the outcome is different if we consider a more realistic system. While the total residual wavefront error for high-contrast imaging systems can be on the order of 120 nm RMS (e.g. Hartung et al. 2014; Males et al. 2016; Rabien et al. 2019), the wavefront error per mode is generally not as strong as assumed in the simulations above. The aberrations described by Zernike modes are expected to follow an

inverse power law in aberration strength, and therefore quickly reduce in amplitude with increasing Noll index (e.g. Sauvage et al. 2007; Lamb et al. 2018). We therefore repeated our simulations testing the impact of individual Zernike modes, this time applying a power law with a slope of -1.5 (a conservative estimate) as a function of radial frequency. The resulting time-averaged normalised fluxes for the star and the companion in this scenario are shown in the bottom panel of Figure 5.4. These more realistic simulations indicate that only the lowest-order aberrations are likely to significantly impact measurements of companion flux.

5.3.2 Realistic simulations of vAPP-enabled differential spectrophotometry data

In addition to our analysis of NCPAs, we also attempted to produce a more realistic simulation of the observational dataset targeting the HD 1160 system described in Section 5.2.1. With this goal, we used HCIPy to generate several noise factors including wavefront aberrations arising from atmospheric turbulence. Uncorrected wavefront aberrations can produce a varying field of residual stellar speckles that can impact companion variability measurements in much the same way as NCPAs (e.g. Hinkley et al. 2007; Martinez et al. 2012, 2013; Males et al. 2021).

First, we used the wind speed, wind direction, and airmass measurements obtained by Sutlieff et al. (2023) for the HD 1160 data set to generate representative turbulence phase screens. We set the seeing to 1.1″, the coherence time 15 ms, and we scale the Fried parameter with the airmass. We simulated the adaptive optics system using the HCIPy adaptive optics layer, with 500 Zernike modes and a lag of two frames. The seeing and the AO loop speed were chosen such that a Strehl ratio of around 85% was achieved in H-band and 98% at 3.7 micron, similar to the performance reported in Skemer et al. (2014a). We generated 100 random realizations simulating Earth's atmosphere and run the AO-system for 22 frames in 0.4 seconds, thereby producing 2200 frames, the same number as the HD 1160 data set. This allowed us to match each frame with a frame from the HD 1160 data and move the companion according to the rotation angle of that frame. We did not add NCPAs for this simulation.

Next, we made the frames more reflective of real data by adding photon noise and background noise using the NoisyDetector module of HCIPy. We calculated the photon noise for each frame using a total power of 40.000 photons, which we matched empirically to the count levels of the HD 1160 data. The background noise comes from the photon noise of the thermal background; as the HD 1160 frames were background-subtracted before the multi-wavelength image cubes were extracted, it is difficult to estimate the actual background levels for our simulated wavelength channel. We therefore chose to include the photon noise of the background through the read noise option of the NoisyDetector module, empirically matching the noise levels to the HD 1160 data as 12 counts. Example frames from these simulations showing the PSFs of the star and the companion are shown in Figure 5.5. The left-hand panel shows the PSFs when we only include the residual wavefront error due to uncorrected atmospheric turbulence in the simulation. This turbulence generates speckles in the wind direction, which add up to form a faintly visible wind-driven halo (e.g. Cantalloube et al. 2018, 2020a; Madurowicz et al. 2019). The excellent performance (i.e. high Strehl

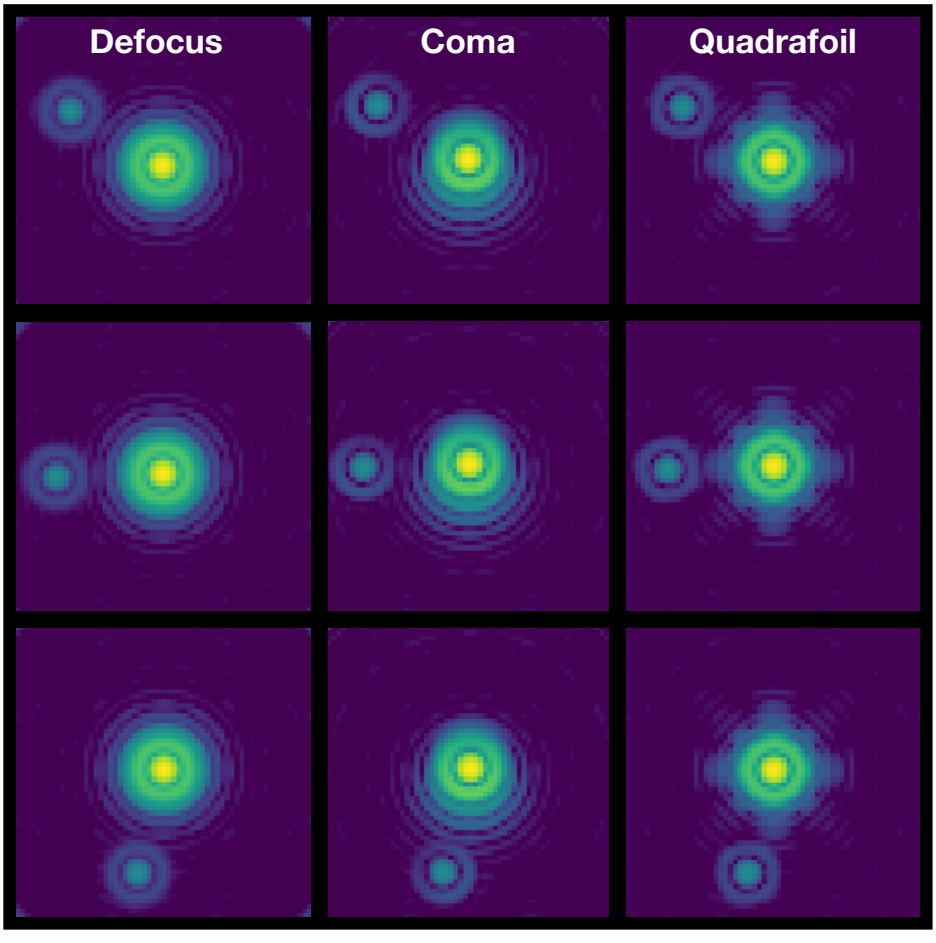

Figure 5.3: Simulated PSFs of a star and companion for a different Zernike mode are shown in each column at three different observing times. The data are in pupil-stabilised mode, so the aberrations remain static while the companion rotates over time. The symmetry in the Zernike mode and the location of the companion together determine the measured companion flux in an aperture.

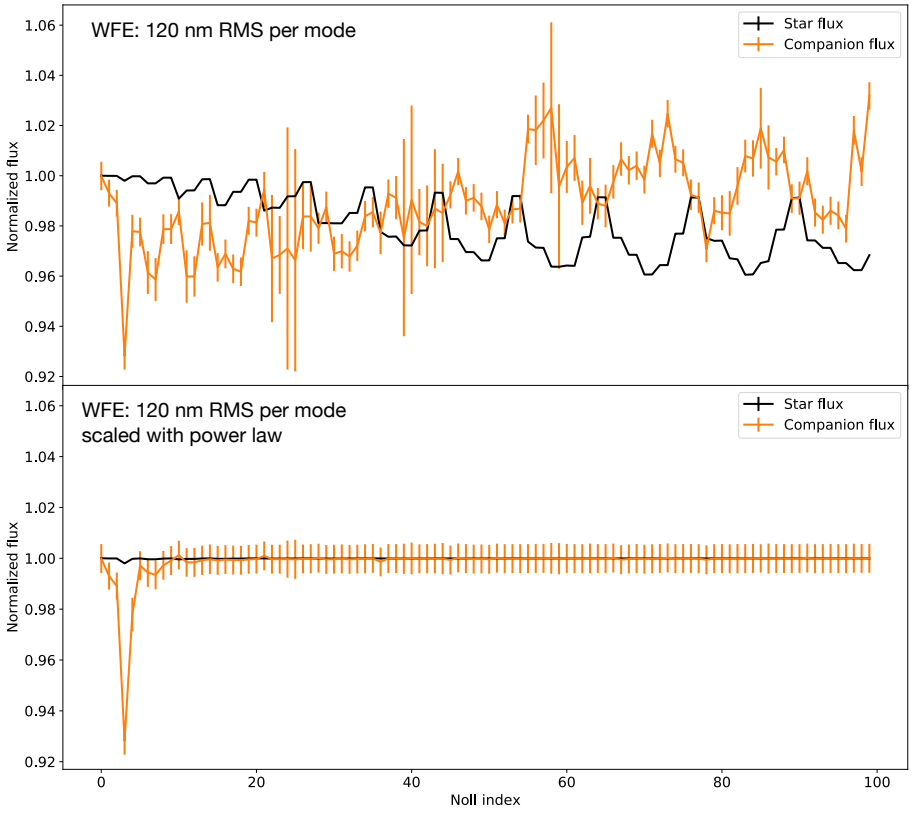

Figure 5.4: Simulated normalized flux of the star (black) and the companion (orange) for the first 100 Zernike modes, given by their Noll indices. The errors bars indicate the maximum and minimum retrieved companion flux over the observing sequence. The error bars for the star are too small to be visible. Top panel: all Zernike modes have the same 120 nm RMS wavefront error. Bottom panel: The power in the modes is scaled by a power law with a slope of -1.5, similar to expected NCPAs. In this more realistic scenario, we find that only the lowest-order aberrations are likely to significantly impact the average flux of the companion over the observing sequence.

ratio) of the simulated adaptive optics system in the L-band means that residual speckles are minimal and are less bright than the companion. The centre panel is the same as the left-hand panel, but with photon noise added to the simulation. Now, only the core of the companion is visible due to the low number of counts. Finally, in the right-hand panel, we also add background noise. The companion is no longer visible in a single frame as the background dominates its signal at its location. The background also significantly contributes to the measured stellar flux.

We then extracted photometry for the star and the companion in each frame for each of the three scenarios shown in Figure 5.5, again using the same photometric masks after derotating the frame. These normalised fluxes are shown as a function of time in Figure 5.6. The left-hand panels are the fluxes of the star and the right-hand panels are those of the companion. We find that the star varies by less than 1% in the residual wavefront error case. This variation shows a clear trend and can be attributed to the reduced AO performance for the larger airmasses at the start and end of the observing sequence. In this case, the companion flux shows higher amplitude trends with a more complex shape than a simple airmass correlation. However, its variability is nonetheless only on the order of 1%. When photon noise is added (second row panels), the stellar flux shows a significantly increased scatter. Moreover, the scatter in the companion flux is between $\pm 30\%$ and binning is required to recover precise photometry. Finally, in the case where all three noise factors are included (bottom row panels), the scatter in the stellar flux is not much greater than before. However, the scatter in the measured companion flux has increased dramatically and sometimes even negative flux values are measured. We note that the scatter in the companion flux that is generated in the simulation has a similar magnitude to the scatter in the raw companion flux in the HD 1160 data set as measured by Sutlieff et al. (2023), whereas the scatter of the simulated stellar flux is less than that of the raw stellar flux in the HD 1160 data. However, this simulation has several key caveats and is not a perfect reflection of real data. There are several important effects that we did not include in the simulation, such as the reduction of atmospheric transmission with increasing airmass.

We further compared the normalised flux distributions of the 2200 simulated frames in all three scenarios, allowing us to explore the respective contributions of each noise source to the measured photometry. These are shown in Figure 5.7, where the left-hand and right-hand panels show the histograms of the stellar and companion fluxes, respectively. If we consider the stellar flux, we see that the stellar flux measurements are dominated by the photon noise of the star itself. The background noise has a far more dramatic impact for the companion and dominates the recovered photometry, as we might intuitively expect from the PSFs in Figure 5.5. Both photon noise and the background noise are random, and so binning the frames will reduce the scatter with the square root of the number of frames per bin (see Section 5.4). This behaviour of the noise was also demonstrated for the HD 1160 data set in Sutlieff et al. (2023), and can be seen following the white noise trend in their Figure 13.

To allow a comparison to the differential light curves of the injected companions shown in Figure 5.2, we divided the simulated companion flux for the scenario including all three noise sources by the simulated stellar flux, thereby producing a raw differential light curve.

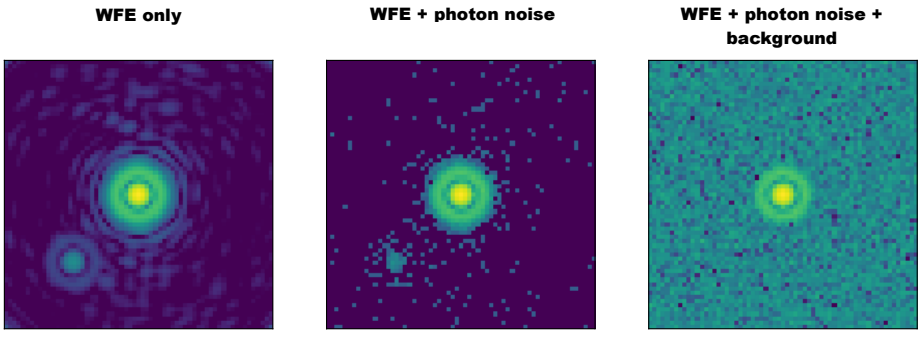

Figure 5.5: Simulated point-spread functions. The left-hand panel shows the PSF for the residual wavefront error after adaptive optics correction. The centre panel shows the same PSF simulated with photon noise, assuming a photon flux of 40.000 photons for a single image. This photon number is empirically matched to the counts in a single frame of the HD 1160 data. The right panel shows the same PSF as the left panel with photon noise and noise from the thermal background. This background noise is implemented as read noise and the amount is also empirically matched with the statistics in a single frame of the HD 1160 data.

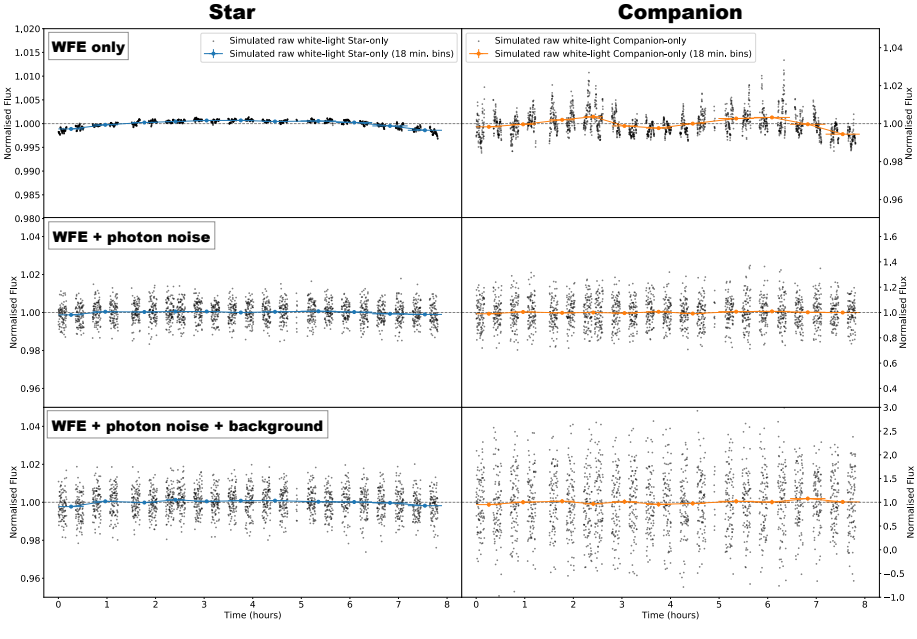

Figure 5.6: Simulated aperture photometry measurements for the star (left panels) and the companion (right panels) for the three aberration and noise scenarios.

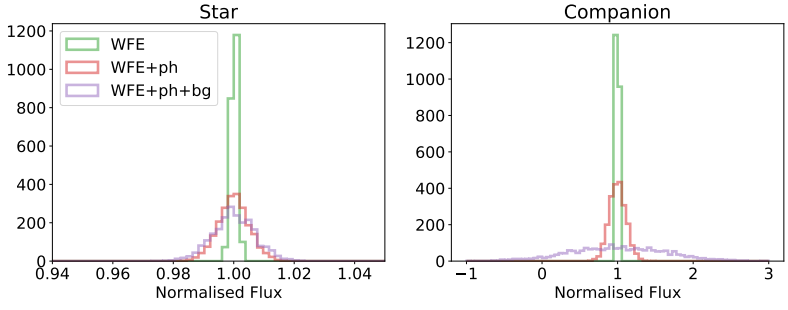

Figure 5.7: Histograms of the simulated photometric measurements for the star in the left panel and the companion in the right panel. The three colors indicate the three aberration and noise scenarios; residual wavefront error after adaptive optics correction, photon noise, and noise due to the thermal background.

We then binned this light curve to the same binning used for the light curves of the injected companions in Section 5.2.4 (i.e. 11 bins of 200 frames per bin). The obtained raw differential light curve is shown in Figure 5.8, and has a scatter and error bars that closely match those of the non-varying artificial companions shown in Figure 5.2. This suggests that the dominant effects in the real data have been accurately accounted for in our simulations.

5

5.4 Artificial companion variability analysis

In this section, we search for periodic signals in the detrended differential white-light curves of the artificial companions. This allows us to test not only whether we can recover the variability properties that were used for the time-varying artificial companions, but also whether residual systematics induce false periodic trends in the light curves of the non-varying artificial companions. We then use the light curves of the non-varying companions to further assess the limiting precision of this data set.

We produced Lomb-Scargle periodograms for each artificial companion using their unbinned detrended differential white-light curves (Lomb 1976; Scargle 1982). Each periodogram was normalised by the variance of the datapoints in the corresponding light curve, following the implementation of (Horne & Baliunas 1986). The periodograms for the artificial companions that were injected without and with variability are shown in the left-hand and right-hand columns of Figure 5.9, respectively, horizontal black dashed lines and brown dotted lines representing the 10% and 1% false-alarm power thresholds, respectively. The powers, periods, and false alarm probabilities of the strongest peaks in the periodograms for each of the companions injected with a variability signal are given in Table 5.1. We find no peaks above 1σ for the artificial companions injected without any variability at 90° and 180° offsets from HD 1160 B, as would be expected for a flat light curve. For the artificial companions injected with variability at the same positions, we find $\sim$5-6σ peaks at approximately the injected period. However, the periodograms for the companions injected at a 270° offset are more surprising. The periodogram of the non-varying companion at this location shows

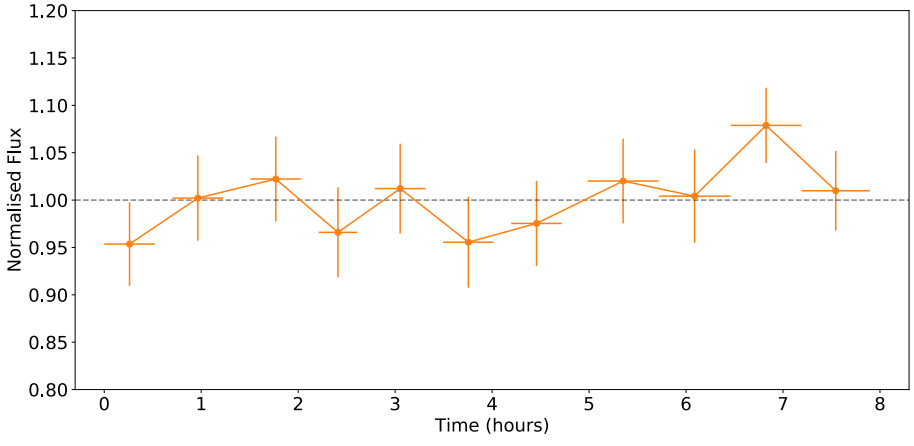

Figure 5.8: The raw differential light curve for the simulated companion in the scenario that includes the residual wavefront error after adaptive optics correction, the photon noise, the photon noise, and the noise due to the thermal background.

a strong peak at a 0.619 hour period, with several other peaks above the 1% false-alarm power threshold. The strongest peak in the 270° time-varying companion periodogram is also at this period, albeit with a lesser power. This may indicate that the light curves of the injected companions at this location are contaminated with one or more short-period periodic systematics. The second strongest peak in the periodogram of the time-varying companion does lie close to the injected period, although it has a shorter period of 2.638 hours.

We further fitted sinusoids to the detrended differential white-light curves of the time-varying artificial companions so that we could directly compare the amplitude and phase of their variability to that of the injected signal. We did this using a non-linear least squares approach with the 3.34 hour and 3.03 hour periods obtained from the periodogram peaks as the initial guesses for the fits to the 90° and 180° light curves, respectively. For the 270° light curve, we used the 2.64 hour period of the second strongest peak in its periodogram as the initial guess, assuming that this peak does arise from the variability signal that we injected. The properties of these sinusoidal fits are given in Table 5.1, and the fits themselves are shown overplotted in purple on the corresponding light curves in the left-hand column of Figure 5.10. The top panel of this figure shows the original injected variability signal, for comparison. The panels in the right-hand column are the same as on the left, but phase-folded to the periods of the respective sinusoids. We can see that while the recovered sinusoids are broadly similar to the injected variability, their amplitudes are consistently slightly higher than what was injected. The phases of the recovered variability signals are also different, although these values appear to be correlated with the recovered period values such that the peaks and troughs of the injected and recovered sinsuoids are roughly aligned. We discuss these results further in Section 5.5.1.

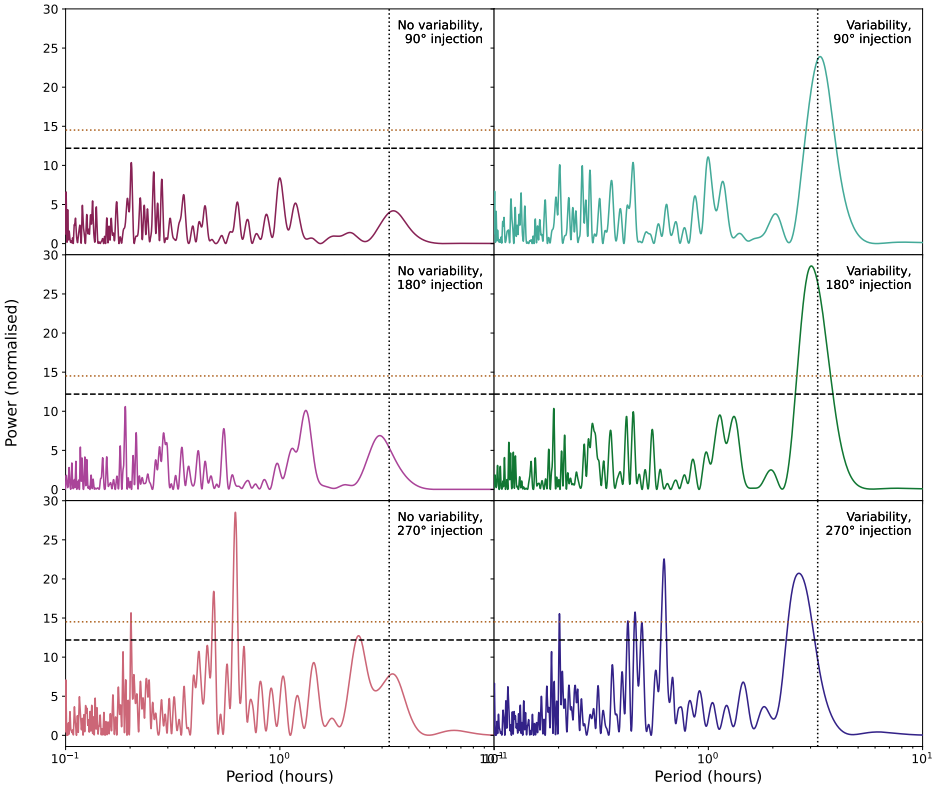

Figure 5.9: The Lomb-Scargle periodograms for the differential white-light curves of each artificial companion. The left-hand panels are the periodograms for the companions injected without any variability, while the right-hand panels are those for the companions injected at the same coordinates but with a sinusoidal variability signal. The vertical dotted lines indicate the ∼3.24 h period of the injected variability signal. The horizontal black dashed lines and brown dotted lines show the power thresholds corresponding to false-alarm probabilities of 0.1 (10%) and 0.01 (1%), respectively.

We also assessed the noise properties of each light curve using the method used by Kipping & Bakos (2011) and Sutlieff et al. (2023). We first binned the unbinned detrended differential white-light curve of each artificial companion to a range of bin sizes, then normalised the data and subtracted one to centre each light curve around zero. The RMS of each light curve was then measured for each bin size. These values are plotted in Figure 5.11, with a black line showing the theoretical white noise model. We find that the RMS values of the light curves of the artificial companions injected with time variability sit higher than those without variability.

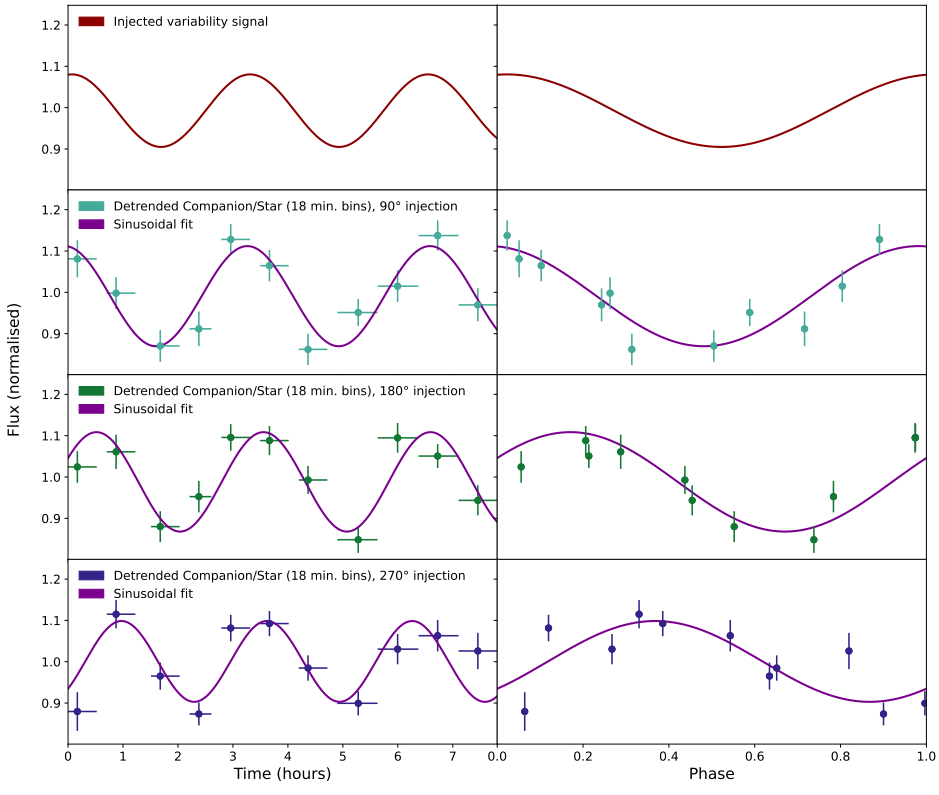

Figure 5.10: The top row shows the sinusoidal variability signal that was given to the artificial companions injected with variability, as a function of time in the left-hand panel and phase-folded to its 3.24 hour period on the right. The left-hand panels of the following three rows show the detrended differential white-light curves of the three artificial companions that were injected with this variability, reproduced from the right-hand column of Figure 5.2, and the purple lines show the best-fitting sinusoids to these light curves. These light curves and sinusoids are then phase-folded to their respective periods in the right-hand panels.

Table 5.1: The properties of the injected variability signal and the sinusoidal variability recovered from the detrended differential white-light curves of each of the time-varying artificial companions. The powers, periods, and false alarm probabilities of the strongest peaks in the periodogram for each of these companions are also given.

Variability property	Injected variability	90° injection	180° injection	270° injection
Pgram. peak power	–	23.9	28.6	22.6
Pgram. peak period	–	3.337	3.027	0.622
Pgram. peak FAP	–	7.13e-07	5.99e-09	2.85e-06
Period	3.239	3.324	3.038	2.644
Semi-amplitude	0.088	0.121	0.120	0.098
Phase	0.228	0.269	0.080	-0.118
y-offset	0.993	0.991	0.988	1.001

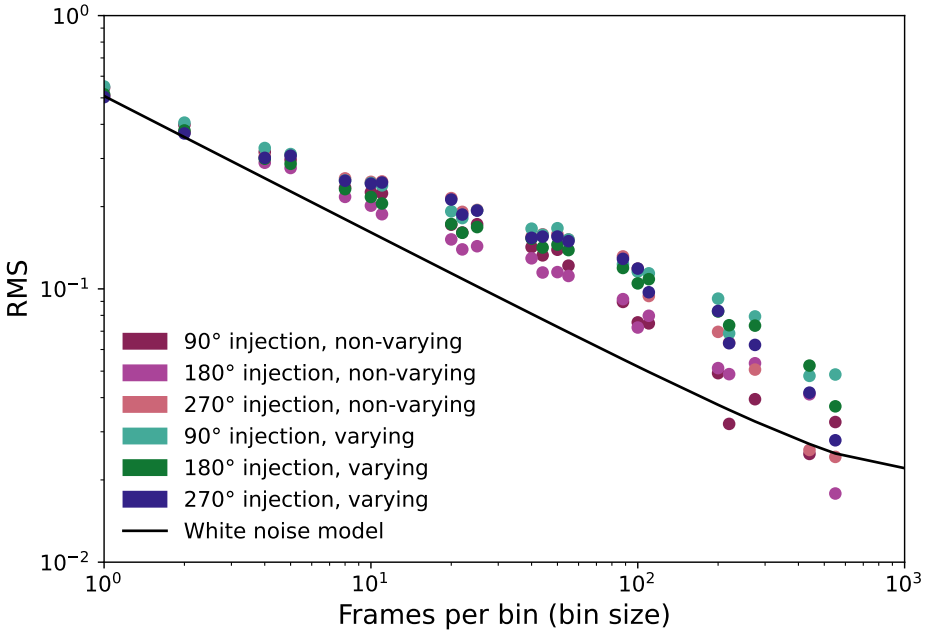

Figure 5.11: The RMS of the binned detrended differential white-light curves of the six injected artificial companions as a function of bin size. The theoretical white noise model is also shown.

5.5 Discussion

5.5.1 Artificial companions

In Section 5.4, we produced Lomb-Scargle periodograms for the detrended differential light curves of each of the six injected artificial companions. We find that we successfully recover the expected variability signals for the companions injected at 90° and 180° offsets from the real companion HD 1160 B. We find no significant peaks for those injected with no variability signal (i.e. a flat line) at these locations, and detected strong peaks at the expected period for those that were injected with sinusoidal variability matching that of HD 1160 B (as measured by Sutlieff et al. 2023). Although the injected variability was chosen to match the fitted sinusoid obtained for the variability of HD 1160 B, these periodogram peaks (5-6σ) are more significant than that measured for the periodic variability of HD 1160 B ($\sim$2.5σ, Sutlieff et al. 2023, Sutlieff et al. in preparation). This could be because the intrinsic variability of HD 1160 B is complex and cannot be perfectly described by a singular sinusoid with a regular period. The variability signals of several other substellar companions in the literature have been attributed to multiple atmospheric features, and in many cases have been seen to evolve over time (e.g. Artigau et al. 2009; Metchev et al. 2015; Karalidi et al. 2016; Apai et al. 2017; Zhou et al. 2022). However, the strength of our recovery of the variability of our artificial companions is more likely a reflection of the caveats of our artificial companion injection approach. The PSF template that we used for the injected companions was produced using the instantaneous PSF of the star in a given frame. This is unique in direct imaging and highly advantageous, as it allows us to capture the frame-to-frame changes due to time-varying systematics that would impact a real companion. However, this also means that the companion has the same colour as the star, so the difference in colour between a star and a real companion are not taken into account. The artificial companions therefore do not suffer from additional systematics that would arise for two objects of different colours, such as their different response to changes in airmass, for which accurate detrending is key (e.g. Broeg et al. 2005; Panwar et al. 2022b). Furthermore, the variability signal that we injected for the time-varying companions was the same in each of the 30 wavelength channels that were combined to produce their white-light fluxes. The variability of real substellar companions such as HD 1160 B is unlikely to be achromatic (e.g. Biller et al. 2013; Yang et al. 2016; Manjavacas et al. 2019b; Zhou et al. 2020b; Bowler et al. 2020b).

While the 90° and 180° injected companions produced the expected results, those at an offset of 270° did not. Although a significant peak was detected close to the injected period for the time-varying companion at this location, a stronger peak was detected at a far shorter 0.619 hour period. Moreover, this peak and others above the 1% false-alarm power threshold are also present in the periodogram of the companion injected with a flat signal. It is clear that the fluxes of the companions at this location are contaminated by periodic systematics. However, the cause of these systematics is not clear from the data.

If we consider the properties of the sinusoids that were fitted to the unbinned differential white-light curves (Table 5.1 and Figure 5.10), we find that their periods and phases are different and that none are a perfect match for the injected sinusoid. This suggests that a

single night of data is insufficient to accurately and reliably measure variability properties for variability of this period. The ∼7.81 hour duration of the data used here only covers ∼2.41 periods of the 3.239 h period of the injected variability, so it might be the case that a longer baseline covering more periods would achieve more consistent results. We also find that the recovered amplitudes are all greater than the injected amplitude. This may indicate that the approach of fitting simple sinusoids to light curves to measure variability tends to produce overestimated amplitudes.

5.5.2 Light curve precision

We also assessed the noise properties of the detrended differential white-light curves of each injected companion by measuring their RMS for a range of bin sizes (Figure 5.11). If we compare the RMS trend for the time-varying artificial companions to those injected without variability, we see that the RMS measurements of those with variability are generally higher, demonstrating that the level of scatter of the datapoints is distinct for companions with and without variability. We also see that these RMS trends do not plateau, matching the conclusion of Sutlieff et al. (2023) that this data set has not yet reached a noise floor and that further increasing the bin size with additional data would lead to an even greater precision.

If we take the RMS values of the non-varying artificial companion light curves at the bin size used in Figure 5.2 (200 frames per bin), we can produce a range for the limiting precision achieved at this bin size. These RMS measurements are 0.0492, 0.0513, and 0.0696 for the 90°, 180°, and 270° companions, respectively, giving a precision range of ∼4.9-7.0%. We note that the RMS measurement for the 270° companion is higher than the other two, likely due to the greater impact of systematics in this light curve, and thus the upper extent of this range is higher. For comparison, the RMS values at this bin size for the corresponding varying companions are 0.0921, 0.827, and 0.0830. We can also compare these results to those found by Sutlieff et al. (2023) for HD 1160 B. They measured ∼8.8% semi-amplitude variability in their detrended differential white-light curve, with a precision of 3.7% for a bin size of 200 frames. This precision was calculatded by dividing the unbinned detrended differential white-light curve of HD 1160 B by the fitted sinusoid to remove the intrinsic variability of the companion, then taking the RMS value (0.037) of the resulting light curve when binned to 200 frames per bin. This 8.8% variability is greater than the precision range estimated above and thus is likely to be astrophysical variability. The RMS values measured for the non-varying artificial companions are broadly consistent with the precision measured by Sutlieff et al. (2023) for HD 1160 B after the variability had been divided out, albeit slightly higher.

5.5.3 Non-common path aberrations

In Section 5.3, we produced a simulated differential spectrophotometry data set and added different aberrations to test their impact on the measured fluxes of the target PSFs.

We found that NCPAs have a significant impact on the measured fluxes of the star and the companion when we assume a wavefront error of 120 nm RMS per Zernike mode, but that

this is significantly lessened when we scale each mode by a more realistic (yet conservative) power law with a slope of -1.5. We see from the bottom panel of Figure 5.4 that in this latter case, high-order modes have minimal impact on the measured fluxes. However, some specific low-order modes can still lead to a reduction in the measured average companion flux over the observing sequence. This is because some modes (i.e. defocus, see Figure 5.3) cause the flux of the target to spread out more than others, hence less flux is contained within an aperture of the same size. Despite this average reduction in flux for some modes, we note that the error bars for these modes are small ($\pm$<1%) compared to some of those in the top panel. This suggests that for a given mode, the flux of the companion remains relatively stable over the observing sequence as it rotates through the field of view, and so the impact of these modes on companion variability measurements may be relatively minimal. In real differential spectrophotometry data, time variability arising from these modes is also likely partially mitigated by the detrending process applied to the differential white-light curves. In Section 5.2.4, we detrended the differential white-light curves of the artificial companions using a multiple linear regression approach including the positions of the companion and the star as decorrelation parameters. Thus, systematic trends associated with the movement of the companion over aberrations may be accounted for in the linear regression model.

For future observations with other instruments, systematics such as these could be further mitigated using focal-plane wavefront sensing techniques that remove NCPAs, such as phase diversity (e.g. Gonsalves 1982; Paxman et al. 1992; Doelman et al. 2017; Miller et al. 2018) or Fast & Furious wavefront sensing (e.g. Keller et al. 2012; Korkiakoski et al. 2014; Wilby et al. 2018; Bos et al. 2020b, 2021). Predictive wavefront control algorithms that predict the evolution of atmospheric turbulence over short timescales will also help to reduce their impact (e.g. Guyon & Males 2017; Jensen-Clem et al. 2019; van Kooten et al. 2020, 2022; Haffert et al. 2021; Fowler et al. 2022).

5.5.4 Simulated noise sources

We also produced a separate simulation in which we attempted to simulate some of the key noise sources that affect real differential spectrophotometry data obtained with LBT+ALES/dgvAPP360; realistic residual wavefront errors, photon noise, and thermal background noise.

We found that the star is bright enough that measurements of its flux are dominated by its photon noise, but that flux measurements of the far fainter companion are instead dominated by noise arising from the thermal background (see Figure 5.7). When we then used this simulation to produce a raw differential light curve of a simulated companion and binned it to the same binning used for the injected companions (Figure 5.8), we found that the scatter of the data points is very similar to those of the non-varying artificial companions. Although this simulation is by no means comprehensive and does not include every source of systematics, this suggests that a significant fraction of the RMS measured for the real data in Section 5.5.2 can be accounted for by the photon noise and thermal background. As mentioned previously, the scatter due to both of these effects can be reduced by binning frames. This is therefore consistent with the trends that we see in Figure 5.11, which show

that increasing the bin size with additional data will continue to improve the precision achieved in differential light curves.

5.6 Conclusions

We present an analysis of the vAPP-enabled ground-based differential spectrophotometry technique for measuring the variability of high-contrast substellar companions, in which we explore the systematics that limit the precision achieved with this technique.

We injected artificial companions with and without simulated variability signals into real observational data at different locations. The data used for this study were the LBT/ALES+dg-vAPP360 observations of the HD 1160 system first presented by Sutlieff et al. (2023), who used this technique to measure the variability of substellar companion HD 1160 B. Injecting artificial companions with no variability allowed us to assess the extent to which telluric, instrumental, and other systematics contaminate the data, while artificial time-varying companions let us test how well the injected variability can be recovered. Uniquely for a direct imaging study, we used the instantaneous stellar PSF in each frame as the template for the artificial companion, thus capturing frame-to-frame systematic variations that would affect a real companion. We injected artificial companions at 90° interval offsets from HD 1160 B, and used the methodology presented by Sutlieff et al. (2023) to process the data and extract spectrophotometry for the host star and each artificial companion. We then produced differential white-light curves for each companion and detrended them using a multiple linear regression approach.

Using Lomb-Scargle periodograms, we find that we successfully recover the injected variability signal to a high significance for the time-varying companions at 90° and 180° offsets from the real companion, and do not find any significant peaks for the non-varying companions injected at these positions. However, the periodograms for both the varying and non-varying companions injected at a 270° offset contain multiple peaks with false-alarm probabilities smaller than 1%, suggesting that companions at this location suffer from periodic systematics.

We also find that the properties of the recovered sinusoids (amplitude, period, and phase) do not perfectly match the injected sinusoid, indicating that a single night of data (∼7.81 h) is insufficient to accurately measure variability properties for variability of a 3.24 h period. Observations with a longer baseline covering a larger number of periods is therefore required to obtain accurate measurements of companion variability properties.

We find that the RMS of the detrended differential white-light curves of the injected companions decreases with increasing bin size according to the white noise model without plateauing, consistent with the result found by Sutlieff et al. (2023) for their light curve of HD 1160 B. This suggests that the data is not systematic-limited and that additional data could allow a greater precision to be reached. We also find that the RMS measurements of the artificial companions injected with variability are generally higher than those without variability. The RMS values for the light curves of the non-varying companions range from 0.0492-0.0696 for a binning of 200 frames per bin, suggesting a limiting precision of 4.9-7.0% at this bin size. The 8.8% semi-amplitude variability measured by Sutlieff et al. (2023) for HD 1160 B

is higher than this level and so we conclude that this remains consistent with astrophysical variability.

We also used simulated data, produced using the Python package HCIPy (Por et al. 2018), to test the effects of specific and known sources of systematics such as NCPAs and AO residuals. We simulated the LBT/ALES+dgvAPP360 instrumental setup and a simulated star-planet system with the same positions and contrast as those of the HD 1160 system. We also simulated the field rotation of the dataset, allowing us to extract photometry for the simulated star and companion using the same focal plane masks used for the real data. First, we tested the impact of NCPAs on the star and companion photometry by adding them to the simulated data using 100 Zernike modes. We find that when we scale the wavefront error of these aberrations with a realistic power law, high-order aberrations do not have a significant impact on the fluxes of the targets, but low-order modes can cause a significant reduction in the average measured flux of the companion over the observing sequence. However, we find that the variation in flux over the observing sequence for a given mode is $<1\%$, suggesting that companion variability measurements may be minimally affected by these aberrations.

We then simulated realistic residual wavefront errors, photon noise, and thermal background noise. We showed that flux measurements of the bright host star are dominated by its photon noise, while thermal background noise is the dominant effect for flux measurements of the simulated companion. We used this simulation to produce a detrended differential light curve and found that the scatter on the datapoints closely match those of the non-varying injected artificial companions when binned to the same bin size, suggesting that these same noise sources are the dominant effects in the real data. As the effects of both photon noise and background noise decrease with increasing bin size, this is consistent with the RMS trends that we measured for the injected companions.

For future observations, techniques such as predictive control and focal-plane wavefront sensing can help to further mitigate systematics arising from wavefront aberrations, and may therefore enable a greater precision to be achieved with vAPP-enabled differential spectrophotometry.

Acknowledgements

The authors would like to thank Frank Backs for valuable discussions that improved this work. BJS is fully supported by the Netherlands Research School for Astronomy (NOVA). JLB acknowledges funding from the European Research Council (ERC) under the European Union's Horizon 2020 research and innovation program under grant agreement No 805445. This paper is based on work funded by the United States National Science Foundation (NSF) grants 1608834, 1614320, and 1614492. The research of DD and FS leading to these results has received funding from the European Research Council under ERC Starting Grant agreement 678194 (FALCONER).

We acknowledge the use of the Large Binocular Telescope Interferometer (LBTI) and the support from the LBTI team, specifically from Emily Mailhot, Jared Carlson, Jennifer Power, Charles E. Woodward, Andrew J. Skemer, Jarron M. Leisenring, Phil Hinz, Michael Skrutskie,

Travis Barman, Ilya Ilyin, Klaus G. Strassmeier, and Ji Wang. The LBT is an international collaboration among institutions in the United States, Italy and Germany. LBT Corporation partners are: The University of Arizona on behalf of the Arizona Board of Regents; Istituto Nazionale di Astrofisica, Italy; LBT Beteiligungsgesellschaft, Germany, representing the Max-Planck Society, The Leibniz Institute for Astrophysics Potsdam, and Heidelberg University; The Ohio State University, representing OSU, University of Notre Dame, University of Minnesota and University of Virginia. We gratefully acknowledge the use of Native land for our observations. LBT observations were conducted on the stolen land of the Ndee/Nnēē, Chiricahua, Mescalero, and San Carlos Apache tribes.

This research has made use of NASA's Astrophysics Data System. This research has made use of the NASA Exoplanet Archive, which is operated by the California Institute of Technology, under contract with the National Aeronautics and Space Administration under the Exoplanet Exploration Program. This research has made use of the SIMBAD database, operated at CDS, Strasbourg, France (Wenger et al. 2000). This research made use of SAOImageDS9, a tool for data visualization supported by the Chandra X-ray Science Center (CXC) and the High Energy Astrophysics Science Archive Center (HEASARC) with support from the JWST Mission office at the Space Telescope Science Institute for 3D visualization (Joye & Mandel 2003). This work made use of the whereistheplanet[1] prediction tool (Wang et al. 2021a). This work makes use of the Python programming language[2], in particular packages including Matplotlib (Hunter 2007), NumPy (Harris et al. 2020), SciPy (Virtanen et al. 2020), Astropy (Astropy Collaboration et al. 2013, 2018, 2022), Photutils (Bradley et al. 2022), scikit-learn (Pedregosa et al. 2011), statsmodels (Seabold & Perktold 2010), pandas (McKinney 2010; Reback et al. 2022), HCIPy (Por et al. 2018), and PynPoint (Amara & Quanz 2012; Stolker et al. 2019).

Data Availability

The data from the HCIPy simulations and LBT/ALES+dgvAPP360 observations underlying this article will be available in the Research Data Management Zenodo repository of the Anton Pannekoek Institute for Astronomy shortly after publication, at https://doi.org/10.5281/zenodo.7603220.

[1] http://whereistheplanet.com/
[2] Python Software Foundation; https://www.python.org/

Bibliography

Ackerman, A. S. & Marley, M. S. 2001, *Precipitating Condensation Clouds in Substellar Atmospheres*, ApJ, 556, 872

Adams, J. C. 1846, *Explanation of the observed irregularities in the motion of Uranus, on the hypothesis of disturbance by a more distant planet; with a determination of the mass, orbit, and position of the disturbing body*, MNRAS, 7, 149

Alibert, Y., Mordasini, C., Benz, W., & Winisdoerffer, C. 2005, *Models of giant planet formation with migration and disc evolution*, A&A, 434, 343

Allain, G., Brousseau, D., Thibault, S., et al. 2018, *First on-sky results, performance, and future of the HiCIBaS-LOWFS*, in Society of Photo-Optical Instrumentation Engineers (SPIE) Conference Series, Vol. 10703, Adaptive Optics Systems VI, ed. L. M. Close, L. Schreiber, & D. Schmidt, 107035T

Allard, F. 2014, *The BT-Settl Model Atmospheres for Stars, Brown Dwarfs and Planets*, in Exploring the Formation and Evolution of Planetary Systems, ed. M. Booth, B. C. Matthews, & J. R. Graham, Vol. 299, 271–272

Allard, F., Hauschildt, P. H., Alexander, D. R., Tamanai, A., & Schweitzer, A. 2001, *The Limiting Effects of Dust in Brown Dwarf Model Atmospheres*, ApJ, 556, 357

Allard, F., Homeier, D., & Freytag, B. 2011, *Model Atmospheres From Very Low Mass Stars to Brown Dwarfs*, in Astronomical Society of the Pacific Conference Series, Vol. 448, 16th Cambridge Workshop on Cool Stars, Stellar Systems, and the Sun, ed. C. Johns-Krull, M. K. Browning, & A. A. West, 91

Allard, F., Homeier, D., & Freytag, B. 2012, *Models of very-low-mass stars, brown dwarfs and exoplanets*, Philosophical Transactions of the Royal Society of London Series A, 370, 2765

Allard, F., Homeier, D., Freytag, B., Schaffenberger, W., & Rajpurohit, A. S. 2013, *Progress in modeling very low mass stars, brown dwarfs, and planetary mass objects.*, Memorie della Societa Astronomica Italiana Supplementi, 24, 128

Allen, C. W. 1955, Astrophysical quantities. (University of London, Athlone Press)

Amara, A. & Quanz, S. P. 2012, *PYNPOINT: an image processing package for finding exoplanets*, MNRAS, 427, 948

Ansdell, M., Gaidos, E., Jacobs, T. L., et al. 2019, *The little dippers: transits of star-grazing exocomets?*, MNRAS, 483, 3579

Apai, D., Karalidi, T., Marley, M. S., et al. 2017, *Zones, spots, and planetary-scale waves beating in brown dwarf atmospheres*, Science, 357, 683

Apai, D., Kasper, M., Skemer, A., et al. 2016, *High-cadence, High-contrast Imaging for Exoplanet Mapping: Observations of the HR 8799 Planets with VLT/SPHERE Satellite-spot-corrected Relative Photometry*, ApJ, 820, 40

Apai, D., Nardiello, D., & Bedin, L. R. 2021, *TESS Observations of the Luhman 16 AB Brown Dwarf System: Rotational Periods, Lightcurve Evolution, and Zonal Circulation*, ApJ, 906, 64

Apai, D., Radigan, J., Buenzli, E., et al. 2013, *HST Spectral Mapping of L/T Transition Brown Dwarfs Reveals Cloud Thickness Variations*, ApJ, 768, 121

Arcangeli, J., Désert, J. M., Parmentier, V., Tsai, S. M., & Stevenson, K. B. 2021, *A new approach to spectroscopic phase curves. The emission spectrum of WASP-12b observed in quadrature with HST/WFC3*, A&A, 646, A94

Artigau, É. 2018, in Handbook of Exoplanets, ed. H. J. Deeg & J. A. Belmonte (Springer, Cham), 94

Artigau, É., Bouchard, S., Doyon, R., & Lafrenière, D. 2009, *Photometric Variability of the T2.5 Brown Dwarf SIMP J013656.5+093347: Evidence for Evolving Weather Patterns*, ApJ, 701, 1534

Ashraf, A., Bardalez Gagliuffi, D. C., Manjavacas, E., et al. 2022, *Disentangling the Signatures of Blended-light Atmospheres in L/T Transition Brown Dwarfs*, ApJ, 934, 178

Astropy Collaboration, Price-Whelan, A. M., Lim, P. L., et al. 2022, *The Astropy Project: Sustaining and Growing a Community-oriented Open-source Project and the Latest Major Release (v5.0) of the Core Package*, ApJ, 935, 167

Astropy Collaboration, Price-Whelan, A. M., Sipőcz, B. M., et al. 2018, *The Astropy Project: Building an Open-science Project and Status of the v2.0 Core Package*, AJ, 156, 123

Astropy Collaboration, Robitaille, T. P., Tollerud, E. J., et al. 2013, *Astropy: A community Python package for astronomy*, A&A, 558, A33

Babcock, H. W. 1953, *The Possibility of Compensating Astronomical Seeing*, PASP, 65, 229

Bailer-Jones, C. A. L., Rybizki, J., Fouesneau, M., Demleitner, M., & Andrae, R. 2021, *Estimating Distances from Parallaxes. V. Geometric and Photogeometric Distances to 1.47 Billion Stars in Gaia Early Data Release 3*, AJ, 161, 147

Bailer-Jones, C. A. L., Rybizki, J., Fouesneau, M., Mantelet, G., & Andrae, R. 2018, *Estimating Distance from Parallaxes. IV. Distances to 1.33 Billion Stars in Gaia Data Release 2*, AJ, 156, 58

Bailey, V., Meshkat, T., Reiter, M., et al. 2014a, *HD 106906 b: A Planetary-mass Companion Outside a Massive Debris Disk*, ApJ, 780, L4

Bailey, V. P., Hinz, P. M., Puglisi, A. T., et al. 2014b, *Large binocular telescope interferometer adaptive optics: on-sky performance and lessons learned*, in Society of Photo-Optical Instrumentation Engineers (SPIE) Conference Series, Vol. 9148, Adaptive Optics Systems IV, ed. E. Marchetti, L. M. Close, & J.-P. Vran, 914803

Baraffe, I., Homeier, D., Allard, F., & Chabrier, G. 2015, *New evolutionary models for pre-main sequence and main sequence low-mass stars down to the hydrogen-burning limit*, A&A, 577, A42

Barman, T. S., Konopacky, Q. M., Macintosh, B., & Marois, C. 2015, *Simultaneous Detection of Water, Methane, and Carbon Monoxide in the Atmosphere of Exoplanet HR8799b*, ApJ, 804, 61

Barnes, J. R., James, D. J., & Collier Cameron, A. 2002, *The boundaries of Doppler imaging: Starspot patterns on M dwarfs*, Astronomische Nachrichten, 323, 333

Basri, G. & Brown, M. E. 2006, *Planetesimals to Brown Dwarfs: What is a Planet?*, Annual Review of Earth and Planetary Sciences, 34, 193

Bayo, A., Rodrigo, C., Barrado Y Navascués, D., et al. 2008, *VOSA: virtual observatory SED analyzer. An application to the Collinder 69 open cluster*, A&A, 492, 277

Berry, M. V. 1987, *The Adiabatic Phase and Pancharatnam's Phase for Polarized Light*, Journal of Modern Optics, 34, 1401

Bethe, H. A. 1939, *Energy Production in Stars*, Physical Review, 55, 434

Beuzit, J. L., Vigan, A., Mouillet, D., et al. 2019, *SPHERE: the exoplanet imager for the Very Large Telescope*, A&A, 631, A155

Biller, B. 2017, *The time domain for brown dwarfs and directly imaged giant exoplanets: the power of variability monitoring*, The Astronomical Review, 13, 1

Biller, B. A., Apai, D., Bonnefoy, M., et al. 2021, *A high-contrast search for variability in HR 8799bc with VLT-SPHERE*, MNRAS, 503, 743

Biller, B. A. & Bonnefoy, M. 2018, in Handbook of Exoplanets, ed. H. J. Deeg & J. A. Belmonte, 101

Biller, B. A., Crossfield, I. J. M., Mancini, L., et al. 2013, *Weather on the Nearest Brown Dwarfs: Resolved Simultaneous Multi-wavelength Variability Monitoring of WISE J104915.57-531906.1AB*, ApJ, 778, L10

Biller, B. A., Grandjean, A., Messina, S., et al. 2022, *Dynamical masses for two M1 + mid-M dwarf binaries monitored during the SPHERE-SHINE survey*, A&A, 658, A145

Biller, B. A., Liu, M. C., Wahhaj, Z., et al. 2010, *The Gemini NICI Planet-finding Campaign: Discovery of a Close Substellar Companion to the Young Debris Disk Star PZ Tel*, ApJ, 720, L82

Biller, B. A., Vos, J., Bonavita, M., et al. 2015, *Variability in a Young, L/T Transition Planetary-mass Object*, ApJ, 813, L23

Biller, B. A., Vos, J., Buenzli, E., et al. 2018, *Simultaneous Multiwavelength Variability Characterization of the Free-floating Planetary-mass Object PSO J318.5-22*, AJ, 155, 95

Birkby, J., Nefs, B., Hodgkin, S., et al. 2012, *Discovery and characterization of detached M dwarf eclipsing binaries in the WFCAM Transit Survey*, MNRAS, 426, 1507

Birkby, J. L. 2018, *Exoplanet Atmospheres at High Spectral Resolution*, arXiv e-prints, arXiv:1806.04617

Birkby, J. L., de Kok, R. J., Brogi, M., et al. 2013, *Detection of water absorption in the day side atmosphere of HD 189733 b using ground-based high-resolution spectroscopy at 3.2μm.*, MNRAS, 436, L35

Bodenheimer, P., D'Angelo, G., Lissauer, J. J., Fortney, J. J., & Saumon, D. 2013, *Deuterium Burning in Massive Giant Planets and Low-mass Brown Dwarfs Formed by Core-nucleated Accretion*, ApJ, 770, 120

Boehle, A., Doelman, D., Konrad, B. S., et al. 2021, *Cryogenic characterization of the grating vector apodizing phase plate coronagraph for the enhanced resolution imager and spectrograph at the Very Large Telescope*, Journal of Astronomical Telescopes, Instruments, and Systems, 7, 045001

Boehle, A., Glauser, A. M., Kenworthy, M. A., et al. 2018, *Cryogenic characterization of the grating vector APP coronagraph for the upcoming ERIS instrument at the VLT*, in Society of Photo-Optical Instrumentation Engineers (SPIE) Conference Series, Vol. 10702, Ground-based and Airborne Instrumentation for Astronomy VII, 107023Y

Bohn, A. J., Ginski, C., Kenworthy, M. A., et al. 2021, *Discovery of a directly imaged planet to the young solar analog YSES 2*, A&A, 648, A73

Bohn, A. J., Kenworthy, M. A., Ginski, C., et al. 2020a, *The Young Suns Exoplanet Survey: Detection of a wide-orbit planetary-mass companion to a solar-type Sco-Cen member*, MNRAS, 492, 431

Bohn, A. J., Kenworthy, M. A., Ginski, C., et al. 2020b, *Two Directly Imaged, Wide-orbit Giant Planets around the Young, Solar Analog TYC 8998-760-1*, ApJ, 898, L16

Boley, A. C. 2009, *The Two Modes of Gas Giant Planet Formation*, ApJ, 695, L53

Bonavita, M., Fontanive, C., Gratton, R., et al. 2022, *Results from The COPAINS Pilot Survey: four new BDs and a high companion detection rate for accelerating stars*, MNRAS, 513, 5588

Bond, I. A., Udalski, A., Jaroszyński, M., et al. 2004, *OGLE 2003-BLG-235/MOA 2003-BLG-53: A Planetary Microlensing Event*, ApJ, 606, L155

Bonnefoy, M., Lagrange, A. M., Boccaletti, A., et al. 2011, *High angular resolution detection of β Pictoris b at 2.18 μm*, A&A, 528, L15

Bonnefoy, M., Zurlo, A., Baudino, J. L., et al. 2016, *First light of the VLT planet finder SPHERE. IV. Physical and chemical properties of the planets around HR8799*, A&A, 587, A58

Bos, S. P., Bottom, M., Ragland, S., et al. 2021, *Fast and furious focal-plane wavefront sensing at W.M. Keck Observatory*, in Society of Photo-Optical Instrumentation Engineers (SPIE) Conference Series, Vol. 11823, Techniques and Instrumentation for Detection of Exoplanets X, ed. S. B. Shaklan & G. J. Ruane, 118231E

Bos, S. P., Doelman, D. S., de Boer, J., et al. 2018, *Fully broadband vAPP coronagraphs enabling polarimetric high contrast imaging*, in Society of Photo-Optical Instrumentation Engineers (SPIE) Conference Series, Vol. 10706, Advances in Optical and Mechanical Technologies for Telescopes and Instrumentation III, ed. R. Navarro & R. Geyl, 107065M

Bos, S. P., Doelman, D. S., Lozi, J., et al. 2019, *Focal-plane wavefront sensing with the vector-Apodizing Phase Plate*, A&A, 632, A48

Bos, S. P., Doelman, D. S., Miller, K. L., & Snik, F. 2020a, *New concepts in vector-apodizing phase plate coronagraphy*, in Society of Photo-Optical Instrumentation Engineers (SPIE) Conference Series, Vol. 11448, Society of Photo-Optical Instrumentation Engineers (SPIE) Conference Series, 114483W

Bos, S. P., Vievard, S., Wilby, M. J., et al. 2020b, *On-sky verification of Fast and Furious focal-plane wavefront sensing: Moving forward toward controlling the island effect at Subaru/SCExAO*, A&A, 639, A52

Boss, A. P. 1997, *Giant planet formation by gravitational instability.*, Science, 276, 1836

Bowler, B. P. 2016, *Imaging Extrasolar Giant Planets*, PASP, 128, 102001

Bowler, B. P., Blunt, S. C., & Nielsen, E. L. 2020a, *Population-level Eccentricity Distributions of Imaged Exoplanets and Brown Dwarf Companions: Dynamical Evidence for Distinct Formation Channels*, AJ, 159, 63

Bowler, B. P., Liu, M. C., Mawet, D., et al. 2017, *Planets around Low-mass Stars (PALMS). VI. Discovery of a Remarkably Red Planetary-mass Companion to the AB Dor Moving Group Candidate 2MASS J22362452+4751425**, AJ, 153, 18

Bowler, B. P., Zhou, Y., Morley, C. V., et al. 2020b, *Strong Near-infrared Spectral Variability of the Young Cloudy L Dwarf Companion VHS J1256-1257 b*, ApJ, 893, L30

Boyajian, T. S., LaCourse, D. M., Rappaport, S. A., et al. 2016, *Planet Hunters IX. KIC 8462852 - where's the flux?*, MNRAS, 457, 3988

Bradley, L., Sipocz, B., Robitaille, T., et al. 2017, *astropy/photutils: v0.4*

Bradley, L., Sipőcz, B., Robitaille, T., et al. 2022, *astropy/photutils: v1.4.0*

Brandl, B., Bettonvil, F., van Boekel, R., et al. 2021, *METIS: The Mid-infrared ELT Imager and Spectrograph*, The Messenger, 182, 22

Brandl, B. R., Absil, O., Agócs, T., et al. 2018, *Status of the mid-IR ELT imager and spectrograph (METIS)*, in Society of Photo-Optical Instrumentation Engineers (SPIE) Conference Series, Vol. 10702, Ground-based and Airborne Instrumentation for Astronomy VII, ed. C. J. Evans, L. Simard, & H. Takami, 107021U

Brandl, B. R., Bettonvil, F., van Boekel, R., et al. 2022, *Status update on the development of METIS, the mid-infrared ELT imager and spectrograph*, in Society of Photo-Optical Instrumentation Engineers (SPIE) Conference Series, Vol. 12184, Ground-based and Airborne Instrumentation for Astronomy IX, ed. C. J. Evans, J. J. Bryant, & K. Motohara, 1218421

Brandl, B. R., Lenzen, R., Pantin, E., et al. 2008, *METIS: the Mid-infrared E-ELT Imager and Spectrograph*, in Society of Photo-Optical Instrumentation Engineers (SPIE) Conference Series, Vol. 7014, Ground-based and Airborne Instrumentation for Astronomy II, ed. I. S. McLean & M. M. Casali, 70141N

Brandt, T. D., Dupuy, T. J., & Bowler, B. P. 2019, *Precise Dynamical Masses of Directly Imaged Companions from Relative Astrometry, Radial Velocities, and Hipparcos-Gaia DR2 Accelerations*, AJ, 158, 140

Briesemeister, Z., Skemer, A. J., Stone, J. M., et al. 2018, *MEAD: data reduction pipeline for ALES integral field spectrograph and LBTI thermal infrared calibration unit*, in Society of Photo-Optical Instrumentation Engineers (SPIE) Conference Series, Vol. 10702, Ground-based and Airborne Instrumentation for Astronomy VII, ed. C. J. Evans, L. Simard, & H. Takami, 107022Q

Briesemeister, Z. W., Skemer, A. J., Stone, J. M., et al. 2019, *High Spatial Resolution Thermal Infrared Spectroscopy with ALES: Resolved Spectra of the Benchmark Brown Dwarf Binary HD 130948BC*, AJ, 157, 244

Broeg, C., Fernández, M., & Neuhäuser, R. 2005, *A new algorithm for differential photometry: computing an optimum artificial comparison star*, Astronomische Nachrichten, 326, 134

Brogi, M., Keller, C. U., de Juan Ovelar, M., et al. 2012, *Evidence for the disintegration of KIC 12557548 b*, A&A, 545, L5

Brogi, M. & Line, M. R. 2019, *Retrieving Temperatures and Abundances of Exoplanet Atmospheres with High-resolution Cross-correlation Spectroscopy*, AJ, 157, 114

Bryan, M. L., Benneke, B., Knutson, H. A., Batygin, K., & Bowler, B. P. 2018, *Constraints on the spin evolution of young planetary-mass companions*, Nature Astronomy, 2, 138

Bryan, M. L., Chiang, E., Bowler, B. P., et al. 2020a, *Obliquity Constraints on an Extrasolar Planetary-mass Companion*, AJ, 159, 181

Bryan, M. L., Chiang, E., Morley, C. V., Mace, G. N., & Bowler, B. P. 2021, *Obliquity Constraints on the Planetary-mass Companion HD 106906 b*, AJ, 162, 217

Bryan, M. L., Ginzburg, S., Chiang, E., et al. 2020b, *As the Worlds Turn: Constraining Spin Evolution in the Planetary-mass Regime*, ApJ, 905, 37

Buenzli, E., Apai, D., Morley, C. V., et al. 2012, *Vertical Atmospheric Structure in a Variable Brown Dwarf: Pressure-dependent Phase Shifts in Simultaneous Hubble Space Telescope-Spitzer Light Curves*, ApJ, 760, L31

Buenzli, E., Apai, D., Radigan, J., Reid, I. N., & Flateau, D. 2014, *Brown Dwarf Photospheres are Patchy: A Hubble Space Telescope Near-infrared Spectroscopic Survey Finds Frequent Low-level Variability*, ApJ, 782, 77

Buenzli, E., Marley, M. S., Apai, D., et al. 2015a, *Cloud Structure of the Nearest Brown Dwarfs. II. High-amplitude Variability for Luhman 16 A and B in and out of the 0.99 μm FeH feature*, ApJ, 812, 163

Buenzli, E., Saumon, D., Marley, M. S., et al. 2015b, *Cloud Structure of the Nearest Brown Dwarfs: Spectroscopic Variability of Luhman 16AB from the Hubble Space Telescope*, ApJ, 798, 127

Burgasser, A. J. 2014, *The SpeX Prism Library: 1000+ low-resolution, near-infrared spectra of ultracool M, L, T and Y dwarfs*, in Astronomical Society of India Conference Series, Vol. 11, Astronomical Society of India Conference Series, 7–16

Burgasser, A. J., Cruz, K. L., Cushing, M., et al. 2010a, *SpeX Spectroscopy of Unresolved Very Low Mass Binaries. I. Identification of 17 Candidate Binaries Straddling the L Dwarf/T Dwarf Transition*, ApJ, 710, 1142

Burgasser, A. J., Simcoe, R. A., Bochanski, J. J., et al. 2010b, *Clouds in the Coldest Brown Dwarfs: Fire Spectroscopy of Ross 458C*, ApJ, 725, 1405

Cadman, J., Rice, K., & Hall, C. 2021, *AB Aurigae: possible evidence of planet formation through the gravitational instability*, MNRAS, 504, 2877

Cantalloube, F., Farley, O. J. D., Milli, J., et al. 2020a, *Wind-driven halo in high-contrast images. I. Analysis of the focal-plane images of SPHERE*, A&A, 638, A98

Cantalloube, F., Gomez-Gonzalez, C., Absil, O., et al. 2020b, *Exoplanet imaging data challenge: benchmarking the various image processing methods for exoplanet detection*, in Society of Photo-Optical Instrumentation Engineers (SPIE) Conference Series, Vol. 11448, Society of Photo-Optical Instrumentation Engineers (SPIE) Conference Series, 114485A

Cantalloube, F., Mouillet, D., Mugnier, L. M., et al. 2015, *Direct exoplanet detection and characterization using the ANDROMEDA method: Performance on VLT/NaCo data*, A&A, 582, A89

Cantalloube, F., Por, E. H., Dohlen, K., et al. 2018, *Origin of the asymmetry of the wind driven halo observed in high-contrast images*, A&A, 620, L10

Carlomagno, B., Absil, O., Kenworthy, M., et al. 2016, *End-to-end simulations of the E-ELT/METIS coronagraphs*, in Society of Photo-Optical Instrumentation Engineers (SPIE) Conference Series, Vol. 9909, Adaptive Optics Systems V, 990973

Carter, A. L., Hinkley, S., Bonavita, M., et al. 2021, *Direct imaging of sub-Jupiter mass exoplanets with James Webb Space Telescope coronagraphy*, MNRAS, 501, 1999

Carter, A. L., Nikolov, N., Sing, D. K., et al. 2020, *Detection of Na, K, and H_2O in the hazy atmosphere of WASP-6b*, MNRAS, 494, 5449

Casagrande, L., Schönrich, R., Asplund, M., et al. 2011, *New constraints on the chemical evolution of the solar neighbourhood and Galactic disc(s). Improved astrophysical parameters for the Geneva-Copenhagen Survey*, A&A, 530, A138

Cassini, M. 1686, *An Extract of the Journal Des Scavans. of April 22 st. N. 1686. Giving an Account of Two New Satellites of Saturn, Discovered Lately by Mr. Cassini at the Royal Observatory at Paris*, Philosophical Transactions of the Royal Society of London Series I, 16, 79

Cassini, S. 1673, *A Discovery of Two New Planets about Saturn, Made in the Royal Parisian Observatory by Signor Cassini, Fellow of Both the Royal Societys, of England and France; English't Out of French*, Philosophical Transactions of the Royal Society of London Series I, 8, 5178

Chabrier, G., Baraffe, I., Allard, F., & Hauschildt, P. 2000, *Evolutionary Models for Very Low-Mass Stars and Brown Dwarfs with Dusty Atmospheres*, ApJ, 542, 464

Chabrier, G., Baraffe, I., Leconte, J., Gallardo, J., & Barman, T. 2009, *The mass-radius relationship from solar-type stars to terrestrial planets: a review*, in American Institute of Physics Conference Series, Vol. 1094, 15th Cambridge Workshop on Cool Stars, Stellar Systems, and the Sun, ed. E. Stempels, 102–111

Chabrier, G., Baraffe, I., Phillips, M., & Debras, F. 2022, *Impact of a new H/He equation of state on the evolution of massive brown dwarfs. New determination of the hydrogen burning limit*, arXiv e-prints, arXiv:2212.07153

Chabrier, G., Johansen, A., Janson, M., & Rafikov, R. 2014, *Giant Planet and Brown Dwarf Formation*, in Protostars and Planets VI, ed. H. Beuther, R. S. Klessen, C. P. Dullemond, & T. Henning, 619

B

Charbonneau, D., Berta, Z. K., Irwin, J., et al. 2009, *A super-Earth transiting a nearby low-mass star*, Nature, 462, 891

Charbonneau, D., Brown, T. M., Latham, D. W., & Mayor, M. 2000, *Detection of Planetary Transits Across a Sun-like Star*, ApJ, 529, L45

Charbonneau, D., Brown, T. M., Noyes, R. W., & Gilliland, R. L. 2002, *Detection of an Extrasolar Planet Atmosphere*, ApJ, 568, 377

Charnay, B., Bézard, B., Baudino, J. L., et al. 2018, *A Self-consistent Cloud Model for Brown Dwarfs and Young Giant Exoplanets: Comparison with Photometric and Spectroscopic Observations*, ApJ, 854, 172

Chauvin, G., Desidera, S., Lagrange, A. M., et al. 2017, *Discovery of a warm, dusty giant planet around HIP 65426*, A&A, 605, L9

Chauvin, G., Lagrange, A. M., Dumas, C., et al. 2004, *A giant planet candidate near a young brown dwarf. Direct VLT/NACO observations using IR wavefront sensing*, A&A, 425, L29

Chauvin, G., Lagrange, A. M., Dumas, C., et al. 2005a, *Giant planet companion to 2MASSW J1207334-393254*, A&A, 438, L25

Chauvin, G., Lagrange, A. M., Lacombe, F., et al. 2005b, *Astrometric and spectroscopic confirmation of a brown dwarf companion to GSC 08047-00232. VLT/NACO deep imaging and spectroscopic observations*, A&A, 430, 1027

Chinchilla, P., Béjar, V. J. S., Lodieu, N., et al. 2020, *USco1621 B and USco1556 B: Two wide companions at the deuterium-burning mass limit in Upper Scorpius*, A&A, 633, A152

Chiu, K., Fan, X., Leggett, S. K., et al. 2006, *Seventy-One New L and T Dwarfs from the Sloan Digital Sky Survey*, AJ, 131, 2722

Ciardi, D. R., von Braun, K., Bryden, G., et al. 2011, *Characterizing the Variability of Stars with Early-release Kepler Data*, AJ, 141, 108

Clénet, Y., Buey, T., Gendron, E., et al. 2018, *The MICADO first-light imager for the ELT: towards the preliminary design review of the MICADO-MAORY SCAO*, in Society of Photo-Optical Instrumentation Engineers (SPIE) Conference Series, Vol. 10703, Adaptive Optics Systems VI, ed. L. M. Close, L. Schreiber, & D. Schmidt, 1070313

Close, L. M., Males, J., Long, J. D., et al. 2020a, *Prediction of the planet yield of the MaxProtoPlanetS high-contrast survey for H-alpha protoplanets with MagAO-X based on first light contrasts*, in Society of Photo-Optical Instrumentation Engineers (SPIE) Conference Series, Vol. 11448, Society of Photo-Optical Instrumentation Engineers (SPIE) Conference Series, 114480U

Close, L. M., Males, J. R., Hedglen, A., Bouchez, A., & Guyon, O. 2020b, *Concept for the GMT High-Contrast Exoplanet Instrument GMagAO-X and the GMT High-Contrast Phasing Testbed with MagAO-X*, arXiv e-prints, arXiv:2004.06808

Close, L. M., Males, J. R., Kopon, D. A., et al. 2012, *First closed-loop visible AO test results for the advanced adaptive secondary AO system for the Magellan Telescope: MagAO's performance and status*, in Society of Photo-Optical Instrumentation Engineers (SPIE) Conference Series, Vol. 8447, Adaptive Optics Systems III, ed. B. L. Ellerbroek, E. Marchetti, & J.-P. Véran, 84470X

Codona, J. L., Kenworthy, M. A., Hinz, P. M., Angel, J. R. P., & Woolf, N. J. 2006, *A high-contrast coronagraph for the MMT using phase apodization: design and observations at 5 microns and 2 λ/D radius*, in Society of Photo-Optical Instrumentation Engineers (SPIE) Conference Series, Vol. 6269, Society of Photo-Optical Instrumentation Engineers (SPIE) Conference Series, 62691N

Côté, O., Allain, G., Brousseau, D., et al. 2018, *A precursor mission to high contrast imaging balloon system*, in Society of Photo-Optical Instrumentation Engineers (SPIE) Conference Series, Vol. 10702, Ground-based and Airborne Instrumentation for Astronomy VII, ed. C. J. Evans, L. Simard, & H. Takami, 1070248

Coulter, D. J., Barnes, J. W., & Fortney, J. J. 2022, *Jupiter and Saturn as Spectral Analogs for Extrasolar Gas Giants and Brown Dwarfs*, ApJS, 263, 15

Crepp, J. R., Johnson, J. A., Fischer, D. A., et al. 2012, *The Dynamical Mass and Three-dimensional Orbit of HR7672B: A Benchmark Brown Dwarf with High Eccentricity*, ApJ, 751, 97

Croll, B., Albert, L., Jayawardhana, R., et al. 2015, *Near-infrared Thermal Emission Detections of a Number of Hot Jupiters and the Systematics of Ground-based Near-infrared Photometry*, ApJ, 802, 28

Crossfield, I. J. M. 2014, *Doppler imaging of exoplanets and brown dwarfs*, A&A, 566, A130

Crossfield, I. J. M., Barman, T., Hansen, B. M. S., Tanaka, I., & Kodama, T. 2012, *Re-evaluating WASP-12b: Strong Emission at 2.315 μm, Deeper Occultations, and an Isothermal Atmosphere*, ApJ, 760, 140

Crossfield, I. J. M., Biller, B., Schlieder, J. E., et al. 2014, *A global cloud map of the nearest known brown dwarf*, Nature, 505, 654

Cruz, K. L., Núñez, A., Burgasser, A. J., et al. 2018, *Meeting the Cool Neighbors. XII. An Optically Anchored Analysis of the Near-infrared Spectra of L Dwarfs*, AJ, 155, 34

Currie, T., Biller, B., Lagrange, A.-M., et al. 2022a, *Direct Imaging and Spectroscopy of Extrasolar Planets*, arXiv e-prints, arXiv:2205.05696

Currie, T., Brandt, G. M., Brandt, T. D., et al. 2022b, *Direct Imaging and Astrometric Discovery of a Superjovian Planet Orbiting an Accelerating Star*, arXiv e-prints, arXiv:2212.00034

Currie, T., Brandt, T. D., Kuzuhara, M., et al. 2020, *SCExAO/CHARIS Direct Imaging Discovery of a 20 au Separation, Low-mass Ratio Brown Dwarf Companion to an Accelerating Sun-like Star*, ApJ, 904, L25

Currie, T., Burrows, A., Itoh, Y., et al. 2011, *A Combined Subaru/VLT/MMT 1-5 μm Study of Planets Orbiting HR 8799: Implications for Atmospheric Properties, Masses, and Formation*, ApJ, 729, 128

Currie, T., Lawson, K., Schneider, G., et al. 2022c, *Images of embedded Jovian planet formation at a wide separation around AB Aurigae*, Nature Astronomy, 6, 751

Curtis, J. L., Agüeros, M. A., Mamajek, E. E., Wright, J. T., & Cummings, J. D. 2019, *TESS Reveals that the Nearby Pisces-Eridanus Stellar Stream is only 120 Myr Old*, AJ, 158, 77

Cushing, M. C., Hardegree-Ullman, K. K., Trucks, J. L., et al. 2016, *The First Detection of Photometric Variability in a Y Dwarf: WISE J140518.39+553421.3*, ApJ, 823, 152

Cutri, R. M., Skrutskie, M. F., van Dyk, S., et al. 2003, *VizieR Online Data Catalog: 2MASS All-Sky Catalog of Point Sources (Cutri+ 2003)*, VizieR Online Data Catalog, II/246

Czesla, S., Schröter, S., Schneider, C. P., et al. 2019, *PyA: Python astronomy-related packages*

Davenport, J. R. A., Becker, A. C., Kowalski, A. F., et al. 2012, *Multi-wavelength Characterization of Stellar Flares on Low-mass Stars Using SDSS and 2MASS Time-domain Surveys*, ApJ, 748, 58

Davies, R. & Kasper, M. 2012, *Adaptive Optics for Astronomy*, ARA&A, 50, 305

de Mooij, E. J. W., Brogi, M., de Kok, R. J., et al. 2012, *Optical to near-infrared transit observations of super-Earth GJ 1214b: water-world or mini-Neptune?*, A&A, 538, A46

de Mooij, E. J. W., Brogi, M., de Kok, R. J., et al. 2013, *The GROUSE project. III. K_s-band observations of the thermal emission from WASP-33b*, A&A, 550, A54

de Mooij, E. J. W., de Kok, R. J., Nefs, S. V., & Snellen, I. A. G. 2011, *The GROUSE project. II. Detection of the K_s-band secondary eclipse of exoplanet HAT-P-1b*, A&A, 528, A49

de Mooij, E. J. W. & Snellen, I. A. G. 2009, *Ground-based K-band detection of thermal emission from the exoplanet TrES-3b*, A&A, 493, L35

De Rosa, R. J., Rameau, J., Patience, J., et al. 2016, *Spectroscopic Characterization of HD 95086 b with the Gemini Planet Imager*, ApJ, 824, 121

Defrère, D., Hinz, P., Skemer, A., et al. 2015, *Exoplanet science with the LBTI: instrument status and plans*, in Society of Photo-Optical Instrumentation Engineers (SPIE) Conference Series, Vol. 9605, Techniques and Instrumentation for Detection of Exoplanets VII, ed. S. Shaklan, 96051G

Diamond-Lowe, H., Berta-Thompson, Z., Charbonneau, D., Dittmann, J., & Kempton, E. M. R. 2020a, *Simultaneous Optical Transmission Spectroscopy of a Terrestrial, Habitable-zone Exoplanet with Two Ground-based Multiobject Spectrographs*, AJ, 160, 27

Diamond-Lowe, H., Berta-Thompson, Z., Charbonneau, D., & Kempton, E. M. R. 2018, *Ground-based Optical Transmission Spectroscopy of the Small, Rocky Exoplanet GJ 1132b*, AJ, 156, 42

Diamond-Lowe, H., Charbonneau, D., Malik, M., Kempton, E. M. R., & Beletsky, Y. 2020b, *Optical Transmission Spectroscopy of the Terrestrial Exoplanet LHS 3844b from 13 Ground-based Transit Observations*, AJ, 160, 188

Diamond-Lowe, H., Mendonca, J. M., Charbonneau, D., & Buchhave, L. A. 2022, *Ground-based Optical Transmission Spectroscopy of the Nearby Terrestrial Exoplanet LTT 1445Ab*, arXiv e-prints, arXiv:2210.11809

Dias, W. S., Alessi, B. S., Moitinho, A., & Lépine, J. R. D. 2002, *New catalogue of optically visible open clusters and candidates*, A&A, 389, 871

Dieterich, S. B., Henry, T. J., Jao, W.-C., et al. 2014, *The Solar Neighborhood. XXXII. The Hydrogen Burning Limit*, AJ, 147, 94

Doelman, D. S., Por, E. H., Ruane, G., Escuti, M. J., & Snik, F. 2020, *Minimizing the Polarization Leakage of Geometric-phase Coronagraphs with Multiple Grating Pattern Combinations*, PASP, 132, 045002

Doelman, D. S., Snik, F., Por, E. H., et al. 2021, *Vector-apodizing phase plate coronagraph: design, current performance, and future development [Invited]*, Appl. Opt., 60, D52

Doelman, D. S., Snik, F., Warriner, N. Z., & Escuti, M. J. 2017, *Patterned liquid-crystal optics for broadband coronagraphy and wavefront sensing*, in Society of Photo-Optical Instrumentation Engineers (SPIE) Conference Series, Vol. 10400, Society of Photo-Optical Instrumentation Engineers (SPIE) Conference Series, 104000U

Doelman, D. S., Stone, J. M., Briesemeister, Z. W., et al. 2022, *L-band Integral Field Spectroscopy of the HR 8799 Planetary System*, AJ, 163, 217

Dou, J., Ren, D., Zhao, G., et al. 2015, *A High-contrast Imaging Algorithm: Optimized Image Rotation and Subtraction*, ApJ, 802, 12

Dubber, S., Biller, B., Bonavita, M., et al. 2022, *An optimized survey strategy for the ERIS/NIX imager: searching for young giant exoplanets and very low mass brown dwarfs using the K-peak custom photometric filter*, MNRAS, 515, 5629

Dupuy, T. J., Forbrich, J., Rizzuto, A., et al. 2016, *High-precision Radio and Infrared Astrometry of LSPM J1314+1320AB. II. Testing Pre-main-sequence Models at the Lithium Depletion Boundary with Dynamical Masses*, ApJ, 827, 23

Dupuy, T. J. & Kraus, A. L. 2013, *Distances, Luminosities, and Temperatures of the Coldest Known Substellar Objects*, Science, 341, 1492

Dupuy, T. J. & Liu, M. C. 2017, *Individual Dynamical Masses of Ultracool Dwarfs*, ApJS, 231, 15

Dupuy, T. J., Liu, M. C., Allers, K. N., et al. 2018, *The Hawaii Infrared Parallax Program. III. 2MASS J0249-0557 c: A Wide Planetary-mass Companion to a Low-mass Binary in the β Pic Moving Group*, AJ, 156, 57

Eddington, A. S. 1920, *The Internal Constitution of the Stars*, Nature, 106, 14

Einstein, A. 1936, *Lens-Like Action of a Star by the Deviation of Light in the Gravitational Field*, Science, 84, 506

Eriksson, S. C., Janson, M., & Calissendorff, P. 2019, *Detection of new strongly variable brown dwarfs in the L/T transition*, A&A, 629, A145

Ermolli, I., Matthes, K., Dudok de Wit, T., et al. 2013, *Recent variability of the solar spectral irradiance and its impact on climate modelling*, Atmospheric Chemistry & Physics, 13, 3945

Ertel, S., Hinz, P. M., Stone, J. M., et al. 2020, *Overview and prospects of the LBTI beyond the completed HOSTS survey*, in Society of Photo-Optical Instrumentation Engineers (SPIE) Conference Series, Vol. 11446, Society of Photo-Optical Instrumentation Engineers (SPIE) Conference Series, 1144607

Espinosa Lara, F. & Rieutord, M. 2011, *Gravity darkening in rotating stars*, A&A, 533, A43

Evans, T. M., Aigrain, S., Gibson, N., et al. 2015, *A uniform analysis of HD 209458b Spitzer/IRAC light curves with Gaussian process models*, MNRAS, 451, 680

Evans, T. M., Pont, F., Sing, D. K., et al. 2013, *The Deep Blue Color of HD 189733b: Albedo Measurements with Hubble Space Telescope/Space Telescope Imaging Spectrograph at Visible Wavelengths*, ApJ, 772, L16

Evans, T. M., Sing, D. K., Kataria, T., et al. 2017, *An ultrahot gas-giant exoplanet with a stratosphere*, Nature, 548, 58

Faherty, J. K., Burgasser, A. J., West, A. A., et al. 2010, *The Brown Dwarf Kinematics Project. II. Details on Nine Wide Common Proper Motion Very Low Mass Companions to Nearby Stars*, AJ, 139, 176

Faherty, J. K., Cruz, K. L., Rice, E. L., & Riedel, A. 2013, *Young brown dwarfs as giant exoplanet analogs* ., Mem. Soc. Astron. Italiana, 84, 955

Faherty, J. K., Gagné, J., Popinchalk, M., et al. 2021, *A Wide Planetary Mass Companion Discovered through the Citizen Science Project Backyard Worlds: Planet 9*, ApJ, 923, 48

Faherty, J. K., Riedel, A. R., Cruz, K. L., et al. 2016, *Population Properties of Brown Dwarf Analogs to Exoplanets*, ApJS, 225, 10

Ferlet, R., Hobbs, L. M., & Vidal-Madjar, A. 1987, *The beta Pictoris circumstellar disk. V. Time variations of the Ca II-K line.*, A&A, 185, 267

Fitzpatrick, E. L. 1999, *Correcting for the Effects of Interstellar Extinction*, PASP, 111, 63

Flasseur, O., Denis, L., Thiébaut, É., & Langlois, M. 2018, *Exoplanet detection in angular differential imaging by statistical learning of the nonstationary patch covariances. The PACO algorithm*, A&A, 618, A138

Fletcher, L. N., Greathouse, T. K., Orton, G. S., et al. 2016, *Mid-infrared mapping of Jupiter's temperatures, aerosol opacity and chemical distributions with IRTF/TEXES*, Icarus, 278, 128

Fontanive, C., Allers, K. N., Pantoja, B., et al. 2020, *A Wide Planetary-mass Companion to a Young Low-mass Brown Dwarf in Ophiuchus*, ApJ, 905, L14

Fowler, J., Van Kooten, M. A. M., & Jensen-Clem, R. 2022, *Battle of the predictive wavefront controls: comparing data and model-driven predictive control for high contrast imaging*, in Society of Photo-Optical Instrumentation Engineers (SPIE) Conference Series, Vol. 12185, Adaptive Optics Systems VIII, ed. L. Schreiber, D. Schmidt, & E. Vernet, 1218582

Franson, K., Bowler, B. P., Bonavita, M., et al. 2023, *Astrometric Accelerations as Dynamical Beacons: Discovery and Characterization of HIP 21152 B, the First T-dwarf Companion in the Hyades*, AJ, 165, 39

Frasca, A., Covino, E., Spezzi, L., et al. 2009, *REM near-IR and optical photometric monitoring of pre-main sequence stars in Orion. Rotation periods and starspot parameters*, A&A, 508, 1313

Fröhlich, C. & Lean, J. 2004, *Solar radiative output and its variability: evidence and mechanisms*, A&A Rev., 12, 273

Fusco, T., Sauvage, J. F., Petit, C., et al. 2014, *Final performance and lesson-learned of SAXO, the VLT-SPHERE extreme AO: from early design to on-sky results*, in Society of Photo-Optical Instrumentation Engineers (SPIE) Conference Series, Vol. 9148, Adaptive Optics Systems IV, ed. E. Marchetti, L. M. Close, & J.-P. Vran, 91481U

Gaia Collaboration, Brown, A. G. A., Vallenari, A., et al. 2018, *Gaia Data Release 2. Summary of the contents and survey properties*, A&A, 616, A1

Gaia Collaboration, Brown, A. G. A., Vallenari, A., et al. 2021, *Gaia Early Data Release 3. Summary of the contents and survey properties*, A&A, 649, A1

Gaia Collaboration, Prusti, T., de Bruijne, J. H. J., et al. 2016, *The Gaia mission*, A&A, 595, A1

Gaia Collaboration, Vallenari, A., Brown, A. G. A., et al. 2022, *Gaia Data Release 3: Summary of the content and survey properties*, arXiv e-prints, arXiv:2208.00211

Galicher, R., Marois, C., Macintosh, B., Barman, T., & Konopacky, Q. 2011, *M-band Imaging of the HR 8799 Planetary System Using an Innovative LOCI-based Background Subtraction Technique*, ApJ, 739, L41

Galicher, R. & Mazoyer, J. 2023, *Imaging exoplanets with coronagraphic instruments*, arXiv e-prints, arXiv:2302.10833

Galilei, G. 1610, Sidereus nuncius magna, longeque admirabilia spectacula pandens lunae facie, fixis innumeris, lacteo circulo, stellis nebulosis, ... Galileo Galileo : nuper a se reperti beneficio sunt observata in apprime vero in quatuor planetis circa Iovis stellam disparibus intervallis, atque periodis, celeritate mirabili circumvolutis ... atque Medicea sidera nuncupandos decrevit (Thomas Baglioni)

Galle, J. G. 1846, *Account of the discovery of Le Verrier's planet Neptune, at Berlin, Sept. 23, 1846*, MNRAS, 7, 153

Garcia, E. V., Currie, T., Guyon, O., et al. 2017, *SCExAO and GPI Y JHBand Photometry and Integral Field Spectroscopy of the Young Brown Dwarf Companion to HD 1160*, ApJ, 834, 162

Gardner, J. P., Mather, J. C., Clampin, M., et al. 2006, *The James Webb Space Telescope*, Space Sci. Rev., 123, 485

Gaudi, B. S. 2012, *Microlensing Surveys for Exoplanets*, ARA&A, 50, 411

Ge, H., Zhang, X., Fletcher, L. N., et al. 2019, *Rotational Light Curves of Jupiter from Ultraviolet to Mid-infrared and Implications for Brown Dwarfs and Exoplanets*, AJ, 157, 89

Gebhard, T. D., Bonse, M. J., Quanz, S. P., & Schölkopf, B. 2022, *Half-sibling regression meets exoplanet imaging: PSF modeling and subtraction using a flexible, domain knowledge-driven, causal framework*, A&A, 666, A9

Gelino, C. & Marley, M. 2000, *Variability in an Unresolved Jupiter*, in Astronomical Society of the Pacific Conference Series, Vol. 212, From Giant Planets to Cool Stars, ed. C. A. Griffith & M. S. Marley, 322

Gelino, C. R., Marley, M. S., Holtzman, J. A., Ackerman, A. S., & Lodders, K. 2002, *L Dwarf Variability: I-Band Observations*, ApJ, 577, 433

Ghosh, S., Mondal, S., Dutta, S., et al. 2021, *Fast photometric variability of very low mass stars in IC 348: detection of superflare in an M dwarf*, MNRAS, 500, 5106

Gibbard, S. G., Roe, H., de Pater, I., et al. 2002, *High-Resolution Infrared Imaging of Neptune from the Keck Telescope*, Icarus, 156, 1

Gibson, N. P., Aigrain, S., Barstow, J. K., et al. 2013, *A Gemini ground-based transmission spectrum of WASP-29b: a featureless spectrum from 515 to 720 nm*, MNRAS, 428, 3680

Gibson, N. P., Aigrain, S., Roberts, S., et al. 2012, *A Gaussian process framework for modelling instrumental systematics: application to transmission spectroscopy*, MNRAS, 419, 2683

Gillon, M., Triaud, A. H. M. J., Jehin, E., et al. 2013, *Fast-evolving weather for the coolest of our two new substellar neighbours*, A&A, 555, L5

Girard, J. H., Leisenring, J., Kammerer, J., et al. 2022, *JWST/NIRCam coronagraphy: commissioning and first on-sky results*, in Society of Photo-Optical Instrumentation Engineers (SPIE) Conference Series, Vol. 12180, Space Telescopes and Instrumentation 2022: Optical, Infrared, and Millimeter Wave, ed. L. E. Coyle, S. Matsuura, & M. D. Perrin, 121803Q

Girardin, F., Artigau, É., & Doyon, R. 2013, *In Search of Dust Clouds: Photometric Monitoring of a Sample of Late L and T Dwarfs*, ApJ, 767, 61

Gomez Gonzalez, C. A., Wertz, O., Absil, O., et al. 2017, *VIP: Vortex Image Processing Package for High-contrast Direct Imaging*, AJ, 154, 7

Gonsalves, R. A. 1982, *Phase Retrieval And Diversity In Adaptive Optics*, Optical Engineering, 21, 829

Goulding, N. T., Barnes, J. R., Pinfield, D. J., et al. 2012, *J-band variability of M dwarfs in the WFCAM Transit Survey*, MNRAS, 427, 3358

Gray, R. 2000, *A digital spectral classification atlas*

Gray, R. O., Corbally, C. J., Garrison, R. F., et al. 2006, *Contributions to the Nearby Stars (NStars) Project: Spectroscopy of Stars Earlier than M0 within 40 pc-The Southern Sample*, AJ, 132, 161

Groff, T., Chilcote, J., Brandt, T., et al. 2017, *First light of the CHARIS high-contrast integral-field spectrograph*, in Society of Photo-Optical Instrumentation Engineers (SPIE) Conference Series, Vol. 10400, Society of Photo-Optical Instrumentation Engineers (SPIE) Conference Series, 1040016

Groff, T. D., Chilcote, J., Kasdin, N. J., et al. 2016, *Laboratory testing and performance verification of the CHARIS integral field spectrograph*, in Society of Photo-Optical Instrumentation Engineers (SPIE) Conference Series, Vol. 9908, Ground-based and Airborne Instrumentation for Astronomy VI, ed. C. J. Evans, L. Simard, & H. Takami, 99080O

Guyon, O. 2018, *Extreme Adaptive Optics*, ARA&A, 56, 315

Guyon, O. & Males, J. 2017, *Adaptive Optics Predictive Control with Empirical Orthogonal Functions (EOFs)*, arXiv e-prints, arXiv:1707.00570

Haffert, S. Y., Bohn, A. J., de Boer, J., et al. 2019, *Two accreting protoplanets around the young star PDS 70*, Nature Astronomy, 3, 749

Haffert, S. Y., Males, J. R., Close, L. M., et al. 2021, *Data-driven subspace predictive control of adaptive optics for high-contrast imaging*, Journal of Astronomical Telescopes, Instruments, and Systems, 7, 029001

Haffert, S. Y., Wilby, M. J., Keller, C. U., & Snellen, I. A. G. 2016, *The Leiden EXoplanet Instrument (LEXI): a high-contrast high-dispersion spectrograph*, in Society of Photo-Optical Instrumentation Engineers (SPIE) Conference Series, Vol. 9908, Ground-based and Airborne Instrumentation for Astronomy VI, ed. C. J. Evans, L. Simard, & H. Takami, 990867

Haffert, S. Y., Wilby, M. J., Keller, C. U., et al. 2018, *On-sky results of the Leiden EXoplanet Instrument (LEXI)*, in Society of Photo-Optical Instrumentation Engineers (SPIE) Conference Series, Vol. 10703, Adaptive Optics Systems VI, ed. L. M. Close, L. Schreiber, & D. Schmidt, 1070323

Haisch, Karl E., J., Lada, E. A., & Lada, C. J. 2001, *Disk Frequencies and Lifetimes in Young Clusters*, ApJ, 553, L153

Hallinan, G., Littlefair, S. P., Cotter, G., et al. 2015, *Magnetospherically driven optical and radio aurorae at the end of the stellar main sequence*, Nature, 523, 568

Harris, C. R., Millman, K. J., van der Walt, S. J., et al. 2020, *Array programming with NumPy*, Nature, 585, 357

Hartung, M., Macintosh, B., Langlois, P., et al. 2014, *On-sky low order non-common path correction of the GPI calibration unit*, in Society of Photo-Optical Instrumentation Engineers (SPIE) Conference Series, Vol. 9148, Adaptive Optics Systems IV, ed. E. Marchetti, L. M. Close, & J.-P. Vran, 91485Q

Hauschildt, P. H., Allard, F., & Baron, E. 1999, *The NextGen Model Atmosphere Grid for* $3000 <= T_{eff} <= 10{,}000$ *K*, ApJ, 512, 377

Hayashi, C. & Nakano, T. 1963, *Evolution of Stars of Small Masses in the Pre-Main-Sequence Stages*, Progress of Theoretical Physics, 30, 460

Heller, R. 2016, *Transits of extrasolar moons around luminous giant planets*, A&A, 588, A34

Heller, R., Rodenbeck, K., & Bruno, G. 2019, *An alternative interpretation of the exomoon candidate signal in the combined Kepler and Hubble data of Kepler-1625*, A&A, 624, A95

Heller, R., Williams, D., Kipping, D., et al. 2014, *Formation, Habitability, and Detection of Extrasolar Moons*, Astrobiology, 14, 798

Helling, C. & Casewell, S. 2014, *Atmospheres of brown dwarfs*, A&A Rev., 22, 80

Henry, G. W., Marcy, G. W., Butler, R. P., & Vogt, S. S. 2000, *A Transiting "51 Peg-like" Planet*, ApJ, 529, L41

Herbst, W. 2012, *The Variability of Young Stellar Objects*, Journal of the American Association of Variable Star Observers, 40, 448

Herschel, W. & Watson, D. 1781, *Account of a Comet. By Mr. Herschel, F. R. S.; Communicated by Dr. Watson, Jun. of Bath, F. R. S.*, Philosophical Transactions of the Royal Society of London Series I, 71, 492

Hinkley, S., Bowler, B. P., Vigan, A., et al. 2015, *Early Results from VLT SPHERE: Long-slit Spectroscopy of 2MASS 0122-2439 B, a Young Companion Near the Deuterium Burning Limit*, ApJ, 805, L10

Hinkley, S., Carter, A. L., Ray, S., et al. 2022a, *The JWST Early Release Science Program for the Direct Imaging and Spectroscopy of Exoplanetary Systems*, PASP, 134, 095003

Hinkley, S., Lacour, S., Marleau, G. D., et al. 2022b, *Direct Discovery of the Inner Exoplanet in the HD206893 System*, arXiv e-prints, arXiv:2208.04867

Hinkley, S., Oppenheimer, B. R., Soummer, R., et al. 2007, *Temporal Evolution of Coronagraphic Dynamic Range and Constraints on Companions to Vega*, ApJ, 654, 633

Hinkley, S., Vigan, A., Kasper, M., Quanz, S. P., & Lacour, S. 2021, in ExoFrontiers; Big Questions in Exoplanetary Science, ed. N. Madhusudhan (IOP Publishing), 5–1

Hinz, P., Arbo, P., Bailey, V., et al. 2012, *First AO-corrected interferometry with LBTI: steps towards routine coherent imaging observations*, in Society of Photo-Optical Instrumentation Engineers (SPIE) Conference Series, Vol. 8445, Optical and Infrared Interferometry III, ed. F. Delplancke, J. K. Rajagopal, & F. Malbet, 84450U

Hinz, P. M., Defrère, D., Skemer, A., et al. 2016, *Overview of LBTI: a multipurpose facility for high spatial resolution observations*, in Society of Photo-Optical Instrumentation Engineers (SPIE) Conference Series, Vol. 9907, Optical and Infrared Interferometry and Imaging V, ed. F. Malbet, M. J. Creech-Eakman, & P. G. Tuthill, 990704

Hinz, P. M., Skemer, A., Stone, J., Montoya, O. M., & Durney, O. 2018, *Design of ALES: a broad wavelength integral field unit for LBTI/LMIRcam*, in Society of Photo-Optical Instrumentation Engineers (SPIE) Conference Series, Vol. 10702, Ground-based and Airborne Instrumentation for Astronomy VII, ed. C. J. Evans, L. Simard, & H. Takami, 107023L

Hoeijmakers, H. J., Schwarz, H., Snellen, I. A. G., et al. 2018, *Medium-resolution integral-field spectroscopy for high-contrast exoplanet imaging. Molecule maps of the β Pictoris system with SINFONI*, A&A, 617, A144

Høg, E., Fabricius, C., Makarov, V. V., et al. 2000a, *Construction and verification of the Tycho-2 Catalogue*, A&A, 357, 367

Høg, E., Fabricius, C., Makarov, V. V., et al. 2000b, *The Tycho-2 catalogue of the 2.5 million brightest stars*, A&A, 355, L27

Horne, J. H. & Baliunas, S. L. 1986, *A Prescription for Period Analysis of Unevenly Sampled Time Series*, ApJ, 302, 757

Horne, K. 1986, *An optimal extraction algorithm for CCD spectroscopy.*, PASP, 98, 609

Houk, N. & Swift, C. 1999, Michigan catalogue of two-dimensional spectral types for the HD Stars ; vol. 5, Vol. 5 (Department of Astronomy, University of Michigan)

Hunter, J. D. 2007, *Matplotlib: A 2D graphics environment*, Computing in Science & Engineering, 9, 90

Huygens, C. 1659, Cristiani Hugenii... Systema Saturnium sive de causis mirandorum Saturni phaenomenon et comite ejus planeta novo (Ex typographia Adriani Vlacq, Hagae-Comitis)

Ilyin, I. V. 2000, *High resolution SOFIN CCD echelle spectroscopy*, PhD thesis, University of Oulu, Division of Astronomy

Indebetouw, R., Mathis, J. S., Babler, B. L., et al. 2005, *The Wavelength Dependence of Interstellar Extinction from 1.25 to 8.0 μm Using GLIMPSE Data*, ApJ, 619, 931

Ingraham, P., Marley, M. S., Saumon, D., et al. 2014, *Gemini Planet Imager Spectroscopy of the HR 8799 Planets c and d*, ApJ, 794, L15

Irwin, J. M., Quinn, S. N., Berta, Z. K., et al. 2011, *LSPM J1112+7626: Detection of a 41 Day M-dwarf Eclipsing Binary from the MEarth Transit Survey*, ApJ, 742, 123

Jackson, R. J. & Jeffries, R. D. 2013, *On the relationship between the size and surface coverage of starspots on magnetically active low-mass stars*, MNRAS, 431, 1883

Janson, M., Asensio-Torres, R., André, D., et al. 2019, *The B-Star Exoplanet Abundance Study: a co-moving 16-25 M_{Jup} companion to the young binary system HIP 79098*, A&A, 626, A99

Jeffers, S. V., Donati, J. F., & Collier Cameron, A. 2007, *Magnetic activity on AB Doradus: temporal evolution of star-spots and differential rotation from 1988 to 1994*, MNRAS, 375, 567

Jenkins, J. M., Twicken, J. D., McCauliff, S., et al. 2016, *The TESS science processing operations center*, in Society of Photo-Optical Instrumentation Engineers (SPIE) Conference Series, Vol. 9913, Software and Cyberinfrastructure for Astronomy IV, ed. G. Chiozzi & J. C. Guzman, 99133E

Jensen-Clem, R., Bond, C. Z., Cetre, S., et al. 2019, *Demonstrating predictive wavefront control with the Keck II near-infrared pyramid wavefront sensor*, in Society of Photo-Optical Instrumentation Engineers (SPIE) Conference Series, Vol. 11117, Society of Photo-Optical Instrumentation Engineers (SPIE) Conference Series, 111170W

Jensen-Clem, R., Mawet, D., Gomez Gonzalez, C. A., et al. 2018, *A New Standard for Assessing the Performance of High Contrast Imaging Systems*, AJ, 155, 19

Johnson, L. J., Norris, C. M., Unruh, Y. C., et al. 2021, *Forward modelling of Kepler-band variability due to faculae and spots*, MNRAS, 504, 4751

Jovanovic, N., Absil, O., Baudoz, P., et al. 2018, *Review of high-contrast imaging systems for current and future ground-based and space-based telescopes: Part II. Common path wavefront sensing/control and coherent differential imaging*, in Society of Photo-Optical Instrumentation Engineers (SPIE) Conference Series, Vol. 10703, Adaptive Optics Systems VI, ed. L. M. Close, L. Schreiber, & D. Schmidt, 107031U

Jovanovic, N., Guyon, O., Martinache, F., et al. 2015a, *Artificial Incoherent Speckles Enable Precision Astrometry and Photometry in High-contrast Imaging*, ApJ, 813, L24

Jovanovic, N., Martinache, F., Guyon, O., et al. 2015b, *The Subaru Coronagraphic Extreme Adaptive Optics System: Enabling High-Contrast Imaging on Solar-System Scales*, PASP, 127, 890

Joye, W. A. & Mandel, E. 2003, *New Features of SAOImage DS9*, in Astronomical Society of the Pacific Conference Series, Vol. 295, Astronomical Data Analysis Software and Systems XII, ed. H. E. Payne, R. I. Jedrzejewski, & R. N. Hook, 489

Jura, M., Malkan, M., White, R., et al. 1998, *A Protocometary Cloud around HR 4796A?*, ApJ, 505, 897

Kammerer, J., Girard, J., Carter, A. L., et al. 2022, *Performance of near-infrared high-contrast imaging methods with JWST from commissioning*, in Society of Photo-Optical Instrumentation Engineers (SPIE) Conference Series, Vol. 12180, Space Telescopes and Instrumentation 2022: Optical, Infrared, and Millimeter Wave, ed. L. E. Coyle, S. Matsuura, & M. D. Perrin, 121803N

Karalidi, T., Apai, D., Marley, M. S., & Buenzli, E. 2016, *Maps of Evolving Cloud Structures in Luhman 16AB from HST Time-resolved Spectroscopy*, ApJ, 825, 90

Karalidi, T., Apai, D., Schneider, G., Hanson, J. R., & Pasachoff, J. M. 2015, *Aeolus: A Markov Chain Monte Carlo Code for Mapping Ultracool Atmospheres. An Application on Jupiter and Brown Dwarf HST Light Curves*, ApJ, 814, 65

Kasper, M., Beuzit, J.-L., Verinaud, C., et al. 2010, *EPICS: direct imaging of exoplanets with the E-ELT*, in Society of Photo-Optical Instrumentation Engineers (SPIE) Conference Series, Vol. 7735, Ground-based and Airborne Instrumentation for Astronomy III, ed. I. S. McLean, S. K. Ramsay, & H. Takami, 77352E

Kawahara, H. 2020, *Global Mapping of the Surface Composition on an Exo-Earth Using Color Variability*, ApJ, 894, 58

Keles, E., Mallonn, M., Kitzmann, D., et al. 2022, *The PEPSI exoplanet transit survey (PETS) I: investigating the presence of a silicate atmosphere on the super-earth 55 Cnc e*, MNRAS, 513, 1544

Keller, C. U., Korkiakoski, V., Doelman, N., et al. 2012, *Extremely fast focal-plane wavefront sensing for extreme adaptive optics*, in Society of Photo-Optical Instrumentation Engineers

(SPIE) Conference Series, Vol. 8447, Adaptive Optics Systems III, ed. B. L. Ellerbroek, E. Marchetti, & J.-P. Véran, 844721

Kenworthy, M. A., Absil, O., Carlomagno, B., et al. 2018a, *A review of high contrast imaging modes for METIS*, in Society of Photo-Optical Instrumentation Engineers (SPIE) Conference Series, Vol. 10702, Ground-based and Airborne Instrumentation for Astronomy VII, ed. C. J. Evans, L. Simard, & H. Takami, 10702A3

Kenworthy, M. A., Codona, J. L., Hinz, P. M., et al. 2007, *First On-Sky High-Contrast Imaging with an Apodizing Phase Plate*, ApJ, 660, 762

Kenworthy, M. A., Snik, F., Keller, C. U., et al. 2018b, *High contrast imaging for the enhanced resolution imager and spectrometer (ERIS)*, in Society of Photo-Optical Instrumentation Engineers (SPIE) Conference Series, Vol. 10702, Ground-based and Airborne Instrumentation for Astronomy VII, ed. C. J. Evans, L. Simard, & H. Takami, 1070246

Keppler, M., Benisty, M., Müller, A., et al. 2018, *Discovery of a planetary-mass companion within the gap of the transition disk around PDS 70*, A&A, 617, A44

Khorshid, N., Min, M., Désert, J. M., Woitke, P., & Dominik, C. 2022, *SimAb: A simple, fast, and flexible model to assess the effects of planet formation on the atmospheric composition of gas giants*, A&A, 667, A147

Kipping, D. & Bakos, G. 2011, *Analysis of Kepler's Short-cadence Photometry for TrES-2b*, ApJ, 733, 36

Kipping, D., Bryson, S., Burke, C., et al. 2022, *An exomoon survey of 70 cool giant exoplanets and the new candidate Kepler-1708 b-i*, Nature Astronomy, 6, 367

Komanduri, R. K., Lawler, K. F., & Escuti, M. J. 2013, *Multi-twist retarders: broadband retardation control using self-aligning reactive liquid crystal layers*, Optics Express, 21, 404

Konacki, M. & Wolszczan, A. 2003, *Masses and Orbital Inclinations of Planets in the PSR B1257+12 System*, ApJ, 591, L147

Konopacky, Q. M., Barman, T. S., Macintosh, B. A., & Marois, C. 2013, *Detection of Carbon Monoxide and Water Absorption Lines in an Exoplanet Atmosphere*, Science, 339, 1398

Konopacky, Q. M., Ghez, A. M., Barman, T. S., et al. 2010, *High-precision Dynamical Masses of Very Low Mass Binaries*, ApJ, 711, 1087

Konopacky, Q. M., Rameau, J., Duchêne, G., et al. 2016, *Discovery of a Substellar Companion to the Nearby Debris Disk Host HR 2562*, ApJ, 829, L4

Korkiakoski, V., Keller, C. U., Doelman, N., et al. 2014, *Fast & Furious focal-plane wavefront sensing*, Appl. Opt., 53, 4565

Kostov, V. & Apai, D. 2013, *Mapping Directly Imaged Giant Exoplanets*, ApJ, 762, 47

Kratter, K. & Lodato, G. 2016, *Gravitational Instabilities in Circumstellar Disks*, ARA&A, 54, 271

Kratter, K. M., Murray-Clay, R. A., & Youdin, A. N. 2010, *The Runts of the Litter: Why Planets Formed Through Gravitational Instability Can Only Be Failed Binary Stars*, ApJ, 710, 1375

Kravchenko, K., Dallilar, Y., Absil, O., et al. 2022, *First on-sky results of ERIS at VLT*, in Society of Photo-Optical Instrumentation Engineers (SPIE) Conference Series, Vol. 12184, Ground-based and Airborne Instrumentation for Astronomy IX, ed. C. J. Evans, J. J. Bryant, & K. Motohara, 121845M

Kreidberg, L., Bean, J. L., Désert, J.-M., et al. 2014, *Clouds in the atmosphere of the super-Earth exoplanet GJ1214b*, Nature, 505, 69

Kreidberg, L., Luger, R., & Bedell, M. 2019, *No Evidence for Lunar Transit in New Analysis of Hubble Space Telescope Observations of the Kepler-1625 System*, ApJ, 877, L15

Kumar, S. S. 1962, *Study of Degeneracy in Very Light Stars.*, AJ, 67, 579

Kuwata, A., Kawahara, H., Aizawa, M., Kotani, T., & Tamura, M. 2022, *Global Mapping of Surface Composition on an Exo-Earth Using Sparse Modeling*, ApJ, 930, 162

Kuzuhara, M., Currie, T., Takarada, T., et al. 2022, *Direct-imaging Discovery and Dynamical Mass of a Substellar Companion Orbiting an Accelerating Hyades Sun-like Star with SCExAO/CHARIS*, ApJ, 934, L18

Lafrenière, D., Marois, C., Doyon, R., Nadeau, D., & Artigau, É. 2007, *A New Algorithm for Point-Spread Function Subtraction in High-Contrast Imaging: A Demonstration with Angular Differential Imaging*, ApJ, 660, 770

Lagrange, A. M., Bonnefoy, M., Chauvin, G., et al. 2010, *A Giant Planet Imaged in the Disk of the Young Star β Pictoris*, Science, 329, 57

Lamb, M., Norton, A., Macintosh, B., et al. 2018, *Application of the phase diversity to estimate the non-common path aberrations in the Gemini planet imager: results from simulation and real data*, in Society of Photo-Optical Instrumentation Engineers (SPIE) Conference Series, Vol. 10703, Adaptive Optics Systems VI, ed. L. M. Close, L. Schreiber, & D. Schmidt, 107035M

Lambrechts, M. & Johansen, A. 2012, *Rapid growth of gas-giant cores by pebble accretion*, A&A, 544, A32

Langlois, M., Gratton, R., Lagrange, A. M., et al. 2021, *The SPHERE infrared survey for exoplanets (SHINE). II. Observations, data reduction and analysis, detection performances, and initial results*, A&A, 651, A71

Langlois, M., Vigan, A., Moutou, C., et al. 2013, *Infrared Differential Imager and Spectrograph for SPHERE: Performance Status with Extreme Adaptive Optics before shipment to ESO/VLT*, in Proceedings of the Third AO4ELT Conference, ed. S. Esposito & L. Fini, 63

Lazzoni, C., Desidera, S., Gratton, R., et al. 2022, *Detectability of satellites around directly imaged exoplanets and brown dwarfs*, MNRAS, 516, 391

Lazzoni, C., Zurlo, A., Desidera, S., et al. 2020, *The search for disks or planetary objects around directly imaged companions: a candidate around DH Tauri B*, A&A, 641, A131

Le Verrier, U. J. 1846a, *Schreiben des Herrn Le Verrier an den herausgeber*, Astronomische Nachrichten, 25, 53

Le Verrier, U. J. 1846b, *Recherches sur les mouvements d'Uranus par U. J. Le Verrier (Fortsetzung).*, Astronomische Nachrichten, 25, 65

Leggett, S. K., Cushing, M. C., Hardegree-Ullman, K. K., et al. 2016, *Observed Variability at 1 and 4 μm in the Y0 Brown Dwarf WISEP J173835.52+273258.9*, ApJ, 830, 141

Leggett, S. K., Golimowski, D. A., Fan, X., Geballe, T. R., & Knapp, G. R. 2003a, *Infrared Colors of L and T Dwarfs*, in Cambridge Workshop on Cool Stars, Stellar Systems, and the Sun, Vol. 12, The Future of Cool-Star Astrophysics: 12th Cambridge Workshop on Cool Stars, Stellar Systems, and the Sun, ed. A. Brown, G. M. Harper, & T. R. Ayres, 120–127

Leggett, S. K., Hawarden, T. G., Currie, M. J., et al. 2003b, *L' and M' standard stars for the Mauna Kea Observatories Near-Infrared system*, MNRAS, 345, 144

Leisenring, J. M., Skrutskie, M. F., Hinz, P. M., et al. 2012, *On-sky operations and performance of LMIRcam at the Large Binocular Telescope*, in Society of Photo-Optical Instrumentation Engineers (SPIE) Conference Series, Vol. 8446, Ground-based and Airborne Instrumentation for Astronomy IV, ed. I. S. McLean, S. K. Ramsay, & H. Takami, 84464F

Lew, B. W. P., Apai, D., Marley, M., et al. 2020a, *Cloud Atlas: Unraveling the Vertical Cloud Structure with the Time-series Spectrophotometry of an Unusually Red Brown Dwarf*, ApJ, 903, 15

Lew, B. W. P., Apai, D., Zhou, Y., et al. 2020b, *Cloud Atlas: Weak Color Modulations Due to Rotation in the Planetary-mass Companion GU Psc b and 11 Other Brown Dwarfs*, AJ, 159, 125

Lew, B. W. P., Apai, D., Zhou, Y., et al. 2016, *Cloud Atlas: Discovery of Patchy Clouds and High-amplitude Rotational Modulations in a Young, Extremely Red L-type Brown Dwarf*, ApJ, 829, L32

Lewis, B., Fitzgerald, M. P., Dodkins, R. H., Davis, K. K., & Lin, J. 2023, *Speckle Space-Time Covariance in High-contrast Imaging*, AJ, 165, 59

Li, C., Xian, H., Jiang, W., & Rao, C. 2012, in Topics in Adaptive Optics, ed. R. K. Tyson (Rijeka: IntechOpen)

Li, Y., Brandt, T. D., Brandt, G. M., et al. 2023, *Surveying Nearby Brown Dwarfs with HGCA: Direct Imaging Discovery of a Faint, High-Mass Brown Dwarf Orbiting HD 176535 A*, arXiv e-prints, arXiv:2301.10420

Limbach, M. A., Soares-Furtado, M., Vanderburg, A., et al. 2023, *The TEMPO Survey. I. Predicting Yields of Transiting Exosatellites, Moons, and Planets from a 30 days Survey of Orion with the Roman Space Telescope*, PASP, 135, 014401

Limbach, M. A. & Turner, E. L. 2013, *On the Direct Imaging of Tidally Heated Exomoons*, ApJ, 769, 98

Limbach, M. A., Vos, J. M., Winn, J. N., et al. 2021, *On the Detection of Exomoons Transiting Isolated Planetary-mass Objects*, ApJ, 918, L25

Lipatov, M., Brandt, T. D., & Batalha, N. E. 2022, *Effects of rotation on the spectra of brown dwarfs*, MNRAS, 517, 2942

Liu, M. C., Dupuy, T. J., & Allers, K. N. 2016, *The Hawaii Infrared Parallax Program. II. Young Ultracool Field Dwarfs*, ApJ, 833, 96

Liu, M. C., Wahhaj, Z., Biller, B. A., et al. 2010, *The Gemini NICI Planet-Finding Campaign*, in Society of Photo-Optical Instrumentation Engineers (SPIE) Conference Series, Vol. 7736, Adaptive Optics Systems II, ed. B. L. Ellerbroek, M. Hart, N. Hubin, & P. L. Wizinowich, 77361K

Lloyd-Hart, M. 2000, *Thermal Performance Enhancement of Adaptive Optics by Use of a Deformable Secondary Mirror*, PASP, 112, 264

Lomb, N. R. 1976, *Least-Squares Frequency Analysis of Unequally Spaced Data*, Ap&SS, 39, 447

Long, J. D., Males, J. R., Morzinski, K. M., et al. 2018, *The hunt for Sirius Ab: comparison of algorithmic sky and PSF estimation performance in deep coronagraphic thermal-IR high contrast imaging*, in Society of Photo-Optical Instrumentation Engineers (SPIE) Conference Series, Vol. 10703, Adaptive Optics Systems VI, 107032T

Looper, D. L., Kirkpatrick, J. D., Cutri, R. M., et al. 2008, *Discovery of Two Nearby Peculiar L Dwarfs from the 2MASS Proper-Motion Survey: Young or Metal-Rich?*, ApJ, 686, 528

Lozi, J., Guyon, O., Kudo, T., et al. 2020, *New NIR spectro-polarimetric modes for the SCExAO instrument*, in Society of Photo-Optical Instrumentation Engineers (SPIE) Conference Series, Vol. 11448, Society of Photo-Optical Instrumentation Engineers (SPIE) Conference Series, 114487C

Luger, R., Agol, E., Bartolić, F., & Foreman-Mackey, D. 2022, *Analytic Light Curves in Reflected Light: Phase Curves, Occultations, and Non-Lambertian Scattering for Spherical Planets and Moons*, AJ, 164, 4

Luger, R., Agol, E., Foreman-Mackey, D., et al. 2019, *starry: Analytic Occultation Light Curves*, AJ, 157, 64

Luger, R., Bedell, M., Foreman-Mackey, D., et al. 2021, *Mapping stellar surfaces III: An Efficient, Scalable, and Open-Source Doppler Imaging Model*, arXiv e-prints, arXiv:2110.06271

Luhman, K. L. 2012, *The Formation and Early Evolution of Low-Mass Stars and Brown Dwarfs*, ARA&A, 50, 65

Luhman, K. L., Patten, B. M., Marengo, M., et al. 2007, *Discovery of Two T Dwarf Companions with the Spitzer Space Telescope*, ApJ, 654, 570

Lyot, B. 1932, *Étude de la couronne solaire en dehors des éclipses. Avec 16 figures dans le texte.*, ZAp, 5, 73

Lyot, B. 1939, *The study of the solar corona and prominences without eclipses (George Darwin Lecture, 1939)*, MNRAS, 99, 580

Macintosh, B., Graham, J. R., Barman, T., et al. 2015, *Discovery and spectroscopy of the young jovian planet 51 Eri b with the Gemini Planet Imager*, Science, 350, 64

Macintosh, B., Graham, J. R., Ingraham, P., et al. 2014, *First light of the Gemini Planet Imager*, Proceedings of the National Academy of Science, 111, 12661

Madurowicz, A., Macintosh, B., Chilcote, J., et al. 2019, *Asymmetries in adaptive optics point spread functions*, Journal of Astronomical Telescopes, Instruments, and Systems, 5, 049003

Madurowicz, A., Macintosh, B. A., Ruffio, J.-B., et al. 2018, *Characterization of lemniscate atmospheric aberrations in Gemini Planet Imager data*, in Society of Photo-Optical Instrumentation Engineers (SPIE) Conference Series, Vol. 10703, Adaptive Optics Systems VI, ed. L. M. Close, L. Schreiber, & D. Schmidt, 107036E

Maire, A. L., Bonnefoy, M., Ginski, C., et al. 2016, *First light of the VLT planet finder SPHERE. II. The physical properties and the architecture of the young systems PZ Telescopii and HD 1160 revisited*, A&A, 587, A56

Maire, A. L., Rodet, L., Lazzoni, C., et al. 2018, *VLT/SPHERE astrometric confirmation and orbital analysis of the brown dwarf companion HR 2562 B*, A&A, 615, A177

Males, J. R., Close, L. M., Guyon, O., et al. 2016, *The path to visible extreme adaptive optics with MagAO-2K and MagAO-X*, in Society of Photo-Optical Instrumentation Engineers (SPIE) Conference Series, Vol. 9909, Adaptive Optics Systems V, ed. E. Marchetti, L. M. Close, & J.-P. Véran, 990952

Males, J. R., Fitzgerald, M. P., Belikov, R., & Guyon, O. 2021, *The Mysterious Lives of Speckles. I. Residual Atmospheric Speckle Lifetimes in Ground-based Coronagraphs*, PASP, 133, 104504

Manjavacas, E., Apai, D., Lew, B. W. P., et al. 2019a, *Cloud Atlas: Rotational Spectral Modulations and Potential Sulfide Clouds in the Planetary-mass, Late T-type Companion Ross 458C*, ApJ, 875, L15

Manjavacas, E., Apai, D., Zhou, Y., et al. 2018, *Cloud Atlas: Discovery of Rotational Spectral Modulations in a Low-mass, L-type Brown Dwarf Companion to a Star*, AJ, 155, 11

Manjavacas, E., Apai, D., Zhou, Y., et al. 2019b, *Cloud Atlas: Hubble Space Telescope Near-infrared Spectral Library of Brown Dwarfs, Planetary-mass Companions, and Hot Jupiters*, AJ, 157, 101

Manjavacas, E., Bonnefoy, M., Schlieder, J. E., et al. 2014, *New constraints on the formation and settling of dust in the atmospheres of young M and L dwarfs*, A&A, 564, A55

Manjavacas, E., Karalidi, T., Tan, X., et al. 2022, *Top-of-the-atmosphere and Vertical Cloud Structure of a Fast-rotating Late T Dwarf*, AJ, 164, 65

Manjavacas, E., Karalidi, T., Vos, J. M., Biller, B. A., & Lew, B. W. P. 2021, *Revealing the Vertical Cloud Structure of a Young Low-mass Brown Dwarf, an Analog to the β-Pictoris b Directly Imaged Exoplanet, through Keck I/MOSFIRE Spectrophotometric Variability*, AJ, 162, 179

Marley, M. S., Saumon, D., Cushing, M., et al. 2012, *Masses, Radii, and Cloud Properties of the HR 8799 Planets*, ApJ, 754, 135

Marois, C., Lafrenière, D., Doyon, R., Macintosh, B., & Nadeau, D. 2006a, *Angular Differential Imaging: A Powerful High-Contrast Imaging Technique*, ApJ, 641, 556

Marois, C., Lafrenière, D., Macintosh, B., & Doyon, R. 2006b, *Accurate Astrometry and Photometry of Saturated and Coronagraphic Point Spread Functions*, ApJ, 647, 612

Marois, C., Macintosh, B., Barman, T., et al. 2008, *Direct Imaging of Multiple Planets Orbiting the Star HR 8799*, Science, 322, 1348

Marois, C., Macintosh, B., & Véran, J.-P. 2010a, *Exoplanet imaging with LOCI processing: photometry and astrometry with the new SOSIE pipeline*, in Society of Photo-Optical Instrumentation Engineers (SPIE) Conference Series, Vol. 7736, Adaptive Optics Systems II, ed. B. L. Ellerbroek, M. Hart, N. Hubin, & P. L. Wizinowich, 77361J

Marois, C., Zuckerman, B., Konopacky, Q. M., Macintosh, B., & Barman, T. 2010b, *Images of a fourth planet orbiting HR 8799*, Nature, 468, 1080

Martinez, P., Kasper, M., Costille, A., et al. 2013, *Speckle temporal stability in XAO coronagraphic images. II. Refine model for quasi-static speckle temporal evolution for VLT/SPHERE*, A&A, 554, A41

Martinez, P., Loose, C., Aller Carpentier, E., & Kasper, M. 2012, *Speckle temporal stability in XAO coronagraphic images*, A&A, 541, A136

Mawet, D., David, T., Bottom, M., et al. 2015, *Discovery of a Low-mass Companion Around HR 3549*, ApJ, 811, 103

Mawet, D., Pueyo, L., Lawson, P., et al. 2012, *Review of small-angle coronagraphic techniques in the wake of ground-based second-generation adaptive optics systems*, in Society of Photo-Optical Instrumentation Engineers (SPIE) Conference Series, Vol. 8442, Space Telescopes and Instrumentation 2012: Optical, Infrared, and Millimeter Wave, ed. M. C. Clampin, G. G. Fazio, H. A. MacEwen, & J. Oschmann, Jacobus M., 844204

Mayor, M. & Queloz, D. 1995, *A Jupiter-mass companion to a solar-type star*, Nature, 378, 355

McKinney, W. 2010, *Data Structures for Statistical Computing in Python*, in Proceedings of the 9th Python in Science Conference, ed. Stéfan van der Walt & Jarrod Millman, 56 – 61

McLean, I. S., McGovern, M. R., Burgasser, A. J., et al. 2003, *The NIRSPEC Brown Dwarf Spectroscopic Survey. I. Low-Resolution Near-Infrared Spectra*, ApJ, 596, 561

McNally, D. 1965, *The distribution of angular momentum among main sequence stars*, The Observatory, 85, 166

Meingast, S., Alves, J., & Fürnkranz, V. 2019, *Extended stellar systems in the solar neighborhood . II. Discovery of a nearby 120° stellar stream in Gaia DR2*, A&A, 622, L13

Menduiña-Fernández, Á., Tecza, M., & Thatte, N. 2020, *HARMONI: first light spectroscopy for the ELT: novel techniques for the calibration of non-common path aberrations*, in Society of Photo-Optical Instrumentation Engineers (SPIE) Conference Series, Vol. 11447, Society of Photo-Optical Instrumentation Engineers (SPIE) Conference Series, 114472L

Mesa, D., Baudino, J. L., Charnay, B., et al. 2018, *New spectro-photometric characterization of the substellar object HR 2562 B using SPHERE*, A&A, 612, A92

Mesa, D., D'Orazi, V., Vigan, A., et al. 2020, *Characterizing brown dwarf companions with IRDIS long-slit spectroscopy: HD 1160 B and HD 19467 B*, MNRAS, 495, 4279

Mesa, D., Vigan, A., D'Orazi, V., et al. 2016, *Characterizing HR 3549 B using SPHERE*, A&A, 593, A119

Meshkat, T., Bonnefoy, M., Mamajek, E. E., et al. 2015a, *Discovery of a low-mass companion to the F7V star HD 984*, MNRAS, 453, 2378

Meshkat, T., Kenworthy, M. A., Quanz, S. P., & Amara, A. 2014, *Optimized Principal Component Analysis on Coronagraphic Images of the Fomalhaut System*, ApJ, 780, 17

Meshkat, T., Kenworthy, M. A., Reggiani, M., et al. 2015b, *Searching for gas giant planets on Solar system scales - a NACO/APP L'-band survey of A- and F-type main-sequence stars*, MNRAS, 453, 2533

Metchev, S. A., Heinze, A., Apai, D., et al. 2015, *Weather on Other Worlds. II. Survey Results: Spots are Ubiquitous on L and T Dwarfs*, ApJ, 799, 154

Miles, B. E., Biller, B. A., Patapis, P., et al. 2022, *The JWST Early Release Science Program for Direct Observations of Exoplanetary Systems II: A 1 to 20 Micron Spectrum of the Planetary-Mass Companion VHS 1256-1257 b*, arXiv e-prints, arXiv:2209.00620

Miles-Páez, P. A. 2021, *Detection of photometric variability in the very low-mass binary VHS J1256-1257AB using TESS and Spitzer*, A&A, 651, L7

Miles-Páez, P. A., Metchev, S., Apai, D., et al. 2019, *Cloud Atlas: Variability in and out of the Water Band in the Planetary-mass HD 203030B Points to Cloud Sedimentation in Low-gravity L Dwarfs*, ApJ, 883, 181

Miles-Páez, P. A., Metchev, S. A., & George, B. 2023, *The photometric periods of rapidly rotating field ultra-cool dwarfs*, MNRAS

Miller, K., Males, J. R., Guyon, O., et al. 2018, *Focal plane wavefront sensing and control strategies for high-contrast imaging on the MagAO-X instrument*, in Society of Photo-Optical Instrumentation Engineers (SPIE) Conference Series, Vol. 10703, Adaptive Optics Systems VI, ed. L. M. Close, L. Schreiber, & D. Schmidt, 107031T

Miller, K., Males, J. R., Guyon, O., et al. 2019, *Spatial linear dark field control and holographic modal wavefront sensing with a vAPP coronagraph on MagAO-X*, Journal of Astronomical Telescopes, Instruments, and Systems, 5, 049004

Miller, K. L., Bos, S. P., Lozi, J., et al. 2021, *Spatial linear dark field control on Subaru/SCExAO. Maintaining high contrast with a vAPP coronagraph*, A&A, 646, A145

Milli, J., Hibon, P., Christiaens, V., et al. 2017, *Discovery of a low-mass companion inside the debris ring surrounding the F5V star HD 206893*, A&A, 597, L2

Miskiewicz, M. N. & Escuti, M. J. 2014, *Direct-writing of complex liquid crystal patterns*, Optics Express, 22, 12691

Monnier, J. D., Zhao, M., Pedretti, E., et al. 2007, *Imaging the Surface of Altair*, Science, 317, 342

Montet, B. T., Johnson, J. A., Fortney, J. J., & Desert, J.-M. 2016, *Benchmark Transiting Brown Dwarf LHS 6343 C: Spitzer Secondary Eclipse Observations Yield Brightness Temperature and Mid-T Spectral Class*, ApJ, 822, L6

Moór, A., Ábrahám, P., Derekas, A., et al. 2006, *Nearby Debris Disk Systems with High Fractional Luminosity Reconsidered*, ApJ, 644, 525

Moór, A., Kóspál, Á., Ábrahám, P., et al. 2015, *Stirring in massive, young debris discs from spatially resolved Herschel images*, MNRAS, 447, 577

Morales, J. C., Gallardo, J., Ribas, I., et al. 2010, *The Effect of Magnetic Activity on Low-Mass Stars in Eclipsing Binaries*, ApJ, 718, 502

Morales Durán, C., Alfonso Garzón, J., & Freire Ferrero, R. 2006, The Rv extinction factor, Vol. 2 (Lecture Notes and Essays in Astrophysics), 189–198

Mordasini, C., Alibert, Y., Benz, W., & Naef, D. 2008, *Giant Planet Formation by Core Accretion*, in Astronomical Society of the Pacific Conference Series, Vol. 398, Extreme Solar Systems, ed. D. Fischer, F. A. Rasio, S. E. Thorsett, & A. Wolszczan, 235

Morley, C. V., Skemer, A. J., Allers, K. N., et al. 2018, *An L Band Spectrum of the Coldest Brown Dwarf*, ApJ, 858, 97

Morzinski, K. M., Close, L. M., Males, J. R., et al. 2016, *MagAO: status and science*, in Society of Photo-Optical Instrumentation Engineers (SPIE) Conference Series, Vol. 9909, Adaptive Optics Systems V, ed. E. Marchetti, L. M. Close, & J.-P. Véran, 990901

Morzinski, K. M., Close, L. M., Males, J. R., et al. 2014, *MagAO: Status and on-sky performance of the Magellan adaptive optics system*, in Society of Photo-Optical Instrumentation Engineers (SPIE) Conference Series, Vol. 9148, Adaptive Optics Systems IV, ed. E. Marchetti, L. M. Close, & J.-P. Vran, 914804

Morzinski, K. M., Males, J. R., Skemer, A. J., et al. 2015, *Magellan Adaptive Optics First-light Observations of the Exoplanet β Pic b. II. 3-5 μm Direct Imaging with MagAO+Clio, and the Empirical Bolometric Luminosity of a Self-luminous Giant Planet*, ApJ, 815, 108

Mugnier, L. M., Cornia, A., Sauvage, J.-F., et al. 2009, *Optimal method for exoplanet detection by angular differential imaging*, Journal of the Optical Society of America A, 26, 1326

Nakajima, T., Oppenheimer, B. R., Kulkarni, S. R., et al. 1995, *Discovery of a cool brown dwarf*, Nature, 378, 463

Naud, M.-E., Artigau, É., Rowe, J. F., et al. 2017, *A Search for Photometric Variability in the Young T3.5 Planetary-mass Companion GU Psc b*, AJ, 154, 138

N'Diaye, M., Dohlen, K., Caillat, A., et al. 2014, *Design optimization and lab demonstration of ZELDA: a Zernike sensor for near-coronagraph quasi-static measurements*, in Society of Photo-Optical Instrumentation Engineers (SPIE) Conference Series, Vol. 9148, Adaptive Optics Systems IV, ed. E. Marchetti, L. M. Close, & J.-P. Vran, 91485H

N'Diaye, M., Dohlen, K., Fusco, T., & Paul, B. 2013, *Calibration of quasi-static aberrations in exoplanet direct-imaging instruments with a Zernike phase-mask sensor*, A&A, 555, A94

Nefs, S. V., Birkby, J. L., Snellen, I. A. G., et al. 2013, *A highly unequal-mass eclipsing M-dwarf binary in the WFCAM Transit Survey*, MNRAS, 431, 3240

Nero, D. & Bjorkman, J. E. 2009, *Did Fomalhaut, HR 8799, and HL Tauri Form Planets Via the Gravitational Instability? Placing Limits on the Required Disk Masses*, ApJ, 702, L163

Nielsen, E. L., De Rosa, R. J., Macintosh, B., et al. 2019, *The Gemini Planet Imager Exoplanet Survey: Giant Planet and Brown Dwarf Demographics from 10 to 100 au*, AJ, 158, 13

Nielsen, E. L., Liu, M. C., Wahhaj, Z., et al. 2012, *The Gemini NICI Planet-Finding Campaign: Discovery of a Multiple System Orbiting the Young A Star HD 1160*, ApJ, 750, 53

Nielsen, M. B., Gizon, L., Schunker, H., & Karoff, C. 2013, *Rotation periods of 12 000 main-sequence Kepler stars: Dependence on stellar spectral type and comparison with v sin i observations*, A&A, 557, L10

Nikolov, N., Sing, D. K., Fortney, J. J., et al. 2018a, *An absolute sodium abundance for a cloud-free 'hot Saturn' exoplanet*, Nature, 557, 526

Nikolov, N., Sing, D. K., Goyal, J., et al. 2018b, *Hubble PanCET: an isothermal day-side atmosphere for the bloated gas-giant HAT-P-32Ab*, MNRAS, 474, 1705

Niu, K. & Tian, C. 2022, *Zernike polynomials and their applications*, Journal of Optics, 24, 123001

Noll, R. J. 1976, *Zernike polynomials and atmospheric turbulence.*, Journal of the Optical Society of America (1917-1983), 66, 207

Öberg, K. I., Murray-Clay, R., & Bergin, E. A. 2011, *The Effects of Snowlines on C/O in Planetary Atmospheres*, ApJ, 743, L16

Ochsenbein, F., Bauer, P., & Marcout, J. 2000, *The VizieR database of astronomical catalogues*, A&AS, 143, 23

Oliphant, T. E. 2006, A guide to NumPy, Vol. 1 (Trelgol Publishing USA)

O'Neal, D., Neff, J. E., Saar, S. H., & Cuntz, M. 2004, *Further Results of TiO-Band Observations of Starspots*, AJ, 128, 1802

Otten, G. P. P. L. 2016, *Suppressing a sea of starlight: Enabling technology for the direct imaging of exoplanets*, PhD thesis, University of Leiden, Netherlands

Otten, G. P. P. L., Snik, F., Kenworthy, M. A., et al. 2017, *On-sky Performance Analysis of the Vector Apodizing Phase Plate Coronagraph on MagAO/Clio2*, ApJ, 834, 175

Otten, G. P. P. L., Snik, F., Kenworthy, M. A., Miskiewicz, M. N., & Escuti, M. J. 2014a, *Performance characterization of a broadband vector Apodizing Phase Plate coronagraph*, Optics Express, 22, 30287

Otten, G. P. P. L., Snik, F., Kenworthy, M. A., et al. 2014b, *The vector apodizing phase plate coronagraph: prototyping, characterization and outlook*, in Advances in Optical and Mechanical Technologies for Telescopes and Instrumentation, ed. R. Navarro, C. R. Cunningham, & A. A. Barto, Vol. 9151, International Society for Optics and Photonics (SPIE), 577 – 586

Pancharatnam, S. 1956, *Generalized theory of interference, and its applications*, Proceedings of the Indian Academy of Sciences - Section A, 44, 247

Panwar, V., Désert, J.-M., Todorov, K. O., et al. 2022a, *A new method to correct for host star variability in multiepoch observations of exoplanet transmission spectra*, MNRAS, 515, 5018

Panwar, V., Désert, J.-M., Todorov, K. O., et al. 2022b, *A new method to measure the spectra of transiting exoplanet atmospheres using multi-object spectroscopy*, MNRAS, 510, 3236

Park, W., Lee, J.-E., Contreras Peña, C., et al. 2021, *Quantifying Variability of Young Stellar Objects in the Mid-infrared Over 6 Years with the Near-Earth Object Wide-field Infrared Survey Explorer*, ApJ, 920, 132

Paxman, R. G., Schulz, T. J., & Fienup, J. R. 1992, *Joint estimation of object and aberrations by using phase diversity*, Journal of the Optical Society of America A, 9, 1072

Pecaut, M. J. & Mamajek, E. E. 2013, *Intrinsic Colors, Temperatures, and Bolometric Corrections of Pre-main-sequence Stars*, ApJS, 208, 9

Pedregosa, F., Varoquaux, G., Gramfort, A., et al. 2011, *Scikit-learn: Machine Learning in Python*, Journal of Machine Learning Research, 12, 2825

Perrin, M. D., Pueyo, L., Van Gorkom, K., et al. 2018, *Updated optical modeling of JWST coronagraph performance contrast, stability, and strategies*, in Society of Photo-Optical Instrumentation Engineers (SPIE) Conference Series, Vol. 10698, Space Telescopes and Instrumentation 2018: Optical, Infrared, and Millimeter Wave, ed. M. Lystrup, H. A. MacEwen, G. G. Fazio, N. Batalha, N. Siegler, & E. C. Tong, 1069809

Perrot, C., Baudoz, P., Boccaletti, A., et al. 2018, *Design study and first performance simulation of the ELT/MICADO focal plane coronagraphs*, arXiv e-prints, arXiv:1804.01371

Pinna, E., Esposito, S., Hinz, P., et al. 2016, *SOUL: the Single conjugated adaptive Optics Upgrade for LBT*, in Society of Photo-Optical Instrumentation Engineers (SPIE) Conference Series, Vol. 9909, Adaptive Optics Systems V, ed. E. Marchetti, L. M. Close, & J.-P. Véran, 99093V

Pinna, E., Rossi, F., Puglisi, A., et al. 2021, *Bringing SOUL on sky*, arXiv e-prints, arXiv:2101.07091

Plummer, M. K. & Wang, J. 2022, *A Unified Spectroscopic and Photometric Model to Infer Surface Inhomogeneity: Application to Luhman 16B*, ApJ, 933, 163

Pollack, J. B., Hubickyj, O., Bodenheimer, P., et al. 1996, *Formation of the Giant Planets by Concurrent Accretion of Solids and Gas*, Icarus, 124, 62

Pont, F., Zucker, S., & Queloz, D. 2006, *The effect of red noise on planetary transit detection*, MNRAS, 373, 231

Por, E. H. 2017, *Optimal design of apodizing phase plate coronagraphs*, in Society of Photo-Optical Instrumentation Engineers (SPIE) Conference Series, Vol. 10400, Society of Photo-Optical Instrumentation Engineers (SPIE) Conference Series, 104000V

Por, E. H., Haffert, S. Y., Radhakrishnan, V. M., et al. 2018, *High Contrast Imaging for Python (HCIPy): an open-source adaptive optics and coronagraph simulator*, in Society of Photo-Optical Instrumentation Engineers (SPIE) Conference Series, Vol. 10703, Adaptive Optics Systems VI, ed. L. M. Close, L. Schreiber, & D. Schmidt, 1070342

Quanz, S. P., Amara, A., Meyer, M. R., et al. 2015, *Confirmation and Characterization of the Protoplanet HD 100546 b—Direct Evidence for Gas Giant Planet Formation at 50 AU*, ApJ, 807, 64

Quanz, S. P., Meyer, M. R., Kenworthy, M. A., et al. 2010, *First Results from Very Large Telescope NACO Apodizing Phase Plate: 4 μm Images of The Exoplanet β Pictoris b*, ApJ, 722, L49

Rabien, S., Angel, R., Barl, L., et al. 2019, *ARGOS at the LBT. Binocular laser guided ground-layer adaptive optics*, A&A, 621, A4

Racine, R., Walker, G. A. H., Nadeau, D., Doyon, R., & Marois, C. 1999, *Speckle Noise and the Detection of Faint Companions*, PASP, 111, 587

Rackham, B. V., Espinoza, N., Berdyugina, S. V., et al. 2022, *Final Report for SAG 21: The Effect of Stellar Contamination on Space-based Transmission Spectroscopy*, arXiv e-prints, arXiv:2201.09905

Radigan, J. 2014, *An Independent Analysis of the Brown Dwarf Atmosphere Monitoring (BAM) Data: Large-amplitude Variability is Rare Outside the L/T Transition*, ApJ, 797, 120

Radigan, J., Jayawardhana, R., Lafrenière, D., et al. 2012, *Large-amplitude Variations of an L/T Transition Brown Dwarf: Multi-wavelength Observations of Patchy, High-contrast Cloud Features*, ApJ, 750, 105

Radigan, J., Lafrenière, D., Jayawardhana, R., & Artigau, E. 2014, *Strong Brightness Variations Signal Cloudy-to-clear Transition of Brown Dwarfs*, ApJ, 793, 75

Ragazzoni, R. 1996, *Pupil plane wavefront sensing with an oscillating prism*, Journal of Modern Optics, 43, 289

Rajan, A., Rameau, J., De Rosa, R. J., et al. 2017, *Characterizing 51 Eri b from 1 to 5 μm: A Partly Cloudy Exoplanet*, AJ, 154, 10

Rappaport, S., Vanderburg, A., Jacobs, T., et al. 2018, *Likely transiting exocomets detected by Kepler*, MNRAS, 474, 1453

Reback, J., jbrockmendel, McKinney, W., et al. 2022, *pandas-dev/pandas: Pandas 1.4.2*

Rebolo, R., Zapatero Osorio, M. R., Madruga, S., et al. 1998, *Discovery of a Low-Mass Brown Dwarf Companion of the Young Nearby Star G 196-3*, Science, 282, 1309

Rebolo, R., Zapatero Osorio, M. R., & Martín, E. L. 1995, *Discovery of a brown dwarf in the Pleiades star cluster*, Nature, 377, 129

Ricker, G. R., Winn, J. N., Vanderspek, R., et al. 2015, *Transiting Exoplanet Survey Satellite (TESS)*, Journal of Astronomical Telescopes, Instruments, and Systems, 1, 014003

Rickman, E. L., Matthews, E., Ceva, W., et al. 2022, *Precise dynamical masses of new directly imaged companions from combining relative astrometry, radial velocities, and HIPPARCOS-Gaia eDR3 accelerations*, A&A, 668, A140

Rickman, E. L., Ségransan, D., Hagelberg, J., et al. 2020, *Spectral and atmospheric characterisation of a new benchmark brown dwarf HD 13724 B*, A&A, 635, A203

Rockenfeller, B., Bailer-Jones, C. A. L., & Mundt, R. 2006, *Variability and periodicity of field M dwarfs revealed by multichannel monitoring*, A&A, 448, 1111

Rodenbeck, K., Heller, R., Hippke, M., & Gizon, L. 2018, *Revisiting the exomoon candidate signal around Kepler-1625 b*, A&A, 617, A49

Röser, S. & Schilbach, E. 2020, *A census of the nearby Pisces-Eridanus stellar stream. Commonalities with and disparities from the Pleiades*, A&A, 638, A9

Rousset, G., Fontanella, J. C., Kern, P., Gigan, P., & Rigaut, F. 1990, *First diffraction-limited astronomical images with adaptive optics*, A&A, 230, L29

Ruane, G., Riggs, A., Mazoyer, J., et al. 2018, *Review of high-contrast imaging systems for current and future ground- and space-based telescopes I: coronagraph design methods and optical performance metrics*, in Society of Photo-Optical Instrumentation Engineers (SPIE) Conference Series, Vol. 10698, Space Telescopes and Instrumentation 2018: Optical, Infrared, and Millimeter Wave, ed. M. Lystrup, H. A. MacEwen, G. G. Fazio, N. Batalha, N. Siegler, & E. C. Tong, 106982S

Ruffio, J.-B., Macintosh, B., Konopacky, Q. M., et al. 2019, *Radial Velocity Measurements of HR 8799 b and c with Medium Resolution Spectroscopy*, AJ, 158, 200

Samland, M., Bouwman, J., Hogg, D. W., et al. 2021, *TRAP: a temporal systematics model for improved direct detection of exoplanets at small angular separations*, A&A, 646, A24

Samland, M., Mollière, P., Bonnefoy, M., et al. 2017, *Spectral and atmospheric characterization of 51 Eridani b using VLT/SPHERE*, A&A, 603, A57

Saumon, D. & Marley, M. S. 2008, *The Evolution of L and T Dwarfs in Color-Magnitude Diagrams*, ApJ, 689, 1327

Sauvage, J.-F., Fusco, T., Rousset, G., & Petit, C. 2007, *Calibration and precompensation of noncommon path aberrations for extreme adaptive optics*, Journal of the Optical Society of America A, 24, 2334

Scargle, J. D. 1982, *Studies in astronomical time series analysis. II. Statistical aspects of spectral analysis of unevenly spaced data.*, ApJ, 263, 835

Scholz, A., Eislöffel, J., & Mundt, R. 2009, *Long-term monitoring in IC4665: fast rotation and weak variability in very low mass objects*, MNRAS, 400, 1548

Scholz, A., Muzic, K., Jayawardhana, R., Quinlan, L., & Wurster, J. 2022, *Rogue Planets and Brown Dwarfs: Predicting the Populations Free-floating Planetary Mass Objects Observable with JWST*, PASP, 134, 104401

Schwarz, H., Ginski, C., de Kok, R. J., et al. 2016, *The slow spin of the young substellar companion GQ Lupi b and its orbital configuration*, A&A, 593, A74

Seabold, S. & Perktold, J. 2010, *statsmodels: Econometric and statistical modeling with python*, in 9th Python in Science Conference

Seager, S. & Sasselov, D. D. 2000, *Theoretical Transmission Spectra during Extrasolar Giant Planet Transits*, ApJ, 537, 916

Siess, L., Dufour, E., & Forestini, M. 2000, *An internet server for pre-main sequence tracks of low- and intermediate-mass stars*, A&A, 358, 593

Simon, A. A., Hueso, R., Sánchez-Lavega, A., & Wong, M. H. 2021, *Midsummer Atmospheric Changes in Saturn's Northern Hemisphere from the Hubble OPAL Program*, The Planetary Science Journal, 2, 47

Simon, A. A., Rowe, J. F., Gaulme, P., et al. 2016, *Neptune's Dynamic Atmosphere from Kepler K2 Observations: Implications for Brown Dwarf Light Curve Analyses*, ApJ, 817, 162

Sivanandam, S., Hinz, P. M., Heinze, A. N., Freed, M., & Breuninger, A. H. 2006, *Clio: a 3-5 micron AO planet-finding camera*, in Society of Photo-Optical Instrumentation Engineers (SPIE) Conference Series, Vol. 6269, Society of Photo-Optical Instrumentation Engineers (SPIE) Conference Series, ed. I. S. McLean & M. Iye, 62690U

Sivaramakrishnan, A. & Oppenheimer, B. R. 2006, *Astrometry and Photometry with Coronagraphs*, ApJ, 647, 620

Skaf, N., Guyon, O., Gendron, É., et al. 2022, *On-sky validation of image-based adaptive optics wavefront sensor referencing*, A&A, 659, A170

Skemer, A. J., Hinz, P., Esposito, S., et al. 2014a, *High contrast imaging at the LBT: the LEECH exoplanet imaging survey*, in Society of Photo-Optical Instrumentation Engineers (SPIE) Conference Series, Vol. 9148, Adaptive Optics Systems IV, ed. E. Marchetti, L. M. Close, & J.-P. Vran, 91480L

Skemer, A. J., Hinz, P., Montoya, M., et al. 2015, *First light with ALES: A 2-5 micron adaptive optics Integral Field Spectrograph for the LBT*, in Society of Photo-Optical Instrumentation Engineers (SPIE) Conference Series, Vol. 9605, Techniques and Instrumentation for Detection of Exoplanets VII, ed. S. Shaklan, 96051D

Skemer, A. J., Hinz, P., Stone, J., et al. 2018, *ALES: overview and upgrades*, in Society of Photo-Optical Instrumentation Engineers (SPIE) Conference Series, Vol. 10702, Ground-based and Airborne Instrumentation for Astronomy VII, ed. C. J. Evans, L. Simard, & H. Takami, 107020C

Skemer, A. J., Hinz, P. M., Esposito, S., et al. 2012, *First Light LBT AO Images of HR 8799 bcde at 1.6 and 3.3 μm: New Discrepancies between Young Planets and Old Brown Dwarfs*, ApJ, 753, 14

Skemer, A. J., Marley, M. S., Hinz, P. M., et al. 2014b, *Directly Imaged L-T Transition Exoplanets in the Mid-infrared*, ApJ, 792, 17

Skemer, A. J., Morley, C. V., Allers, K. N., et al. 2016a, *The First Spectrum of the Coldest Brown Dwarf*, ApJ, 826, L17

Skemer, A. J., Morley, C. V., Zimmerman, N. T., et al. 2016b, *The LEECH Exoplanet Imaging Survey: Characterization of the Coldest Directly Imaged Exoplanet, GJ 504 b, and Evidence for Superstellar Metallicity*, ApJ, 817, 166

Skrutskie, M. F., Cutri, R. M., Stiening, R., et al. 2006, *The Two Micron All Sky Survey (2MASS)*, AJ, 131, 1163

Skrutskie, M. F., Jones, T., Hinz, P., et al. 2010, *The Large Binocular Telescope mid-infrared camera (LMIRcam): final design and status*, in Society of Photo-Optical Instrumentation Engineers (SPIE) Conference Series, Vol. 7735, Ground-based and Airborne Instrumentation for Astronomy III, ed. I. S. McLean, S. K. Ramsay, & H. Takami, 77353H

Snellen, I., de Kok, R., Birkby, J. L., et al. 2015, *Combining high-dispersion spectroscopy with high contrast imaging: Probing rocky planets around our nearest neighbors*, A&A, 576, A59

Snellen, I. A. G., Brandl, B. R., de Kok, R. J., et al. 2014, *Fast spin of the young extrasolar planet β Pictoris b*, Nature, 509, 63

Snik, F., Otten, G., Kenworthy, M., et al. 2012, *The vector-APP: a broadband apodizing phase plate that yields complementary PSFs*, in Society of Photo-Optical Instrumentation Engineers (SPIE) Conference Series, Vol. 8450, Modern Technologies in Space- and Ground-based Telescopes and Instrumentation II, 84500M

Solanki, S. K. & Unruh, Y. C. 1998, *A model of the wavelength dependence of solar irradiance variations*, A&A, 329, 747

Soummer, R. 2005, *Apodized Pupil Lyot Coronagraphs for Arbitrary Telescope Apertures*, ApJ, 618, L161

Soummer, R., Pueyo, L., & Larkin, J. 2012, *Detection and Characterization of Exoplanets and Disks Using Projections on Karhunen-Loève Eigenimages*, ApJ, 755, L28

Sparks, W. B. & Ford, H. C. 2002, *Imaging Spectroscopy for Extrasolar Planet Detection*, ApJ, 578, 543

Spiegel, D. S., Burrows, A., & Milsom, J. A. 2011, *The Deuterium-burning Mass Limit for Brown Dwarfs and Giant Planets*, ApJ, 727, 57

Stauffer, J., Marley, M. S., Gizis, J. E., et al. 2016, *Spitzer Space Telescope Mid-IR Light Curves of Neptune*, AJ, 152, 142

Stevenson, K. B., Bean, J. L., Seifahrt, A., et al. 2014, *Transmission Spectroscopy of the Hot Jupiter WASP-12b from 0.7 to 5 μm*, AJ, 147, 161

Stolker, T., Bonse, M. J., Quanz, S. P., et al. 2019, *PynPoint: a modular pipeline architecture for processing and analysis of high-contrast imaging data*, A&A, 621, A59

Stone, J. M., Barman, T., Skemer, A. J., et al. 2020, *High-contrast Thermal Infrared Spectroscopy with ALES: The 3-4 μm Spectrum of κ Andromedae b*, AJ, 160, 262

Stone, J. M., Eisner, J., Skemer, A., et al. 2016, *L-band Spectroscopy with Magellan-AO/Clio2: First Results on Young Low-mass Companions*, ApJ, 829, 39

Stone, J. M., Skemer, A., Hinz, P., et al. 2022, *On-sky performance and results of the recently upgraded ALES integral field spectrograph*, in Society of Photo-Optical Instrumentation Engineers (SPIE) Conference Series, Vol. 12184, Ground-based and Airborne Instrumentation for Astronomy IX, ed. C. J. Evans, J. J. Bryant, & K. Motohara, 1218442

Stone, J. M., Skemer, A. J., Hinz, P., et al. 2018, *On-sky operations with the ALES integral field spectrograph*, in Society of Photo-Optical Instrumentation Engineers (SPIE) Conference Series, Vol. 10702, Ground-based and Airborne Instrumentation for Astronomy VII, ed. C. J. Evans, L. Simard, & H. Takami, 107023F

Strassmeier, K. G. 2009, *Starspots*, A&A Rev., 17, 251

Strassmeier, K. G., Ilyin, I., Järvinen, A., et al. 2015, *PEPSI: The high-resolution échelle spectrograph and polarimeter for the Large Binocular Telescope*, Astronomische Nachrichten, 336, 324

Strassmeier, K. G., Ilyin, I., & Steffen, M. 2018a, *PEPSI deep spectra. I. The Sun-as-a-star*, A&A, 612, A44

Strassmeier, K. G., Ilyin, I., & Weber, M. 2018b, *PEPSI deep spectra. II. Gaia benchmark stars and other M-K standards*, A&A, 612, A45

Strassmeier, K. G., Ilyin, I., Weber, M., et al. 2018c, *Want a PEPSI? Performance status of the recently commissioned high-resolution spectrograph and polarimeter for the 2x8.4m Large Binocular Telescope*, in Society of Photo-Optical Instrumentation Engineers (SPIE) Conference Series, Vol. 10702, Ground-based and Airborne Instrumentation for Astronomy VII, ed. C. J. Evans, L. Simard, & H. Takami, 1070212

Su, K. Y. L., Rieke, G. H., Stansberry, J. A., et al. 2006, *Debris Disk Evolution around A Stars*, ApJ, 653, 675

Sutlieff, B. J., Birkby, J. L., Stone, J. M., et al. 2023, *Measuring the variability of directly imaged exoplanets using vector Apodizing Phase Plates combined with ground-based differential spectrophotometry*, MNRAS, 520, 4235–4257

Sutlieff, B. J., Bohn, A. J., Birkby, J. L., et al. 2021, *High-contrast observations of brown dwarf companion HR 2562 B with the vector Apodizing Phase Plate coronagraph*, MNRAS, 506, 3224

Tackett, S., Herbst, W., & Williams, E. 2003, *Periodic Variability in the Pre-Main-Sequence Object CB 34V*, AJ, 126, 348

Tan, X. & Showman, A. P. 2019, *Atmospheric Variability Driven by Radiative Cloud Feedback in Brown Dwarfs and Directly Imaged Extrasolar Giant Planets*, ApJ, 874, 111

Tan, X. & Showman, A. P. 2021, *Atmospheric circulation of brown dwarfs and directly imaged exoplanets driven by cloud radiative feedback: effects of rotation*, MNRAS, 502, 678

Tannock, M. E., Metchev, S., Heinze, A., et al. 2021, *Weather on Other Worlds. V. The Three Most Rapidly Rotating Ultra-cool Dwarfs*, AJ, 161, 224

Teachey, A., Kipping, D., Burke, C. J., Angus, R., & Howard, A. W. 2020, *Loose Ends for the Exomoon Candidate Host Kepler-1625b*, AJ, 159, 142

Teachey, A. & Kipping, D. M. 2018, *Evidence for a large exomoon orbiting Kepler-1625b*, Science Advances, 4, eaav1784

Teinturier, L., Vieira, N., Jacquet, E., et al. 2022, *Mapping the surface of partially cloudy exoplanets is hard*, MNRAS, 511, 440

Thibault, S., Allain, G., Côté, O., et al. 2019, *Stringent and result-oriented training requirements at the heart of research funding opportunities: the case of the CSA FAST funding activity and the HiCIBaS project*, in Society of Photo-Optical Instrumentation Engineers (SPIE) Conference Series, Vol. 11143, Fifteenth Conference on Education and Training in Optics and Photonics: ETOP 2019, 1114304

Thiemann, H. B., Norton, A. J., Dickinson, H. J., McMaster, A., & Kolb, U. C. 2021, *SuperWASP variable stars: classifying light curves using citizen science*, MNRAS, 502, 1299

Todorov, K., Luhman, K. L., & McLeod, K. K. 2010, *Discovery of a Planetary-mass Companion to a Brown Dwarf in Taurus*, ApJ, 714, L84

Todorov, K. O., Désert, J.-M., Huitson, C. M., et al. 2019, *Ground-based optical transmission spectrum of the hot Jupiter HAT-P-1b*, A&A, 631, A169

Tofflemire, B. M., Wisniewski, J. P., Kowalski, A. F., et al. 2012, *The Implications of M Dwarf Flares on the Detection and Characterization of Exoplanets at Infrared Wavelengths*, AJ, 143, 12

Tremblin, P., Amundsen, D. S., Chabrier, G., et al. 2016, *Cloudless Atmospheres for L/T Dwarfs and Extrasolar Giant Planets*, ApJ, 817, L19

Tremblin, P., Phillips, M. W., Emery, A., et al. 2020, *Rotational spectral modulation of cloudless atmospheres for L/T brown dwarfs and extrasolar giant planets*, A&A, 643, A23

Unruh, Y. C., Solanki, S. K., & Fligge, M. 1999, *The spectral dependence of facular contrast and solar irradiance variations*, A&A, 345, 635

van der Marel, N., Bosman, A. D., Krijt, S., Mulders, G. D., & Bergner, J. B. 2021, *If you like C/O variations, you should have put a ring on it*, A&A, 653, L9

Van Der Walt, S., Colbert, S. C., & Varoquaux, G. 2011, *The NumPy array: a structure for efficient numerical computation*, Computing in Science & Engineering, 13, 22

van der Walt, S., Schönberger, J. L., Nunez-Iglesias, J., et al. 2014, *scikit-image: image processing in Python*, PeerJ, 2, e453

van Kooten, M. A. M., Doelman, N., & Kenworthy, M. 2020, *Robustness of prediction for extreme adaptive optics systems under various observing conditions. An analysis using VLT/SPHERE adaptive optics data*, A&A, 636, A81

van Kooten, M. A. M., Jensen-Clem, R., Cetre, S., et al. 2022, *Predictive wavefront control on Keck II adaptive optics bench: on-sky coronagraphic results*, Journal of Astronomical Telescopes, Instruments, and Systems, 8, 029006

van Sluijs, L., Birkby, J. L., Lothringer, J., et al. 2022, *Carbon monoxide emission lines reveal an inverted atmosphere in the ultra hot Jupiter WASP-33 b and indicate an eastward hot spot*, arXiv e-prints, arXiv:2203.13234

Vanderburg, A. & Rodriguez, J. E. 2021, *First Doppler Limits on Binary Planets and Exomoons in the HR 8799 System*, ApJ, 922, L2

Vigan, A., Dohlen, K., N'Diaye, M., et al. 2022, *Calibration of quasi-static aberrations in exoplanet direct-imaging instruments with a Zernike phase-mask sensor. IV. Temporal stability of non-common path aberrations in VLT/SPHERE*, A&A, 660, A140

Vigan, A., Fontanive, C., Meyer, M., et al. 2021, *The SPHERE infrared survey for exoplanets (SHINE). III. The demographics of young giant exoplanets below 300 au with SPHERE*, A&A, 651, A72

Vigan, A., N'Diaye, M., Dohlen, K., et al. 2019, *Calibration of quasi-static aberrations in exoplanet direct-imaging instruments with a Zernike phase-mask sensor. III. On-sky validation in VLT/SPHERE*, A&A, 629, A11

Virtanen, P., Gommers, R., Oliphant, T. E., et al. 2020, *SciPy 1.0: Fundamental Algorithms for Scientific Computing in Python*, Nature Methods, 17, 261

Vos, J. M., Allers, K. N., & Biller, B. A. 2017, *The Viewing Geometry of Brown Dwarfs Influences Their Observed Colors and Variability Amplitudes*, ApJ, 842, 78

Vos, J. M., Allers, K. N., Biller, B. A., et al. 2018, *Variability of the lowest mass objects in the AB Doradus moving group*, MNRAS, 474, 1041

Vos, J. M., Biller, B. A., Allers, K. N., et al. 2020, *Spitzer Variability Properties of Low-gravity L Dwarfs*, AJ, 160, 38

Vos, J. M., Biller, B. A., Bonavita, M., et al. 2019, *A search for variability in exoplanet analogues and low-gravity brown dwarfs*, MNRAS, 483, 480

Vos, J. M., Burningham, B., Faherty, J. K., et al. 2023, *Patchy Forsterite Clouds in the Atmospheres of Two Highly Variable Exoplanet Analogs*, ApJ, 944, 138

Vos, J. M., Faherty, J. K., Gagné, J., et al. 2022, *Let the Great World Spin: Revealing the Stormy, Turbulent Nature of Young Giant Exoplanet Analogs with the Spitzer Space Telescope*, ApJ, 924, 68

Wagner, K., Apai, D., Kasper, M., et al. 2020a, *Direct Imaging Discovery of a Young Brown Dwarf Companion to an A2V Star*, ApJ, 902, L6

Wagner, K., Stone, J., Dong, R., et al. 2020b, *First Images of the Protoplanetary Disk around PDS 201*, AJ, 159, 252

Wang, J. J., Gao, P., Chilcote, J., et al. 2022, *Atmospheric Monitoring and Precise Spectroscopy of the HR 8799 Planets with SCExAO/CHARIS*, AJ, 164, 143

Wang, J. J., Graham, J. R., Dawson, R., et al. 2018, *Dynamical Constraints on the HR 8799 Planets with GPI*, AJ, 156, 192

Wang, J. J., Kulikauskas, M., & Blunt, S. 2021a, *whereistheplanet: Predicting positions of directly imaged companions*, Astrophysics Source Code Library, record ascl:2101.003

Wang, J. J., Rajan, A., Graham, J. R., et al. 2014, *Gemini planet imager observational calibrations VIII: characterization and role of satellite spots*, in Society of Photo-Optical Instrumentation Engineers (SPIE) Conference Series, Vol. 9147, Ground-based and Airborne Instrumentation for Astronomy V, ed. S. K. Ramsay, I. S. McLean, & H. Takami, 914755

Wang, J. J., Ruffio, J.-B., De Rosa, R. J., et al. 2015, *pyKLIP: PSF Subtraction for Exoplanets and Disks*, Astrophysics Source Code Library, record ascl:1506.001

Wang, J. J., Ruffio, J.-B., Morris, E., et al. 2021b, *Detection and Bulk Properties of the HR 8799 Planets with High-resolution Spectroscopy*, AJ, 162, 148

Ward-Duong, K., Patience, J., Follette, K., et al. 2020, *Gemini Planet Imager Spectroscopy of the Dusty Substellar Companion HD 206893 b*, in American Astronomical Society Meeting Abstracts, Vol. 235, American Astronomical Society Meeting Abstracts #235, 254.03

Ward-Duong, K., Patience, J., Follette, K., et al. 2021, *Gemini Planet Imager Spectroscopy of the Dusty Substellar Companion HD 206893 B*, AJ, 161, 5

Wenger, M., Ochsenbein, F., Egret, D., et al. 2000, *The SIMBAD astronomical database. The CDS reference database for astronomical objects*, A&AS, 143, 9

Whiteford, N., Glasse, A., Chubb, K. L., et al. 2023, *Retrieval study of cool, directly imaged exoplanet 51 Eri b*, arXiv e-prints, arXiv:2302.07939

Wilby, M. J., Keller, C. U., Sauvage, J. F., et al. 2018, *Laboratory verification of Fast & Furious phase diversity: Towards controlling the low wind effect in the SPHERE instrument*, A&A, 615, A34

Wilcomb, K. K., Konopacky, Q. M., Barman, T. S., et al. 2020, *Moderate-resolution K-band Spectroscopy of Substellar Companion κ Andromedae b*, AJ, 160, 207

Wilson, J., Gibson, N. P., Lothringer, J. D., et al. 2021, *Gemini/GMOS optical transmission spectroscopy of WASP-121b: signs of variability in an ultra-hot Jupiter?*, MNRAS, 503, 4787

Wilson, J., Gibson, N. P., Nikolov, N., et al. 2020, *Ground-based transmission spectroscopy with FORS2: A featureless optical transmission spectrum and detection of H_2O for the ultra-hot Jupiter WASP-103b*, MNRAS, 497, 5155

Wilson, J. C., Hinz, P. M., Skrutskie, M. F., et al. 2008, *LMIRcam: an L/M-band imager for the LBT combined focus*, in Society of Photo-Optical Instrumentation Engineers (SPIE) Conference Series, Vol. 7013, Optical and Infrared Interferometry, ed. M. Schöller, W. C. Danchi, & F. Delplancke, 70133A

Wilson, P. A., Rajan, A., & Patience, J. 2014, *The brown dwarf atmosphere monitoring (BAM) project. I. The largest near-IR monitoring survey of L and T dwarfs*, A&A, 566, A111

Wolszczan, A. 1994, *Confirmation of Earth-Mass Planets Orbiting the Millisecond Pulsar PSR B1257+12*, Science, 264, 538

Wolszczan, A. & Frail, D. A. 1992, *A planetary system around the millisecond pulsar PSR1257 + 12*, Nature, 355, 145

Wright, E. L., Eisenhardt, P. R. M., Mainzer, A. K., et al. 2010, *The Wide-field Infrared Survey Explorer (WISE): Mission Description and Initial On-orbit Performance*, AJ, 140, 1868

Wright, J. T. 2018, in Handbook of Exoplanets, ed. H. J. Deeg & J. A. Belmonte, 4

Wright, J. T. & Gaudi, B. S. 2013, in Planets, Stars and Stellar Systems. Volume 3: Solar and Stellar Planetary Systems, ed. T. D. Oswalt, L. M. French, & P. Kalas, 489

Xuan, J. W., Bryan, M. L., Knutson, H. A., et al. 2020, *A Rotation Rate for the Planetary-mass Companion DH Tau b*, AJ, 159, 97

Xuan, J. W., Wang, J., Ruffio, J.-B., et al. 2022, *A Clear View of a Cloudy Brown Dwarf Companion from High-resolution Spectroscopy*, ApJ, 937, 54

Yang, H., Apai, D., Marley, M. S., et al. 2016, *Extrasolar Storms: Pressure-dependent Changes in Light-curve Phase in Brown Dwarfs from Simultaneous HST and Spitzer Observations*, ApJ, 826, 8

Zernike, v. F. 1934, *Beugungstheorie des schneidenver-fahrens und seiner verbesserten form, der phasenkontrastmethode*, Physica, 1, 689

Zhang, X. 2020, *Atmospheric regimes and trends on exoplanets and brown dwarfs*, Research in Astronomy and Astrophysics, 20, 099

Zhang, Z., Liu, M. C., Claytor, Z. R., et al. 2021, *The Second Discovery from the COCONUTS Program: A Cold Wide-orbit Exoplanet around a Young Field M Dwarf at 10.9 pc*, ApJ, 916, L11

Zhou, Y., Apai, D., Bedin, L. R., et al. 2020a, *Cloud Atlas: High-precision HST/WFC3/IR Time-resolved Observations of Directly Imaged Exoplanet HD 106906b*, AJ, 159, 140

Zhou, Y., Apai, D., Lew, B. W. P., et al. 2019, *Cloud Atlas: High-contrast Time-resolved Observations of Planetary-mass Companions*, AJ, 157, 128

Zhou, Y., Apai, D., Metchev, S., et al. 2018, *Cloud Atlas: Rotational Modulations in the L/T Transition Brown Dwarf Companion HN Peg B*, AJ, 155, 132

Zhou, Y., Apai, D., Schneider, G. H., Marley, M. S., & Showman, A. P. 2016, *Discovery of Rotational Modulations in the Planetary-mass Companion 2M1207b: Intermediate Rotation Period and Heterogeneous Clouds in a Low Gravity Atmosphere*, ApJ, 818, 176

Zhou, Y., Bowler, B. P., Apai, D., et al. 2022, *Roaring Storms in the Planetary-mass Companion VHS 1256-1257 b: Hubble Space Telescope Multiepoch Monitoring Reveals Vigorous Evolution in an Ultracool Atmosphere*, AJ, 164, 239

Zhou, Y., Bowler, B. P., Morley, C. V., et al. 2020b, *Spectral Variability of VHS J1256-1257b from 1 to 5 μm*, AJ, 160, 77

Zieba, S., Zwintz, K., Kenworthy, M. A., & Kennedy, G. M. 2019, *Transiting exocomets detected in broadband light by TESS in the β Pictoris system*, A&A, 625, L13

Contribution from co-authors

Here I list bibliographic information for the papers included in this thesis. The relative contribution of each co-author is indicated by the order of the author list.

Chapter 2: High-contrast observations of brown dwarf companion HR 2562 B with the vector Apodizing Phase Plate coronagraph
Ben J. Sutlieff, Alexander J. Bohn, Jayne L. Birkby, Matthew A. Kenworthy, Katie M. Morzinski, David S. Doelman, Jared R. Males, Frans Snik, Laird M. Close, Philip M. Hinz, and David Charbonneau
Monthly Notices of the Royal Astronomical Society, 2021, Volume 506, Issue 3, pp. 3224-3238

Chapter 3: Measuring the variability of directly imaged exoplanets using vector Apodizing Phase Plates combined with ground-based differential spectrophotometry
Ben J. Sutlieff, Jayne L. Birkby, Jordan M. Stone, David S. Doelman, Matthew A. Kenworthy, Vatsal Panwar, Alexander J. Bohn, Steve Ertel, Frans Snik, Charles E. Woodward, Andrew J. Skemer, Jarron M. Leisenring, Klaus G. Strassmeier, and David Charbonneau
Monthly Notices of the Royal Astronomical Society, 2023, Volume 520, Issue 3, pp. 4235–4257

Chapter 4: Exploring the directly imaged HD 1160 system through spectroscopic characterisation and high-cadence variability monitoring
Ben J. Sutlieff, Jayne L. Birkby, Jordan M. Stone, Frank Backs, Annelotte Derkink, David S. Doelman, Matthew A. Kenworthy, Alexander J. Bohn, Steve Ertel, Frans Snik, Charles E. Woodward, Ilya Ilyin, Andrew J. Skemer, Jarron M. Leisenring, Klaus G. Strassmeier, and David Charbonneau
To be submitted for publication in *Monthly Notices of the Royal Astronomical Society*

Chapter 5: Investigating the application of adaptive optics and high-contrast imaging techniques in the production of precise exoplanet light curves
Ben J. Sutlieff, David S. Doelman, Jayne L. Birkby, Matthew A. Kenworthy, Jordan M. Stone, Frans Snik, Steve Ertel, and Alexander J. Bohn
To be submitted for publication in *Monthly Notices of the Royal Astronomical Society*

English summary

The planets of our own Solar System possess cloud structures and weather systems with a great diversity of shapes, sizes, lifetimes, and brightnesses. Here on Earth, we experience small, short-lived storms, as well as hurricanes that can last for several days. Jupiter is famous for its iconic 'Great Red Spot', a gigantic storm that has raged on for centuries, and its distinct latitudinal cloud bands (Figure A). As a planet rotates on its axis, these features rotate in and out of view and thereby induce changes in the total brightness of the planet as seen from afar. The motivation for this thesis was to look for similar brightness changes in exoplanets – planets beyond our own solar system – and hence gain an insight into their weather, atmospheric structure, and visual appearance. The properties of these variations, such as their amplitude, periodicity, and shape, provide a unique avenue to obtain valuable information about the physical processes that govern exoplanet atmospheres. Clouds and weather are not the only sources of brightness variability in substellar companions; such changes can also arise from aurorae, similar to the aurora borealis and aurora australis on Earth, or magnetic spots if the object is of a higher mass. Another possible source of variability in exoplanets could be satellites in orbit around the exoplanet, such as exomoons or binary planets. Such satellites would cause periodic drops in the brightness of an exoplanet if its orbit happened to be aligned with the line of sight of the observer. To date, no exomoons have been conclusively detected around an exoplanet, although several candidates have been identified.

Observations with space-based facilities such as the Hubble Space Telescope (HST) have detected brightness variability in the light curves of several substellar companions, consistent with both ground- and space-based studies of isolated brown dwarfs and planetary mass objects. A wide range of variability amplitudes have been detected, from ubiquitous $\geq$0.2% variability found in surveys of L and T dwarfs, up to the 38% peak-to-valley variations seen in the light curve of VHS1256-1257b, the most variable planetary-mass companion observed to date. The periodicity of such variability is typically short, ranging from $\sim$1 hour to $\geq$20 hours, and generally reflects the rotation period of the substellar object. Furthermore, variability evolution has been seen in the light curves of several substellar objects, caused by evolution in the atmospheric features that give rise to the variability. Such evolution has been observed over a range of timescales, including both rapid evolution from one night to the next and longer-term trends over months or years.

Although variability has been successfully measured for numerous substellar companions using space-based telescopes, it is highly challenging to obtain precise photometric measure-

EN

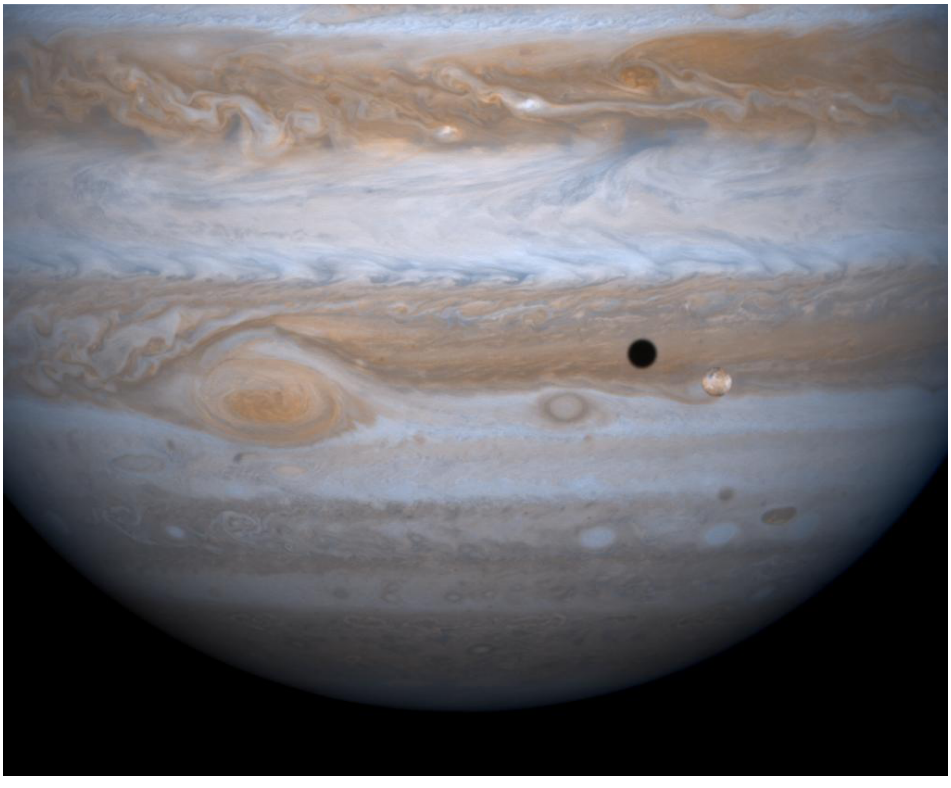

Figure A: A view of Jupiter taken by NASA's Cassini spacecraft. Large storms and atmospheric turbulence can be seen at the interfaces between Jupiter's latitudinal cloud bands. The dark spot is a shadow cast by Io, one of Jupiter's Galilean moons, which itself can be seen slightly to the right of its shadow. Credit: NASA/JPL/University of Arizona.

ments for the population of close-separation, high-contrast, directly imaged exoplanets only accessible to ground-based observatories. The larger mirror diameters and high-contrast imaging systems of ground-based telescopes allow us to detect these companions, but any intrinsic variability signal in their light curves is overwhelmed by non-astrophysical variability introduced by turbulence in Earth's atmosphere and instrumental systematics. This contaminant variability can be removed by dividing the light curve of the companion by that of a simultaneous photometric reference; a separate source that is also contaminated by these systematics but is otherwise non-variable, observed simultaneously to the companion. Variability studies of stars or isolated substellar objects often use known non-variable field stars for this purpose. However, the fields of view of ground-based high-contrast imaging systems are generally narrow, so field stars are rarely available for use as photometric references. Furthermore, these systems generally use focal-plane coronagraphs to block the target star. This is a critical step needed to achieve the necessary contrast to observe faint companions, but this means that an exoplanet's host star also cannot be used as a photometric reference.

In this thesis, one of my main goals is to explore new approaches for measuring the variability of directly imaged exoplanets using ground-based telescopes. The vector Apodizing Phase Plate (vAPP) coronagraph is a unique type of coronagraph that does *not* block the light from the target star, but rather enables the detection of high-contrast companions by modifying its phase (Figure B). Thus, the light from the host star is preserved and may be suitable for use as a simultaneous photometric reference, enabling measurements of exoplanet variability.

In Chapter 2, I present observations of brown dwarf companion HR 2562 B with the 180° grating-vAPP (gvAPP) coronagraph and the Magellan Adaptive Optics (MagAO) system on the 6.5-m Magellan Clay telescope at Las Campanas Observatory, Chile. These are the first reported observations of a substellar companion obtained with a vAPP coronagraph. I process the data using three different post-processing techniques to test which approach recovers the companion at the highest signal-to-noise (S/N). One of these is Flipped Differential Imaging (FDI), a new algorithm I developed to take advantage of the symmetry of the two complementary PSFs of the vAPP. Although I am unable to recover HR 2562 B in our FDI processed image, I explain the impact of instrumental scattered light and wind-driven halo which degrade the symmetry of the vAPP and consequently reduce the effectiveness of the algorithm, and thus that FDI may still prove effective for future datasets obtained under more optimal atmospheric conditions. The companion is detected in the images produced by applying classical Angular Differential Imaging (ADI) and Principal Component Analysis (PCA) algorithms. Although HR 2562 B was not recovered at a sufficient S/N to allow for a variability analysis in this instance, I am nonetheless able to obtain 3.94 µm narrow-band photometry of this faint companion, which is complementary to previous studies at other wavelengths. I combine my complementary 3.94 µm narrow-band photometry of HR 2562 B with literature data obtained with the Spectro-Polarimetric High-contrast Exoplanet REsearch (SPHERE) instrument and the Gemini Planet Imager (GPI), and compare its spectrum to atmospheric models to derive values for its physical properties. I find that the results of these comparisons are highly dependent on the wavebands considered, leading to a wide range of allowable values for the physical properties of HR 2562 B, including

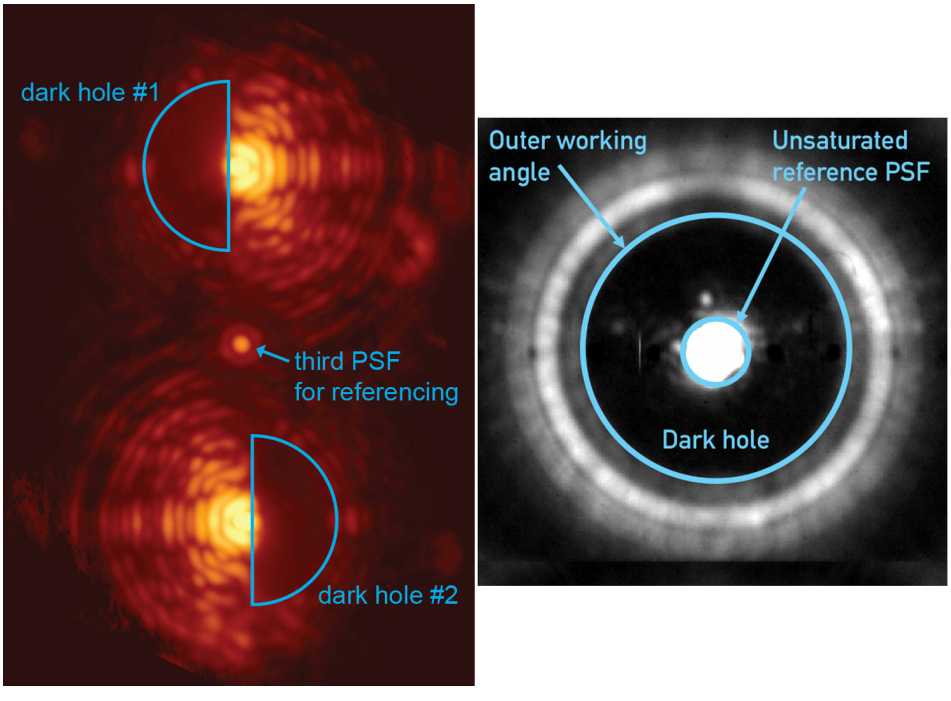

Figure B: Example observations of stars observed with a gvAPP (left-hand panel) coronagraph and dgvAPP360 coronagraph (right-hand panel). The gvAPP produces three images of the target star; two of which have 180° 'dark holes' allowing high-contrast exoplanets to be detected. The dgvAPP360 instead produces a 360° dark hole around an unsaturated image of the target star in the centre. Credit: Leiden University; University of Arizona (left-hand panel), Sutlieff et al. (2023); Chapter 3 (right-hand panel).

effective temperatures of $1200 \leq T_{eff}(K) \leq 1700$ and surface gravities of $4.0 \leq \log(g)(dex) \leq 5.0$. Although I am therefore unable to significantly further constrain the physical parameters of the companion, these consistent measurements lend additional weight to those found in the literature and highlight the degeneracies that arise from fitting atmospheric models to brown dwarf atmospheres. I further highlight that future observations between 2.4-3.2 µm will be more effective in distinguishing cooler brown dwarfs due to the onset of absorption bands in this region. By also comparing the spectrum of HR 2562 B to template spectra, I conclude that it has a spectral type at the L/T transition and a mass of 29 ± 15 M_{Jup}.

In Chapter 3, I present a novel, ground-based approach for constructing light curves of high-contrast companions directly by combining the technique of differential spectrophotometric monitoring with the vAPP coronagraph. Here, the vAPP coronagraph provides an image of the star for use as a simultaneous photometric reference to eliminate systematics from the light curve of a companion. The vAPP is combined with an integral field spectrograph (IFS) to disperse the light from the target into individual spectra. These spectra can then be recombined into a single 'white-light' data point. This has the advantage of smoothing out wavelength-dependent flat-fielding errors and allows wavelength regions with instrumental absorption or highly variable telluric bands to be excluded, meaning systematic effects can be significantly reduced, thus yielding greater stability and precision in the final white-light curve. This allows me to search for variability arising from clouds and other features in the atmospheres of exoplanets and brown dwarfs. I test this approach using 2.8-4.2 µm observations of substellar companion HD 1160 B obtained with the 360° double-grating vAPP (dgvAPP360) and the Arizona Lenslets for Exoplanet Spectroscopy (ALES) IFS on the Large Binocular Telescope in Arizona. I develop a new data reduction pipeline to process this data and extract aperture photometry, producing a differential white-light curve for the companion. I then use a linear regression approach to fit and remove residual systematics from the light curve. I find significant 8.8% semi-amplitude sinusoidal variability in the single-night light curve of HD 1160 B, with a ∼3.24 h period. Individual wavelength channels spanning 3.59-3.99 µm further show tentative evidence of increasing variability with wavelength. After thorough investigation and rejection of systematic noise sources, I attribute this variability as likely due to heterogeneous features in the atmosphere of HD 1160 B, rotating in and out of view as it rotates. If the period of this variability reflects the rotation period of HD 1160 B, physical limitations suggest that it is rotating close to its breakup period. The precision achieved in the detrended differential white-light curve of HD 1160 B is the greatest yet reached in ground-based high-contrast imaging light curves of sub-arcsecond companions, with a 3.7% precision per 18-minute bin. I find no evidence yet of a systematic noise floor, indicating that additional observations would further improve the precision. This new technique is therefore a promising avenue for future work aiming to map storms or find transiting exomoons around giant exoplanets. In this chapter, I also use observations obtained by NASA's Transiting Exoplanet Survey Satellite (TESS) to confirm that the host star HD 1160 A is non-varying to the 0.03% level.

In Chapter 4, I present further observations of HD 1160 B with the LBT dgvAPP360 and ALES. I use the differential spectrophotometry approach described in the previous chapter

EN

to aim to confirm the variability of this companion over the course of a second night of observations. Although I recover the ∼3.2 h variability seen on the first night, I do not detect periodic variability on the second night. This may indicate that the variability, and therefore the atmosphere, of HD 1160 B is undergoing rapid time evolution, and highlights the complexity of interpreting the light curves of high-contrast substellar companions. I also confirm the repeatability of this technique by analysing the precision achieved in the detrended differential white-light curves from each night, which I find share similar noise properties. This suggests that vAPP-enabled differential spectrophotometric monitoring achieves a repeatable precision at the ∼4% level over multiple epochs. In addition to the variability analysis in this chapter, I also combine each night of data to carry out a spectral characterisation of HD 1160 B in the 2.8-4.2 µm range using BT-Settl atmospheric models. These spectra are the first for this target in the mid-infrared and are therefore highly complementary to previous studies in the literature. I find that the spectrum of HD 1160 B on each night are consistent at most wavelengths, but that the companion appears systematically fainter on the second night at 3.0-3.2 µm. If this difference is astrophysical, this difference could be due to the intrinsic variability of HD 1160 B. I fit these spectra with atmospheric models, considering each night separately and both nights together. In a similar way to HR 2562 B in Chapter 2, this process produces different values for the physical properties of HD 1160 B depending on the night considered. I find effective temperature T_{eff} estimates ranging from $T_{eff} = 2804^{+152}_{-74}$ K on the first night, consistent with the literature, to a much cooler $T_{eff} = 2310^{+93}_{-82}$ K on the second night. The luminosity estimates inferred for HD 1160 B in this chapter are lower than those in the literature, but the radius estimates are mostly consistent. Overall, I conclude that the spectrum of HD 1160 B on the second night of our observations is not consistent with results from the literature. The differences in the results obtained for each spectrum highlight the impact that variability can have on atmospheric model fitting for substellar companions. I estimate the mass of HD 1160 B to be 16-81 M_{Jup}, comfortably above the deuterium burning limit, but allowing the possibility that it is a low mass star above the hydrogen burning limit. In this chapter I also present R = 50,000 high-resolution optical spectroscopy of HD 1160 B's host star, HD 1160 A, obtained with the Potsdam Echelle Polarimetric and Spectroscopic Instrument (PEPSI) simultaneously to the LBT/ALES+dgvAPP360 observations. HD 1160 A was previously classified as an A0 V star using observations obtained with photographic plates. By comparing my new spectrum of HD 1160 A to atmospheric models, I re-evaluate its spectral type to A1 IV-V and characterise its physical properties. I find a T_{eff} of 9200^{+200}_{-100} K, log(g) of $3.5^{+0.5}_{-0.3}$, and $v\sin i$ of 96^{+6}_{-4} km s^{-1}, the first $v\sin i$ estimate obtained for this target. Considering this $v\sin i$ alongside the known near edge-on inclination angle of the HD 1160 system, I show that HD 1160 A rotates slower than the typical A-type star.

Finally, in Chapter 5 I inject artificial companions with both non-varying and varying signals to real data obtained with the LBT dgvAPP360 and ALES. By doing this, I am able to assess the extent to which residual telluric and instrumental systematics contaminate and limit the precision of the differential light curves obtained with the technique of vAPP-enabled ground-based differential spectrophotometry developed in Chapter 3. I also produce a simulated data set and introduce a range of systematics arising from atmospheric turbulence, such as non-common path aberrations (NCPAs) described by a series of polynomials known as Zernike

modes. Using these simulations, I am able to investigate how different aberrations impact the relative aperture photometry of a star and substellar companion over the course of a time series when different size apertures are used to measure the flux of each object. Artificial companion injection is an ideal way to assess the extent to which unknown systematics limit the precision achieved with this technique, while the simulated data allows me to measure the strength of some of the systematics that are expected, such as those caused by Zernike modes. First, I process the data containing the injected companions and extract photometry for each companion to explore how well their known variability signals can be recovered in their differential light curves, and hence the level to which their light curves are contaminated by systematics. I find that varying companions can be distinguished from non-varying companions, but that variability amplitudes and periods cannot accurately be recovered when observations cover only a small number of periods. By considering how the root mean square values of the differential light curves vary with binning, I find that there are still residual systematics in the data but that the data does not reach a noise floor, thus the precision can be improved further with increased bin sizes. This is consistent with the result found in Chapter 3. The simulated data in this chapter was produced using the Python package HCIPy to reflect the LBT/ALES+dgvAPP360 instrumental setup, and includes a simulated star-planet system with similar properties to the HD 1160 system. First, I tested the impact of NCPAs on the star and companion photometry by adding them to the simulated data using 100 Zernike modes. I find that when I scale the wavefront error of these aberrations with a realistic power law, high-order aberrations do not have a significant impact on the fluxes of the star and companion, but that low-order modes can cause a significant reduction in the average measured flux of the companion over the observing sequence. However, I find that the variation in flux over the observing sequence for a given mode is $<1\%$, suggesting that companion variability measurements may be minimally affected by these aberrations. I then simulated realistic residual wavefront errors, photon noise, and thermal background noise, and found that thermal background noise is the dominant source of scatter in raw companion photometry. In a simulated detrended differential light curve, the scatter on the datapoints closely matches those of the non-varying injected artificial companions when binned to the same bin size, suggesting that these same noise sources are the dominant effects in the real data. As the effects of both photon noise and background noise decrease with increasing bin size, this is consistent with the RMS trends that I measured for the injected companions. I highlight that predictive control and focal-plane wavefront sensing techniques will help to further reduce systematics in data of this type, enabling a greater precision to be achieved with vAPP-enabled differential spectrophotometry.

Combined, these chapters investigate the feasibility of using adaptive optics, state of the art high-contrast imaging techniques, and integral field spectrographs to create light curves of exoplanets directly. In the future, this will enable the mapping of their storms and features, and searches for their exomoons. I show that with the new techniques that I have developed we can reach 4% precision levels, repeatable on separate nights, and I highlight that improvements in wavefront sensing and systematics detrending could provide even greater precision, which will ultimately bring the features of distant worlds into sharper view.

EN

Nederlandse samenvatting

De planeten van ons eigen zonnestelsel bezitten wolkenstructuren en weersystemen met een grote verscheidenheid aan vormen, afmetingen, levensduren en helderheden. Hier op aarde ervaren wij kleine, kortstondige stormen, maar ook orkanen die meerdere dagen kunnen duren. Jupiter is beroemd om zijn iconische 'Grote Rode Vlek', een gigantische storm die al eeuwenlang woedt, en om zijn duidelijke latitudinale wolkenbanden (figuur A). Als een planeet om zijn as draait, draaien deze kenmerken in en uit het zicht en veroorzaken daardoor veranderingen in de totale helderheid van de planeet, gezien vanuit de verte. De motivatie voor dit proefschrift was om te zoeken naar soortgelijke helderheidsveranderingen bij exoplaneten - planeten buiten ons eigen zonnestelsel - en zo inzicht te krijgen in hun weer, atmosferische structuur en visuele verschijning. De eigenschappen van deze variaties, zoals hun amplitude, periodiciteit en vorm, bieden een unieke mogelijkheid om waardevolle informatie te verkrijgen over de fysische processen die de atmosfeer van exoplaneten bepalen. Wolken en weer zijn niet de enige bronnen van helderheidsvariabiliteit in substellaire begeleiders; dergelijke veranderingen kunnen ook het gevolg zijn van het noorderlicht, vergelijkbaar met de aurora borealis en de aurora australis op aarde, of magnetische vlekken als het object een hogere massa heeft. Een andere mogelijke bron van variabiliteit bij exoplaneten zouden satellieten in een baan om de exoplaneet kunnen zijn, zoals exomanen of dubbelplaneten. Dergelijke satellieten zouden periodieke dalingen in de helderheid van een exoplaneet veroorzaken als zijn baan toevallig op één lijn ligt met de gezichtslijn van de waarnemer. Tot nu toe zijn nog geen exomanen rond een exoplaneet met zekerheid ontdekt, hoewel er wel verschillende kandidaten zijn geïdentificeerd.

Waarnemingen met ruimtetelescopen zoals de Hubble Space Telescope (HST) hebben helderheidsvariabiliteit ontdekt in de lichtkrommen van verschillende substellaire begeleiders, wat overeenkomt met zowel grond- als ruimtestudies van geïsoleerde bruine dwergen en objecten met een planeet massa. Er is een breed scala aan variabiliteitsamplitudes waargenomen, van de alomtegenwoordige variabiliteit van $\geq$0,2% in onderzoeken naar L- en T-dwergen tot de piek-tot-dal variaties van 38% in de lichtkromme van VHS1256-1257b, de meest variabele begeleider met planeetmassa die tot nu toe is waargenomen. De periodiciteit van deze variabiliteit is meestal kort, van $\sim$1 uur tot $\geq$20 uur, en weerspiegelt in het algemeen de rotatieperiode van het substellaire object. Reeds is in de lichtkrommen van verscheidene substellaire objecten een evolutie van de variabiliteit waargenomen, veroorzaakt door een evolutie van de atmosferische kenmerken die de variabiliteit veroorzaken. Een dergelijke

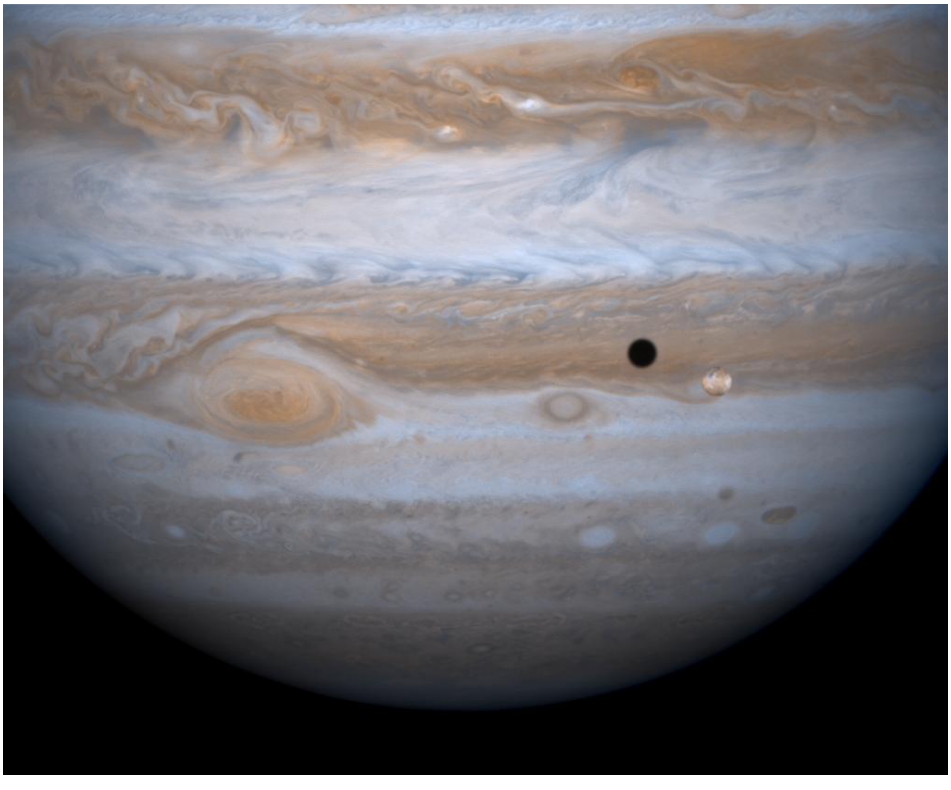

Figuur A: Een beeld van Jupiter genomen door NASA's Cassini ruimtevaartuig. Grote stormen en atmosferische turbulentie zijn te zien op de grensvlakken tussen de latitudinale wolkenbanden van Jupiter. De donkere vlek is een schaduw van Io, een van Jupiters Galileïsche manen, die zelf iets rechts van zijn schaduw te zien is. Bron: NASA/JPL/University of Arizona.

evolutie is waargenomen op verschillende tijdschalen, waaronder zowel een snelle evolutie van de ene nacht op de andere als een lange termijn trend over maanden of jaren.

Hoewel de variabiliteit van een groot aantal substellaire objecten met succes is gemeten met ruimtetelescopen, is het een grote uitdaging om nauwkeurige fotometrische metingen te verrichten voor de populatie van exoplaneten die dicht bij elkaar staan, een hoog contrast hebben en direct in beeld worden gebracht. De grotere spiegeldiameters en contrastrijke beeldvormingssystemen van grondtelescopen stellen ons in staat deze begeleiders te detecteren, maar elk intrinsiek variabiliteitssignaal in hun lichtkrommen wordt overweldigd door niet-fysische variabiliteit die wordt veroorzaakt door turbulentie in de aardatmosfeer en instrumentele systematiek. Deze verontreinigende variabiliteit kan worden verwijderd door de lichtkromme van de begeleider te delen door die van een gelijktijdige fotometrische referentie; een afzonderlijke bron die ook verontreinigd is door deze systematiek maar verder niet veranderlijk is, en die gelijktijdig met de begeleider wordt waargenomen. In studies naar de variabiliteit van sterren of geïsoleerde substellaire objecten worden hiervoor vaak bekende niet-variabele veldsterren gebruikt. De beeldvelden van contrastrijke beeldvormingssystemen op de grond zijn echter meestal smal, zodat veldsterren zelden beschikbaar zijn om als fotometrische referentie te worden gebruikt. Bovendien maken deze systemen meestal gebruik van een coronograaf in het brandpuntsvlak om de geobserveerde ster te blokkeren. Dit is een kritische stap die nodig is om het contrast te bereiken dat nodig is om zwakke begeleiders waar te nemen, maar dit betekent ook dat de ster van de exoplaneet niet als fotometrische referentie kan worden gebruikt.

In dit proefschrift is één van mijn hoofddoelen het verkennen van nieuwe benaderingen voor het meten van de variabiliteit van direct in beeld gebrachte exoplaneten met telescopen op de grond. De vector Apodizing Phase Plate (vAPP) coronagraaf is een uniek type coronagraaf dat het licht van de geobserveerde ster *niet* blokkeert, maar de detectie van contrastrijke begeleiders mogelijk maakt door de fase ervan te wijzigen (figuur B). Het licht van de ster blijft dus behouden en kan worden gebruikt als gelijktijdige fotometrische referentie, waardoor metingen aan de variabiliteit van exoplaneten mogelijk zijn.

In dit hoofdstuk 2, presenteer ik waarnemingen van bruine dwerg HR 2562 B met de 180° grating-vAPP (gvAPP) coronagraaf en het Magellan Adaptive Optics (MagAO) systeem op de 6,5-m Magellan Clay telescoop in Las Campanas Observatory, Chili. Dit zijn de eerste gerapporteerde waarnemingen van een substellaire begeleider met een vAPP-coronagraaf. Ik verwerk de gegevens met drie verschillende nabewerkingstechnieken om te testen welke benadering de begeleider met de hoogste signaal-ruisverhouding (S/N) terugvindt. Één daarvan is Flipped Differential Imaging (FDI), een nieuw algoritme dat ik heb ontwikkeld om te profiteren van de symmetrie van de twee complementaire PSF's van de vAPP. Hoewel ik HR 2562 B niet kan terugvinden in ons met FDI verwerkte beeld, kan ik wel concluderen dat instrumenteel verstrooid licht en een door de wind veroorzaakte halo, de symmetrie van de vAPP aantasten en daardoor de effectiviteit van het algoritme verminderen, en dus dat FDI nog steeds effectief kan blijken voor toekomstige datasets die onder meer optimale atmosferische omstandigheden zijn verkregen. De begeleider wordt gedetecteerd in de beelden die zijn geproduceerd door toepassing van klassieke Angular Differential Imaging (ADI)

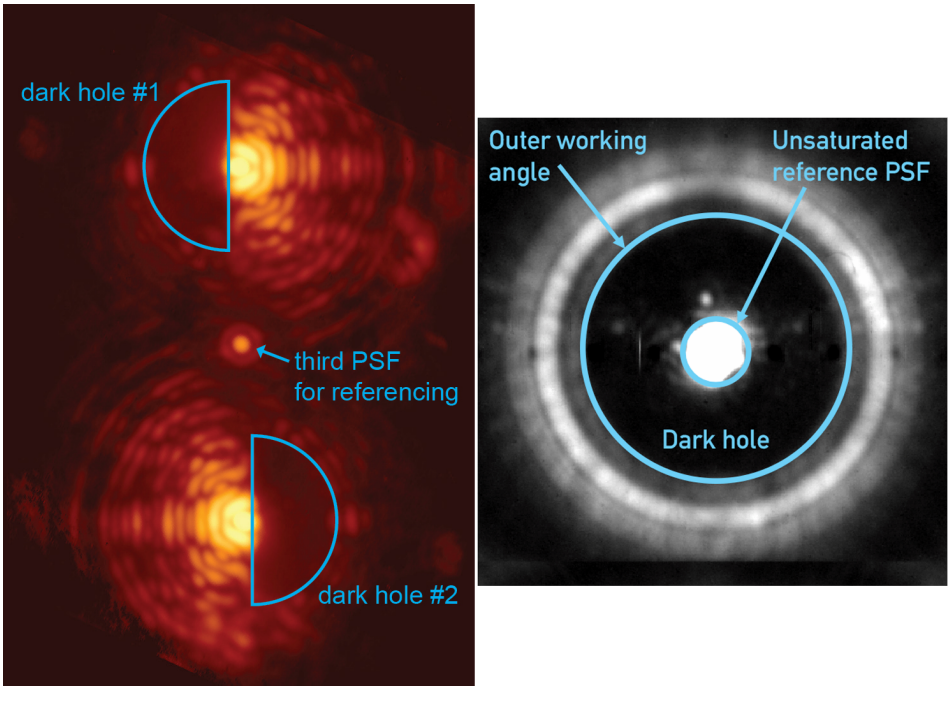

Figuur B: Voorbeelden van waarnemingen van sterren met een gvAPP (linkerpaneel) coronagraaf en een dgvAPP360 coronagraaf (rechterpaneel). De gvAPP produceert drie beelden van de geobserveerde ster; twee daarvan hebben 180 graden 'donkere gaten' waardoor contrastrijke exoplaneten kunnen worden gedetecteerd. De dgvAPP360 produceert daarentegen een donker gat van 360 graden rond een onverzadigd beeld van de geobserveerde ster in het midden. Bron: Universiteit Leiden; University of Arizona (linkerpaneel), Sutlieff et al. (2023); Chapter 3 (rechterpaneel).

en Principal Component Analysis (PCA) algoritmen. Hoewel HR 2562 B niet met voldoende S/N is gedetecteerd om een variabiliteitsanalyse uit te voeren, heb ik toch in een smalle golflengteband rondom 3,94 µm fotometrie van deze zwakke begeleider verkregen, die een aanvulling vormt op eerdere studies op andere golflengten. Ik combineer mijn aanvullende smalle golflengteband 3,94 µm fotometrie van HR 2562 B met literatuurgegevens verkregen met het Spectro-Polarimetric High-contrast Exoplanet REsearch (SPHERE) instrument en de Gemini Planet Imager (GPI), en vergelijk zijn spectrum met atmosferische modellen om waarden voor zijn fysische eigenschappen af te leiden. Ik ontdek dat de resultaten van deze vergelijkingen sterk afhankelijk zijn van de beschouwde golfbanden, wat leidt tot een breed scala van toegestane waarden voor de fysische eigenschappen van HR 2562 B, waaronder effectieve temperaturen van $1200 \leq T_{eff}(K) \leq 1700$ en oppervlakte gravitatieveldsterkte van $4{,}0 \leq \log(g)(\text{dex}) \leq 5{,}0$. Hoewel ik daarom de fysische parameters van de begeleider niet significant verder kan beperken, geven deze consistente metingen extra gewicht aan die in de literatuur en benadrukken ze de degeneratie die ontstaat bij het vergelijken van atmosferische modellen met data van bruine dwergatmosferen. Verder benadruk ik dat toekomstige waarnemingen tussen 2,4-3,2 µm effectiever zullen zijn in het onderscheiden van koelere bruine dwergen vanwege het begin van absorptiebanden in dit gebied. Door ook het spectrum van HR 2562 B te vergelijken met standaardspectra, concludeer ik dat hij een spectraaltype heeft rond de L/T-overgang en een massa van 29 ± 15 M_{Jup}.

In dit hoofdstuk 3 presenteer ik een nieuwe nieuwe methode om de lichtkrommen van contrastrijke begeleiders te meten door gebruik te maken van een combinatie van differentiële spectrofotometrische controle en een vAPP-coronagraaf. Hierbij levert de vAPP-coronagraaf een beeld van de ster voor gebruik als gelijktijdige fotometrische referentie om systematiek uit de lichtkromme van een begeleider te elimineren. De vAPP wordt gecombineerd met een Integral Field Spectograph (IFS) om het licht van het doelwit in afzonderlijke spectra te dispergeren. Deze spectra kunnen dan opnieuw worden gecombineerd tot een enkel 'witlicht' datapunt. Dit heeft het voordeel dat golflengte-afhankelijke flat field fouten worden uitgevlakt en dat golflengtegebieden met instrumentele absorptie of sterk wisselende atmosferische absorptie kunnen worden uitgesloten, wat betekent dat systematische effecten aanzienlijk kunnen worden verminderd, waardoor de uiteindelijke witlichtkromme stabieler en nauwkeuriger wordt. Hierdoor kan ik zoeken naar variabiliteit door wolken en andere kenmerken in de atmosferen van exoplaneten en bruine dwergen. Ik test deze aanpak aan de hand van 2,8-4,2 µm waarnemingen van de substellaire begeleider HD 1160 B, verkregen met de 360° vAPP (dgvAPP360) en de Arizona Lenslets for Exoplanet Spectroscopy (ALES) IFS op de Large Binocular Telescope in Arizona. Ik ontwikkel een nieuwe dataeductiepijplijn om deze data te verwerken en er diafragma fotometrie uit te halen, die een differentiële witlichtkromme voor de begeleider oplevert. Vervolgens gebruik ik een lineaire regressiemethode om de lichtkromme aan te passen en resterende systematische fouten te corrigeren. Ik vind een aanzienlijke sinusvormige variabiliteit van $8,8\%$ in de lichtkromme van HD 1160 B, met een periode van $\sim$3,24 uur. Afzonderlijke golflengtebanden van 3,59-3,99 µm laten verder aanwijzingen zien voor toenemende variabiliteit met de golflengte. Na grondig onderzoek en het uitsluiten van systematische ruis bronnen, schrijf ik deze variabiliteit toe aan heterogene kenmerken in de atmosfeer van HD 1160 B, die in en uit beeld roteren naarmate

hij draait. Als de periode van deze variabiliteit de rotatieperiode van HD 1160 B weerspiegelt, wijzen fysische beperkingen erop dat de rotatieperiode dicht bij de theoretisch maximale rotatieperiode ligt. De nauwkeurigheid van de differentiële witlichtcurve van HD 1160 B is de grootste die tot nu toe is gemeten me in een lichtkromme voor direct waargenomen objecten vanaf het aardoppervlak met een separatie van minder dan een boogseconde van de ster, en met een nauwkeurigheid van $3,7\%$ per tijdsinterval van 18 minuten. Ik vind nog geen aanwijzingen voor een systematische ruisondergrens, wat erop wijst dat aanvullende waarnemingen de precisie nog zouden kunnen verbeteren. Deze nieuwe techniek is daarom veelbelovend voor toekomstig werk om stormen in kaart te brengen of verduisteringen door exomanen rond reuzenexoplaneten te vinden. In dit hoofdstuk gebruik ik ook waarnemingen van NASA's Transiting Exoplanet Survey Satellite (TESS) om te bevestigen dat de ster HD 1160 A niet varieert met een precisie van 0,03%.

In dit hoofdstuk 4 presenteer ik verdere waarnemingen van HD 1160 B met de LBT dgvAPP360 en ALES. Ik gebruik de in het vorige hoofdstuk beschreven differentiële spectrofotometrie om de variabiliteit van deze begeleider te bevestigen tijdens een tweede waarnemingsnacht. Hoewel ik de variabiliteit van ∼3,2 uur van de eerste nacht terugvind, zie ik geen periodieke variabiliteit in de tweede nacht. Dit kan erop wijzen dat de variabiliteit, en daarmee de atmosfeer, van HD 1160 B een snelle evolutie in de tijd doormaakt, en benadrukt de complexiteit van de interpretatie van lichtkrommen van substellaire objecten met een hoog contrast. Ik bevestig ook de herhaalbaarheid van deze techniek door de nauwkeurigheid van de voor trends gecorrigeerde differentiële witlichtkrommen van elke nacht te analyseren. Dit suggereert dat differentiële spectrofotometrie met behulp van vAPP een herhaalbare precisie bereikt op het niveau van ∼4% over meerdere tijdperken. In aanvulling op de variabiliteitsanalyse in dit hoofdstuk, combineer ik ook elke nacht gegevens om een spectrale karakterisering van HD 1160 B in de 2,8-4,2 µm golflengteband uit te voeren met behulp van BT-Settl atmosferische modellen. Deze spectra zijn de eerste voor dit object in het midden-infrarood en vormen daarom een grote aanvulling op eerdere studies in de literatuur. Ik stel vast dat het spectrum van HD 1160 B op elke nacht consistent is op de meeste golflengten, maar dat de begeleider systematisch zwakker lijkt op de tweede nacht in het golflengtegebied van 3,0-3,2 µm. Als dit verschil astrofysisch is, zou het te wijten kunnen zijn aan de intrinsieke variabiliteit van HD 1160 B. Ik heb deze spectra vergeleken met atmosferische modellen, waarbij elke nacht afzonderlijk en beide nachten samen zijn beschouwd. Net als bij HR 2562 B in hoofdstuk 2 levert dit proces verschillende waarden op voor de fysische eigenschappen van HD 1160 B, afhankelijk van de beschouwde nacht. Ik vind schattingen van de effectieve temperatuur T_{eff} variërend van $T_{eff} = 2804^{+152}_{-74}$ K in de eerste nacht, in overeenstemming met de literatuur, tot een veel koelere $T_{eff} = 2310^{+93}_{-82}$ K in de tweede nacht. De helderheidsschattingen voor HD 1160 B in dit hoofdstuk zijn lager dan die in de literatuur, maar de radiusschattingen komen grotendeels overeen. In het algemeen concludeer ik dat het spectrum van HD 1160 B op de tweede nacht van onze waarnemingen niet consistent is met resultaten uit de literatuur. De verschillen in de resultaten voor elk spectrum maken duidelijk welke invloed variabiliteit kan hebben op het vergelijken van atmosferische modellen met observaties van substellaire objecten. Ik schat de massa van HD 1160 B op 16-81 M_{Jup}, ruim boven de deuteriumgrens, maar met de mogelijkheid dat het

NL

een ster is met een lage massa boven de waterstofgrens. In dit hoofdstuk presenteer ik ook R = 50.000 optische spectroscopie met hoge resolutie van de gastheerster van HD 1160 B, HD 1160 A, verkregen met het Potsdam Echelle Polarimetric and Spectroscopic Instrument (PEPSI) tegelijktijdig met de LBT/ALES+dgvAPP360-waarnemingen. HD 1160 A was eerder geclassificeerd als een A0 V-ster op basis van waarnemingen met fotografische platen. Door mijn nieuwe spectrum van HD 1160 A te vergelijken met atmosferische modellen, weerleg ik het spectraaltype naar A1 IV-V en karakteriseer ik zijn fysische eigenschappen. Ik vind een $T_{\rm eff}$ van 9200^{+200}_{-100} K, log(g) van $3{,}5^{+0{,}5}_{-0{,}3}$, en $v\sin i$ van 96^{+6}_{-4} km s^{-1}, de eerste $v\sin i$ schatting voor dit doelwit. Gezien deze $v\sin i$ en de bekende inclinatiehoek van het HD 1160-systeem, laat ik zien dat HD 1160 A langzamer roteert dan de typische A-type ster.

Ten slotte, in hoofdstuk 5 injecteer ik kunstmatige begeleiders met zowel niet-variërende als variërende signalen in echte gegevens verkregen met de LBT dgvAPP360 en ALES. Hierdoor kan ik beoordelen in hoeverre aardatmosferische absorptie en instrumentele systematiek de precisie van de differentiële lichtkrommen verkregen met de techniek van vAPP-gebaseerde differentiële spectrofotometrie vanaf het aardoppervlak, zoals eerder beschreven in hoofdstuk 3, beïnvloedt en beperkt. Ik produceer ook een gesimuleerde dataset en introduceer een reeks aan systematische effecten zoals atmosferische turbulentie, non-common path aberrations (NCPA's) beschreven door een reeks van polynomen die bekend staan als Zernike modes. Met deze simulaties kan ik onderzoeken hoe verschillende aberraties de relatieve diafragmafotometrie van een ster en een substellaire begeleider in de loop van een tijdreeks beïnvloeden wanneer diafragma's van verschillende grootte worden gebruikt om de flux van elk object te meten. Kunstmatige injectie van een begeleider is een ideale manier om te beoordelen in hoeverre onbekende systematiek de precisie die met deze techniek wordt bereikt beperkt, terwijl de gesimuleerde gegevens mij in staat stellen de sterkte van sommige verwachte systematiek te meten, zoals die veroorzaakt door Zernike-modes. Eerst verwerk ik de gegevens met de geïnjecteerde begeleiders en voer voor elke begeleider fotometrie uit om na te gaan hoe goed hun bekende variabiliteitssignalen kunnen worden teruggevonden in hun differentiële lichtkrommen, en dus in hoeverre hun lichtkrommen zijn beïnvloed door systematiek. Ik vind dat variërende begeleiders kunnen worden onderscheiden van niet-variërende begeleiders, maar dat variabiliteitsamplitudes en -perioden niet nauwkeurig kunnen worden teruggevonden wanneer de waarnemingen slechts een klein aantal perioden bestrijken. Door na te gaan hoe de kwadratische gemiddelden van de differentiële lichtkrommen variëren met het opdelen in verschillende tijdsintervallen, vind ik dat er nog steeds systematiek in de gegevens zit, maar dat de gegevens geen ruisvloer bereiken, zodat de precisie verder kan worden verbeterd door de data in grotere tijdsintervallen op te delen. Dit komt overeen met het resultaat dat ik eerder had gevonden in hoofdstuk 3. De gesimuleerde gegevens in dit hoofdstuk zijn geproduceerd met het Python pakket HCIPy om de LBT/ALES+dgvAPP360 instrumentele opstelling weer te geven, en omvatten een gesimuleerd ster-planet systeem met vergelijkbare eigenschappen als het HD 1160 systeem. Eerst heb ik het effect van NCPA's op de fotometrie van de ster en de begeleider getest door ze aan de gesimuleerde gegevens toe te voegen met behulp van 100 Zernike-modi. Als ik de golffrontfout van deze aberraties schaal met een realistische machtswet, blijkt dat aberraties van hoge orde geen significante invloed hebben op de gemeten helderheid van de

ster en de begeleider, maar dat modi van lage orde een significante vermindering van de gemiddelde helderheid van de begeleider over de waarnemingsreeks kunnen veroorzaken. Ik vind echter dat de helderheidsvariatie over de waarnemingsreeks voor een bepaalde modus $<1\%$ is, wat suggereert dat de metingen van de variabiliteit van de begeleider minimaal worden beïnvloed door deze aberraties. Vervolgens heb ik realistische residuele golffront-fouten, fotonruis en thermische achtergrondruis gesimuleerd en vastgesteld dat thermische achtergrondruis de belangrijkste bron van verstrooiing is in de fotometrie van de ruwe data van de begeleider. In een gesimuleerde gecorrigeerde differentiële lichtkromme komt de verstrooiing van de datapunten nauw overeen met die van de niet-variërende geïnjecteerde kunstmatige metgezellen wanneer ze in dezelfde bin size worden ingedeeld, wat suggereert dat dezelfde ruisbronnen de dominante effecten zijn in de echte gegevens. Aangezien de effecten van zowel fotonruis als achtergrondruis afnemen met toenemende opgedeelde tijds-interval grootte, komt dit overeen met de trends van het kwadratisch gemiddelde die ik heb gemeten voor de geïnjecteerde begeleiders. Ik benadruk dat voorspellende controle en focal-plane wavefront sensing technieken zullen helpen om systematiek in dit soort gegevens verder te verminderen, waardoor een grotere precisie kan worden bereikt met vAPP-enabled differentiële spectrofotometrie.

Samen onderzoeken deze hoofdstukken de haalbaarheid van het gebruik van adaptieve optiek, geavanceerde contrastrijke beeldvormingstechnieken en integrale veldspectrografen om rechtstreeks lichtkrommen van exoplaneten te maken. In de toekomst zal dit het in kaart brengen van hun stormen en kenmerken en het zoeken naar hun exomanen mogelijk maken. Ik laat zien dat we met de nieuwe technieken die ik heb ontwikkeld een nauwkeurigheid van 4% kunnen bereiken, herhaalbaar op afzonderlijke nachten, en ik benadruk dat verbeteringen in wavefrontdetectie en systematische detrending een nog grotere nauwkeurigheid kunnen opleveren, die uiteindelijk de kenmerken van verre werelden scherper in beeld zullen brengen.

Translated by DeepL and Lennart van Sluijs

Publications

First-author articles

2 Measuring the variability of directly imaged exoplanets using vector Apodizing Phase Plates combined with ground-based differential spectrophotometry
Ben J. Sutlieff, Jayne L. Birkby, Jordan M. Stone, David S. Doelman, Matthew A. Kenworthy, Vatsal Panwar, Alexander J. Bohn, Steve Ertel, Frans Snik, Charles E. Woodward, Andrew J. Skemer, Jarron M. Leisenring, Klaus G. Strassmeier, and David Charbonneau
Monthly Notices of the Royal Astronomical Society, 2023, Volume 520, Issue 3, pp. 4235–4257 (**Chapter 3**)

1 High-contrast observations of brown dwarf companion HR 2562 B with the vector Apodizing Phase Plate coronagraph
Ben J. Sutlieff, Alexander J. Bohn, Jayne L. Birkby, Matthew A. Kenworthy, Katie M. Morzinski, David S. Doelman, Jared R. Males, Frans Snik, Laird M. Close, Philip M. Hinz, and David Charbonneau
Monthly Notices of the Royal Astronomical Society, 2021, Volume 506, Issue 3, pp. 3224-3238 (**Chapter 2**)

Co-authored articles

5 Applying a temporal systematics model to vector Apodizing Phase Plate coronagraphic data: TRAP4vAPP
Pengyu Liu, Alexander J. Bohn, David S. Doelman, **Ben J. Sutlieff**, Matthias Samland, Matthew A. Kenworthy, Frans Snik, Jayne L. Birkby, Beth A. Biller, Jared R. Males, Katie M. Morzinski, Laird M. Close, and Gilles P. P. L. Otten
Accepted for publication in *Astronomy & Astrophysics*

4 Vector-apodizing phase plate coronagraph: design, current performance, and future development
D. S. Doelman, F. Snik, E. H. Por, S. P. Bos, G. P. P. L. Otten, M. Kenworthy, S. Y. Haffert, M. Wilby, A. J. Bohn, **B. J. Sutlieff**, K. Miller, M. Ouellet, J. de Boer, C. U. Keller, M. J. Escuti, S. Shi, N. Z. Warriner, K. Hornburg, J. L. Birkby, J. Males, K. M. Morzinski, L. M. Close, J. Codona, J. Long, L. Schatz, J. Lumbres, A. Rodack, K. Van Gorkom, A. Hedglen, O. Guyon, J. Lozi, T. Groff, J. Chilcote, N. Jovanovic, S. Thibault, C. de Jonge, G. Allain, C. Vallée, D. Patel, O. Côté, C. Marois, P. Hinz, J. Stone, A. Skemer, Z. Briesemeister, A.

Boehle, A. M. Glauser, W. Taylor, P. Baudoz, E. Huby, O. Absil, B. Carlomagno, and C. Delacroix
Applied Optics, 2021 vol. 60, issue 19, p. D52

3 Discovery of an Edge-on Circumstellar Debris Disk around BD+45° 598: A Newly Identified Member of the β Pictoris Moving Group
Sasha Hinkley, Elisabeth C. Matthews, Charlène Lefevre, Jean-Francois Lestrade, Grant Kennedy, Dimitri Mawet, Karl R. Stapelfeldt, Shrishmoy Ray, Eric Mamajek, Brendan P. Bowler, David Wilner, Jonathan Williams, Megan Ansdell, Mark Wyatt, Alexis Lau, Mark W. Phillips, Jorge Fernandez Fernandez, Jonathan Gagné, Emma Bubb, **Ben J. Sutlieff**, Thomas J. G. Wilson, Brenda Matthews, Henry Ngo, Danielle Piskorz, Justin R. Crepp, Erica Gonzalez, Andrew W. Mann, and Gregory Mace
The Astrophysical Journal, 2021, Volume 912, Issue 2, id.115, 11 pp.

2 Assessing the Impact of Space School UK
Daniel Robson, Henry Lau, Áine O'Brien, Lucy Williams, **Ben Sutlieff**, Heidi Thiemann, Louise McCaul, George Weaver, and Tracey Dickens
Proceedings of the 3rd Symposium on Space Educational Activities, 2019, pp. 138-144.

1 Constraining the presence of giant planets in two-belt debris disc systems with VLT/SPHERE direct imaging and dynamical arguments
Elisabeth Matthews, Sasha Hinkley, Arthur Vigan, Grant Kennedy, **Ben Sutlieff**, Dawn Wickenden, Sam Treves, Trevor David, Tiffany Meshkat, Dimitri Mawet, Farisa Morales, Andrew Shannon, and Karl Stapelfeldt
Monthly Notices of the Royal Astronomical Society, 2018, Volume 480, Issue 2, pp. 2757-2783

Acknowledgements

Wow! And there it is. Over the course of these four and a half years I have often found myself wondering what thoughts and feelings I would have at the end of this journey. As it turns out, the answer is a lot! This PhD has been an intense and exhilarating journey; at times challenging, stressful, and scary, but also incredibly exciting, rewarding, and fun. Now that I've had a chance to catch my breath and look back on it all, the strongest feeling is that of gratitude. I feel so grateful to have had the opportunity to work on such exciting research, and at an institute at which I have felt so at home. I feel very lucky to have been able to visit some amazing places for work, from mountaintop observatories to far-flung conferences (even if these trips sometimes involved being tear-gassed, shot at, and intimidated by earthquakes...[1]). But most of all, I feel grateful to the many people who have been part of my journey. In this section, I would like to take a few pages to thank these people. Whether I've remembered to include your name here or not, I hope you know who you are - none of this would have been possible without you, and I'll always be thankful for your support.

First of all, Jayne - thank you for guiding me on this journey. Before my interview with you I had fully decided that I was going to move to Germany for my PhD, but it didn't take long for your enthusiasm and our shared excitement about exoplanets to change my mind, and I haven't looked back. You have taught me so much about how to be an effective astronomer and independent researcher. Although our project was a risky one, you supported me in overcoming the challenges that this presented and showed me that in patience, perseverance, and innovation lies success. Your detailed and rigorous feedback on my paper drafts has made me a better writer, and when in doubt I'll always remember to focus on what makes an idea important and interesting. Thank you for our observing runs and conference adventures, which were always both incredibly interesting and incredibly fun, and true highlights of my PhD. Thank you for making a point of always introducing me to everyone we met. I'm proud of the work that we've achieved together, and excited that we get to continue our collaboration when I'm a doctor.

Matt, thank you for being an excellent co-advisor. I am so grateful for your encouragement during the more challenging parts of my PhD, and for your patience in explaining the intricacies and technical details of high-contrast imaging observations and instrumentation. I always enjoyed our meetings discussing all things related to vAPPs, which were incredibly

[1] Sorry Mum!

valuable, as well as those where we diverged onto more tangential topics. Thank you for teaching me that no paper can be perfect, and that a time comes when one must stop polishing the cannonball and send their work off into the world. I'll never forget our dramatic Mario Kart showdown at that arcade in Shinjuku (or you and Jayne battling it out on Dance Dance Revolution, for that matter). I hope we get the chance sometime soon to carry out our plan of hiking in Scotland followed by a well-earned beer or two.

Sera, thank you for being my promotor - I appreciate that it might have been a little strange advising an exoplanet PhD candidate! I'm so grateful for your reassurance that I was on the right track, both for my PhD timeline and for the job search. Our super-efficient meetings worked wonders for reducing my imposter syndrome when it reared its head.

I would also like to express my gratitude to the many wonderful collaborators and colleagues that I have had the pleasure of working with over these years, and without whom this project would not have gotten very far. Firstly, the entire exoZoo research group led by Jayne - Eleanor, Lennart, Sophia, Mitch, and all of those who have joined recently (I remember when there were just three of us!). We might have been widely spread both geographically and scientifically, but I'm very grateful to have been part of such a fun and supportive research group. Thank you for all the group meetings, practice presentations, sci-fi references, and biscuits. Next, my colleagues in Leiden - David and Alex, thank you for making so much time for me during my visits to Leiden (both physical and virtual) and for answering all of my questions about vAPPs and everything else. Working with you both was a lot of fun! David, thank you in particular for all your support and hard work for my final chapter. Alex, thank you for your guidance when it came to SED fitting and for helping to improve my code. Frans, your joy and enthusiasm is contagious. I really enjoyed our discussions covering all sorts of topics, and will never again look at beetles with quite the same perspective. Pengyu, it was great working with you on the TRAP4vAPP project. I'm excited that it's going to be published soon, and that we get to continue to collaborate here in Edinburgh! Steven, Jos, Sebastiaan, Kelsey, Christoph, Maaike, Emiel, Rob, Patrick, Dilovan, Nienke, and many more - thank you for the many interesting discussions, and for making Leiden Observatory such a joy to visit. I would also like to thank all of the (exo)planetary people in Oxford for their warm and friendly welcomes when I visited, and for the all of the nice discussions that we had (not to mention the pub trips). Thank you to the amazing folks from Arizona's Extreme Wavelength Control Lab for supporting our MagAO observations and keeping me entertained with excellent blog posts. Joseph, Lauren, Logan, Katie, Jared, Laird, and more - it was always such a blast when you were around. Thank you to the LBT, ALES, and PEPSI teams for building such a great and unique instrument setup and for your enthusiasm for our new technique. Jordan, thank you for taking the time to set up the data cubes and help me understand how ALES works, and for your invaluable feedback and comments that helped shape the main paper of this thesis. Steve, Chick, Andy, Jarron, Klaus, Ilya, Phil, and Dave, I am grateful for your support for these projects and for all of your insightful and helpful comments. Thank you also to those involved in the design, manufacture, and implementation of vAPP coronagraphs around the world that I have not yet mentioned; the science in this thesis is possible thanks to your efforts. Gilles, thank you for your work in laying these foundations and for our useful discussions

at Lyot and ahead of our MagAO run. I found your thesis to be highly illuminating early in my PhD, and I often found myself referring back to it over the years. Anna, thank you for our useful and interesting discussions at the vAPP Hackathon. Frank, Annelotte, and Vatsal - the occasions when casual office conversation led to us working on papers together were some of the most rewarding collaborative experiences of my PhD. Thank you for bringing your skills and knowledge to this project! Sasha, I'm so glad that I decided to approach you for a summer project way back in 2016. Thank you so much for welcoming me to the wonderful world of exoplanet imaging and for encouraging me to pursue my ambitions. I'm especially thankful for your enthusiastic and dedicated approach in supporting your students; I probably learned just as much from you about how to be a good mentor as I did about exoplanets. It's very cool that we're still working together on a few things today. Elisabeth, I'm sorry to once again embarrass you with some nice words - but you have been such a great role model and mentor to me at every stage of my career so far. Thank you for all your advice and support over the years, for the fun scientific discussions, and for showing that the best scientific collaborations are built on honesty and empathy. Our field is a better place with you in it. Beth, thank you for your patience in waiting for me to finish this thesis and join you in Edinburgh - I'm excited for the work we're going to do!

The API is a unique and special place to work, at which I have felt so very at home over these past few years. I will always treasure my time spent there, and already miss it dearly. Thank you to everyone in the API community for creating such a welcoming and accepting environment. There are not many institutes where everyone from the faculty staff, postdocs, PhD candidates, and master's students interact so regularly and are so sincerely invested in each other's lives. The list of people who made my time at API so amazing is very long. Firstly, the API secretariat - I can't thank you enough for your support, hard work, and kindness. Thank you for keeping the institute together and functioning, even when a global pandemic took us by surprise. Milena, you're the life of the party - your lively energy never failed to brighten my mood. Susan, thank you for always lending a sympathetic ear and for reminding me that in spite of all the challenges, every PhD candidate gets to their defence day in the end. Renee, I've heard the tales of your legendary skill at Tetris - I only wish I could have seen it in action. Lucas, thank you for helping me to figure things out during the most stressful part of my PhD. Kim, we didn't get to interact much what with it being my final year and all, but thanks for all your work behind the scenes and for embracing the API spirit! Mai and Mara - we haven't met yet, but I'm sure we will soon. Welcome to the API! I'd also like to thank the API Equity, Diversity and Inclusion Committee and the PhD & Postdoc councils for their effort and dedication to making the API a better place. Everyone should get to feel as comfortable and at home there as I have.

Carsten, thank you for leading the API into its 100th year and beyond. I'm very grateful for your support over the years and really appreciate the way you always took a keen interest in my work. I'm sorry that the plans for the Beta Pic data set didn't work out, but perhaps I'll give it another try in the future! Jean-Michel, thank you for reaching out and offering support at a challenging time, and for checking in on how I was doing whenever we ran into each other. Antonija, I was very glad to have you as my API mentor, especially during the

lockdowns when normal office interactions felt so far away. Thank you for all your advice on time management and paper writing. Ralph, thank you for our corridor chats and for the yearly delivery of delicious plums from your garden. I'll never forget your call to tell me that I had gotten the job at API, which arrived while I was brushing my teeth. Jason, cheers for our many fun (and often funny) conversations, and for always being available to offer help and guidance on my PhD path (and for making sure that my watch was always set correctly 👀). Nathalie, thank you for bringing positive energy and generously buying all those nice coffees when I needed a boost in my final phase of thesis writing. Rudy, I'll fondly remember your Dutch humour, Dikkie Dik, and our top notch effort as the astro-muppets at the Oerknal pub quiz back in my first year. Samaya, thank you for brightening my day with our cheerful hellos in the API corridors! Oliver, Phil, Anna, Jacco, Silvia, Lex, Alex, Stephen, Antonia, Philipp, Joeri, Mike, Alessandra - thank you all also for being part of the soul of the API.

Esther, thank you for your dedication in organising the API's outreach programme and for putting together such a nice team to help with the events. I really enjoyed participating in the many stargazing nights, eclipse sightings, and more. Rasjied, cheers for all the observing we did both at APO and with WHT, and for arranging that VIP tour of the DOT on La Palma! Christianne, to this day I still think about some of the advice you gave us during 'Mastering Your PhD'. Thank you for teaching me to pay attention to my brain and the value of taking a 10 minute break to walk around the building. Martin, thank you for the many long conversations, card games, and strong beers at Oerknal over the years. I'm not sure whether those nights actually made me wiser, but it definitely often felt like they did. At least now I know to always, *always*, make sure that there's a candle on the table. Also, I think that the pub quiz we produced together might be one of the greatest achievements of our lives.

Thank you to my fellow exoplaneteers and the API disk enthusiasts for the many stimulating and enjoyable discussions at EDM and beyond. Eleanor, Lennart, Claire, Vatsal, Niloo, Dion, Fabienne, Kevin, Bob, Rico, Hinna, Saugata, Lorenzo, Kamen, Gaby, Christian, James, Melissa, Jacob, Lucia, Kaustubh, Jean-Michel, Carsten - thank you for nurturing an environment where it was easy to ask questions and share knowledge.

Eva, you started out as my official API buddy, but who knew how close we would become? You have been my most dependable and supportive friend, gym buddy, confidante, and teammate through the best and worst of times. Thank you for always being there when I needed to laugh, cry, or talk things through, for your kindness and empathy, and for all of your invaluable advice. We've been through so much together, and my life would not be the same without you. Your encouragement, competitive spirit, and fierce determination have pushed me to always aim higher, further, faster, and stronger. Thank you for the BGS-Maslow Sundays, the cycle trips, the Ghibli movie nights, the intense workouts, the rocket launches, and so much more. Annie, thank you for teaming up with me to wind up Eva, and for introducing me to so many great board games. I'll never forget your incredible sense of humour; I only hope that mijn Nederlandse luistervaardigheid are good enough to watch your show someday. Shout-out to Marley for being such a wonderfully sweet cat[1].

[1] There are 9 cats mentioned in these acknowledgements. I wonder if it's apparent who they all are.

Frank, we've had so many escapades over the years that I hardly know where to start. Thank you for always being up for anything, whether its an international (mis)adventure with minimal notice, a long and winding cycle across the country, or our usual mischief at the API. We'll probably always wonder what would have happened if we had stopped at that party in Twello, but I think its fair to say we've had plenty of fun without it. And with any luck, there's a lot more still to come. Cheers for being there through the highs and lows of PhD life, and for teaching me all about stars, stats, and Dutch life. Annelotte, whenever I was feeling stressed out with how much work there was to do, you had a way of making me believe that it would all work out ok. And it always did! Thank you for always being so kind and cheerful, and for the many fun office chats. Your ability to tell so much about a star just by looking at its spectra by eye will never cease to amaze me. Everyone at the API owes a debt of gratitude to you and your incredible event planning skills for all of the various social occasions that you helped to arrange, from barbecues to the API outing. I'm so glad that the two of you will be by my side for my defence.

Kenzie, cheers for all of the laughs and for bringing out my most ridiculous side, and also for your profound and heartfelt advice whenever I needed it. En natuurlijk, for introducing me to The Mummy. I have gained so much knowledge and excitement for FRBs from you, which is proof of your brilliance as a scientist, as well as your skill and enthusiasm as a communicator. I hope they have dilutin' juice over in Boston. By the way, I'm already working on ideas for Cairo Crew 3, so you and Frank better stay tuned. Gregor, our honorary Avenger - I'll miss our catch ups in the park and at the pub. Elliot, thank you for always being so happy to see me, it always made my day. I look forward to visiting y'all across the pond soon!

Eleanor, I'll never not be impressed by the sheer number of plates that you keep spinning at the same time without going completely mad. I'm so grateful to have shared my PhD journey with you as the Amsterdam contingent of exoZoo. Thank you for all the support you provided at times of need, and for the lovely dinner parties and conversations that flowed late into the night. Calum, thank you for your enthusiastic and generous catering and for geeking out with me about the latest developments in spaceflight. Thank you both for being the best hosts, and for all the laughs we had on set and during that all-nighter in the editing suite. I'm so glad that I'll likely get to see you pretty often, between Edinburgh and Amsterdam.

Lennart, thank you for all of our afternoon walks around Science Park, catch-up coffees, and supportive chats during the challenging parts of our PhDs. All the best for finishing your thesis, and hopefully I can come and visit you when you're in Michigan!

David, the observer of unimaginable, unreachable worlds! Thank you for all the fun we've had in the office, in the pub, and out exploring the national parks, and for your beautiful La Palma hiking route recommendations. Life just won't be the same without your calm, reassuring presence. I can't wait to hear all about your adventure learning how to be a safari expert.

Vlad, your time at API may have come to an end but you'll long be remembered as someone who brought us all together. You have been such a big part of my life in Amsterdam; you always wear your heart on your sleeve and are at your happiest just being surrounded by

the people you care about. Thank you for welcoming me to API with your mischievous grin and a steady supply of tea, and for our many incredible adventures and great nights out, of which I'm certain there are more to come!

Inés, an evening was 100% guaranteed to be a great one if you were there. I hope your karaoke and dancing enthusiasm is just as appreciated in Manchester as it was in Amsterdam. Thank you for choosing me to be your paranymph, for all our joyful conversations about languages, and for helping me plan my defence. Let's climb a mountain soon. Andrés, it was great getting to know you - cheers for the fun we had making the Inés quiz. Maxwell, I know you were a little sceptical of me at first, but I'm glad we became friends in the end. Thank you for not biting me.

Arkadip, thank you for wowing everyone with your spectacular photography and drone footage, and for fulfilling my endless cravings for chai. I've already got your framed lightning photo on my new desk in Edinburgh. I might not know that much about sports, but I always enjoyed hanging out with you to watch it anyway.

Alex, your incredible laugh always brought me so much joy. Thank you for the many great conversations we've had over many beers, for joining me in exploring the country, and for putting up with my ridiculously naive football predictions and commentary. I wish we'd had time to do more cycle camping trips, but that one we did do was fantastic (type 2) fun. Alicia, thank you for your wonderful socially-distanced deliveries of baked goods in the thick of lockdown. All the best to Freddie and Luna - cheers for keeping me company in exchange for food. Can't wait to visit you all in Oxford.

Vatsal, our very own shooting star. Thank you for giving the world the dance phenomenon that is the Vatsal floss. I'll miss your endless positivity that never failed to cheer me up, and your incredible cooking. Your aubergine roasting methodology may seem a little unorthodox, but I can't deny it works a treat. Cheers for all the movie recommendations (Lagaan, amirite?), and for our shared love of excellent urban design. Elspeth, I was so happy to have someone else around who really understands how cool birds are. I'll never forget the excitement of gathering a whole group of us at De Biesbosch and seeing the ospreys battling it out in the sky while the white-tailed eagle soared by. Thank you for teaching me how to identify, harvest, and cook chicken of the woods. I look forward to visiting you both in Coventry, and following the updates as things grow in your allotment. I hope Sisi is settling in and avoiding drama with the British cats.

Claire, thank you for your support through all the ups and downs and for being the perfect person to complain about all the nonsense going on in the UK with. You're one of the toughest people I know - I'm nowhere near brave enough to swim in the icy waters of Sloterplas! I'm glad we got to go on some great cycles together on those glorious Dutch summer days and talk about bikes while zooming along.

Deniz, your optimism and lovely energy always made me smile. Thank you for convincing us to visit cool bars other than Oerknal, even if some of them were all the way over in West. I hope you've finally moved into the bedroom in your apartment, for goodness sake.

Sinem, thanks for organising nice hangouts in the park - it was so fun surprising Deniz for his birthday!

Geert, the greatest sound guy that ever lived - we made quite the paranymph team! I'll really miss your sarcasm and comedic timing. Thank you for all the fun times on set, I hear there's Oscars buzz building...

Difeng, thanks for your quiet humour and for sharing so many great card games with us. I hope we get the chance to play that gigantic board game sometime. Anwesh, I'm grateful for our many interesting and pleasant conversations that covered such a wide range of topics. Evert, cheers for all the laughs and good times at Oerknal. Lieke, everyone at API is so glad that you imported the borrel from Leiden! Cheers for all the VrijMiBoCo fun, the barbecues, and for having the best rooftop hangout spot in all of Amsterdam. Hanneke, thank you for the lovely in-depth chats about Dutch/British culture, baby names, and politics, and for putting up with all the noise and chaos that us new kids brought to C4.144. Niloo & Patrick, thank you for your kindness and generosity, and for letting me stay at your place when I was in Leiden (+ eat your delicious cooking). Best of luck in Sweden! Let's play some games sometime soon. Dimitris, thank you for randomly popping into our office from time to time to bring some cheer to everyone! I'm so glad I made it to your defence party just in time for a hug. Pragya, thank you for your support and encouragement during my final months of thesis writing. Hearing your experiences really helped me believe I could make it to the finish line. Dante, Mark, Mitchel, and Omar, cheers for all the laughs and tomfoolery in the final year or two of my PhD (and for all the Slackmojis, of course - you know who you are). Stefanie, thank you for organising so many nice social occasions for everyone! I'll have to finally tell you that story next time I'm in Amsterdam. Floris, the API chess grandmaster. Thanks for your easy-going energy and your willingness to cameo in our defence movies. Kate, thank you for encouraging me to take the occasional break to socialise in the final phase of my PhD, and for your excellent karaoke choices. Oli, cheers for all the laughs and for sharing so many interesting facts and Dutch articles on WhatsApp. I can't wait to see your AI-generated thesis cover. Juan, I'm grateful for all the fun conversations we had at Oerknal early in my PhD - I hope we get the chance to catch up in Scotland soon. Koushik, Jure - thanks for the nice times we had on our high-altitude Benelux trip (and Jure, thanks for driving all that way!). Sarah, thanks for being part of our defence movie-making. The moment that phone started calling will be remembered as one of the best bloopers. Thallis, thanks for your advice about Brazil and for helping us figure out how to get those Maracanã football tickets. New Ben, keep fighting the good fight. Wendy, thank you for being part of our quaranteam during the lockdowns, and for the amazing rice cooker.

Thank you to the APIs who were in the final phases of their PhD when I was just starting - Alice, Macla, Georgi, Manos, Alicia, Smriti, Nina, Ylva, Mathieu, Daniele, Amruta, Samayra, Jakob, Kaustubh, Aastha, Matteo, Gullo - for warmly welcoming us new arrivals to the community and social scene, and for taking the time to impart some of your wisdom. And thank you to the many APIs I have not yet mentioned - Devarshi, Bas, Yves, Iris, Wanga, León, Niek, Pushpita, Caspar, Swapnil, Akshatha, Javier, Gibwa, Mark K., Kelly, Emily (and Delta, of course), Sam, Athira, Tomer, Emanuele, Tobi, Tuomo, Zsolt, Uddipta, Tana, Per-Gunnar,

Yuyang, David G., Leon, and more - for being part of this special place. I am grateful for my interactions with all of you at the many borrels, coffee breaks, pizza talks, defence receptions, Christmas parties, and API outings.

I would also like to thank my wonderful friends beyond Amsterdam. But first, I'm so sorry for how awful I have been at keeping in touch with you all over these 4.5 years - between the sometimes all-consuming nature of writing this thesis and the exhaustion of life during a global pandemic, I've often struggled to stay connected. It's one of my biggest regrets of this stage in my life. Nonetheless, I'm always so grateful for the occasions that we have been able to catch up, and hopefully I'll get to see more of you soon!

Tom & Chloe, the Finchams. Tom, thank you for being one of my oldest friends. We've been through and grown up so much together and although our lives have taken us in different directions, I'm so pleased that we're still in each other's lives. Thank you for all the fun, philosophical discussions, and your sage advice whenever I needed it. Chloe, it's been so lovely getting to know you and to see you and Tom build your lives together. Thank you for choosing me to be godfather to Teddy, a role I am deeply honoured to fulfil. I can't wait to meet Lily as well, and truly hope that I can be a bigger part of your lives now that I'm in the UK. Oh, and thank you for your wedding - who could have guessed that it would turn out to be such a key day in my life too?

Will, thank you for always being down to catch up whenever I'm in Somerset, and for sharing so much excellent music with me. When are we going to see Public Service Broadcasting for the 5th time? Let's plan a steam train journey through the Highlands. Sophie, I cannot thank you enough for your beautiful design for the cover of this thesis. It's amazing how you were able to take my vague and disconnected initial thoughts and create such a work of art. It was a pleasure working with you. Greg, we're not in touch much these days, but I always read and enjoy your film reviews. Verity, thanks for always bringing the energy. Sorry I haven't been to Mars yet, but I promise that you'll be one of the first to know if I do.

Cece, thank you for the lovely dinners and conversation that bookended my visit to Japan. I was at something of a crossroads in my life around that time, and it was quite special to catch up with an old friend on the other side of the world after so many years.

Shades, thank you for being one of the first people to show me that the space outside of my comfort zone is where the most growth and inspiration can be found, and for all your support and advice that helped make me who I am today. Thank you to you and your family for the amazing adventure in India - I miss you all, and will always be grateful for your kindness and generosity in welcoming me into your home. Kunal, you're the coolest guy. Thank you for taking me to all the best spots in Delhi. Elena, you are one of the most warm and sincere people I know. Thank you for always rooting for me and encouraging me to believe in myself, and for all your heartfelt messages in birthday/Christmas cards. Can I come and visit you in Cyprus soon? Max, I miss your unlimited levels of energy and enthusiasm! Thank you for all the laughs, and for organising all the amazing scavenger hunts.

Matt, thank you for visiting me in Amsterdam more than anyone! Thanks for being such a great flatmate back in Exeter, and for our adventures in the Netherlands in recent times. I'll

never forget our epic 137 km cycle through the forests and cities, nor the beer at the end of it. Joe, your feats of physical and mental endurance inspire me to push myself harder than ever. Thanks to you and Matt for convincing me to commit to the Amsterdam marathon, and for the good times we had that weekend. Let's do another challenge soon. Dan, the one and only head tenant. I miss your amazing dry humour and sarcasm, and all of our fun evenings discussing anything and everything at St John's Road. I loved listening to The Dan & Joe Show, you guys should bring it back. Rob, congrats on finishing your PhD too! Watching you and Meg grow loose tea project has brought me so much quiet joy, and I'm so excited to try all of your teas now that I'm back in the UK. Manraaj, thank you for the music and the vibes. I'm genuinely a big fan, and often find myself checking Spotify to see if you've dropped anything new. Ross, thanks for being a fellow astronomer in our little physics gang! Cheers for all the good times in Slovenia and Portugal, and for being the chief instigator of so many parties and gatherings in Exeter. I hope you and Ebony are loving life over in London. Jordan, congratulations on making it over the PhD finish line as well, and in such a different field from that of our MPhys. Kareem, thank you for taking Frank, Kenzie, and I on such great nights out in Cairo and Alexandria.

Shareen, thank you for all of our wonderful conversations about culture, philosophy, life, and more. I always love hearing all of your life updates whenever we catch up, and I'm so glad we got to see each other in Amsterdam before the pandemic closed all the borders. I hope I can finally get around to reading some more of your fantastic book recommendations now that I've finished writing this one.

Emma, I'm so glad we got to do our MPhys project together. Thank you for all of your support then and over the years that followed, for helping me settle in Edinburgh, and for sharing so many cute animal photos and videos. Best of luck for the last little bit of your PhD, you're almost there! Vic, thank you for all of your sound advice, and more importantly your infinite enthusiasm for Parkrun. I'm not sure I'd be running quite so much today if you and Emma hadn't gotten me down to the Quay first thing on those Saturday mornings.

The Space School mentor crew! Thank you to Áine, Ben, Colin/George, David, Dhan-Sham (for the inspiration), Heidi, Henry, Jack, Louise, Lucy, Nutter, Parth, Reena, Robson, Rosie, Sheila, Steph, Thor, Tim, Tracey, and many others for more than a decade of support (and fun). We're all off doing different things now, but it's pretty special being part of a group like this that looks out for each other and checks in from time to time. I hope we'll get to see more of each other now that I'm back in the UK.

Anna, I'm so glad we're still in touch after all these years! From Space School, to CERN, to Somerset, to Amsterdam, through it all you always knew where your towel was. Thank you for being such a supportive friend, for the postcard from Antarctica which I keep pinned up to this day, and most importantly for all of the tea.

Thank you to the Wells & Mendip Astronomers (Chris, Hugh, Adrian, Dick, Jo, Pete, Mark, Dani, Keith, Brian, Josh, Lilli, and countless others) for all of your encouragement over the last 10 years and for creating such a wonderful and friendly community to share our excitement for space. I hope I can see you all in person again the next time I'm in Somerset!

Edward, I'm so glad that we've been able to reconnect online in recent years. Thank you for always being interested in what I'm up to, and for all the nice photos of places and animals that you share on Facebook. They always help to lift me up when I'm feeling down.

I would also like to thank some of the many amazing people I have met while travelling. Andrea, I couldn't have wished for a better friend for our journey through Africa. When I'm feeling worried, I often think of you and am inspired by your courage in leaving your small hometown in Alberta to travel around the world on your own. Thank you for all of the postcards (they're on my wall!), and for convincing me to jump off that cliff in Zimbabwe. Nancy & Garrick, thank you for your generosity, kindness, and sense of fun, and for helping me figure out my U.S. visa application. Nancy, it was a joy to answer your students' space questions, and Garrick, I very much enjoyed that book you snuck into my bag on our last day of camping. Miles, Savanah - it was so great to meet you on our adventure in the north! Thank you for being the perfect company on that boat trip, and for bringing so much fun and warmth to a very cold place. To the folks from the Mongol Rally - Suz, Roger, Rob, Michele, Cody, Nancy, Scott, Morven, Adam, Charles, Richard, and so many more - thank you for all of the support, laughs, and hijinks on the road and for being such a key part of the trip of a lifetime. The occasions when a few of us get to meet up in one place or another to catch up and reminisce are very special to me. An additional thanks go to Nick and Josh, without whom that infamous incident in Ashgabat might have turned out so much worse than it did.

Mijn Nederlands is misschien niet zo goed, maar ik moet natuurlijk ook Nederland zelf bedanken. Bedankt dat jullie mijn thuis zijn voor deze belangrijke en speciale tijd in mijn leven. Het leven is gemakkelijk in Amsterdam. Ik zal uw prachtige fietspaden, uitstekende spoorweginfrastructuur en mooie landschap missen. Ik kom terug, vroeger of later.

Thank you to Carolyn, Kev, Lindsey, and Hugo for all of the delicious food, the escape to Mull, and for providing me with a home for a sizable part of my PhD. I'm very grateful for the sense of support and balance I felt at South View, which kept me motivated and cheerful during what otherwise could have been a very tough lockdown. A special thanks must also go to Basil & Chicku, for their vital supporting role in my writing process and enthusiasm for joining my Zoom meetings.

My family - this thesis is dedicated to you. You got me here, and I love you all. Thank you for your unconditional love throughout this journey and my entire life, and for always supporting me in my dreams. Thank you for your infinite patience when I was at my most grumpy and stressed. I would not be here today without the encouragement and opportunities that you gave me. Tracey & Ashley, thank you for all of your generosity and our happy catch-up calls. Your care packages of shortbread and dark chocolate treats helped carry me through the tough times. Nanna & Grandad, I am so grateful for all of your delicious cooking and baking, and for everything you've taught me about birds and nature, respectively. Gary, my brother, thank you for sharing so many games, movies, and shows with me, and for all of our energetic and excitable conversations about them. And for putting up with me, even when I wind you up. It's been so exciting watching you do so brilliantly on your own PhD journey. Kirby, thank you for keeping me company and warming my heart during those long final days of writing. Charlie, thank you for your 11 years of loyal friendship and our long walks

in the countryside - we all miss you. My parents, Mum & Dad, it's impossible to express how much I appreciate everything that you've given me. Thank you for working so tirelessly to give me so many opportunities, and for always being there to help me overcome any obstacle big or small. Mum, thank you for instilling in me a love for nature and the outdoors, and for taking me to and encouraging me to go to so many events and talks where I could grow and meet like-minded people. Dad, not many fathers and sons can say that they've had an adventure together like ours, especially in a little Suzuki Wagon (didn't I say I'd get it in here somewhere?). I can't wait for the next one.

Briony, my love, thank you for everything - I cannot imagine completing this journey without you by my side. Thank you for always bringing me so much calm and happiness in the midst of a storm, and for always being there for me on the best days and the worst days. Thank you for believing in me even when I doubted myself, and for giving me the confidence to make it here. You understand me more than anyone, and I'm so grateful for all of our amazing adventures, slow days indoors, and quiet moments. We make the best team.

Thank you, everyone. You all mean the world to me. Here's to the next thing.

Ben Sutlieff,
Edinburgh, 24th April 2023[1]

[1] Who am I kidding? I didn't write these acknowledgements in a single day...

I like it here.
Brian Sutlieff